UNIVERSITY OF CALGARY

Elastic Wave-equation Depth Migration of Seismic Data for Isotropic and Azimuthally Anisotropic Media

by

Richard Andrew Bale

A THESIS

SUBMITTED TO THE FACULTY OF GRADUATE STUDIES

IN PARTIAL FULFILMENT OF THE REQUIREMENTS FOR THE

DEGREE OF DOCTOR OF PHILOSOPHY

DEPARTMENT OF GEOLOGY AND GEOPHYSICS

CALGARY, ALBERTA

APRIL, 2006

UNIVERSITY OF CALGARY

FACULTY OF GRADUATE STUDIES

The undersigned certify that they have read, and recommend to the Faculty of Graduate Studies for acceptance, a thesis entitled "Elastic Wave-equation Depth Migration of Seismic Data for Isotropic and Azimuthally Anisotropic Media" submitted by Richard Andrew Bale in partial fulfilment of the requirements of the degree of Doctor of Philosophy.

Supervisor, Dr. Gary F. Margrave, Department of Geology and Geophysics

Co-supervisor, Dr. Robert R. Stewart, Department of Geology and Geophysics

Dr. Edward S. Krebes, Department of Geology and Geophysics

Dr. Michael P. Lamoureux, Department of Mathematics and Statistics

Dr. David W. Hobill, Department of Physics

External Examiner, Dr. Mauricio D. Sacchi, Department of Physics,
University of Alberta

Date

ABSTRACT

Two separate seismic processing steps for multicomponent data, shear-wave splitting correction and migration, are brought together in this thesis. The framework for doing this is the theory of elastic anisotropic propagator matrices, combined with generalized phase-shift plus interpolation (PSPI). The resulting extrapolation can be written as matrix pseudodifferential operators acting on vector wavefields. Each extrapolation step includes a decomposition based on eigenvectors of the Kelvin-Christoffel equation, a phase-shift step based on eigenvalues of the Kelvin-Christoffel equation and a recomposition step. It is the decomposition and recomposition operations which enable the shear-wave splitting correction within migration.

Practical implementation of this approach is achieved by a new method of adaptive spatial windowing, designed to minimize the number of Fourier transforms which are required to represent the pseudodifferential operator. The windows are made up of elementary Gaussian functions, and are selected based on minimizing a phase error criterion over a range of phase angles. This method is referred to as phase-shift plus adaptive windowing (PSPAW).

Another algorithm is derived for the special case of isotropic elastic media. This algorithm is closer in spirit to the original scalar PSPI algorithm, and relies upon approximate separation of the dependence on P-wave and S-wave velocities.

Both PSPAW and PSPI algorithms are tested on examples and compared with a reference, which is computed using the full pseudodifferential operator.

For both methods, a prestack depth migration scheme is constructed by the addition of an appropriate imaging condition. The PSPAW algorithm is used to apply prestack depth migration on a synthetic modelled dataset with a faulted HTI (transversely isotropic with horizontal symmetry axis) layer, and compared with isotropic migration on the same data.

Finally, the PSPI algorithm is tested on a new elastic version of the Marmousi dataset, known as Marmousi-2. The results reveal both the potential benefits of the method and areas where challenges remain.

ACKNOWLEDGEMENTS

I had the benefit of two excellent supervisors during my Ph.D. studies, Gary Margrave and Rob Stewart. This dissertation owes much to their respective contributions, guidance, and encouragement. Gary's combination of broad geophysical experience and attention to mathematical detail helped keep me on the path towards my goal. Rob, in addition to encouraging my initial enquiry into graduate studies, was a great help in developing my understanding of the research process and the importance of clear communication. Additionally I'd like to acknowledge Ed Krebes for his wonderfully comprehensive course on seismic wave propagation which provided much of the foundation on which this work has built.

I had the unusual privilege of coming to graduate study after several years in the geophysical industry. I owe thanks to both WesternGeco and Veritas, my former and current employers respectively, for enabling this study period without hardship. There are also many individuals, too numerous to name who have influenced my geophysical understanding. I would however like to mention specifically Steve Horne of Schlumberger, whose insights into anisotropic wave propagation I have valued greatly.

It was my original contact with CREWES as an industry sponsor which led me to Ph.D. studies in Calgary. I benefited greatly from the environment provided both by the CREWES consortium and the POTSI project. Among the many other CREWES people who have been valued for both their expertise and their friendship, I'd like to mention Jon Downton and Louis Chabot. I'd also like to thank Kevin Hall for his continual support of the Impala computing cluster and for tolerating my continual abuse of it. I'll clean my files up once I've defended, Kevin! Various people associated with POTSI, have provided stimulating discussion and ideas. In addition to the POTSI leaders, Gary Margrave and Michael Lamoureux, I'd like to thank Hugh Geiger and Jeff Grossman. Jeff's work on scalar extrapolation had a huge influence on my elastic work.

In addition to Gary Margrave who read and suffered through early drafts, I'd like to thank Pat Daley for his painstaking work in proof reading this dissertation.

Finally, I'd like to thank my wife, Ann, and my two daughters Melissa and Kirsten, for their willingness to go along with this adventure, which started as an eighteen month "vacation" from our life in the UK, and ultimately become a permanent move to Calgary.

During the last four and a half years, they have shown amazing fortitude and understanding when I've shown more attention to my computer than to them. I'm sure they're as glad as I am that the end is in sight. Every sentence in this dissertation has been checked for grammar and style by Ann. Usually the sentences have become shorter.

DEDICATION

For my wife Ann, and my daughters, Melissa and Kirsten.

TABLE OF CONTENTS

LIST OF TABLES

LIST OF FIGURES

LIST OF SYMBOLS AND ABBREVIATIONS

Below are listed the most important mathematical symbols used within this dissertation. Others are defined within the text as they are used.

$\mathbf{a}^T$	Transpose of (arbitrary) vector **a**.
$\mathbf{A}$	System matrix or fundamental elasticity matrix
$\mathbf{b}$	Displacement-traction vector
$\hat{\mathbf{b}}_i$	i^{th} column eigenvector (column of **D**)
c_{jlmn}	Stiffness tensor
$\mathbf{d}$	Polarization vector
$\mathbf{d}^{(M)}$	Polarization for mode $M \in \{P, S1, S2, SH, SV\}$
$\mathbf{D}$	Composition matrix (eigenvector matrix for system matrix **A**).
$\mathbf{D}_D$, $\mathbf{D}_U$	Down-going and up-going parts of decomposition matrix.
e_{jl}	Strain tensor
f	Temporal frequency
$\hat{\mathbf{g}}_i$	i^{th} row eigenvector (row of $\mathbf{D}^{-1}$)
k_x, k_y, k_z	Horizontal (inline), horizontal (crossline) and vertical wavenumber
$q_M^{U,D}$	Vertical slowness for mode M, and direction U or D.
Q, **R**, **T**	Elastic matrices (Stroh notation)
$\mathbf{s}$	Slowness vector
s_x, s_y, s_z	Horizontal (inline), horizontal (crossline) and vertical slowness
$s_z^{(M)}$	Vertical slowness, phase velocity, for mode $M \in \{P, S1, S2, SH, SV\}$
u_j	Particle displacement in the j^{th} direction
v	Velocity. For anisotropic media phase velocity.
v_M	Phase velocity, for mode $M \in \{P, S1, S2, SH, SV\}$
$\mathbf{v}$	Wavemode vector, containing amplitudes of six wavemodes (3 up-going and 3 down-going)
$\mathbf{W}(z_n+, z_n-)$	Interface propagator at depth z_n
$\mathbf{w}_D$, $\mathbf{v}_U$	Down-going source wavemodes, up-going receiver wavemodes.
x, y, z	Cartesian spatial coordinates

X, Y, Z	Source and receiver component directions
Γ_{ik}^{0} , $\Gamma_{ik}(\mathbf{s})$	Kelvin-Christoffel matrix, unit vector form and slowness form.
Λ	Diagonal eigenvalue matrix for **A**
$\mathbf{\Lambda}_D$, $\mathbf{\Lambda}_U$	Down-going and up-going parts of eigenvalue matrix.
ρ	Density
σ_{jl}	Stress tensor
$\boldsymbol{\tau}$	Traction vector (defined by $\tau_j = -\sigma_{j3}/(i\omega)$)
ω	Angular frequency
Ω_j	Spatial windowing function for j[th] window
GPSPI	Generalized phase shift plus interpolation
HTI	Transverse isotropy with a horizontal axis of symmetry
NSPS	Non-stationary phase shift
P	Compressional mode
POU	Partition of Unity
PSPAW	Phase shift plus adaptive windowing
PSPI	Phase shift plus interpolation
SV	Vertical shear mode-wave (polarized in plane of propagation)
SH	Horizontal shear-wave mode (polarized orthogonal to propagation plane)
S1, S2	Fast and slow shear-wave mode
VTI	Transverse isotropy with a vertical axis of symmetry
ΨDO	Pseudodifferential operator

CHAPTER ONE: INTRODUCTION

"If we knew what it was we were doing, it would not be called research, would it?"
-Albert Einstein

1.1 Exploration geophysics context

The permeability of many hydrocarbon reservoirs is enhanced by the presence of fractures. Knowledge of the fracture system is crucial to understanding the flow of reservoir fluids and planning for optimal drilling. The fractal nature of geologic processes suggests that fractures can be expected on all length scales, and this fits with observation (Lynn, 2004a; 2004b). At the upper end of the scale we have faults, which are visible in seismic images. Moving down in scale, other fractures will lie well beneath the limit of seismic resolvability. According to equivalent media theory, they nonetheless can be observed through seismic anisotropy. Azimuthal anisotropy, in particular HTI associated with vertical fractures, is one of the principal reasons for acquiring elastic seismic data, via multicomponent surveys. The shear-wave splitting, or "birefringence", associated with shear-wave propagation in fractured media is particularly diagnostic of the fracture orientation and intensity (Crampin and Chastin, 2003).

Sometimes, the goal is analysis of the shear-wave data in order to determine these parameters, and it is sufficient to use the data in this way without attempting to go further with imaging. However, often azimuthal anisotropy is also present in the overburden above a reservoir. Here, the anisotropy of these layers is not intrinsically interesting, but poses an impediment to imaging. Shear-wave splitting introduces time delays which cause the image to become confused and hard to interpret. For simple horizontally stratified media, and for near vertical propagation, the splitting effect can often be removed by static shifting of the fast and slow shear-wave modes to align them. However, in structurally complex geological settings, the passage through the overlying anisotropic region cannot be treated by simple time shifts.

Moreover, a target such as a fractured reservoir may itself be structurally complex, requiring a simultaneous treatment of azimuthal anisotropy and reservoir geometry issues. In cases where the structure is sufficient to cause significant deviation of the anisotropy axis from horizontal (i.e. tilted fractures) a more general form of anisotropy than HTI must be accommodated. Nevertheless, it is the present author's belief that there are many cases where the combination of anisotropy and faulting can be regarded as a good approximation as structured HTI.

A "canonical" example problem is to properly focus internal faults within a vertically fractured carbonate reservoir. Currently this is difficult to achieve with standard approaches to imaging of multicomponent data, which regard structure and azimuthal anisotropy as two separate problems. Therefore, a new approach in which they are addressed simultaneously and consistently is called for, and will be pursued here.

1.2 Elastic wave propagation

The earth is an elastic medium.[1]

Neglecting absorption, the equation which best describes the propagation of seismic waves in the earth is the elastic wave equation. This is in contrast to the acoustic wave equation which describes propagation of waves in a fluid medium, such as the ocean. The elastic wave equation is framed in terms of tensor operators acting on vector quantities. The acoustic wave equation is written in terms of scalar operators acting on scalar quantities. The scalar wave equation is much simpler to analyze, and easier to manipulate in order to construct inverse algorithms. It is also a good approximation, in many cases, to the behaviour of compressional waves within the elastic earth.

For these reasons, exploration seismology has focused primarily on use of the scalar acoustic wave equation, on which to base the development of processing and imaging algorithms. This is not the case for global seismology, which generally requires elastic theory from the outset. This is probably due to the relative importance of shear waves for global seismology[2].

Recently, interest has grown within exploration seismology in improved reservoir characterization from the analysis of both shear wave and anisotropic behaviour. This

[1] Actually, this statement is already a simplification. The earth is at least a viscoelastic medium, in which absorption losses give rise to attenuation and dispersion effects. However, these effects will not be addressed within this thesis.

[2] As a historical note, the compressional and shear wave abbreviations "P-wave" and "S-wave" stand for primary- and secondary-wave respectively, owing to their relative arrival times on earthquake seismograms.

has become possible through the use of multicomponent data to record the elastic wavefield (Thomsen, 1999; Stewart et al., 2002; 2003). It is therefore appropriate to consider elastic wave equation formulation for processing and imaging algorithms in exploration seismology. This is perhaps most obvious when dealing with shear waves and converted waves. However, it is also true that a proper treatment of anisotropy fundamentally demands an elastic viewpoint, even when only P-waves (or quasi-P waves, to be precise) are contemplated.

The theory of elastic wave propagation is comprehensively dealt with in many standard geophysical texts (e.g. Aki and Richards, 2002). Anisotropic wave theory is also well described in various textbooks (Musgrave, 1970; Auld, 1973). The following two sections give a brief summary of the theory which is pertinent to the subject of elastic wavefield extrapolation.

1.2.1 Momentum and constitutive equations

Wave propagation in elastic, anisotropic, heterogeneous media is governed by the momentum equation (Newton's second law)

$$\rho \ddot{u}_j = \sigma_{jl,l} + f_j , \tag{1-1}$$

where ρ is density, u_j is the component of displacement in the j^{th} direction, σ_{jl} is the stress tensor, and f_j is a body force. The body force term may refer to gravity or to an applied source term, depending on context. In this case it is taken to be an optional source term.

Above, and throughout this thesis, the convention used is that "$,l$ " denotes partial differentiation with respect to x_l, the l^{th} spatial coordinate. The Einstein summation convention is also used, whereby twice-repeated indices indicate an implied summation. Indices repeated more than twice will be taken to imply that the summation convention is suspended. All indices take the values 1, 2 and 3, though to clarify x,y and z are used when appropriate. The second time derivative of u is indicated by $\ddot{u}$.

The constitutive equation, which describes the relationship between the stress σ_{jl} and the strain e_{mn} (generalized Hooke's law), is given by

$$\sigma_{jl} = c_{jlmn} e_{mn}, \tag{1-2}$$

where c_{jlmn} is the 4th rank stiffness tensor. In turn the strain tensor is given by:

$$e_{mn} = \frac{1}{2}\left(u_{m,n} + u_{n,m}\right). \tag{1-3}$$

Equation (1-3) shows that the strain tensor is symmetric. Simple physical arguments can be used to show the symmetry of the stress tensor. These symmetries, taken together, imply that the stiffness tensor is symmetric under interchanges of *j* with *l*, and *m* with *n*. Energy considerations further imply symmetry under interchange of *jl* with *mn*. The net result is, that for the most general elastic medium, there are "only" 21 independent elastic coefficients rather than the 81 of an arbitrary 4th rank tensor. Also the following coordinate transformation rule is useful for creating arbitrary symmetries:

$$c'_{ijkl} = \left(\frac{\partial x'_i}{\partial x_m}\right)\left(\frac{\partial x'_j}{\partial x_n}\right)\left(\frac{\partial x'_k}{\partial x_p}\right)\left(\frac{\partial x'_l}{\partial x_q}\right) c_{mnpq}. \tag{1-4}$$

An alternative representation of the stiffness uses Voigt (Musgrave, 1970) notation to replace the 4th rank tensor c_{jlmn} by a symmetric 6x6 matrix $\mathbf{C}$ as follows:

$$\mathbf{C} \equiv \begin{pmatrix} c_{1111} & c_{1122} & c_{1133} & c_{1123} & c_{1113} & c_{1112} \\ & c_{2222} & c_{2233} & c_{2223} & c_{2213} & c_{2212} \\ & & c_{3333} & c_{3323} & c_{3313} & c_{3312} \\ & & & c_{2323} & c_{2313} & c_{2312} \\ & & & & c_{1313} & c_{1312} \\ & & & & & c_{1212} \end{pmatrix}$$

$$= \begin{pmatrix} C_{11} & C_{12} & C_{13} & C_{14} & C_{15} & C_{16} \\ & C_{22} & C_{23} & C_{24} & C_{25} & C_{26} \\ & & C_{33} & C_{34} & C_{35} & C_{36} \\ & & & C_{44} & C_{45} & C_{46} \\ & & & & C_{55} & C_{56} \\ & & & & & C_{66} \end{pmatrix}, \tag{1-5}$$

where the lower half of the matrix is implied by symmetry.

Likewise the stress and strain tensors may be written in a vector form as

$$\boldsymbol{\sigma} \equiv \begin{pmatrix} \sigma_{xx} \\ \sigma_{yy} \\ \sigma_{zz} \\ \sigma_{yz} \\ \sigma_{xz} \\ \sigma_{xy} \end{pmatrix} \quad \text{and} \quad \mathbf{e} \equiv \begin{pmatrix} e_{xx} \\ e_{yy} \\ e_{zz} \\ 2e_{yz} \\ 2e_{xz} \\ 2e_{xy} \end{pmatrix}, \tag{1-6}$$

so that the stress-strain relationship of equation (1-2) is rewritten as:

$$\boldsymbol{\sigma} = \mathbf{Ce}\,. \tag{1-7}$$

Note, however, that (1-7) is not a tensor equation as it is not invariant under rotation.

For isotropic media, the stiffness tensor takes the form (e.g. Aki and Richards, 2002)

$$c_{ijkl} = \lambda \delta_{ij}\delta_{kl} + \mu\left(\delta_{ik}\delta_{jl} + \delta_{il}\delta_{jk}\right) \tag{1-8}$$

and equation (1-5) becomes

$$\mathbf{C} \equiv \begin{pmatrix} \lambda+2\mu & \lambda & \lambda & & & \\ \lambda & \lambda+2\mu & \lambda & & & \\ \lambda & \lambda & \lambda+2\mu & & & \\ & & & \mu & & \\ & & & & \mu & \\ & & & & & \mu \end{pmatrix}. \tag{1-9}$$

In equation (1-9), the elements omitted are equal to zero. The parameters λ and μ are the well-known Lamé moduli.

Combining equations (1-1), (1-2) and (1-3), and considering a source free medium, the elastic wave equation is obtained as

$$\rho \ddot{u}_j = \frac{\partial}{\partial x_l}\left(c_{jlmn} u_{m,n}\right). \tag{1-10}$$

In a homogeneous medium, or one where the spatial variation of the medium parameters is slow when compared with the wavelength of propagation, the spatial derivative of the stiffness tensor may be neglected to give

$$\rho \ddot{u}_j = c_{jlmn} u_{m,nl} \,. \tag{1-11}$$

1.2.2 The Kelvin-Christoffel equation

The polarization vector, defined as a unit vector with the direction of particle displacement, is denoted by $\mathbf{d} = (d_1 \quad d_2 \quad d_3)^T$. The slowness vector, defined as the vector with direction parallel to phase velocity[1] and magnitude equal to the reciprocal of phase velocity, is denoted by $\mathbf{s} = (s_1 \quad s_2 \quad s_3)^T$.[2]

Substitution of plane-wave trial solutions of the form $\mathbf{u} = U\, e^{i\omega(\mathbf{s}\cdot\mathbf{x}-t)}\,\mathbf{d}$, into (1-11), gives the Kelvin-Christoffel equation (Musgrave, 1970), which can be written in either of two forms

$$\left(\Gamma^0_{ik}(\hat{\mathbf{n}}) - v^2 \rho \delta_{ik}\right) d_k = 0 \,, \tag{1-12}$$

or

$$\left(\Gamma_{ik}(\mathbf{s}) - \rho \delta_{ik}\right) d_k = 0 \,, \tag{1-13}$$

where $\Gamma^0_{ik}(\hat{\mathbf{n}}) = c_{ijkl} \hat{n}_j \hat{n}_l$ and $\Gamma_{ik}(\mathbf{s}) = c_{ijkl} s_j s_l$ are the two forms of the Christoffel matrix, $\hat{\mathbf{n}} = v\mathbf{s}$ is the unit vector in the slowness direction, with v being an eigenmode velocity, and δ_{ik} is the Krönecker delta function.

The first form, equation (1-12), gives rise to a true eigenvalue problem, in which the eigenvalues are $v^2 \rho$. In general, there are three such values corresponding to qP (quasi-P), qS1 (quasi-S1) and qS2 (quasi-S2) modes[3]. Since $\mathbf{\Gamma}^0$ is real, symmetric and positive definite, for real $\hat{\mathbf{n}}$ (Musgrave, 1970), all eigenvalues are real and positive, giving real velocities, which can be chosen positive. The normalized eigenvectors are the polarizations, $\mathbf{d}$, which are orthogonal for a given $\hat{\mathbf{n}}$.

---

[1] The term "velocity" is used throughout this dissertation to indicate "wavespeed". This is based on common usage within exploration geophysics, even though usually referring to scalar quantities.

[2] Here, and subsequently within, the superscript *T* indicates the transpose of a vector or matrix. It is often used simply to allow a column vector to be rewritten as a transposed row vector within the text.

[3] The qualifying term "quasi" is necessary when dealing with anisotropic materials. In such materials it is no longer possible to identify P-waves as those which have displacements in the same direction as their propagation direction, and S-waves as those which have displacements orthogonal to their propagation

The second form, equation (1-13), is more convenient for wavefield extrapolation, since we may fix the radial (horizontal) slowness $\mathbf{s}_r = (s_x, s_y) \equiv (s_1, s_2)$, and solve for the vertical slowness $s_z \equiv s_3$. In this alternative problem, the "eigenvalues" (a misuse of the term, but common in the literature) are the values of s_z. The characteristic equation $\det(\Gamma_{jl} - \rho\delta_{jl}) = 0$ has 6 roots for s_z. For non-evanescent waves (real s_z), the matrix $\mathbf{\Gamma}$ is real and symmetric; however, it is *not* the case that the resulting polarization "eigenvectors" are orthogonal. For example, if we consider the qP, qS1 and qS2 waves associated with a given radial slowness, $\mathbf{s}_r$, (but different vertical slownesses), they correspond to three different slowness directions, $\hat{\mathbf{n}}$, and have non-orthogonal polarizations. This is illustrated in Figure 1.1.

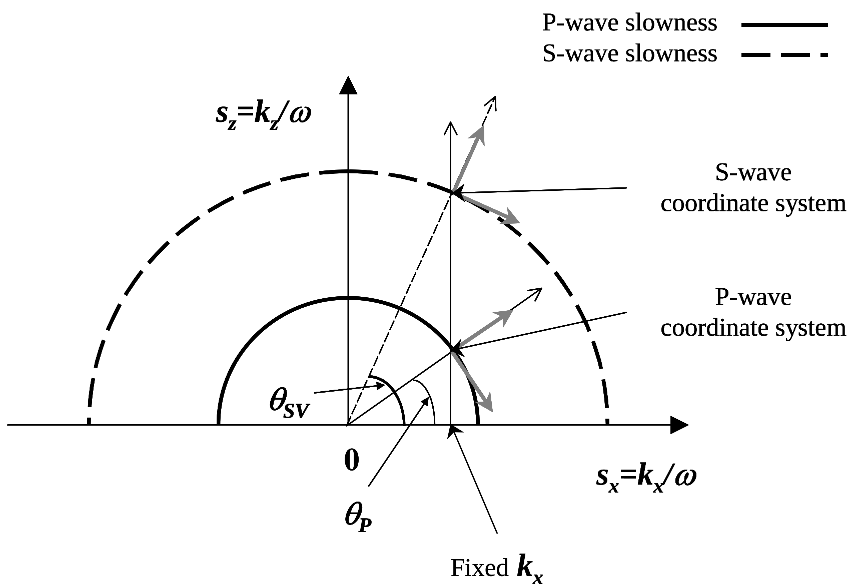

Figure 1.1. P-wave and S-wave phase velocities (bold and dashed curves). Phase angles θ_P and θ_{SV} (isotropic case) for a given horizontal slowness, s_x, corresponding to fixing k_x for a given frequency ω.

---

direction. The direction of propagation and displacement are not simply related for anisotropic materials except in certain favoured directions.

1.3 HTI: Transverse isotropy with a horizontal symmetry axis

The methods for wavefield extrapolation developed in this thesis are applicable to a range of anisotropic symmetries, provided there is a horizontal symmetry plane. However, it is useful to focus on one specific symmetry system for illustrative purposes. An important type of anisotropy for exploration and reservoir description is transverse anisotropy with a horizontal symmetry axis, more succinctly known as "HTI anisotropy", or simply "HTI".[1] HTI is believed often to be associated with the presence of vertical fractures embedded in an otherwise isotropic rock matrix. Such fractures may give rise to increased permeability and are therefore of great interest for increased production from hydrocarbon reservoirs. Consequently, there is much active research into the behaviour of both P-wave and S-wave propagation in HTI rocks. The presence of fractures gives the rock a greater strength in directions parallel to the fracturing compared with the perpendicular direction, much as a deck of playing cards is more rigid parallel to the card faces than it is perpendicular to them (see Figure 1.2). HTI can also arise due to differential stresses within the earth.

With respect to seismic wave propagation, there is a variation in the seismic velocity with direction for both P- and S-waves in an HTI medium. The plane parallel to the fractures is known as the isotropy plane (since all directions are equivalent within it). The vertical plane perpendicular to the fractures is known as the symmetry plane. Generally speaking waves propagating parallel to the isotropy plane experience a more rigid medium, and so travel with a higher velocity, than waves parallel to the symmetry plane. For S-wave velocities, HTI also causes a dependence on the polarization of the S-wave. S-waves polarized parallel to the isotropy plane propagate faster than those polarized orthogonal to it. These are often referred to as the fast and slow shear waves, or as S1 and S2.

---

[1] HTI is a particular case of "azimuthal anisotropy". Azimuthal anisotropy occurs whenever the velocity depends upon the azimuth of the ray-path, but not upon the angle relative to vertical. Multiple vertical fracture sets are also azimuthally anisotropic, but may not necessarily be HTI.

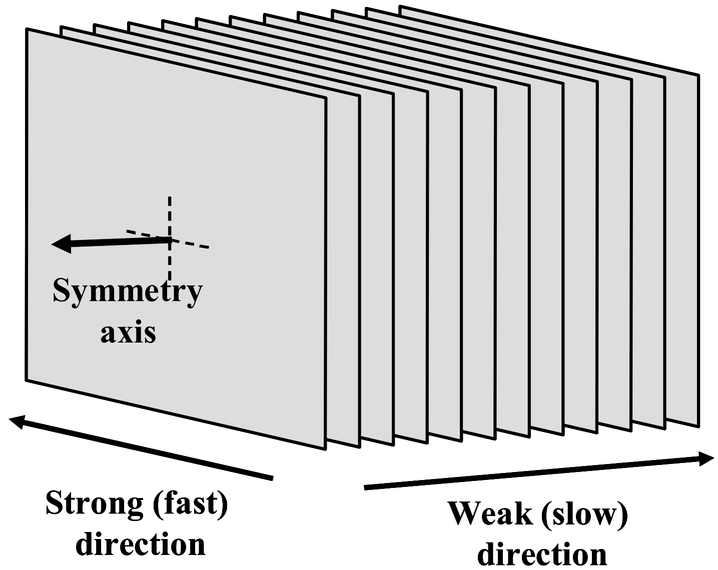

Figure 1.2. Schematic depiction of an HTI medium. The presence of vertical fractures causes different strengths of the rock parallel and perpendicular to the fractures. HTI can also arise due to differential stresses within the earth.

A general introduction to HTI can be found in Thomsen (1988). As with his paper on transverse isotropy with a vertical axis (VTI) (Thomsen, 1986), largely based on the work of Daley and Hron (1977), Thomsen's primary purpose is to simplify existing theory and introduce convenient intuitive parameterization. Thomsen (1988) also elucidates the phenomenon of shear-wave splitting, or shear-wave birefringence, which is uniquely characteristic of azimuthally anisotropic media. The paper includes an explanation of the Alford rotation method for determining the orientation of fractures in such media – an explanation which is more detailed than the account given in Alford's original SEG abstract (Alford, 1986). Another useful reference on anisotropy in general, including transverse isotropy, is Winterstein (1990). Winterstein's purpose is to standardize terminology within the exploration seismology community. This thesis follows his terminology in most cases.[1] More recently, a substantial effort has been made by Tsvankin and colleagues at the Colorado School of Mines to provide useful descriptions of both P-wave and converted-wave kinematic behaviour for different

[1] Though for example the abbreviation "TIH" used by Winterstein, is discarded in favour of the currently more usual "HTI". However, both terms are in common use.

anisotropic symmetries, including VTI (e.g. Tsvankin, 1996), HTI (e.g. Tsvankin, 1997), and orthorhombic media (e.g. Grechka and Tsvankin, 1999).

When expressed in a coordinate system such that the symmetry axis is parallel to the *x*-axis, an HTI medium has a stiffness matrix [equation (1-5)], which has the form

$$\mathbf{C} = \begin{pmatrix} C_{11} & C_{13} & C_{13} & & & \\ C_{13} & C_{33} & C_{23} & & & \\ C_{13} & C_{23} & C_{33} & & & \\ & & & C_{44} & & \\ & & & & C_{66} & \\ & & & & & C_{66} \end{pmatrix}, \tag{1-14}$$

with the constraint $C_{44} = \frac{1}{2}\left(C_{33} - C_{23}\right)$, and spaces indicating zeros.

The number of independent variables for an HTI medium can be seen from equation (1-14) to be 5, taking into account the constraint. This assumes the symmetry axis is aligned with the *x*-axis. In general, the direction of the symmetry axis is itself an independent variable. Hence a total of 6 quantities are needed to uniquely specify an HTI medium. The stiffness tensor for an arbitrary set of coordinate axes can be calculated from the coordinate frame defined by the symmetry axis using equation (1-4). The result can then be re-expressed as a 6x6 matrix form by using the Voigt mapping, as defined in equation (1-5).

Alternatively the coordinate transformation can be written directly as a Bond transformation (Auld, 1973, pp.73-85; Winterstein, 1990) applied directly to the stiffness matrix, **C,** as

$$\mathbf{C}' = \mathbf{MCN}^T . \tag{1-15}$$

(See above references for definitions of **M** and **N**).

The effect of choosing such an arbitrary reference frame, in which the symmetry axis is not aligned with either of the coordinate axes, is that the stiffness matrix no longer has the simple form of equation (1-14). Instead it has several other non-zero terms.

1.4 Recursive wavefield extrapolation

Many modeling and migration algorithms are fundamentally based on the concept of extrapolation, in which the wavefield is marched along a specified axis in small steps, using some form of wave equation. Broadly speaking there are two main types of algorithms – time extrapolation and depth extrapolation.

Extrapolation in time is the favoured approach for forward modeling, and is the basis for finite difference modeling as well as techniques such as pseudospectral modeling (Carcione et al., 2002). It also has been advocated as a method for migration, known as "reverse time migration", (Baysal et al., 1983). Extrapolation in time is based upon use of the full two-way wave equation, and offers the advantage that multi-pathing is naturally included. This can also become a disadvantage when the velocity model is not known with sufficient accuracy, since artifacts can arise from multiply scattered energy.

The alternative, extrapolation in depth, is based instead upon the concept of a one-way wave equation. Use of a one-way wave equation avoids some of the complexity associated with multiple scattering, is more robust to velocity errors, and is in general more computationally efficient than methods based on the full two-way wave equation.

1.4.1 The one-way wave equation

In two dimensions, the scalar Helmholtz equation is written

$$\frac{\partial^2\psi}{\partial x^2}+\frac{\partial^2\psi}{\partial z^2}+\frac{\omega^2}{c^2(x,z)}\psi=0\,. \tag{1-16}$$

In cases where the medium velocity, c, depends on depth alone, Fourier transform along the x coordinate, gives

$$\frac{\partial^2\varphi}{\partial z^2}+\left(\frac{\omega^2}{c^2(z)}-k_x^2\right)\varphi=0\,, \tag{1-17}$$

where

$$\varphi(k_x, z) = \int_{-\infty}^{\infty} \psi(x,z)\, e^{ik_x x} dx \qquad (1\text{-}18)$$

is the Fourier transform of the wavefield $\psi(x,z)$. If c is constant over the depth interval of interest, the one-way wave equation can be derived by a simple factorization of (1-17),

$$\left(\frac{\partial}{\partial z} + ik_z\right)\left(\frac{\partial}{\partial z} - ik_z\right)\varphi = 0\,, \qquad (1\text{-}19)$$

where

$$k_z = \sqrt{\frac{\omega^2}{c^2} - k_x^2}\ . \qquad (1\text{-}20)$$

The solution of (1-19) is a linear combination of solutions which obey one of the two one-way equations

$$\left(\frac{\partial}{\partial z} + ik_z\right)\varphi = 0\,, \qquad (1\text{-}21)$$

and

$$\left(\frac{\partial}{\partial z} - ik_z\right)\varphi = 0\,. \qquad (1\text{-}22)$$

The separability of equation (1-19) results directly from the z independence of the velocity c, and implies that solutions decouple into upward and downward terms. Solutions to (1-21) are up-going waves, whereas solutions to (1-22) are down-going. Using one-way wave equation solutions, when the medium varies with depth, corresponds to neglecting interaction (transmission and reflection) effects.

In terms of the original wavefield, the one-way wave equations are formally written

$$\left(\frac{\partial}{\partial z} + i\Gamma\right)\psi(x,z) = 0\,, \qquad (1\text{-}23)$$

and

$$\left(\frac{\partial}{\partial z} - i\Gamma\right)\psi(x,z) = 0\,, \tag{1-24}$$

where

$$\Gamma \equiv \sqrt{\left(\frac{\omega}{c}\right)^2 + \frac{\partial^2}{\partial x^2}}\,. \tag{1-25}$$

Assigning a meaning to the square-root operator, Γ, is possible in this case because of the *x* independence of the velocity *c*, so that

$$\Gamma^2 = \left(\frac{\omega}{c}\right)^2 + \frac{\partial^2}{\partial x^2}\,. \tag{1-26}$$

Use of a square-root operator when *c* varies with *x* is not strictly correct. However this approximation has been successfully used in many seismic extrapolation algorithms. The one-way extrapolator which satisfies (1-16), and propagates the wavefield from depth z_0 to *z*, is given by

$$\varphi(k_x, z) = \exp\left[ik_z(z - z_0)\right]\varphi(k_x, z_0)\,, \tag{1-27}$$

as can be verified by direct substitution.

By using equation (1-27) recursively the wavefield may be extrapolated to arbitrary depths from the depth at which it has been measured, usually taken as $z = 0$.

1.4.2 Historical review

In exploration geophysics, the idea of using recursive wavefield extrapolation, together with an imaging condition, as a tool for mapping reflectors to their correct positions, grew out of the early work of Claerbout and the Stanford Exploration Project group (Claerbout, 1971; Claerbout and Doherty, 1972). Their methods used finite difference approximations, based upon the "15-degree" paraxial ray equation, which is identical to the Schrödinger equation of quantum mechanics, and later a "45-degree" equation. Both of these are derived from the scalar Helmholtz equation (1-16) by truncated series expansions of increasing order. An important realization was the need to use depth as the vertical coordinate rather than time, when dealing with lateral velocity variations (Judson et al., 1980; Schultz and Sherwood, 1980).

The method of space-frequency domain extrapolation using convolutional filters derived from the wavenumber operator response has especially been championed by Berkhout and associates at Delft University (Berkhout, 1981; Wapenaar, 1989). Spatial domain filters have the attractive property that they can be easily varied to accommodate velocity changes in the lateral directions. The most widely used space-frequency filters are explicit, or finite impulse response (FIR), filters. Their main disadvantage is that stability is not automatic. The simplest approach is to design filters according to their exact wavenumber domain response, and then truncate them in the spatial domain. This always results in operators which amplify the wavefield excessively for simple velocity models (Holberg, 1988). This issue has been (and remains) one of the most active areas of research for wavefield extrapolation (Hale, 1991). The difficulty is that there is an inevitable trade-off between stability and accuracy for steep reflector dips.

As an alternative to spatial domain convolution, Gazdag advocated direct application of the extrapolation operators in the frequency-wavenumber domain (Gazdag, 1978). This technique, commonly referred to as "phase-shift migration", has the immediate advantage of combining steep dip accuracy with guaranteed stability, but at the cost of inability to handle lateral velocity variations. For this reason, it was soon followed by a modification in which the extrapolation is performed several times with different velocities, and the results interpolated. This is the well-known phase-shift plus interpolation (PSPI) algorithm (Gazdag and Sguazerro, 1984). Although not apparent at the time, these authors were gradually moving towards the idea of implementing extrapolation as a pseudodifferential operator. This relationship was eventually brought to light during the later work on non-stationary phase-shift migration by Margrave and Ferguson (1999), as discussed in the next section.

Other ideas abound for either improving the performance of phase-shift extrapolation in the presence of velocity variations, or combining phase-shift with finite difference in hybrid approaches. For example, there is a class of algorithms based upon a dual-domain approach. In these, a phase-shift correction in the wavenumber domain is followed by an inverse Fourier transform to the spatial domain where a correction for the local velocity variation is applied. The simplest is a 'static' shift based upon the difference between the reference and actual velocity. This is known variously as split-step or phase-screen migration (Stoffa et al., 1990). A method which improves upon split-step in accuracy for similar cost is the Fourier finite difference method of Ristow and Ruhl (Ristow and Ruhl, 1994; Ruhl et al., 1995). In this method, the spatial domain operator is a finite-difference correction to the phase-shift. There are also techniques, known as generalized phase-screen (Le Rousseau and de Hoop, 2001), which extend the phase-screen method by repeated alternation between wavenumber and space domains.

It is worth commenting here that many of the methods described above, within the context of exploration geophysics, have been independently pre-discovered or re-discovered in other disciplines, such as ocean acoustics and atmospheric physics. Often different terminology obscures the connections.

1.4.3 Pseudodifferential operator (ΨDO) forms of wavefield extrapolator

The above discussion of the phase-shift migration method alerts us to a fundamental contradiction when using the wave-number domain for spatially varying operators. The correct operator apparently has a simultaneous dependence upon both the spatial variable, x, and upon its Fourier dual variable k_x. The implication is that the operator can no longer be expressed as a pure Fourier transform, but rather by a pseudodifferential operator (ΨDO). There is a rich mathematical body of ΨDO theory, a branch of partial differential equations theory. An introduction to the subject is found in Saint Raymond's book (Saint Raymond, 1991). A detailed description would include discussion of such matters as Sobolev spaces, wavefront sets and microlocal analysis - topics outside the scope of this thesis. For our purposes, a ΨDO may be thought of as a generalization of the Fourier transform. For example, the equation which describes generalized PSPI (GPSPI) for the scalar wave-equation is

$$\psi(x,z)=\frac{1}{2\pi}\int_{-\infty}^{\infty}\alpha(x,k_x,0)\,\varphi(k_x,z)\,e^{-ik_x x}dk_x \;, \qquad (1\text{-}28)$$

where

$$\alpha(x,k_x,z) \equiv \exp\left(iz\sqrt{\left(\frac{\omega}{c(x)}\right)^2 - k_x^2}\right), \tag{1-29}$$

is the wavefield extrapolator, with spatially varying velocity $c(x)$.

The term α is known as the “symbol” of the operator. As can be seen from (1-29), the symbol is a mixed domain kernel in which the spatial and wavenumber dependence is treated on equal terms. Equation (1-28) is still an approximation in the sense that it is based upon the square-root operator of equation (1-25), which is only correct for a homogeneous medium.

The implementation of the square-root operator, using a ΨDO, is non-unique. For example, there is an adjoint form of equation (1-28), which is known as nonstationary phase shift (NSPS) (Margrave and Ferguson, 1999; Ferguson, 2000). In ΨDO terminology, GPSPI is in anti-standard form, while NSPS is in standard form. There is also an intermediate form, known as the Weyl operator. The standard, anti-standard and Weyl ΨDO implementations of phase-shift extrapolation have somewhat differing properties, and can give visibly different results for large depth steps, though their behaviour converges as the depth step shrinks (Ferguson and Margrave, 2002).

In practice, efficiency demands that the full ΨDOs of GPSPI or NSPS are approximated using a set of spatially invariant reference operators and an interpolation scheme, such as Gazdag's PSPI, in order to allow use of the fast Fourier transform.

Other authors have applied the mathematical tools of ΨDOs to the analysis of phase-screen type operators. An interesting application is the generalized phase-screen approach of Le Rousseau and de Hoop (2001a; 2001b) mentioned in the previous section. They use ΨDO theory to evaluate the square-root operator in a heterogeneous medium.

1.4.4 Alternatives to the square-root operator

As noted in section 1.4.1, the square-root operator is only exact for media with no transverse (*x*-direction) variation. Although the square-root approximation will be the basis for the elastic operators used in this thesis, it is worth noting that work has been done by several researchers to move beyond the square-root operator. Fishman and

McCoy (1985) derive an exact extrapolator for what they refer to as "range independent" media with transverse variation. Some care is needed when reading this paper from an exploration seismology background, as the direction of propagation (the range direction) they use is horizontal direction, while their transverse direction is vertical. The theory is applicable to depth extrapolation in exploration seismology if the range is considered to be the vertical direction instead. The exact operator is derived by considering the full Helmholtz operator

$$\Omega^2(x) = \left(\frac{\omega}{c(x)}\right)^2 + \frac{\partial^2}{\partial x^2} \ , \qquad (1\text{-}30)$$

as the composition of an unknown ΨDO, Ω, with itself, using the composition equation of pseudodifferential calculus (Saint Raymond, 1991, p.37).

1.4.5 Elastic wavefield extrapolation migration

The basic theory of elastic wavefield extrapolation is not new. Wapenaar and Berkhout (1989) give a comprehensive exposition of this theory using both two-way and one-way wave equations, for the case of isotropic media. Zhe and Greenhalgh (1997) proposed a migration algorithm for elastic waves in isotropic media. Their extrapolation step consists of decomposing the displacement into potentials via the Helmholtz decomposition, extrapolating the potentials using a split-step technique (Stoffa et al., 1990), and then recomposing to displacement. Their method uses a finite-difference wavefield decomposition, which requires knowledge of the wavefield at a few adjacent depth intervals in order to compute the vertical derivative. The depth steps are initialized below the surface by applying a few steps of reverse time migration. Etgen (1988) performed wavefield separation in the wavenumber domain using Fourier transformed divergence and curl operators, applied to the displacement data, before scalar migration of P- and SV- potentials with a Stolt (1978) algorithm. Hou and Marfurt (2002) sidestep the decomposition problem by extrapolating each component of displacement using scalar extrapolators, and applying the separation step as part of the imaging condition. They found that doing this enabled a PS separation which is less sensitive to model errors. A possible disadvantage, particularly for anisotropic media, is the need to extrapolate each of 3 components using 3 different models.

The Helmholtz decomposition for elastic waves is only valid for homogeneous isotropic media. As shown by Dellinger and Etgen (1990), the Helmholtz decomposition can be generalized to anisotropic media by using the Kelvin-Christoffel equation. Though not originally suggested for application within a migration scheme, this idea, combined with Etgen's (1988) migration technique above (or other methods) offers a possible approach to *anisotropic* elastic migration.

1.5 Thesis origins

> *"I may not have gone where I intended to go, but I think I have ended up where I intended to be."*
> -Douglas Adams

The original idea for this thesis came from thinking about shear-wave splitting, and the limitations of the vertical propagation based theory. This vertical propagation, normal-incidence assumption is basic to many of the techniques conventionally used to correct shear-wave spitting effects. For example, Thomsen (1988, p.305) states

> "Assume that a conventional stack of a CMP gather forms a trace which is an accurate surrogate for a normal-incidence, multiple-free, noise reduced trace. Although this assumption is not one to be taken casually, the results of Alford (1986b) and Willis et al. (1986) suggest that it is acceptable in the present context."

Similarly, in a paper describing the Linear Transform Technique (LTT) developed by the Edinburgh Anisotropy Project, Li (1997, p.47) states

> "Assuming orthogonally polarized and vertically propagating split shear waves, shear-wave splitting can be simulated by a two-component eigensystem, with the eigenvectors representing the polarizations, and the eigenvalues representing the amplitudes, of the two split shear waves."

Following Li (1998), an equation which describes the recorded response from a P-S mode conversion at depth, for 2-D geometry, after vertical propagation through a homogeneous HTI medium is

$$\begin{pmatrix} U_x(\omega) \\ U_y(\omega) \end{pmatrix} = \mathbf{R}^T(\phi) \begin{pmatrix} f_1(\omega)e^{i\omega\tau_1} & 0 \\ 0 & f_2(\omega)e^{i\omega\tau_2} \end{pmatrix} \mathbf{R}(\phi) \begin{pmatrix} U_{PS}(\omega) \\ 0 \end{pmatrix}. \qquad (1\text{-}31)$$

Here U_{PS} represents the effective shear wave source due to a mode conversion at depth, U_x and U_y are the recorded wavefields for inline (X) and crossline (Y) geophones respectively, ϕ is the azimuthal angles of the fracture strike, measured with respect to the (inline) *x*-axis, and $R(\phi)$ is a 2-D rotation matrix through angle ϕ. The diagonal matrix nested between the rotations describes propagation delays for the fast (S1) and slow (S2) modes by τ_1 and τ_2 respectively, and amplitude modulation by f_1 and f_2 respectively.

Since it is a modeling equation, the corresponding processing step is the inverse of equation (1-31) which determines U_{PS} from measurements of U_x and U_y. The inverse equation reads,

$$\begin{pmatrix} U_x(\omega,z) \\ U_y(\omega,z) \end{pmatrix} = \mathbf{R}^T(\phi) \begin{pmatrix} e^{-i\omega\tau_1(z)} & 0 \\ 0 & e^{-i\omega\tau_2(z)} \end{pmatrix} \mathbf{R}(\phi) \begin{pmatrix} U_x(\omega,0) \\ U_y(\omega,0) \end{pmatrix}, \qquad (1\text{-}32)$$

where the depth dependence has now been made explicit, amplitude effects have been omitted, and no assumption is made that the displacement of the wavefield at depth is aligned with the source-receiver azimuth.

As indicated above, the implicit assumptions of equations of (1-31) and (1-32) are:

1. Vertical propagation
2. Orthogonal S1 and S2

Notice also that in going from equation (1-31) to equation (1-32) U_{PS}, a wavefield associated with the shear-wave mode arising from conversion, has been rather casually replaced by a displacement wavefield, U_x (and U_y). This identification of shear-wave modes with horizontal components of the displacement only strictly makes sense for waves propagating in the vertical direction. It is a common approximation in converted-wave processing, but is certainly incorrect in general.

While these assumptions may be acceptable for low relief structure and small offset ranges, they are clearly inappropriate assumptions for data where depth migration is considered to be necessary. So for example, to simply substitute migrated versions of U_x and U_y into the inverse of equation (1-31), would *not* be a valid approach to correcting for shear wave splitting in structurally complex areas. Let us consider, in general terms, how equation (1-32) might be modified to accommodate depth migration. The obvious modification is to replace the simple shift operators $\exp(i\omega\tau_{1,2})$ with wavefield extrapolation operators of the form $\exp(ik_z^{1,2}\Delta z)$ in a recursive scheme. This would incorporate angle dependence into the shift operations, and allow for the inclusion of angle dependent velocities for both shear modes. A (slightly) more subtle modification, which is necessary, is to replace the rotation matrices **R** with angle dependent rotation matrices, to move beyond both the vertical incidence and orthogonality assumptions. Thus, one might expect a modified form of equation (1-32), suitable for use within a recursive wavefield extrapolation type depth migration scheme to look something like,

$$\begin{pmatrix} U_x(s,\omega,z+\Delta z) \\ U_y(s,\omega,z+\Delta z) \end{pmatrix} = \mathbf{R}^T(s)\begin{pmatrix} e^{-i\omega q_1 \Delta z} & 0 \\ 0 & e^{-i\omega q_2 \Delta z} \end{pmatrix}\mathbf{R}(s)\begin{pmatrix} U_x(s,\omega,z) \\ U_y(s,\omega,z) \end{pmatrix} \qquad (1\text{-}33)$$

where the rotation matrices and the phase shift operators now depend on the horizontal slowness s (‘s’ is used to denote slowness, in preference to the more usual ‘p’, to avoid possible confusion with polarization). In the case of the phase shift operators, the vertical wavenumbers q_1 and q_2 are determined from the horizontal slowness s, using appropriate phase velocities for the S1 and S2 modes respectively.

Equation (1-33) has been obtained heuristically, and cannot be taken as proven. The intention, rather, is to illustrate the natural progression from vertical incidence based processing of birefringent shear-waves towards incorporation in more advanced imaging scheme. In Chapter 2 an extrapolation equation is obtained from propagator matrix theory, which has the essential qualities of equation (1-33), but is more general, as it includes P-wave mode propagation and uses the full displacement-stress formulation needed to represent up-going and down-going solutions.

The differences between the "conventional" approach to multicomponent processing for birefringence and the proposed approach are illustrated in Figure 1.3. In the conventional approach, (a), the rotation to S1 and S2 is performed first, followed by migration. The P-wave migration (not shown), is performed separately. For elastic wave equation migration, the rotation to S1 and S2 is integral to the migration, and all modes are migrated together.

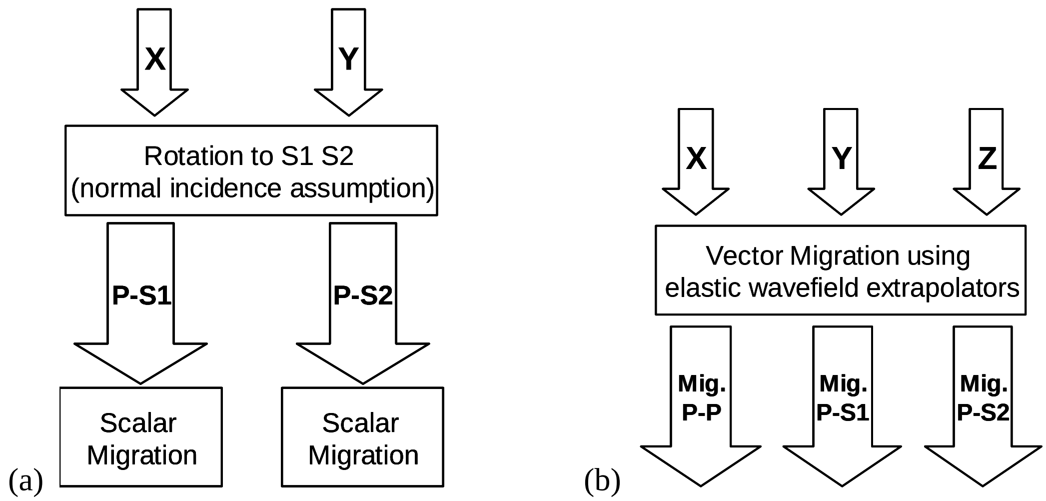

Figure 1.3. Schematic view of current practice for shear-wave splitting (a), in which rotations to S1 and S2 are performed first, followed by migration, compared with proposed approach, (b) in which the rotation is integral to the migration.

1.6 Thesis objective and program

The primary objective of this thesis is to formalize the ideas outlined in section 1.5 – to embed the shear-wave splitting correction within an elastic wave-equation migration algorithm. A secondary objective is to explore methods of modifying the migration extrapolators, in order handle the lateral variation of parameters for both isotropic and HTI media.

In Chapter 2, the basic elastic anisotropic extrapolation equations are obtained, by derivation from the Kelvin-Christoffel equation, following the theory of anisotropic propagator matrices. The treatment is based upon layered media which are laterally homogeneous.

In Chapter 3, the extension to laterally heterogeneous media is addressed. The methods used are elastic versions of GPSPI and NSPS operators. Some issues of stability are discussed.

In Chapter 4, two alternative approaches to handling heterogeneity are introduced. The first known as phase-shift plus adaptive windowing (PSPAW), is applicable to the HTI case. The second, an elastic version of the standard PSPI algorithm, is specifically designed for isotropic media.

In Chapter 5, a prestack shot-record migration, based on these extrapolators, is introduced. The imaging condition is also discussed. The operator is illustrated with some representative impulse responses, and reciprocity relations are discussed. The migration is demonstrated on two synthetic models, the first isotropic, and a second similar to this but containing a faulted HTI layer.

In Chapter 6, the migration is applied to a new elastic version of the well-known Marmousi model, called Marmousi-2 (Martin et al., 2002). Though isotropic, this model is structurally complex. It is a major test of the capabilities of the elastic migration, and pinpoints some issues for future investigation.

CHAPTER TWO: ELASTIC WAVEFIELD EXTRAPOLATION IN HTI MEDIA

"Shear wave splitting (seismic birefringence) is the most diagnostic, informative and easily observable evidence of azimuthal seismic anisotropy."
- Crampin and Chastin (2003)

2.1 Introduction

In this chapter, extrapolation in a layered HTI medium is considered. The derivation of the extrapolators is based on one-way plane wave solutions to the Kelvin-Christoffel equation (Musgrave, 1970). This is then extended to a layered medium based on continuity considerations. The extrapolation is equivalent to the theory of propagator matrices described by Thomson (1950) and Haskell (1953), and introduced to seismology by Gilbert and Backus (1966). Propagator matrices are most commonly discussed within the context of the reflectivity method of forward modeling. For a full treatment of the reflectivity method, including the theory of propagator matrices, the reader is referred to the relevant literature (e.g. Woodhouse, 1974; Kennett, 1983). For a detailed analysis of the anisotropic case, two related papers by Fryer and Frazer (1984, 1987) are recommended. A similar analysis for the elastostatic (time-invariant) case was derived by Stroh (1962), and is well-known in the material science and mathematical mechanics literature (e.g. Ting, 1996; Shuvalov, 2001).

The operator which extrapolates the three elastic modes can be described by a combination of a diagonal matrix containing phase shifts for each mode, and an "interface-propagator" matrix which includes terms describing mode conversions. The terms of the interface-propagator can be used selectively, for example, to omit conversion between P and S, but include conversion between S1 and S2 modes arising from a change in the principal axes orientation. A similar selective approach was applied to forward modeling by Silawongsawat (1998).

Examples are provided to illustrate the operators for both isotropic and HTI media. The extension to laterally varying media, via PSPI and NSPS type algorithms, is discussed in Chapters 3 and 4.

2.1.1 One-way wave equation: scalar (acoustic) case

Consider the Fourier transformed scalar Helmholtz equation (1-17). An important feature of equation (1-17) is the isolation of the main propagation direction, taken here to be the vertical direction, z. Doing so enables analysis in terms of one-way solutions which are either upward or downward propagating. By selecting only the down-going solution, the wavefield may be extrapolated in a way which neglects unwanted backward scattering. The one-way extrapolator which satisfies (1-17) is

$$\tilde{\phi}(s_x, s_y, z, \omega) = \exp[i\omega s_z (z - z_0)]\,\tilde{\phi}(s_x, s_y, z_0, \omega), \tag{2-1}$$

where $s_z = \sqrt{1/c^2 - (s_x^2 + s_y^2)}$ is the vertical slowness. That (2-1) is a solution to (1-17) can be verified by direct substitution.

2.2 Elastic (vector) extrapolation

Now let us turn our attention to elastic, vector wavefields.

2.2.1 Eigensolutions to elastic-wave equation

The propagation of plane waves in an elastic medium is governed by the Kelvin-Christoffel equation [equations (1-12) and (1-13)]. Because it is a vector equation, solutions are sought via eigenvalue-eigenvector analysis.

2.2.1.1 Eigenvalues

For a solution it is required that the determinant vanish giving the so-called characteristic equation

$$\det(\boldsymbol{\Gamma}(\mathbf{s}_r, s_z) - \rho\mathbf{I}) = 0 \tag{2-2}$$

In general, the sixth-degree equation implied by equation (2-2) has no analytic solution, and must be solved numerically. Fortunately, for anisotropy of sufficient symmetry, equation (2-2) is cubic in s_z^2, and may be analytically solved (Fryer and Frazer, 1987). Appendix A gives a proof of the necessary and sufficient conditions on the structure of the stiffness matrix **C**, for a cubic solution for s_z^2 to exist.

Analytic solutions for the slownesses under different anisotropic symmetries are given in Musgrave's book (Musgrave, 1970). An analysis of the slowness solutions to

(2-2) for HTI symmetry, and their associated branch points (which define the transition from propagating to evanescent behaviour), is provided in Appendix B.

In the HTI case, as in the VTI case, the cubic for s_z^2 factors into a quadratic and a linear term, making its solution quite straightforward. The solutions form pairs $\pm s_z$, which correspond to up- and down-going waves. The three pairs of vertical slownesses correspond to different wave-modes $s_z^{(P)}$, $s_z^{(S1)}$ and $s_z^{(S2)}$, and have corresponding polarization vectors $\mathbf{d}^{(P)}, \mathbf{d}^{(S1)}$ and $\mathbf{d}^{(S2)}$. For HTI the polarizations of up- and down-going waves are simply related by changing the sign of the Z component and leaving the horizontal components unchanged. For a generic mode, these are indicated by $s_z^{(M)}$ and $\mathbf{d}^{(M)}$, where $M \in \{P, S1, S2\}$, dropping the preceding qualifier, "q", (see section 1.2.2, and footnote on page 6) for brevity.

The phase velocity, v_M, is given by $1/v_M^2 = \mathbf{s}_r \cdot \mathbf{s}_r + \left(s_z^{(M)}\right)^2$. In general v_M is a function of the slowness (phase) direction. For the isotropic case, v_M is constant and we can solve for vertical slowness easily via $s_z^{(M)} = \pm\sqrt{v_M^{-2} - s_r^2}$.

For $s_r^2 \leq 1/v_M^2$ solutions are real, but for $s_r^2 > 1/v_M^2$ they are imaginary, corresponding to evanescent waves. This gives rise to three distinct regions: (I) $|s_r| < 1/v_P < 1/v_S$ leading to real s_z for all modes; (II) $1/v_P < |s_r| < 1/v_S$ leading to real $s_z^{(SV,SH)}$ but imaginary $s_z^{(P)}$; and (III) $1/v_P < 1/v_S < |s_r|$ for which all s_z are imaginary.

Likewise, for anisotropy, complex values for s_z can arise when the Kelvin-Christoffel equation is solved. There are four such regions, since the two S-wave velocities differ, creating an additional region between $1/v_{S1}$ and $1/v_{S2}$. Figure 2.1 shows the variation of vertical slowness for each mode as a function of horizontal slowness for (a) isotropic, and (b) HTI cases, with parameters given in Table 2.1. These model parameters are scaled from the model in Table 3 of Lou and Rial (1995), which was derived using Hudson's theory (Hudson, 1981). This medium has a shear wave anisotropy [i.e. Thomsen's γ (1988)] of approximately 11.5%. The HTI slowness curves shown are for propagation in the plane which contains the axis of symmetry. For propagation in this plane, the behaviour is equivalent to a VTI medium, and the two shear modes decouple. The S1 mode, defined as the fastest mode for vertical propagation, has behaviour equivalent to an SH-wave, and the S2 mode behaves as SV. As for VTI, the SV wave results from the second solution to the term that is quadratic in s_z^2 from the Kelvin-Christoffel equation (the first solution is the P-wave). The SH-wave arises from solution of the linear term in s_z^2.

ij \ kl	**11**	**22**	**33**	**23**	**13**	**12**
11	23.6e9	6.99e9	6.99e9	0	0	0
22	6.99e9	24.86e9	9.1e9	0	0	0
33	6.99e9	9.1e9	24.86e9	0	0	0
23	0	0	0	7.88e9	0	0
13	0	0	0	0	6.09e9	
12	0	0	0	0	0	6.09e9

Table 2.1: c_{ijkl} for HTI model with symmetry axis aligned with *x* direction, all values in Pa.

2.2.1.2 Eigenvectors

Determination of the polarization vectors is less straightforward. A solution to equation (1-13) is of the form (Shuvalov, 2001)

$$\mathbf{d} = \mathrm{adj}\left(\mathbf{\Gamma}(\mathbf{s}) - \rho \mathbf{I}\right)\mathbf{w} , \qquad (2\text{-}3)$$

where **w** is an arbitrary vector, **I** is the identity matrix (i.e. the matrix form of Krönecker delta), and $\mathrm{adj}(\mathbf{A})$ means the adjugate or cofactor matrix of **A** (Strang, 1988, p.232), obtained by replacing each element of **A** by its signed cofactor, and transposing, as follows:

$$\mathrm{adj}(\mathbf{A}) = \begin{pmatrix} C_{11} & C_{21} & C_{31} \\ C_{12} & C_{22} & C_{32} \\ C_{13} & C_{23} & C_{33} \end{pmatrix}, \qquad (2\text{-}4)$$

where the cofactors of **A** are: $C_{11} = \det\begin{pmatrix} a_{22} & a_{23} \\ a_{32} & a_{33} \end{pmatrix}, C_{12} = -\det\begin{pmatrix} a_{12} & a_{13} \\ a_{32} & a_{33} \end{pmatrix},$ etc.

The adjugate matrix should not be confused with the adjoint matrix. The definition of adjugate in (2-4) is constructed so that $\mathbf{A}\,\mathrm{adj}(\mathbf{A}) = \det(\mathbf{A})\mathbf{I}$, and, when the determinant is non-zero, the inverse of **A** exists and is given by $\mathbf{A}^{-1} = \mathrm{adj}(\mathbf{A})/\det(\mathbf{A})$.[1] That equation (2-3) solves equation (1-13) follows directly from the fact that $\det(\boldsymbol{\Gamma}(\mathbf{s}) - \rho\mathbf{I}) = 0$. However, simple substitution of the three eigenvalues, $s_z^{(P)}$, $s_z^{(S1)}$ and $s_z^{(S2)}$, into equation (2-3) does not necessarily lead to distinct eigenvectors, unless **w** is also changed, due to the presence of degenerate solutions and/or null rows in the adjugate matrix. Fryer and Frazer (1987) provide a solution, which corresponds to choosing $\mathbf{w} = \begin{pmatrix}0 & 0 & 1\end{pmatrix}^T$ for P-waves, and then trying $\mathbf{w} = \begin{pmatrix}0 & 1 & 0\end{pmatrix}^T$ and $\mathbf{w} = \begin{pmatrix}1 & 0 & 0\end{pmatrix}^T$ for each S-wave mode in turn. They do not consider more general choices for **w**, though they would also provide solutions of equation (2-3).

An example of degeneracy is the isotropic case within the *x*-*z* plane (i.e. setting $s_y = 0$). The normalized polarization vectors are well-known from physical and geometrical principles to be

$$\mathbf{d}^{(P)} = \begin{pmatrix} v_P s_x \\ 0 \\ v_P s_z^{(P)} \end{pmatrix}, \quad \mathbf{d}^{(SH)} = \begin{pmatrix} 0 \\ 1 \\ 0 \end{pmatrix}, \quad \mathbf{d}^{(SV)} = \begin{pmatrix} -v_S s_z^{(SV)} \\ 0 \\ v_S s_x \end{pmatrix}. \qquad \text{(2-5)}$$

As shown in Appendix C, the first of these can be obtained (within a scale factor) by using the P-wave eigenvalue and setting $\mathbf{w} = \begin{pmatrix}1 & 0 & 0\end{pmatrix}^T$. However, Appendix C also shows that substituting the S-wave eigenvalue into $\mathrm{adj}(\boldsymbol{\Gamma}(\mathbf{s}) - \rho\mathbf{I})$ always gives the second

[1] It is useful to think of the adjugate as a “determinant-free” inverse – unlike the true inverse, the adjugate is well defined even for singular matrices.

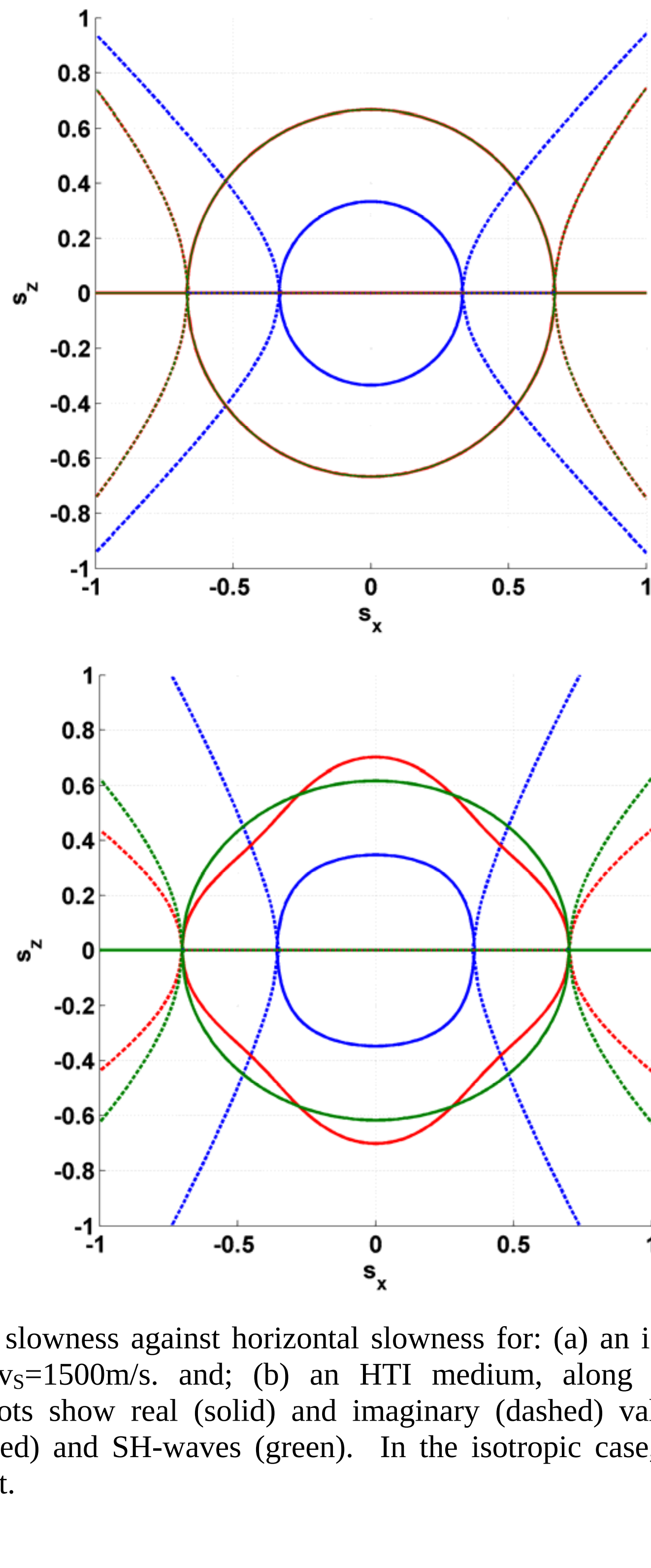

(a)

(b)

Figure 2.1. Vertical slowness against horizontal slowness for: (a) an isotropic medium, with v_P=3000m/s, v_S=1500m/s. and; (b) an HTI medium, along plane containing symmetry axis. Plots show real (solid) and imaginary (dashed) values for P-waves (blue), SV-waves (red) and SH-waves (green). In the isotropic case, the SV and SH curves are coincident.

eigenvector, irrespective of **w**. To obtain the SV-wave eigenvector, the SH-wave solution must first be factored out of $\mathrm{adj}(\mathbf{\Gamma}(\mathbf{s})-\rho\mathbf{I})$.

In equation (2-5), the vectors have complex-valued elements for some wavenumbers, and can be written in the form, $\mathbf{d}=\mathbf{d}_R+i\mathbf{d}_I$, known as *bivectors* (Shuvalov, 2001). Using the same classification as for the vertical slownesses the following behaviour is observed, for the isotropic case: in region (I) all elements of the polarizations are real; in region (II) all elements are real except $d_3^{(P)}$, which is imaginary; in region (III) all elements are real, except for $d_3^{(P)}$ and $d_1^{(SV)}$.

Figure 2.2 shows the real and imaginary components of $\mathbf{d}^{(P)}$ and $\mathbf{d}^{(SV)}$ for an isotropic medium, as a function of horizontal slowness, s_x. The second elements are omitted, as they are zero. Of particular interest are the complex elements that arise in the zone between P- and S-wave evanescent cut-offs. In equation (2-5) and Figure 2.2, a polarity convention is used such that the SV horizontal polarization points in the positive *x*-direction. The P-wave amplitudes are symmetric about the vertical, while SV-wave amplitudes are antisymmetric. This convention gives rise to polarizations which vary continuously with propagation direction for 2-D geometries. Unfortunately, an extension 3-D always involves a discontinuity.[1]

Figure 2.3, Figure 2.4 and Figure 2.5 show both slowness and polarization simultaneously for the propagating solutions to equation (1-13). For each of these figures, the complete plot is shown in (a), and a zoom on detail for propagation angles near 90° from vertical is shown in (b). The coloured curves represent the vertical slowness as a function of horizontal slowness, while the black arrows represent the polarization direction at 5° intervals, for each of the modes. Figure 2.3 shows the solution for the HTI medium of Table 2.1, with the axis of symmetry aligned parallel to the *x*-axis. Figure 2.4 and Figure 2.5 show the corresponding solutions for axes of symmetry rotated by 45° and 90° from the *x*-axis respectively. Figure 2.6 compares the polarization within

---

[1] The reason for this is a mathematical result known as Brouwer's fixed point theorem, which shows the impossibility of defining a smoothly varying vector field everywhere on a surface topologically equivalent to a sphere. A mundane example is the hair on your head, which has a singularity where all hairs diverge (though since it is only partially covered, this example is not quite perfect).

the horizontal plane for the 0° and 45° degree cases shown in Figure 2.3 and Figure 2.4 respectively.

Two observations from Figure 2.3 to Figure 2.6 are particularly relevant to the subject of wavefield extrapolation through HTI media. First, the variation of the phase velocity with angle for the shear waves is significant, depends upon the direction of the symmetry axis relative to the propagation plane, and is quite different for the two shear modes. Second, the polarization directions are determined by a combination of the symmetry direction and the angle of propagation. In particular for the 45° axis of symmetry the horizontal components of polarization do not remain invariant with phase angle. In fact it is only along the symmetry plane and the isotropy plane that the horizontal polarization remains constant. The implication is that the assumptions of standard shear-wave splitting processing methods, embodied in equations (1-31) and (1-32) will be increasingly in error as the angle of wave propagation increases.

2.2.2 Two-way equation

Following the formalism of Shuvalov (2001), (see also Ting, 1996), the Fourier transform of (1-11) with respect to *x*, *y* and *t*, gives

$$T_{ik}u_{k,33} - i\omega(R_{ik}+R_{ki})u_{k,3} - \omega^2 Q_{ik}u_k + \rho\omega^2 u_i = 0\,, \tag{2-6}$$

where $u_i(\mathbf{s}_r, z, \omega)$ is the Fourier transform of $u_i((x,y),z,t)$, and the 3-by-3 matrices, **Q**, **R** and **T**, are given by

$$\begin{aligned} Q_{ik} &\equiv c_{i1k1}s_1^2 + (c_{i1k2}+c_{i2k1})s_1 s_2 + c_{i2k2}s_2^2 \\ R_{ik} &\equiv c_{i1k3}s_1 + c_{i2k3}s_2 \\ T_{ik} &\equiv c_{i3k3} \end{aligned}\,. \tag{2-7}$$

In matrix notation, equation (2-6) is written

$$\mathbf{T}\frac{d^2\mathbf{u}}{dz^2} - i\omega\left(\mathbf{R}+\mathbf{R}^T\right)\frac{d\mathbf{u}}{dz} - \omega^2(\mathbf{Q}-\rho\mathbf{I})\mathbf{u} = 0\,. \tag{2-8}$$

Equation (2-8) is a second-order differential vector equation which is analogous to the second-order differential scalar equation (1-17). As in the scalar case, the vertical direction is isolated from the other two spatial directions by the Fourier transform.

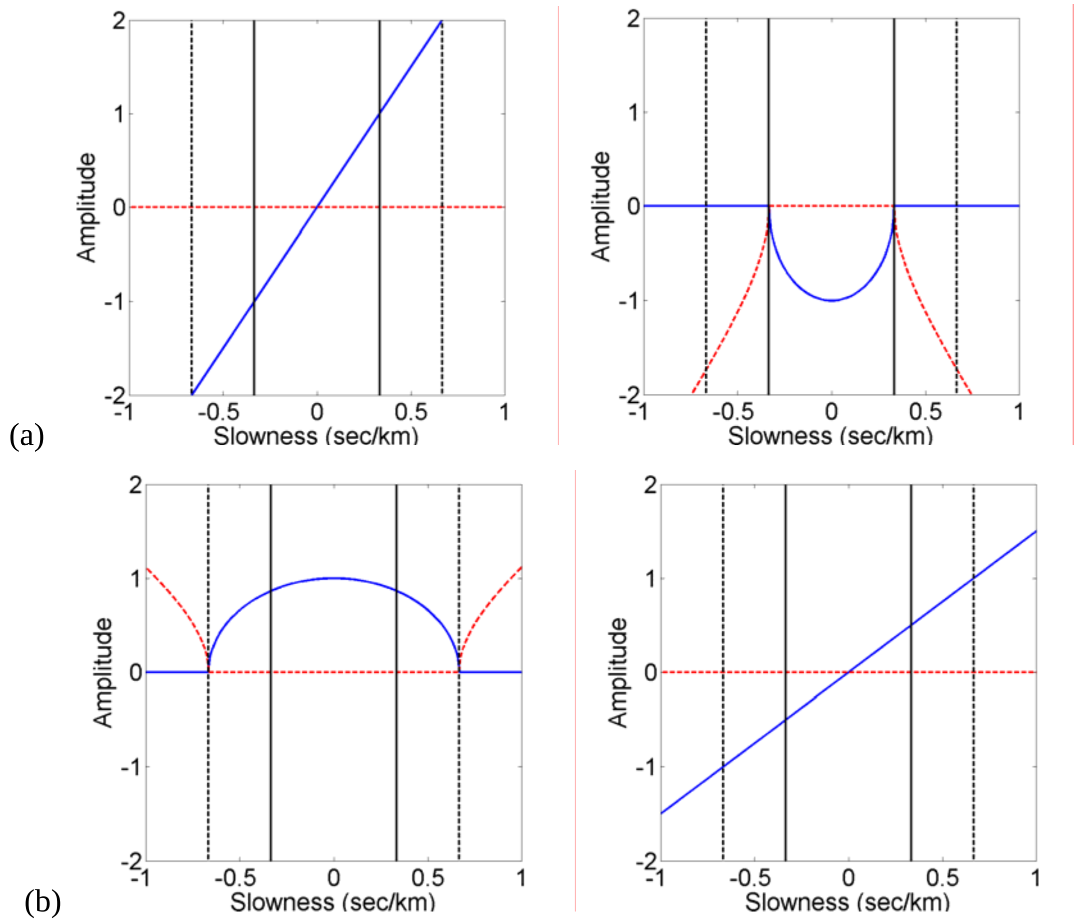

Figure 2.2. (a) P-wave polarization as a function of horizontal slowness, for an up-going wave in an isotropic medium with v_P=3000m/s, v_S=1500m/s. The X (left) and Z (right) components are shown. Real parts are blue solid, imaginary parts are red dashed. The vertical lines show the evanescent cut-off boundaries for P-waves (solid lines) and for S-waves (dashed lines). (b) SV-wave polarization for the same medium, X-(left) and Z-(right) components.

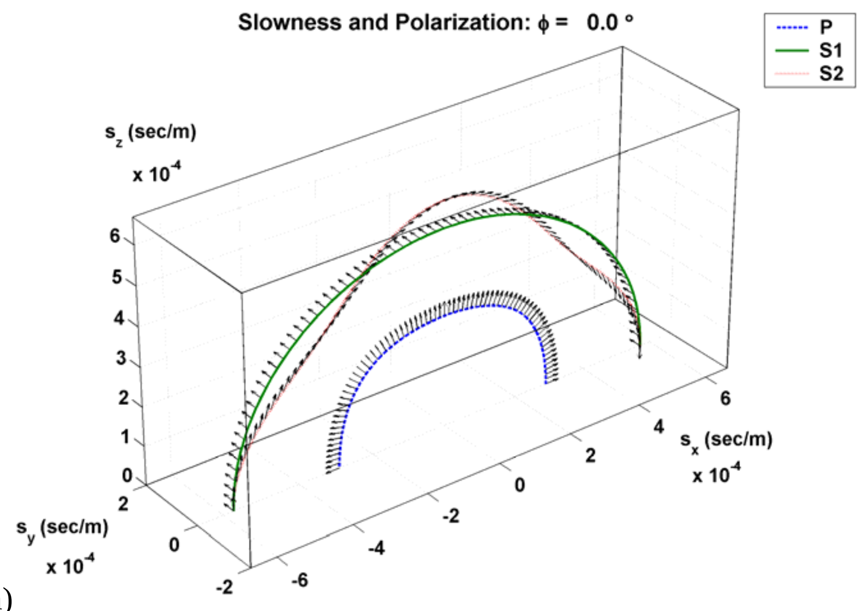

(a)

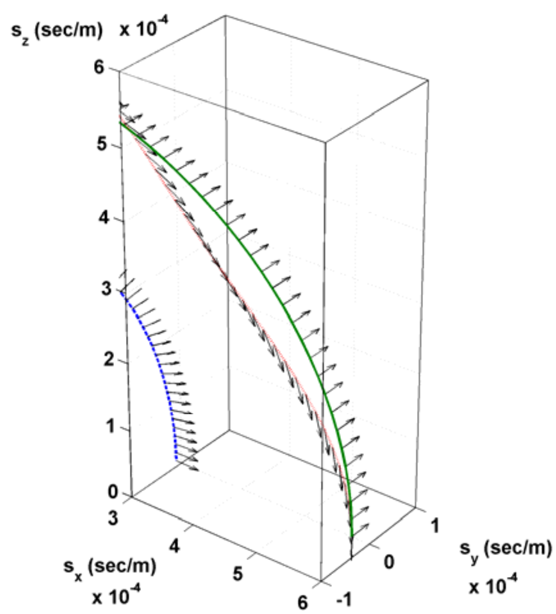

(b)

Figure 2.3. Combined slowness and polarization plot for propagating (non-evanescent) slownesses in HTI media, given by **Table 2.1** with axis of symmetry parallel to *x*-axis. Blue dashed line shows P-wave slowness, green solid line shows S1 (SH) -wave slowness, and red dotted line shows S2 (SV)-wave slowness. Detail of two shear modes in (b) shows deviation of polarization for S2 mode from tangent to slowness curve.

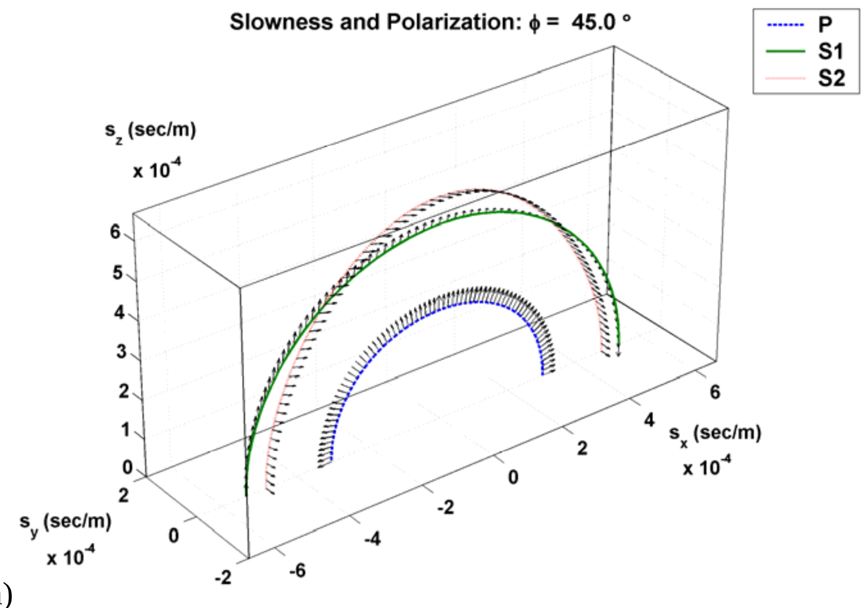

(a)

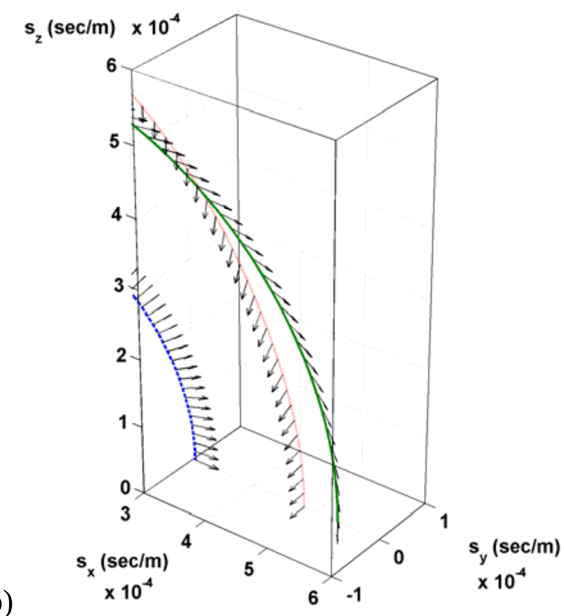

(b)

Figure 2.4. Combined slowness and polarization plot for HTI media of **Table 2.1** with axis of symmetry rotated 45° clockwise from *x*-axis. Blue dashed line shows P-wave slowness, green solid line shows S1 (SH) -wave slowness, and red dotted line shows S2 (SV)-wave slowness. Note the gradual change of the S-wave polarizations as propagation angle increases to 90°.

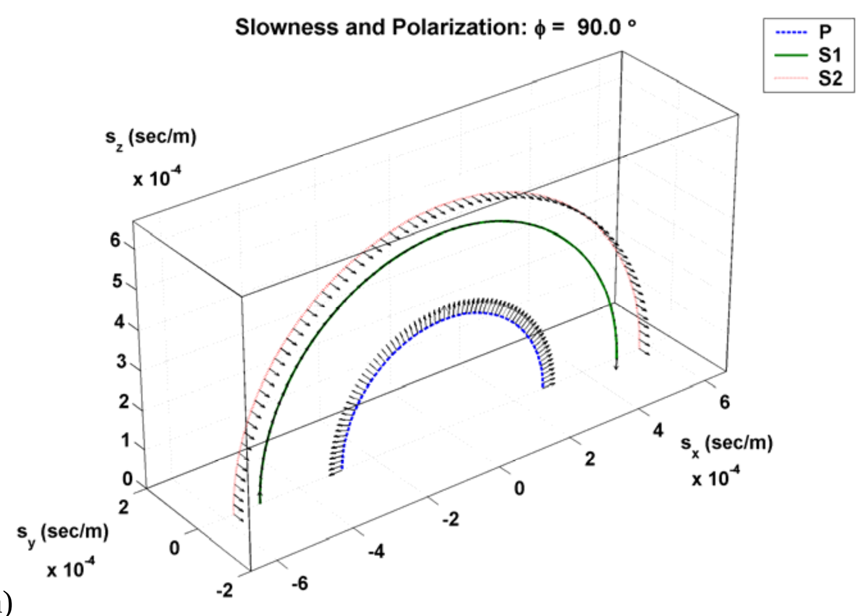

(a)

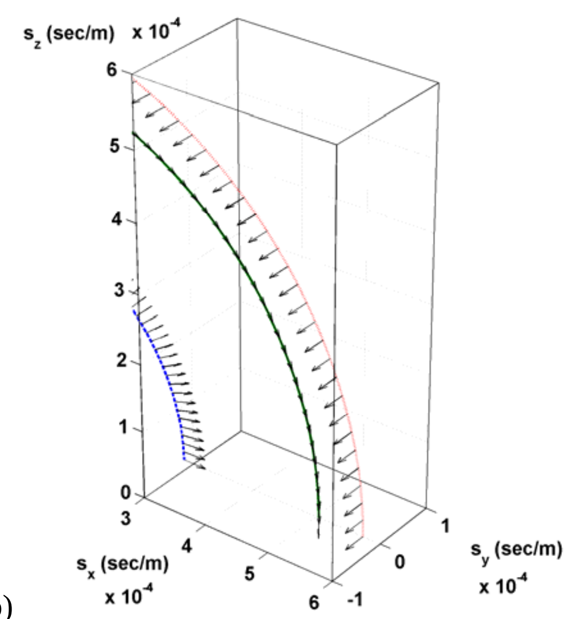

(b)

Figure 2.5. Combined slowness and polarization plot for HTI media of **Table 2.1** with axis of symmetry rotated 90° clockwise from *x*-axis. Blue dashed line shows P-wave slowness, green solid line shows S1 (SH) -wave slowness, and red dotted line shows S2 (SV)-wave slowness. This is propagation in the isotropy plane for which velocity of each mode is constant with propagation direction, and polarizations are the same as for isotropic modes.

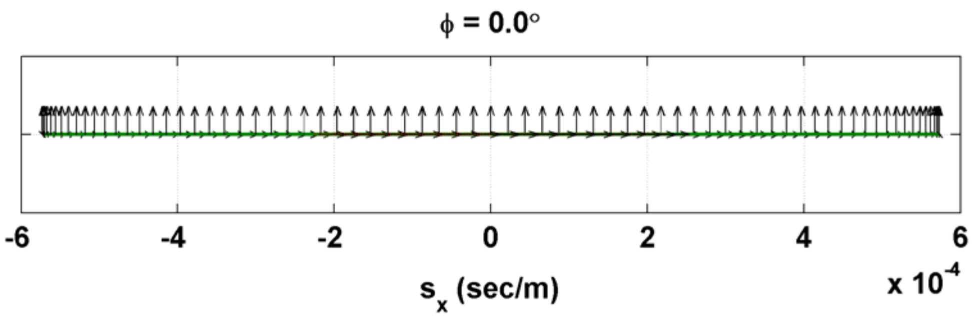

(a)

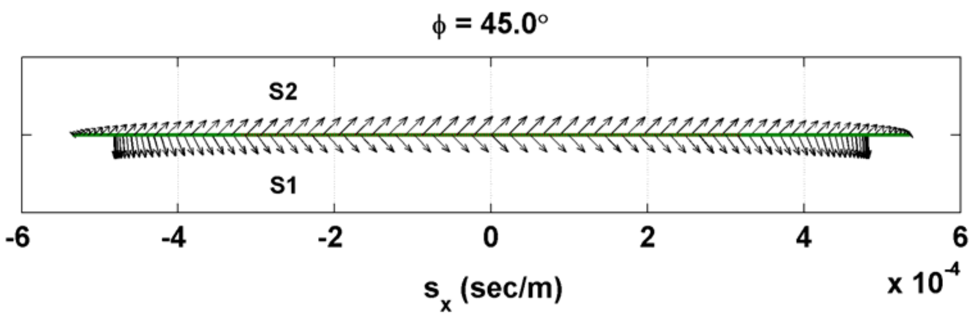

(b)

Figure 2.6. Projection of polarizations onto horizontal plane for axis of symmetry at 0° (a), and 45° (b) to propagation plane, corresponding to Figure 2.3 and Figure 2.4, respectively. For propagation in the plane of the symmetry axis, the projections of polarization onto the horizontal plane do not vary with horizontal slowness. This is also true for propagation in the isotropy plane (see Figure 2.5). However, for propagation in planes with other orientations such as shown in (b), the projections onto the horizontal plane can vary considerably.

It is reassuring to verify that equation (2-8) is transformed into the Kelvin-Christoffel equation (1-13), by applying a further Fourier transform over *z* and dividing through by ω^2 to get

$$\left[\mathbf{\Gamma}(\mathbf{s}_r, s_z) - \rho\mathbf{I}\right] \mathbf{u}(\mathbf{s}_r, s_z, \omega) = 0 . \qquad (2\text{-}9)$$

where $\mathbf{\Gamma}(\mathbf{s}) = s_z^2\mathbf{T} + \left(\mathbf{R} + \mathbf{R}^T\right)s_z + \mathbf{Q}$ is the Christoffel matrix as given in equation (1-13).

2.2.3 Derivation of one-way extrapolator

A one-way equation for elastic waves in a layered anisotropic medium is now derived. The development closely follows the approach and notation of Fryer and Frazer (1984; 1987), an extension of Kennett's (1983) theory.

As an alternative to the second order differential equation in (2-8), the momentum and constitutive equations in (1-1) and (1-2) can be combined into a *first-order* differential equation in z

$$\frac{d\mathbf{b}}{dz} = i\omega\mathbf{A}\mathbf{b}\,, \tag{2-10}$$

where $\mathbf{b}$ is a vector containing displacement and the vertical components of traction – properties which are continuous across a horizontal plane – given by

$$\mathbf{b} = \begin{pmatrix} \mathbf{u} \\ \boldsymbol{\tau} \end{pmatrix}, \text{ for } \boldsymbol{\tau} = -\frac{1}{i\omega}\begin{pmatrix}\sigma_{13} & \sigma_{23} & \sigma_{33}\end{pmatrix}^T, \tag{2-11}$$

and where
$$\mathbf{A} = -\begin{pmatrix} \mathbf{T}^{-1}\mathbf{R}^T & \mathbf{T}^{-1} \\ \mathbf{R}\mathbf{T}^{-1}\mathbf{R}^T - \mathbf{Q} + \rho\mathbf{I} & \mathbf{R}\mathbf{T}^{-1} \end{pmatrix}. \tag{2-12}$$

In seismology, $\mathbf{A}$ is referred to as the *system matrix* (Kennett, 1983; Fryer and Frazer, 1984). In the mechanics literature, $\mathbf{A}$ is sometimes referred to as the *fundamental elasticity matrix* (Ting, 1996). Equation (2-10) is an eigenproblem involving a 6-by-6 system, so that there are in general six eigenvalues and eigenvectors. These have a one-to-one relationship with the three pairs of eigenvalues and corresponding paired eigenvectors which arise from the Kelvin-Christoffel equation (1-13). Introducing the notational convenience for vertical slowness, $q \equiv s_z \equiv s_3$, the eigendecomposition of $\mathbf{A}$ is

$$\mathbf{D}^{-1}\mathbf{A}\mathbf{D} = \boldsymbol{\Lambda} = diag\begin{pmatrix} q_P^U & q_{S1}^U & q_{S2}^U & q_P^D & q_{S1}^D & q_{S2}^D \end{pmatrix}, \tag{2-13}$$

where the subscripts P, S1 and S2 refer to the three modes, and the superscripts U and D distinguish between up- and down-going solutions respectively. $\mathbf{D}$ is a matrix containing the six eigenvectors of $\mathbf{A}$ as its columns.

Assuming a vertically homogeneous layer, such that $\mathbf{D}$ is independent of z, equation (2-13) can be combined with equation (2-10) to give

$$\frac{d\mathbf{v}}{dz} = i\omega\boldsymbol{\Lambda}\mathbf{v}\,, \tag{2-14}$$

where

$$\mathbf{b} = \mathbf{D}\mathbf{v} \quad \text{and} \quad \mathbf{v} = \begin{pmatrix} \mathbf{v}_U \\ \mathbf{v}_D \end{pmatrix}, \tag{2-15}$$

where

$$\mathbf{v}_U = \begin{pmatrix} v_P^U \\ v_{S1}^U \\ v_{S2}^U \end{pmatrix} \text{ and } \mathbf{v}_D = \begin{pmatrix} v_P^D \\ v_{S1}^D \\ v_{S2}^D \end{pmatrix}.$$

The three elements of $\mathbf{v}_U$ are the amplitudes of up-going P, S1 and S2 waves, while the elements of $\mathbf{v}_D$ are the down-going amplitudes. $\mathbf{D}$ is a composition operator which constructs the displacement-stress from the wave-mode amplitudes, whereas $\mathbf{D}^{-1}$, is a decomposition operator, such that

$$\mathbf{v} = \mathbf{D}^{-1}\mathbf{b}, \tag{2-16}$$

provided $\mathbf{D}$ is not singular, which is the case for propagating waves. For values of slowness where $\mathbf{D}$ becomes singular, corresponding to the boundaries between propagating and evanescent wavenumbers, the use of complex velocities with small imaginary parts will avoid the singular behavior.

Equation (2-14) has the solution

$$\mathbf{v}(z) = e^{i\omega\mathbf{\Lambda}(z-z_0)}\,\mathbf{v}(z_0). \tag{2-17}$$

Equation (2-17) describes two-way extrapolation in a homogeneous medium. Since the extrapolator for this case is diagonal, solutions can be split into up- and down-going one-way solutions

$$\mathbf{v}_U(z) = e^{i\omega\mathbf{\Lambda}_U(z-z_0)}\mathbf{v}_U(z_0), \tag{2-18}$$

and

$$\mathbf{v}_D(z) = e^{i\omega\mathbf{\Lambda}_D(z-z_0)}\mathbf{v}_D(z_0), \tag{2-19}$$

where

$$\boldsymbol{\Lambda}_U = diag\left(q_P^U \quad q_{S1}^U \quad q_{S2}^U\right) \text{ and } \boldsymbol{\Lambda}_D = diag\left(q_P^D \quad q_{S1}^D \quad q_{S2}^D\right). \tag{2-20}$$

Equations (2-18)-(2-20) describe the extrapolation of the up and down going decomposed wavefields which can be used for backward extrapolating the (up-going) receiver wavefield and forward extrapolating the (down-going) source wavefield within each depth step.

Recall that the columns of **D** are the six eigenvectors, which will be denoted

$$\hat{\mathbf{b}}_i = \varepsilon_i \begin{pmatrix} \mathbf{u}_i \\ \boldsymbol{\tau}_i \end{pmatrix}, \quad i = 1, \ldots, 6, \tag{2-21}$$

where the normalization factors ε_i are to be determined. The notation $\hat{\mathbf{b}}_i$ is used to indicate a unit length eigenvector as opposed to a general displacement-stress vector **b**. Then, with the rows of $\mathbf{D}^{-1}$ denoted by $\hat{\mathbf{g}}_i^T$, the following orthogonality relationship obviously holds:

$$\hat{\mathbf{g}}_j^T \hat{\mathbf{b}}_i = \delta_{ij}. \tag{2-22}$$

Various authors (e.g. Fryer and Frazer, 1984) have shown the simple but very useful relationship

$$\hat{\mathbf{g}}_i = \mathbf{J}\hat{\mathbf{b}}_i, \text{ for } \mathbf{J} \equiv \begin{pmatrix} \mathbf{0}_3 & \mathbf{I}_3 \\ \mathbf{I}_3 & \mathbf{0}_3 \end{pmatrix}, \tag{2-23}$$

where $\mathbf{I}_3$ and $\mathbf{0}_3$ are the 3-by-3 identity and zero matrices. Consequently, the inverse of **D** is given by

$$\mathbf{D}^{-1} = (\mathbf{JD})^T. \tag{2-24}$$

Both **D** and $\mathbf{D}^{-1}$ are thus easily computed, given the eigenvectors $\hat{\mathbf{b}}_i$. The top half of each $\hat{\mathbf{b}}_i$ is $\mathbf{u}_i$, an eigenvector of the Kelvin-Christoffel equation, (1-13). To obtain the stress vectors which make up the bottom half of each $\mathbf{b}_i$, equations (1-2), (2-7) and (2-11) are used, giving

$$\boldsymbol{\tau}_i = -(\mathbf{R} + s_z\mathbf{T})\mathbf{u}_i \,. \tag{2-25}$$

The six eigenvectors correspond to up and down-going P, S1 and S2 waves. Using the same notational convention as in equation (2-13), we have

$$\begin{aligned}\mathbf{D} &= \begin{pmatrix}\mathbf{D}_U & \mathbf{D}_D\end{pmatrix} \\ &= \begin{pmatrix}\hat{\mathbf{b}}_P^U & \hat{\mathbf{b}}_{S1}^U & \hat{\mathbf{b}}_{S2}^U & \hat{\mathbf{b}}_P^D & \hat{\mathbf{b}}_{S1}^D & \hat{\mathbf{b}}_{S2}^D\end{pmatrix}\end{aligned}, \tag{2-26}$$

where

$$\begin{aligned}\hat{\mathbf{b}}_M^{U,D} &= \varepsilon_M^{U,D}\begin{pmatrix}\mathbf{u}_M^{U,D} \\ \boldsymbol{\tau}_M^{U,D}\end{pmatrix} = \varepsilon_M^{U,D}\begin{pmatrix}\mathbf{u}_M^{U,D} \\ -\left(\mathbf{R} + q_M^{U,D}\mathbf{T}\right)\mathbf{u}_M^{U,D}\end{pmatrix}, \\ M &\in \{P, S1, S2\}.\end{aligned} \tag{2-27}$$

Finally, the eigenvector normalization factor is given (Fryer and Frazer, 1984) by

$$\varepsilon_M^{U,D} = \frac{1}{\sqrt{2\mathbf{u}_M^{U,D}\cdot\boldsymbol{\tau}_M^{U,D}}} \,. \tag{2-28}$$

Combining equations (2-15)-(2-19) and (2-26) gives the one-way extrapolation equations in terms of the displacement-stress vectors for a homogeneous medium

$$\mathbf{b}_U(z) = \mathbf{D}_U e^{i\omega\boldsymbol{\Lambda}_U(z-z_0)}\,\mathbf{D}_U^{-L}\,\mathbf{b}_U(z_0), \tag{2-29}$$

and

$$\mathbf{b}_D(z) = \mathbf{D}_D e^{i\omega\boldsymbol{\Lambda}_D(z-z_0)}\,\mathbf{D}_D^{-L}\,\mathbf{b}_D(z_0), \tag{2-30}$$

where $\mathbf{D}_U^{-L}$ and $\mathbf{D}_D^{-L}$ are the *left* inverses (e.g. Strang, 1988, p.90) of $\mathbf{D}_U$ and $\mathbf{D}_D$, containing the upper and lower three rows of $\mathbf{D}^{-1}$, respectively.

In Appendix D the displacement-stress eigenvectors are calculated for the special case of an isotropic medium.

The square-root in equation (2-28) has an argument which is zero at the evanescent cut-off points, giving rise to a singularity which must be avoided. The singularity can be avoided by the introduction of complex P- and S- velocities, with small relative imaginary parts, before computing the eigenvectors. Physically, this corresponds to introducing a small viscous effect and thus departing from perfect elasticity. The addition of imaginary velocity is a step which is also valuable for reducing wrap around of the phase-shift operator. The relative magnitude of the imaginary parts required to manage the singularities is larger than required for wrap-around control, and is found empirically. However, even with this precaution, the square-root still can cause complications since it introduces a branch cut. The steps needed to properly address this issue are discussed in Appendix E.

2.2.4 Vertical heterogeneity

It is usual in wavefield extrapolation to approximate vertical heterogeneity by a stack of homogeneous layers, each of thickness Δz, with discontinuous medium properties at interfaces between layers (Figure 2.7). This is a good approximation to a continuously variable medium provided the step size is not too large.

Conventionally the dynamic (i.e. amplitude) changes due to variation in the medium are often ignored in this process. But how does the extrapolator then incorporate changes in the polarization which carry information on shear-wave splitting?

The displacement-stress vector b is continuous across an interface. The wave-mode vector v, is not. The most obvious approach to extrapolation is to decompose **b** at the top interface of each layer to get **v**, extrapolate **v** within the layer using equation (2-17) [or (2-18) and (2-19) for one-way extrapolation], and then recompose **b** at the lower interface where the continuity of **b** is invoked to provide a boundary condition for the next depth step. The complete extrapolation is described by recursive application of equations (2-29) (for up-going waves), or (2-30) (for down-going waves), as illustrated in Figure 2.7. This approach is revisited in Chapter 3, where lateral heterogeneity is contemplated.

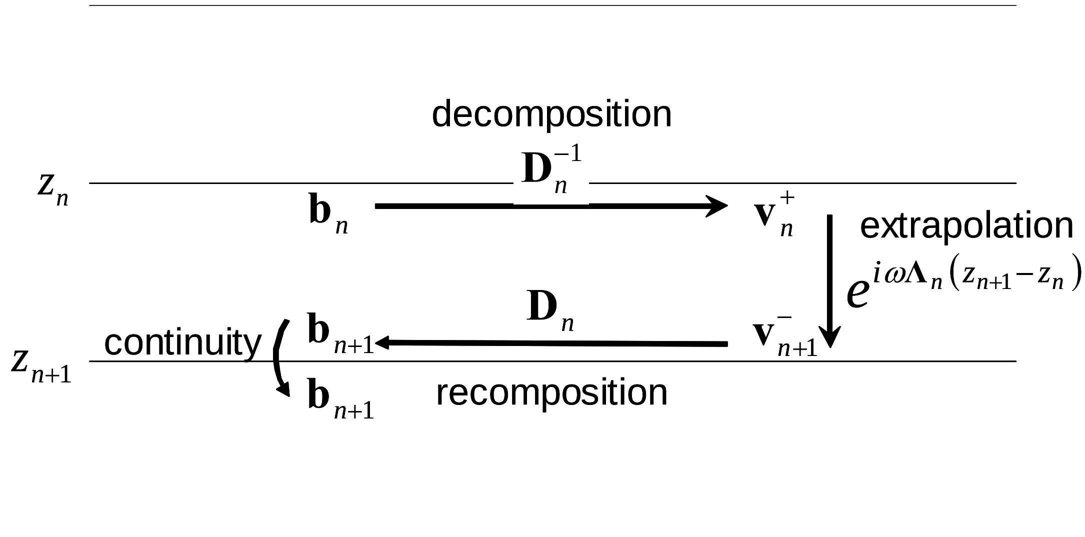

Figure 2.7. Extrapolation in a vertically heterogeneous medium. The medium is approximated by a series of homogeneous layers or "thin slabs". For each layer, the displacement-stress wavefield **b** is decomposed into eigenmodes, which are extrapolated. The resulting wavefield is recomposed to displacement-stress, and continuity is invoked to provide a boundary condition for the next depth step.

2.2.4.1 Interface propagators

A more economical approach is possible for a medium which varies only with depth, as considered here. This approach is based on computing the *interface-propagator* which extrapolates **v** infinitesimally across each horizontal interface. In this thesis, an interface-propagator is a special case of the wavefield propagators used by Kennett (1983), in which the propagation distance is infinitesimal, but across a discontinuity. Based on continuity of **b** it is readily shown (e.g. Kennett, 1983) that the required interface-propagator to cross an interface at z_n, from z_n- just above the interface to z_n+ just below the interface (Figure 2.8)., is simply given by

$$\mathbf{W}(z_n+, z_n-) = \mathbf{D}_n^{-1}\mathbf{D}_{n-1}, \tag{2-31}$$

so that

$$\mathbf{v}(z_n+) = \mathbf{W}(z_n+, z_n-)\mathbf{v}(z_n-), \tag{2-32}$$

where $\mathbf{D}_{n-1}$ is the composition matrix in layer *n*-1 above the interface, and $\mathbf{D}_n$ is the composition matrix in layer *n*, below the interface.

Hence, all that is required to generate the interface-propagator are the matrices $\mathbf{D}$ and $\mathbf{D}^{-1}$, for each layer.

Using equations (2-24) and (2-26), the interface-propagator of equation (2-31) is given by

$$\begin{aligned} \mathbf{W}(z_n+, z_n-) &= \begin{pmatrix} \hat{\mathbf{g}}^U_{P,n} & \hat{\mathbf{g}}^U_{S1,n} & \hat{\mathbf{g}}^U_{S2,n} & \hat{\mathbf{g}}^D_{P,n} & \hat{\mathbf{g}}^D_{S1,n} & \hat{\mathbf{g}}^D_{S2,n} \end{pmatrix}^T \\ &\quad \times \begin{pmatrix} \hat{\mathbf{b}}^U_{P,(n-1)} & \hat{\mathbf{b}}^U_{S1,(n-1)} & \hat{\mathbf{b}}^U_{S2,(n-1)} & \hat{\mathbf{b}}^D_{P,(n-1)} & \hat{\mathbf{b}}^D_{S1,(n-1)} & \hat{\mathbf{b}}^D_{S2,(n-1)} \end{pmatrix}, \\ &= \begin{pmatrix} \mathbf{W}_{UU}(z_n+, z_n-) & \mathbf{W}_{UD}(z_n+, z_n-) \\ \mathbf{W}_{DU}(z_n+, z_n-) & \mathbf{W}_{DD}(z_n+, z_n-) \end{pmatrix} \end{aligned} \tag{2-33}$$

where

$$\mathbf{W}_{KL}(z_n+, z_n-) = \begin{pmatrix} \hat{\mathbf{g}}^K_{P,n} \cdot \hat{\mathbf{b}}^L_{P,(n-1)} & \hat{\mathbf{g}}^K_{P,n} \cdot \hat{\mathbf{b}}^L_{S1,(n-1)} & \hat{\mathbf{g}}^K_{P,n} \cdot \hat{\mathbf{b}}^L_{S2,(n-1)} \\ \hat{\mathbf{g}}^K_{S1,n} \cdot \hat{\mathbf{b}}^L_{P,(n-1)} & \hat{\mathbf{g}}^K_{S1,n} \cdot \hat{\mathbf{b}}^L_{S1,(n-1)} & \hat{\mathbf{g}}^K_{S1,n} \cdot \hat{\mathbf{b}}^L_{S2,(n-1)} \\ \hat{\mathbf{g}}^K_{S2,n} \cdot \hat{\mathbf{b}}^L_{P,(n-1)} & \hat{\mathbf{g}}^K_{S2,n} \cdot \hat{\mathbf{b}}^L_{S1,(n-1)} & \hat{\mathbf{g}}^K_{S2,n} \cdot \hat{\mathbf{b}}^L_{S2,(n-1)} \end{pmatrix}, \tag{2-34}$$

$$K, L \in \{U, D\}.$$

Note that if there is no contrast in properties across the interface, both layers have the same eigenvectors, and the orthogonality property (2-22) comes into play, so that $\mathbf{W}$ is the identity matrix.

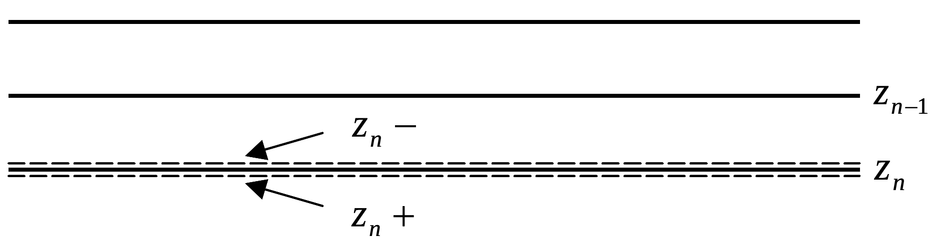

Figure 2.8. Layered medium, consisting of homogenous layers with discontinuities at interfaces. Interface-propagator $\mathbf{W}(z_n+, z_n-)$ translates wavefield from above interface at z_n to just below.

Equation (2-34) describes four 3-by-3 matrices corresponding to the combinations of up and down-going waves in layers (*n*-1) and *n*. For the purposes of one-way extrapolation, we will be interested in $\mathbf{W}_{DD}$ for the source side and $\mathbf{W}_{UU}$ for the receiver side, consistent with the assumption that backscattered energy can be ignored.
To clarify this last statement, consider the wave-mode vector **v** either side of the interface:

$$\mathbf{v}(z_n +) = \mathbf{W}(z_n +, z_n -)\mathbf{v}(z_n -). \tag{2-35}$$

Now assume that there is *no* up-going wave so that, at both $z_n -$ and $z_n +$ we have

$$\mathbf{v}(z) = \begin{pmatrix} \mathbf{0} \\ \mathbf{v}_D(z) \end{pmatrix}. \tag{2-36}$$

where **0** is the 3-vector of zero values. Substitution into (25) then gives

$$\mathbf{v}_D(z_n +) = \mathbf{W}_{DD}(z_n +, z_n -)\mathbf{v}_D(z_n -). \tag{2-37}$$

Now, defining $\mathbf{\Lambda}_D = diag\begin{pmatrix} q_P^D & q_{S1}^D & q_{S2}^D \end{pmatrix}$, and using equation (2-17), the complete extrapolation from the bottom of layer (*n*-1) to the bottom of layer *n*, can be written

$$\mathbf{v}_D(z_n +) = \mathbf{W}_{DD}(z_n +, z_n -)e^{i\omega\mathbf{\Lambda}_D(z_n - z_{n-1})}\mathbf{v}_D(z_{n-1} +). \tag{2-38}$$

The one-way decomposition and composition relationships are given by

$$\mathbf{v}_D = \mathbf{D}_D^{-L}\mathbf{b}, \tag{2-39}$$

and

$$\mathbf{b}_D = \mathbf{D}_D\mathbf{v}_D, \tag{2-40}$$

where $\mathbf{D}_D = \begin{pmatrix} \hat{\mathbf{b}}_P^D & \hat{\mathbf{b}}_{S1}^D & \hat{\mathbf{b}}_{S2}^D \end{pmatrix}$ is the 6-by-3 matrix which generates the displacement-stress vector associated with only down-going P, S1 and S2 waves, and $\mathbf{D}_D^{-L} = \begin{pmatrix} \hat{\mathbf{g}}_P^D & \hat{\mathbf{g}}_{S1}^D & \hat{\mathbf{g}}_{S2}^D \end{pmatrix}^T$ is the 3-by-6 matrix which takes a displacement-stress vector and extracts the down-going wave-modes. Substitution of (2-39) into (2-40) shows that the matrix $\mathbf{D}_D\mathbf{D}_D^{-L}$ is a *projection* of **b** onto its down-going part, $\mathbf{b}_D$.

The combination of equation (2-39) applied at an initial depth, recursive application of equation (2-38), and the use of equation (2-40) at a final depth, describes forward extrapolation of the down-going elastic wavefield. Similar equations involving $\mathbf{W}_{UU}\left(z_n-, z_n+\right)$ describe backward extrapolation of the up-going wavefield.

For use within a prestack migration algorithm, forward extrapolation using $\mathbf{W}_{DD}$ and backward extrapolation using $\mathbf{W}_{UU}$ will be required. It is therefore convenient, and potentially more efficient, to find a way of computing one from the other. A relationship between these matrices is derived in Appendix F, and shown to be simply

$$\mathbf{W}_{UU}(z_n+, z_n-) = \overline{\mathbf{W}_{DD}}(z_n+, z_n-). \tag{2-41}$$

2.2.5 Comparison with Alford rotation

Alford (1986) is generally credited with a method of rotating shear-wave data to their natural coordinate system, based upon normal incidence considerations. In fact Alford's paper acknowledges that the theoretical basis was developed by Crampin (1981), which Alford's paper "ruthlessly simplifies" (Alford, 1986). In fairness, Alford's intention was to: (a) provide a criterion by which the optimal rotation angle could be estimated, and; (b) demonstrate the benefit of doing so on a field data example. Both of these objectives were realized. Since Alford rotation is something of an industry standard, it is worth examining the relationship to the interface propagators which are implicit in the extrapolation algorithm of this thesis.

2.2.5.1 Alford rotation

Equation (8) of Alford (1986) reads

$$\mathbf{V}(\theta) = \mathbf{R}^T(\theta)\mathbf{U}\mathbf{R}(\theta), \tag{2-42}$$

where $\mathbf{R}$ is a 2x2 rotation matrix through an angle θ, taken to be the rotation angle between the acquisition inline direction and the "natural coordinates" determined by fast (S1) and slow (S2) shear-wave directions. Specifically,

$$\mathbf{R}(\theta)=\begin{pmatrix}\cos\theta & \sin\theta\\ -\sin\theta & \cos\theta\end{pmatrix}. \tag{2-43}$$

The diagonal matrix **U** is referred to as the "natural solution", which would result from solving the wave propagation problem using the natural coordinate system. The (non-diagonal) matrix **V** is the representation of these solutions in the field acquisition coordinates. Alford rotation was originally based upon assuming a single anisotropic medium. Often the method of (2-42) is generalized for more than one layer via "layer stripping" (Winterstein and Meadows, 1991; Thomsen et al., 1999) in which case the total effect is obtained by composition of the right hand side matrices. For two layers with orientations this gives

$$\begin{aligned}\mathbf{V}(\theta)&=\mathbf{R}^T(\theta)\mathbf{U}_2\mathbf{R}(\theta)\mathbf{R}^T(\varphi)\mathbf{U}_1\mathbf{R}(\varphi)\\ &=\mathbf{R}^T(\theta)\mathbf{U}_2\mathbf{R}(\theta-\varphi)\mathbf{U}_1\mathbf{R}(\varphi)\end{aligned}, \tag{2-44}$$

where the first layer (i.e. the anisotropic layer encountered *first* during the wave propagation from source to receiver) has orientation φ and the second layer θ. The matrix $\mathbf{R}(\theta-\varphi)$ in (2-44) is a matrix which describes the reorientation of the natural (or principle) axes in passing from the first to second layers. As pointed out by Thomsen et al. (1999, Appendix E), there is in fact a matrix missing from equation (2-44), describing the transmission effect of S1 in the first layer to S1 in the second layer etc.

2.2.5.2 Vertical incidence case of interface propagator

In Appendix G it is shown that for a vertical (normal) incidence wave at an interface between two media with identical HTI moduli but different orientations φ and θ of the symmetry axis, the interface propagator has submatrices

$$\mathbf{W}_{DD}(\theta,\varphi)=\mathbf{W}_{UU}(\theta,\varphi)=\begin{pmatrix}\cos(\theta-\varphi) & -\kappa\sin(\theta-\varphi) & 0\\ \kappa\sin(\theta-\varphi) & \cos(\theta-\varphi) & 0\\ 0 & 0 & 1\end{pmatrix}, \tag{2-45}$$

and

$$\mathbf{W}_{DU}(\theta,\varphi)=\begin{pmatrix} 0 & i\chi\sin(\theta-\varphi) & 0 \\ i\chi\sin(\theta-\varphi) & 0 & 0 \\ 0 & 0 & 0 \end{pmatrix}=-\mathbf{W}_{UD}(\theta,\varphi), \qquad (2\text{-}46)$$

where

$$\kappa=\frac{V_{S1}+V_{S2}}{2\sqrt{V_{S1}V_{S2}}} \text{ and } \chi=\frac{V_{S1}-V_{S2}}{2\sqrt{V_{S1}V_{S2}}}\,. \qquad (2\text{-}47)$$

The velocities V_{S1} and V_{S1} are the fast (S1) and slow (S2) shear-wave velocities for propagation parallel to the vertical axis. The difference between $\mathbf{W}_{DD}$ and $\mathbf{W}_{UU}$ and the rotation matrix in (2-44) can be explained by the transmission effects across the interface. They are compensated by the non-zero terms contained in the reflection matrices $\mathbf{W}_{UD}$ and $\mathbf{W}_{UD}$. The quantities κ and χ can be rewritten in terms of Thomsen's dimensionless parameter γ (Thomsen, 1988), which relates fast and slow shear-wave velocities via

$$V_{S1}=V_{S2}(1+\gamma). \qquad (2\text{-}48)$$

After substitution of (2-48) into (2-47), and development as a power series, the results are

$$\kappa=\frac{1+\gamma/2}{(1+\gamma)^{1/2}}=1+\frac{\gamma^2}{8}+O(\gamma^3), \qquad (2\text{-}49)$$

and

$$\chi=\frac{\gamma}{2(1+\gamma)^{1/2}}=\frac{\gamma}{2}-\frac{\gamma^2}{4}+O(\gamma^3). \qquad (2\text{-}50)$$

From (2-49), the horizontal parts of the matrices $\mathbf{W}_{DD}$ and $\mathbf{W}_{UU}$ used in extrapolation differ from the standard rotation matrix in equation (2-44) by small terms of order γ^2. Since γ itself is generally small compared to one, the standard rotation matrix is a good approximation to these propagators, in the specific case of vertical wave propagation.

However, the derivation of (2-45) and (2-46) is related to the case where the HTI moduli did not change across the interface, only the symmetry axis. In the case where there is a significant change in medium properties, this conclusion may not hold true. More importantly, the basic assumption underlying Alford's and related approaches, namely that of vertical incidence, is obviously suspect when dealing with at least moderate structure, or large offset.

2.2.6 Examples of interface propagators

Figure 2.9 shows interface-propagators graphically for an interface between two isotropic media with a P-wave velocity change from 2800m/s to 3200m/s, and an S-wave velocity change from 1400m/s to 1600m/s. The propagators are shown for P-wave angles of (a) 0° and (b) 60°. Figure 2.10 shows the same for an isotropic medium over an HTI medium with an axis of symmetry at 45° azimuth. Salient points are: (i) that there are no off-diagonal terms for isotropic contrasts at vertical incidence, since there are no mode conversions, but at non-zero angles of incidence there are off-diagonal terms corresponding to conversion between P and SV modes; and (ii) for the HTI case there is strong normal incidence conversion to S1 and S2 modes from SV or SH modes, corresponding to shear-wave splitting, described approximately by a rotation matrix with 45° azimuth. This also occurs at non-zero angles, but is asymmetric, such that a simple rotation matrix based on 45° azimuth is no longer a good approximation (Figure 2.10(b)).

The formulation of the extrapolator in terms of interface-propagators, as in equation (2-38), is more efficient than explicit mappings between v and b at each interface, but also affords another advantage. Since the one-way interface-propagators $\mathbf{W}_{DD}$ and $\mathbf{W}_{UU}$ are 3-by-3 matrices which describe the conversion between modes across interfaces, it is possible to be selective about which mode conversions are honoured when extrapolating the wavefield. Doing so can reduce sensitivity to errors in the model, and so prevent the generation of spurious artifacts. The same approach was taken by Silawongsawat (1998) in the context of forward modelling, as an aid to interpretation of the modelled results. The simplest approximation is to use only the diagonal elements of the interface-propagators, which corresponds to ignoring all mode conversions during extrapolation.

In this case, the algorithm reduces to a pure scalar extrapolation for each mode, as in equation (2-1), except that the amplitudes are corrected for transmission effects.

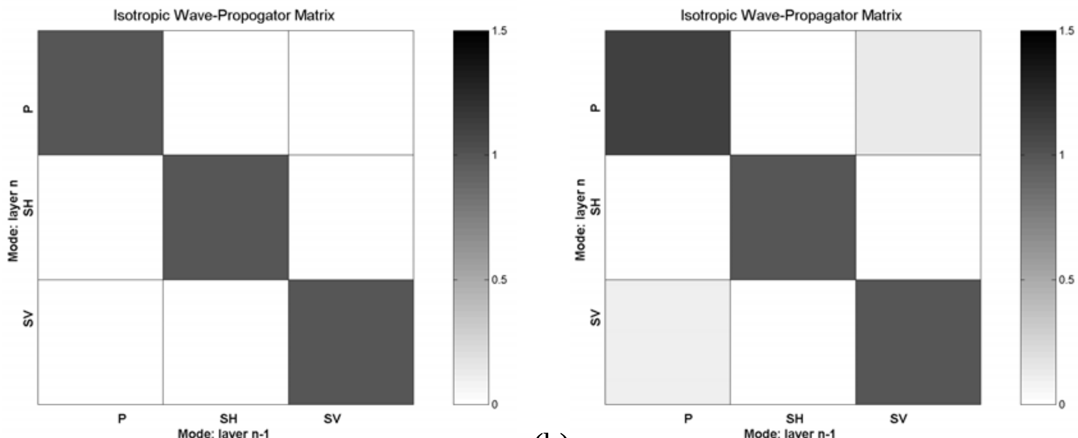

(a) (b)

Figure 2.9. Interface-propagator matrices for isotropic medium contrast, from layer *n*-1 (v_P=2800m/s, v_S=1400m/s) to layer *n* (v_P=3200m/s, v_S=1600m/s). P-wave incidence angles are (a) 0° and (b) 60°.

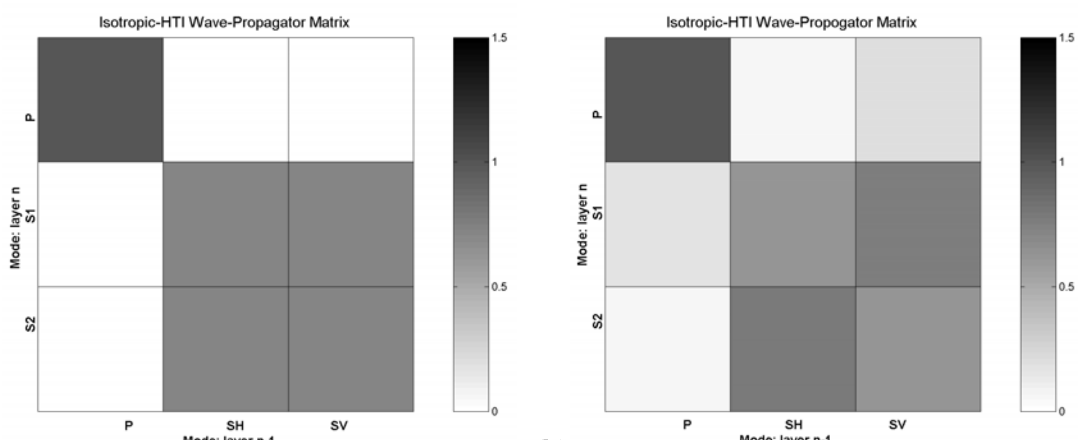

(a) (b)

Figure 2.10. Interface-propagator matrices for isotropic (layer *n*-1) to HTI (layer *n*) medium contrast. P-wave incidence angles are (a) 0° and (b) 60°. The axis of symmetry for the second medium is at 45° azimuth.

2.2.7 Boundary conditions

In order to commence downward extrapolation, we first need either a displacement-stress vector, $\mathbf{b}(z_0)$, or the wave-mode vector $\mathbf{v}(z_0)$ in the top layer. Since generally only displacement (or velocity, the time derivative of displacement) is measured, there remains the problem of determining the stress vector, or alternatively the wave-modes directly. Two scenarios are now considered, and it is shown how this problem is resolved in each case, without additional measurements.

2.2.7.1 Free surface boundary condition

The simplest case is when the wavefield is recorded on a free surface, such as the earth-air interface. A free surface has zero stress, which is easily incorporated into the vector $\mathbf{b}(z_0)$, which simply becomes:

$$\mathbf{b}(z_0) = \begin{pmatrix} \mathbf{u}(z_0) \\ \mathbf{0} \end{pmatrix}, \tag{2-51}$$

where $\mathbf{0}$ is the 3-vector of zero values. This can then be substituted into equation (2-39) to obtain the down-going wave-mode vector, $\mathbf{v}_D(z_0)$. This is then used to initiate the recursion of equation (2-38).

2.2.7.2 One-way boundary condition

A second possible scenario assumes that up-down separation has been applied, so that it can be assumed that waves propagate in only the down-going direction (or up-going, if at the receiver side). In this case we have a wave-mode vector of the following form:

$$\mathbf{v}(z_0) = \begin{pmatrix} \mathbf{0} \\ \mathbf{v}_D(z_0) \end{pmatrix}. \tag{2-52}$$

From equation (2-39), we can deduce:

$$\mathbf{u}(z_0) = \mathbf{D}'_D \mathbf{v}_D(z_0), \tag{2-53}$$

where $\mathbf{D}'_D = \begin{pmatrix} \mathbf{u}_P^D & \mathbf{u}_{S1}^D & \mathbf{u}_{S2}^D \end{pmatrix}$ is the 3-by-3 matrix containing the first 3 rows of $\mathbf{D}_D$.

Inverting equation (2-53) we get:

$$\mathbf{v}_D(z_0) = \left[\mathbf{D}'_D\right]^{-L} \mathbf{u}(z_0). \qquad (2\text{-}54)$$

In this case, the algorithm commences with equation (2-54), which then initiates the recursive extrapolation of equation (2-38).

The down-going cases described here are relevant for the shot side. Similar equations obtain for the up-going waves in both cases, as is required on the receiver side.

2.3 Comment on dimensionality

The theory discussed up to this point (with the exception of the illustrative scalar case in section 1.4) is applicable in three dimensions. In particular equations such as (1-13) and (2-8) have been written for slowness vectors $\mathbf{s} \in R^3$. From here onwards, the theory is restricted to two dimensions, for simplicity and in order to be consistent with the examples provided. In doing so, a non-physical assumption is introduced which is standard for two-dimensional imaging of seismic data. This is the line-source assumption, which allows us to neglect dependence on the *y*-direction, by positing an infinitely long seismic source parallel to the *y*-axis, and generating a cylindrical wavefront. This is entirely consistent with the assumptions made in the two-dimensional modelling codes used for the tests in Chapter 5 and 6.

For real world applications, it is necessary to take account of the localized nature of a physical source. This can be done by introducing corrections which arise when the *y*-axis is integrated out of the equations. The most obvious of these is the amplitude correction required to compensate for the difference in two-dimensional and three-dimensional energy decay or "spreading".

An important caveat needs to be mentioned however. Although the wave propagation is henceforth restricted to two dimensions, the particle displacement is still taken to be a three dimensional quantity. It is a fundamental feature of elastic wave propagation, that the slowness (or phase velocity) vector and the displacement vector are not required to be in the same plane. So even if the former is restricted to two dimensions, the latter need not be. The simplest example is that of a pure SH wave, which propagates within the vertical plane containing the source and receiver, but is polarized orthogonal to that plane.

If this were not the case, then the very phenomenon of immediate interest, namely shear-wave splitting, would not be possible. This idealization is consistent with the fact that shear-wave splitting may be observed from two dimensional seismic surveys conducted over an earth which has no variation in the crossline direction, but does exhibit azimuthal anisotropy.

2.4 Extrapolator impulse responses

2.4.1 Homogeneous isotropic medium

The first example used to illustrate the algorithm is wavefield extrapolation in a homogeneous isotropic medium. The P and S velocities are 3000m/s and 1500m/s respectively. Figure 2.11 demonstrates the operator construction by way of an impulse response for a 200m *downward* extrapolation of the *up-going* wavefield. The "impulse" is a bandlimited spike on the u_z component (a). After the decomposition step (here assuming a free surface condition), the P and SV (labelled S2 in figures) inputs, $v_P(z_0)$ and $v_{SV}(z_0)$, are shown in (b). Since this is isotropic, there is no SH response. The extrapolated P and SV modes, $v_P(z_1 = z_0 + 200m)$ and $v_{SV}(z_1)$, are shown in (c). Finally the displacements at the new depth, $u_x^U(z_1)$ and $u_z^U(z_1)$, are shown in (d).

During extrapolation, a small (1%) imaginary velocity has been added to the true velocity in order to both stabilize the decomposition by avoiding singularities and to suppress Fourier wrap around artifacts. This acts as a sort of numerical anelasticity that preferentially suppresses artifacts with large traveltimes such as Fourier wrap-around events.

Figure 2.12 shows the frequency-wavenumber (F-K) amplitude spectra of the extrapolated result as in Figure 2.11 (d), though in this case only 0.01% imaginary velocity was used, in order to better see the full F-K response. In the F-K domain, the relationship between propagating and evanescent areas is easily seen, with an interference effect occurring where both P- and S-modes are propagating. In Figure 2.13 the output from Figure 2.11 is extrapolated back upwards to the original depth. The residual energy on the X component arises because the P-wave evanescent area between the maximum P- and SV-wave slownesses cannot be recovered.

2.4.2 Homogeneous HTI medium

In Figure 2.14, the operator in an HTI medium is illustrated by way of impulse responses, using the same input as for the isotropic example in Figure 2.11 Two examples are shown: one, (a), for an axis of symmetry aligned with the *x* direction; and another, (b), for an axis of symmetry at 45° azimuth to the x axis. Only the extrapolated wave-modes are shown in both cases. The anisotropy gives rise to triplications along the plane which contains the symmetry axis, as can be seen in (a), and to an S2 response in the case where the symmetry axis is rotated as is seen in (b).

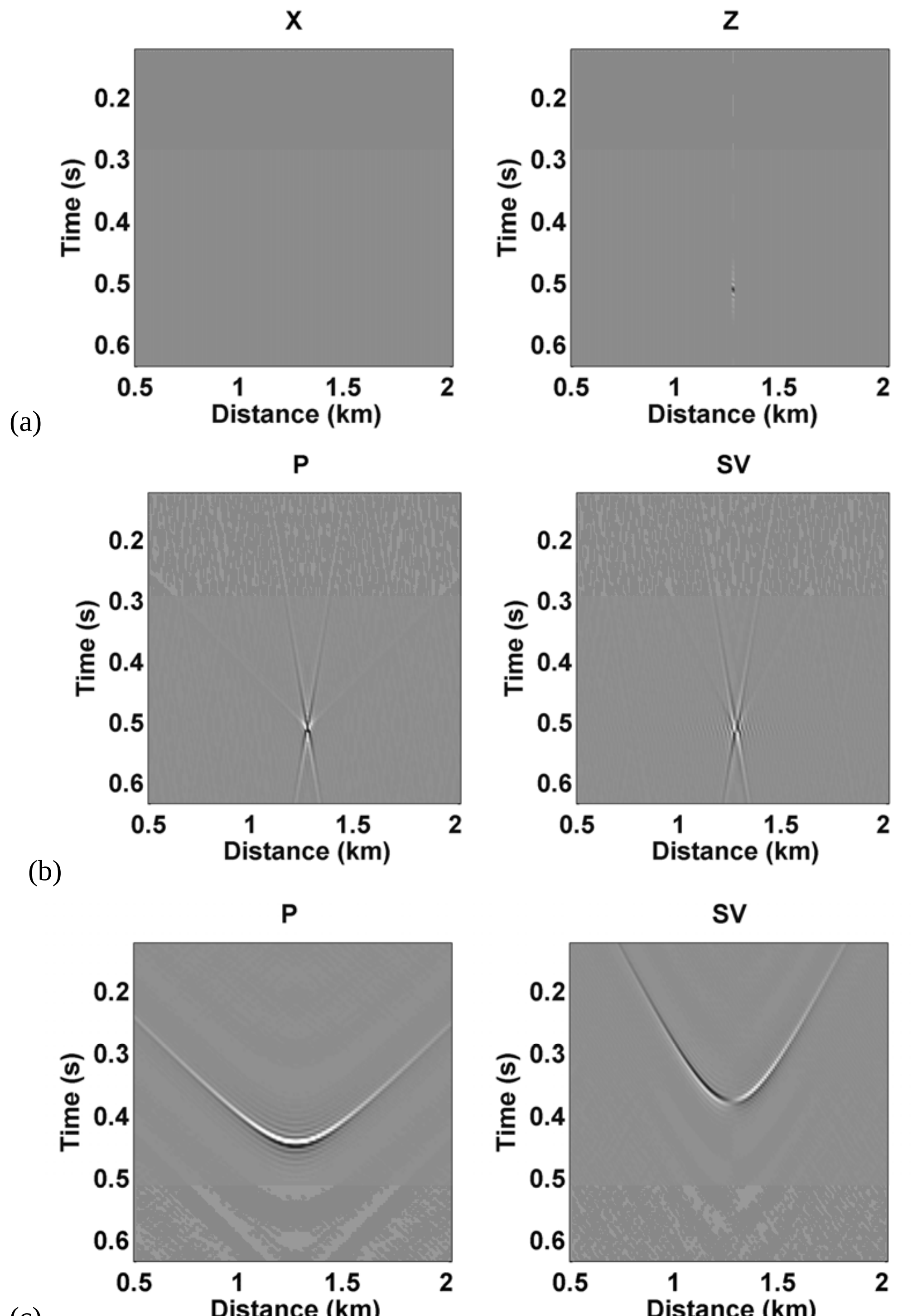

Figure 2.11. Wavefield extrapolator impulse response construction for homogeneous, isotropic medium: (a) input bandlimited spike on Z component; (b) after decomposition into up-going P and SV (S2) modes; (c) after extrapolation downward by 200m;

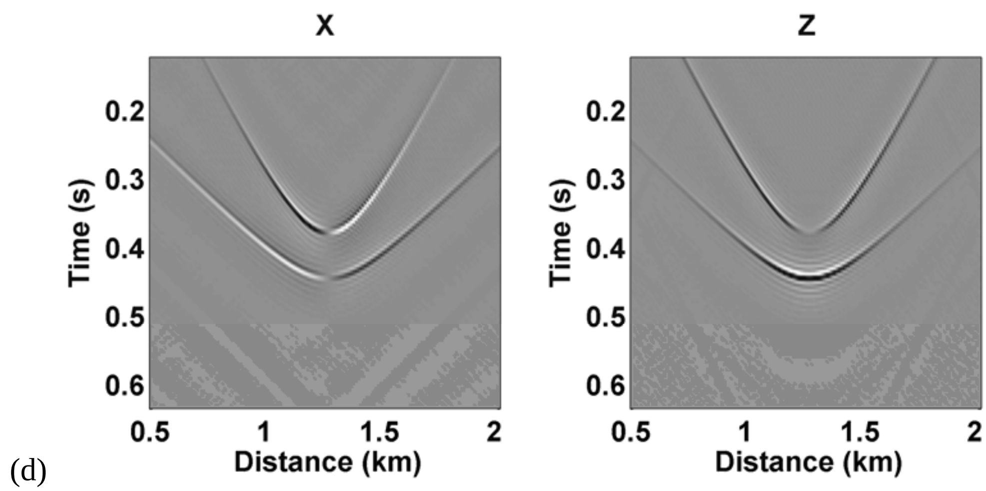

Figure 2.11 (continued) (d) after recomposition to X and Z components. Plots have the same display scaling applied.

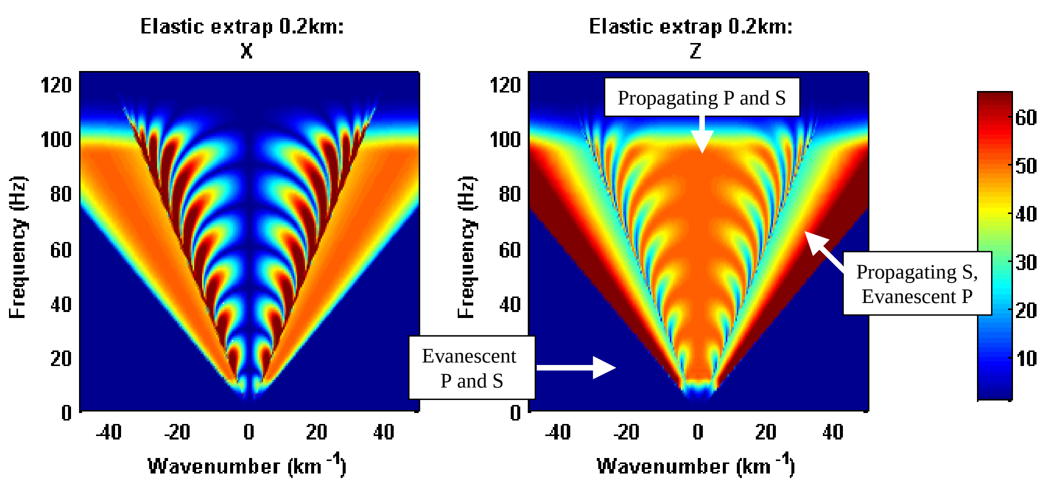

Figure 2.12. FK spectra of extrapolated displacements, as in Figure 2.12(d) but using only 0.01% imaginary velocity.

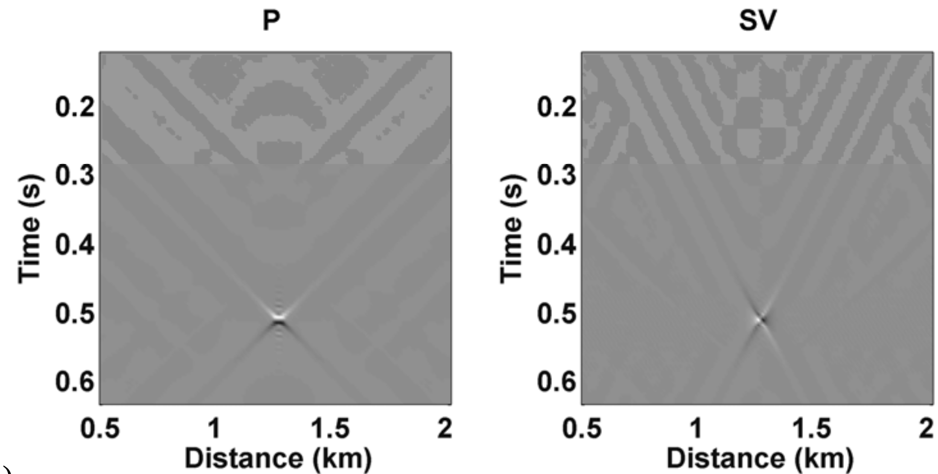

(a)

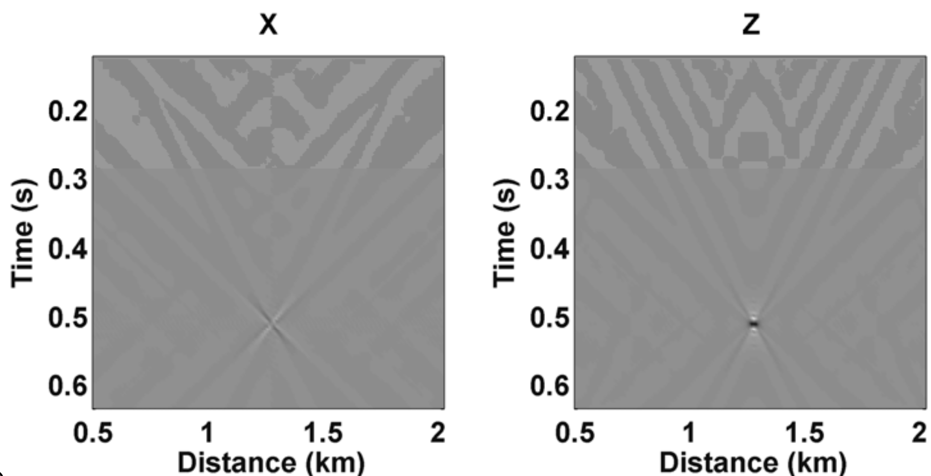

(b)

Figure 2.13. Result of applying inverse extrapolation operator to impulse response shown in Figure 2.11: (a) upward extrapolated P and SV modes; (b) after recomposition to X and Z components. Compare (a) with Figure 2.11 (b) and (b) with Figure 2.11(a). Plots have the same display scaling applied as in Figure 2.11.

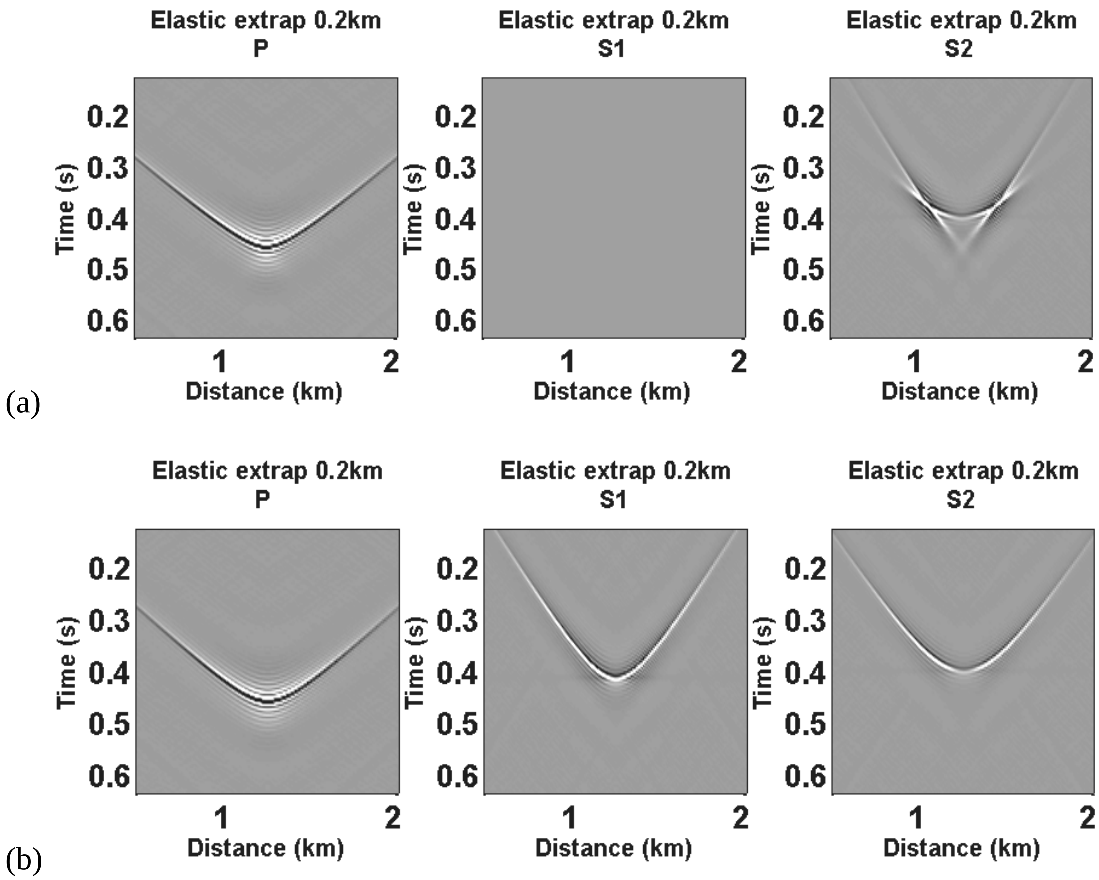

Figure 2.14. A comparison of impulse responses for HTI media with different symmetry axes. The wave-modes prior to recomposition are shown, for the same impulse input as in Figure 2.11, after extrapolation 200m downwards in an HTI medium: (a) with axis of symmetry along the *x* direction; (b) with axis of symmetry at 45° azimuth to the *x* direction. Note the presence of triplications for the SV (S2) mode when the plane contains the symmetry axis.

2.5 Application to modelled data

2.5.1 Homogeneous HTI medium

The wavefield extrapolation is now applied to modelled data, in a homogeneous HTI medium. The modelled data are generated using the pseudospectral method (Bale, 2002a; 2002b), for an HTI medium with an axis of symmetry at 45° azimuth to the x axis. The geometry for the modelling is shown in Figure 2.15. The source is a vertical displacement force at 1000 m depth. An absorbing boundary is placed along all four edges of the domain, so that only up-going waves are recorded, apart from some low level residual reflection due to imperfect absorption. The wavefield was recorded at three different levels, A, B, and C, as shown in Figure 2.15. This allows direct comparison of the data extrapolated from A to B or C, with the true data at those depths.

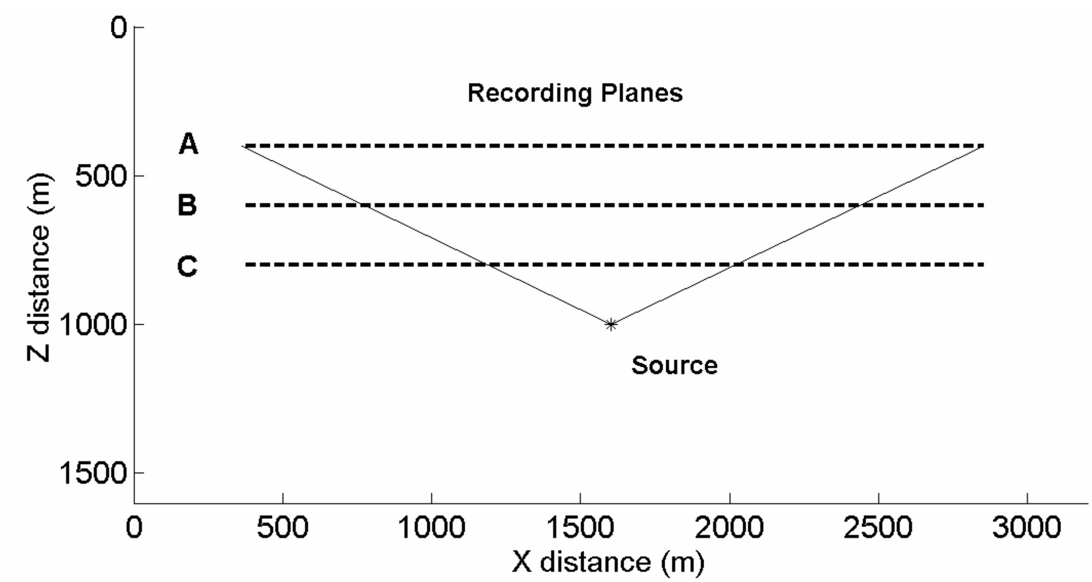

Figure 2.15. Geometry of modelled data. Vertical displacement source generates P and S waves at a depth of 1000m, these are recorded at three different levels shown by dashed lines: A (400m), B (600m) and C (800m). Solid diagonal lines show angular aperture limitation during extrapolation.

Figure 2.16 shows the result of downward extrapolating the data from level A to level B. The input data are shown in (a). The extrapolation is broken down into the following steps: (b) decomposition into wave-modes, P, S1 and S2, at A; (c) extrapolation and recomposition at B. Compare the result in (c) with the modelled wavefield at level B, shown in (d). The differences are primarily the result of aperture limitations, since the angular aperture at A is smaller than that at B, for the same width of recording array. This effect comes into play during downward (backward) extrapolation of the receivers in shot migration, and is inherent in the geometry.

By contrast, consider Figure 2.17, which shows the upward extrapolation of the wavefield from level C, (a), to levels B, (b) and A, (c). As can be seen by comparison with the modelled results in Figure 2.16, extrapolation gives accurate results in this direction. This is because the angular aperture of the input wavefield is broader than that of either output. This geometry (with the z axis inverted) is relevant to downward (forward) extrapolation of a shot. The results in Figure 2.16 and Figure 2.17 confirm that the elastic wavefield extrapolation is working as intended for an HTI medium.

2.5.2 Vertically heterogeneous HTI medium

The final example illustrates the effect of vertical heterogeneity on the extrapolation. The model used, as shown in Figure 2.18, consists of two layers: an isotropic layer overlying the same HTI layer as used in the previous example.

Figure 2.19 shows the results of extrapolating input at level C by 400m upwards to level A: (a) using the full matrix for the one-way interface-propagator across the interface, corresponding to all transmission conversions; (b) including only diagonal terms of the matrix, corresponding to neglecting all conversions; and, (c) excluding the P-to-S conversions but including the S1 to S2 conversions. The weaker, flatter events are spurious reflections from the model boundary and should be ignored. The result from using the full matrix, in (a), compares well with the modelled data in (d), even recovering the weak P-to-S conversion visible after the first arrival on the X component. While ignoring the P-to-S conversions has a small impact on the extrapolated data (compare (c) with (a), and with (d)), it is evident that ignoring all conversions, (b), is inadequate in this example. To do so ignores the rotation of the anisotropy symmetry axis. Including the

S1-S2 conversion terms in the interface-propagator matrix essentially embeds a generalized Alford rotation within the extrapolation, and is a necessary step when imaging in the presence of azimuthal anisotropy.

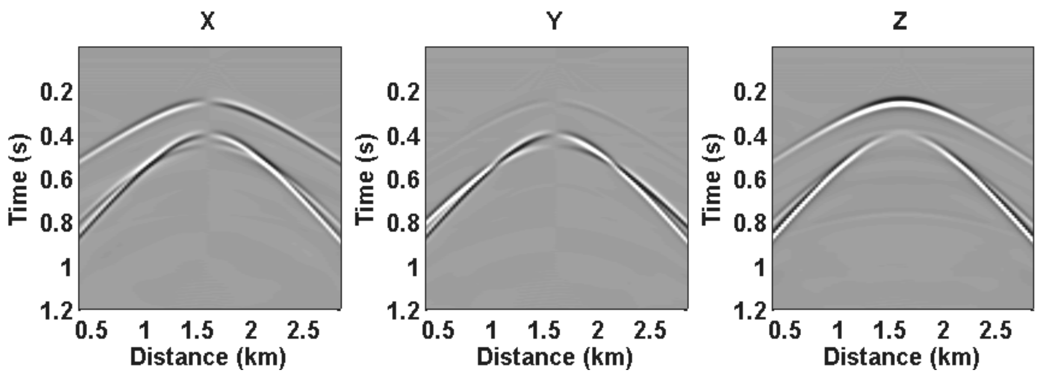

(a)

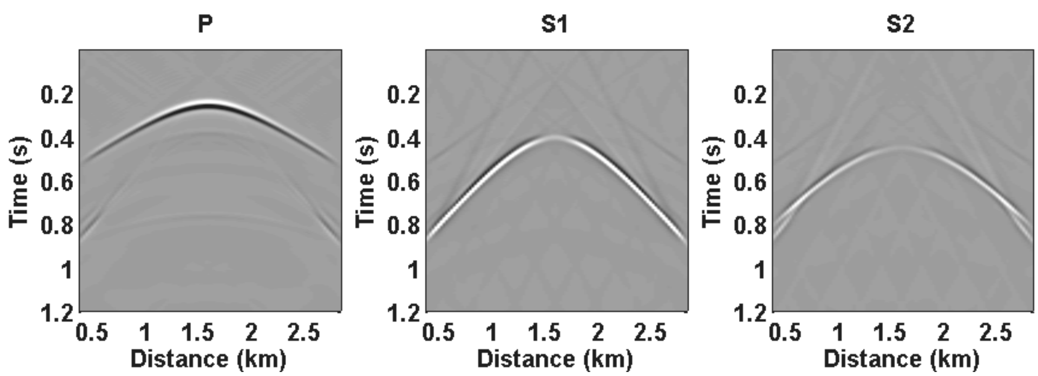

(b)

Figure 2.16. Downward extrapolation of modelled HTI data: (a) displacement wavefield recorded at A (see Figure 2.15); (b) after wavefield decomposition into P, S1 and S2 modes.

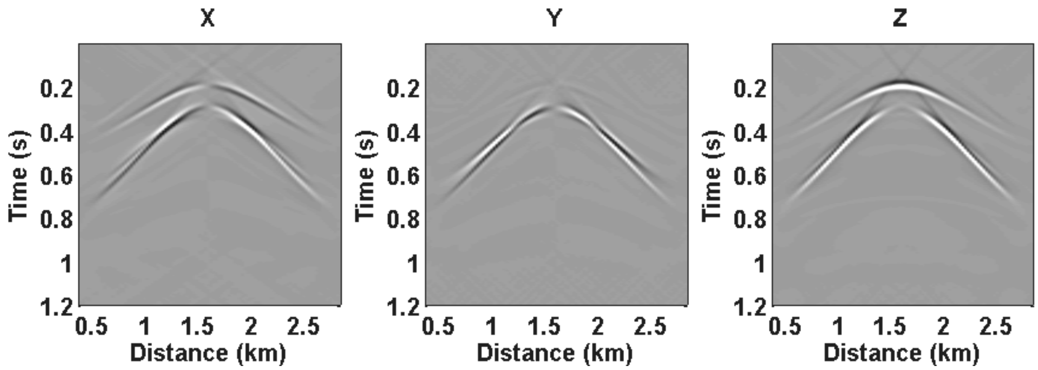

(c)

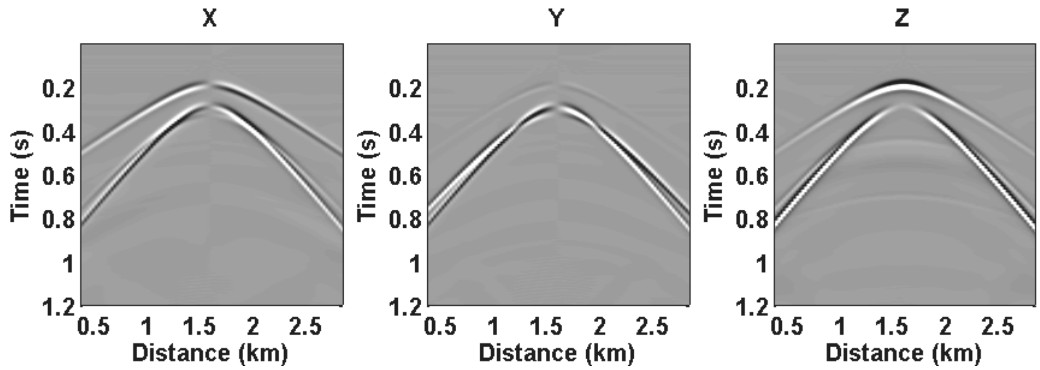

(d)

Figure 2.16 (continued) Downward extrapolation of modelled HTI data: (c) after extrapolation and recomposition to displacement at B; (d) data recorded at B from forward modelling. Compare the result of extrapolation, (c), with modelled data at B, (d).

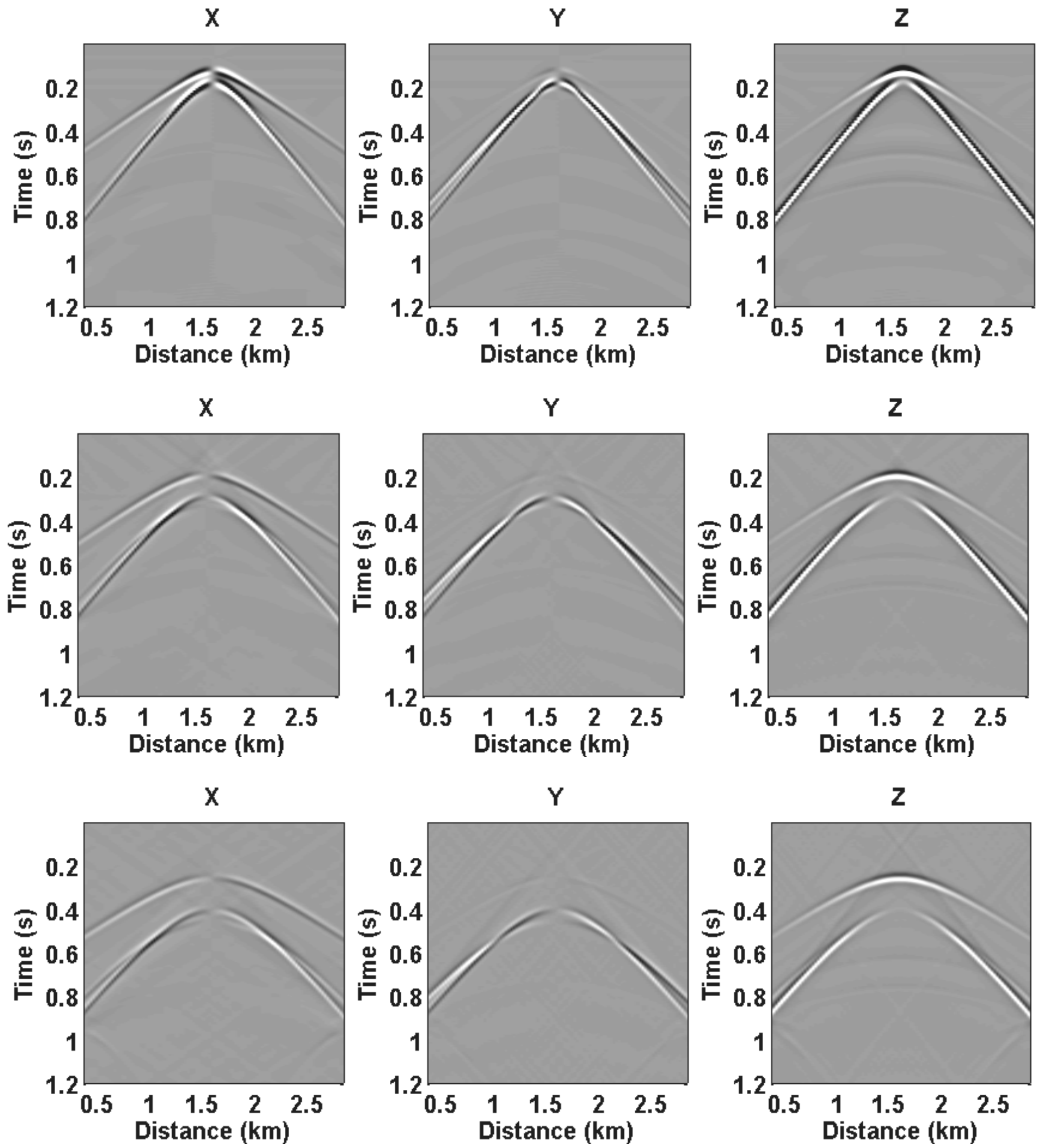

(a)

(b)

(c)

Figure 2.17. Upward extrapolation of modelled HTI data: (a) displacement wavefield recorded at C (see Figure 2.15); (b) extrapolated upwards to B - compare with Figure 2.16(d); (c) extrapolated upwards to A – compare with Figure 2.16(a).

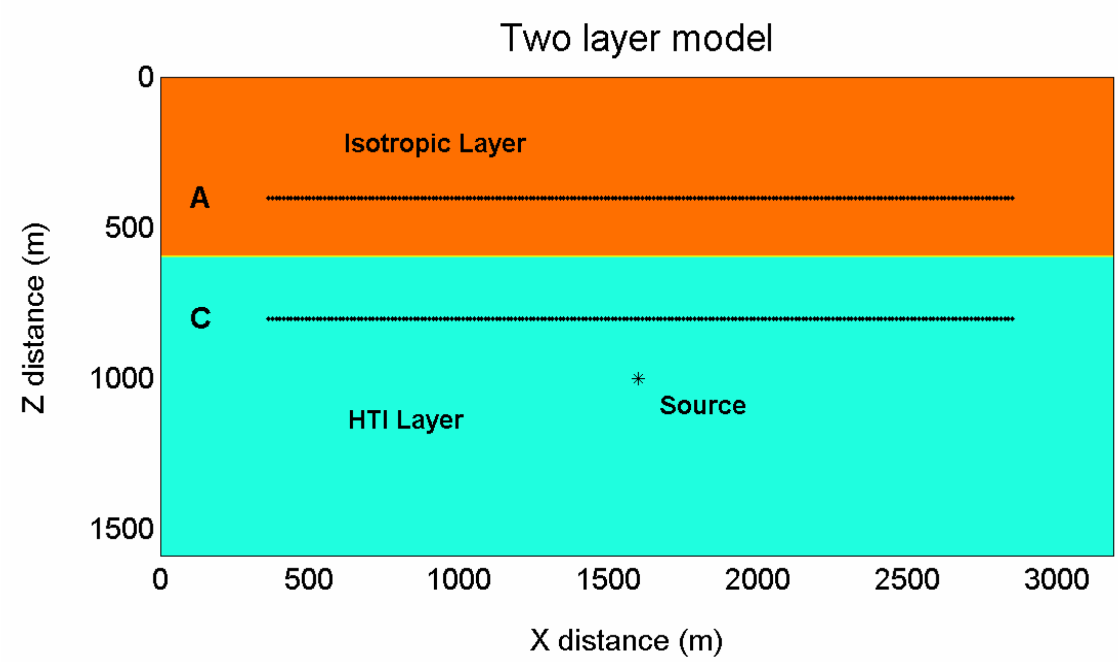

Figure 2.18. Two-layer model consisting of an isotropic medium overlaying an HTI medium with axis of symmetry at 45° azimuth. Modelled data generated at levels A and C, located as before.

2.6 Chapter summary

The extrapolation of elastic waves consists of first decomposing the displacement wavefield into wave-modes P, S1 and S2, using an appropriate boundary condition assumption, and then recursive application of phase-shift operators and an "interface-propagator" matrix operation which handles the effects of medium changes at each depth interface. This is equivalent to reconstructing the displacement-stress vector which is continuous across each interface. The operators which achieve this are found by solving the Kelvin-Christoffel equation. The eigenvalues of the Kelvin-Christoffel equation lead directly to the phase-shift operators, while the eigenvectors give the polarizations of displacement. The relationship between stress and displacement is then used to compute eigenvectors of the appropriate one-way equation, and from these the interface-propagators are determined. The solution to the Kelvin-Christoffel equation is analytic for the HTI case, and the up- and down-going solutions are also simply related in this case. The choice of whether to use down-going or up-going solutions depends on whether we are forward extrapolating a downward propagating source wavefield, or backward extrapolating an upward propagating receiver wavefield.

The structure of the interface-propagator matrices allows the selective inclusion of forward-scattered mode-conversions in the extrapolator. This allows the neglect of conversions which might become generators of spurious noise, due to model inaccuracies. In particular, the author suggests that in many (though by no means all) cases, P-to-S conversion may be safely neglected (except, of course, for conversion on reflection, which would be dealt with in migration by an appropriate imaging condition). However, in the case of the interface between an isotropic and an HTI medium, it is found that inclusion of the S1-S2 conversions is important for proper extrapolation of the wavefield. It is therefore expected that this form of extrapolator will be useful in imaging fractured media where shear-wave splitting is a significant factor. Use of this kind of extrapolator could be regarded as a form of generalized Alford rotation, which is not limited by assumptions of dip or offset.

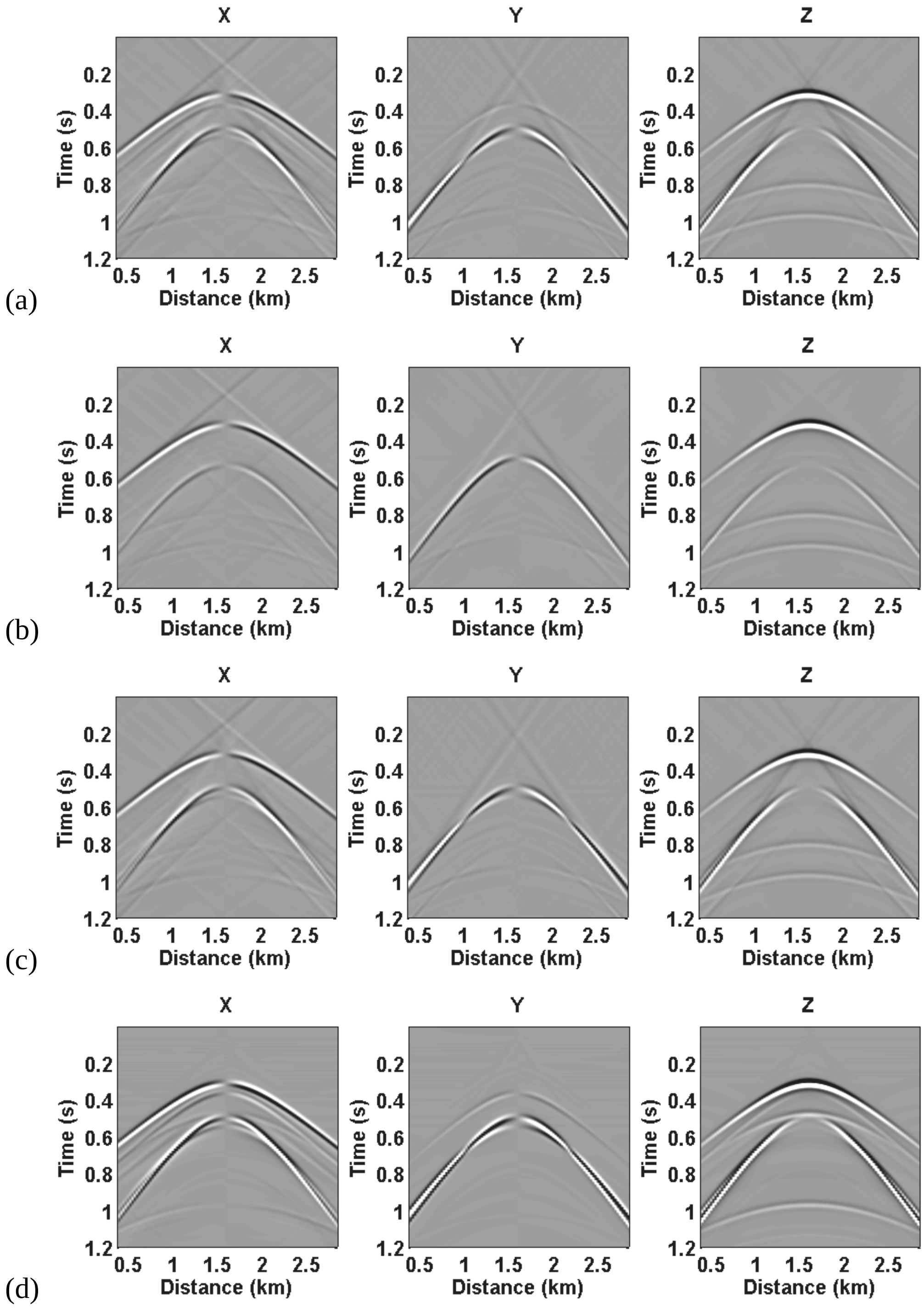

Figure 2.19. Upward extrapolation, from C to A, through two layer model of Figure 2.18: (a) extrapolation using full one-way interface-propagator matrices across boundary, including all mode conversions; (b) extrapolation using only diagonal matrices, neglecting all conversions; (c) extrapolation using matrix with P-S conversions neglected; (d) modeled data at level A.

CHAPTER THREE: ADAPTING ELASTIC WAVEFIELD EXTRAPOLATION TO LATERALLY VARYING HTI MEDIA

3.1 Introduction

In Chapter 2, the design of wavefield extrapolators for elastic, HTI (transversely isotropic, with a horizontal symmetry axis) media was discussed. That chapter assumed that the medium varies only in the vertical direction. Here the extension to more realistic media which have lateral variation of properties is investigated. The problem of *acoustic* extrapolation in laterally varying media has been the subject of much previous research within the CREWES and POTSI consortia at the University of Calgary (Margrave and Ferguson, 1999; 2000; Ferguson and Margrave, 2002; Grossman et al., 2002a). The conceptual framework which has been developed is to represent the ideal extrapolation operator as a ΨDO in which the phase shift applied depends on both x and k_x simultaneously.

There are two elementary, alternative ways this can be done, depending on whether the operator integral transforms the wavefield from the Fourier domain back to the spatial domain, referred to as "phase shift pluse interpolation" (PSPI) (Gazdag and Sguazerro, 1984), or from the spatial domain forward to the Fourier domain, referred to as non-stationary phase shift (NSPS) (Margrave and Ferguson, 1999). For the PSPI method, the appropriate comparison with NSPS is based upon its more general form (Margrave and Ferguson, 1999), referred to here as GPSPI. GPSPI and NSPS correspond to the standard and adjoint forms of a ΨDO respectively. In either case, practical implementation of the operator is usually achieved by a windowed Fourier transform so that FFT codes can be used. There are different ways to implement this, including the original interpolation method of Gazdag and Sguazzero's (1984) PSPI and an adaptive windowing approach. For scalar extrapolation, a Gabor domain method known as adaptive Gabor phase-shift (AGPS), which aims to optimize spatial windowing based on the spatial variation of the model, was investigated by Grossman et al. (2002a; 2002b). In the present chapter, discussion is primarily concerned with the ideal limiting forms of the two methods. The implications of windowing the operators are also discussed without considering details of the window design. An adaptive method for designing spatial windows for elastic extrapolation will be discussed in Chapter 4.

In this chapter, the goal is to show how the GPSPI and NSPS approaches apply to *elastic* wavefield extrapolation, and to discuss some specific issues which arise in this context. In the next section the key results of Chapter 2 are briefly restated in a form which is convenient for the development here, before proceeding to look at GPSPI and NSPS formulations of that theory. The alternative formulation using the "interface-propagator" matrix is investigated, due to the possible efficiency advantages. However, it proves to have limitations due to implicit inconsistencies between decompostion and recomposition steps. The subsequent section illustrates the extrapolation operators with numerical examples for laterally discontinuous media.

3.2 Review of laterally homogeneous case

Writing equation (2-29) [or (2-30)] with the up and downgoing indices, *U* and *D*, suppressed, but instead indexing the depths explicitly, the elastic extrapolation operator for wave propagation in a 2-D[1] laterally homogeneous HTI medium with horizontal slowness $s_x = k_x/\omega$, is

$$\mathbf{b}(s_x, z_{n+1}, \omega) = \mathbf{D}_n e^{i\omega\mathbf{\Lambda}_n(z_{n+1}-z_n)} \mathbf{D}_n^{-L} \mathbf{b}(s_x, z_n, \omega), \tag{3-1}$$

with $\mathbf{b}$ as defined in equation (2-11).

The 6-by-3 matrix $\mathbf{D}_n$ contains the eigenvectors, $\hat{\mathbf{b}}_n^{(M)}$, for each mode $M \in \{P, S1, S2\}$, which are one-way solutions to equation (2-10) in layer *n*. The direction of propagation is implied by context: up-going for backward extrapolation of the receiver wavefield, down-going for forward extrapolation of the source wavefield. The subscript *n* refers to the layer below the n^{th} interface, with layers chosen sufficiently finely such that vertical variation of the medium may be neglected. Layer *n* lies between z_n and z_{n+1}. The diagonal matrix $\mathbf{\Lambda}_n = diag\begin{pmatrix} q_n^P & q_n^{S1} & q_n^{S2} \end{pmatrix}$ contains the vertical slownesses for each mode in layer *n*.

[1] See comments in section 2.3

Both $\mathbf{D}_n$ and $\mathbf{\Lambda}_n$ depend on s_x, but not on ω, nor, in this case, on *x*.

Alternatively, a more compact solution can be sought, premultiplying both sides of equation (3-1) by $\mathbf{D}_{n+1}^{-L}$, as for equation (2-38), to obtain

$$\mathbf{v}(s_x, z_{n+1}+, \omega) = \mathbf{W}(s_x; z_{n+1}+, z_{n+1}-) e^{i\omega \mathbf{\Lambda}_n (z_{n+1}-z_n)} \mathbf{v}(s_x, z_n+, \omega), \qquad (3\text{-}2)$$

where

$$\mathbf{b}(s_x, z_n, \omega) = \mathbf{D}_n(s_x)\mathbf{v}(s_x, z_n+, \omega) = \mathbf{D}_{n-1}(s_x)\mathbf{v}(s_x, z_n-, \omega),$$

and

$$\mathbf{W}_{n+1}(s_x) = \mathbf{W}(s_x; z_{n+1}+, z_{n+1}-) = \mathbf{D}_{n+1}^{-L}(s_x)\mathbf{D}_n(s_x).$$

As discussed in Chapter 2, the three elements of $\mathbf{v}$ are the amplitudes of P, S1 and S2 waves, which can be independently extrapolated in a homogeneous medium. Recall that **v**, unlike **b**, is *not* necessarily continuous at z_n, which necessitates the use of the - and + qualifiers, to indicate just above and just below z_n, respectively (see Figure 2.7). Computation with equation (3-2) requires approximately half the memory of equation (3-1), and test results suggest it is approximately four times more CPU efficient, corresponding to the difference in operation count between applying two 3-by-6 matrix multiplies compared with a single 3-by-3 matrix multiply. Hence it is preferable, where possible, to formulate extrapolation in this form. An important question posed in this chapter is whether this same simplification can be used for laterally heterogeneous media. It will be seen that some difficulties arise.

3.2.1 GPSPI and NSPS elastic extrapolation

Just as for the scalar case, the elastic extrapolation can be implemented via a ΨDO under the locally homogeneous approximation, as discussed in section 1.4.3. Both the standard (GPSPI) and adjoint (NSPS) forms of extrapolation can be defined as in the scalar case.

Let us now consider GPSPI and NSPS equivalents to equation (3-1), and the circumstances under which they may be transformed to the more efficient form of equation (3-2). The key modification is that $\mathbf{D}_n$ and $\mathbf{\Lambda}_n$ now depend on *both* s_x and *x*. The GPSPI form of equation (3-1) is

$$\mathbf{b}_{PSPI}(x, z_{n+1}, \omega) = \frac{\omega}{2\pi}\int_{-\infty}^{\infty} \mathbf{D}_n(x, s_x)\mathbf{E}_n(x, s_x, \omega)\mathbf{D}_n^{-L}(x, s_x)\tilde{\mathbf{b}}(s_x, z_n, \omega)\, e^{-i\omega s_x x} ds_x \,, \tag{3-3}$$

where

$$\tilde{\mathbf{b}}(s_x, z_n, \omega) = \int_{-\infty}^{\infty} \mathbf{b}(x, z_n, \omega) e^{i\omega s_x x} dx \,,$$

$$\mathbf{E}_n(x, s_x, \omega) = e^{i\omega \mathbf{\Lambda}_n(x, s_x)(z_{n+1} - z_n)} \,,$$

and

$$\mathbf{\Lambda}_n(x, s_x) = diag\left(q_n^P(x, s_x) \quad q_n^{S1}(x, s_x) \quad q_n^{S2}(x, s_x)\right).$$

Similarly the NSPS form of the elastic extrapolator may be defined as follows

$$\tilde{\mathbf{b}}_{NSPS}(s_x, z_{n+1}, \omega) = \int_{-\infty}^{\infty} \mathbf{D}_n(x, s_x)\mathbf{E}_n(x, s_x, \omega)\mathbf{D}_n^{-L}(x, s_x)\mathbf{b}(x, z_n, \omega)\, e^{i\omega s_x x} dx \,. \tag{3-4}$$

Equation (3-3) and (3-4) are similar to inverse and forward Fourier transforms, but since the kernel depends on both *x* and s_x, they are not standard Fourier transforms, but are instead pseudodifferential or Fourier integral operators[1]. To numerically compute equations (3-3) or (3-4) requires applying the kernel $\mathbf{D}_n \mathbf{E}_n \mathbf{D}_n^{-L} e^{i\omega s_x x}$, a 6x6 matrix operation, for *each* input value of *x*, and *each* output value of s_x. This can be thought of as a *matrix* of matrix operators, and cannot be directly implemented using FFT code.

[1] Fourier integral operators (FIOs) are a superset of ΨDOs, as they can have more general phase functions. Here, we are in fact dealing with FIOs which also happen to be ΨDO s.

3.2.1.1 Practical implementation issues

The practical implementation of equations (3-3) or (3-4) is a complex issue. The standard PSPI approach is to first find the range of velocity variation and to design operators for each of a number of reference velocities within that range, then to apply spatially invariant operators for each reference velocity, and finally to interpolate the results based upon the spatially varying velocity. Unfortunately, while this is very effective for an acoustic extrapolation with only a single velocity parameter, we are here dealing with an operator which depends upon several parameters. The issues which arise due to the multiparameter nature of the medium are addressed in Chapter 4.

An alternative approach is to apply regular spatial windows for the operators, using either the parameter set corresponding to the center of the window, or some kind of window average. Assuming reasonably smooth variation of the medium, this appears a more economical approach, certainly for 2-D (or any narrow azimuth) cases. Other possibilities include an adaptive windowing approach, such as adaptive Gabor phase-shift (AGPS) (Grossman et al., 2002a; 2002b), or some kind of hybrid scheme. For example, in a model where there are two main units, each with smooth internal variation but abrupt change across the boundary (e.g. entering an HTI region), it might be appropriate to keep the anisotropy parameters fixed within each unit, and use a standard PSPI approach to vary the velocities internally to the units, or an alternative method such as split-step (Stoffa et al., 1990). Further discussion of the window design detail is deferred to Chapter 4. Here is assumed that a set of windows is predetermined.

3.2.1.2 Windowed forms

Following Margrave and Ferguson (1999), (3-3) and (3-4) can be reformulated in terms of windows Ω_j to obtain

$$\mathbf{b}_{PSPI}\left(x, z_{n+1}, \omega\right) = \frac{\omega}{2\pi}\sum_j \Omega_j\left(x - x_j\right)\int_{-\infty}^{\infty} \mathbf{P}_n\left(x_j, s_x, \omega\right)\mathbf{b}\left(s_x, z_n, \omega\right) e^{-i\omega s_x x} ds_x \,, \qquad (3\text{-}5)$$

and

$$\mathbf{b}_{NSPS}(s_x, z_{n+1}, \omega) = \sum_j \mathbf{P}_n(x_j, s_x, \omega) \int_{-\infty}^{\infty} \Omega_j(x - x_j) \mathbf{b}(x, z_n, \omega) e^{i\omega s_x x} dx, \qquad (3\text{-}6)$$

where

$$\mathbf{P}_n(x, s_x, \omega) = \mathbf{D}_n(x, s_x) \mathbf{E}_n(x, s_x, \omega) \mathbf{D}_n^{-L}(x, s_x).$$

Equations (3-5) and (3-6) arise from (3-3) and (3-4) when $\mathbf{P}_n(x, s_x, \omega)$ is approximated by the sum of windowed locally constant functions

$$\mathbf{P}_n(x, s_x, \omega) \cong \sum_j \Omega_j(x - x_j) \mathbf{P}_n(x_j, s_x, \omega). \qquad (3\text{-}7)$$

The window functions Ω_j can be piecewise constant as in Margrave and Ferguson (1999), or linear (triangular), or a smoother function such as a Gaussian. An important characteristic of these windows is that they must form a partition of unity

$$\sum_j \Omega_j(x - x_j) = 1, \forall x. \qquad (3\text{-}8)$$

Piecewise constant and linear windows can be constructed to satisfy (3-8). Gaussians do not strictly satisfy (3-8), but can be modified by normalization to do so (as can any set of well-behaved windows which cover the domain of *x*). Partitions of unity (POUs) are further discussed in Grossman et al. (2002b) and Bale et al. (2002).

3.2.2 Interface-propagator method

For laterally homogeneous media, equation (3-2) describes an efficient extrapolation using 3-by-3 interface-propagator matrices. The question of whether such an approach is viable for laterally heterogeneous extrapolation, using ΨDO (GPSPI/NSPS) type operators, will now be considered.

3.2.2.1 Exact interface-propagator derivation

First, the extrapolation of the wave-mode vector, **v**, is written using two pseudodifferential equations, one of an NSPS type, and the second of a GPSPI type. The choice is motivated somewhat by the observation, for the scalar case, that NSPS and GPSPI applied in combination have a tendency to cancel errors (Margrave and Ferguson, 1998). This can obviously be done in more than one way, arriving at different but similar results. The following is used

$$\begin{aligned}\mathbf{b}(s_x, z_{n+1}, \omega) &= \int_{-\infty}^{\infty} \mathbf{D}_n(x', s_x)\mathbf{v}(x', z_{n+1}-, \omega)\, e^{i\omega s_x x'} dx' \\ &= \int_{-\infty}^{\infty} \mathbf{D}_n(x', s_x)\mathbf{E}_n(x', s_x, \omega)\mathbf{v}(x', z_n+, \omega)\, e^{i\omega s_x x'} dx',\end{aligned} \tag{3-9}$$

and

$$\mathbf{v}(x, z_{n+1}+, \omega) = \frac{\omega}{2\pi}\int_{-\infty}^{\infty} \mathbf{D}_n^{-L}(x, s_x)\mathbf{b}(s_x, z_{n+1}, \omega)\, e^{-i\omega s_x x} ds_x \,. \tag{3-10}$$

Substitution of equation (3-9) into (3-10) gives

$$\mathbf{v}(x, z_{n+1}+, \omega) = \frac{\omega}{2\pi}\int_{-\infty}^{\infty} \mathbf{W}_n(x, x', \omega)\mathbf{v}(x', z_{n+1}-, \omega) dx', \tag{3-11}$$

where

$$\mathbf{W}_n(x, x', \omega) = \int_{-\infty}^{\infty} \mathbf{D}_n^{-L}(x, s_x)\mathbf{D}_{n-1}(x', s_x)\, e^{i\omega s_x (x'-x)} ds_x \,.$$

Since application of equation (2-32) entails a 3-by-3 matrix operation for each input point, x', and each output point, x, it will be considerably less efficient than the homogeneous version of equation (3-2).

As before, windowed versions of the spatially varying filters are introduced, in the hopes of deriving a more efficient interface-propagator for heterogeneous media. Equation (3-9) becomes

$$\begin{aligned}\mathbf{b}(s_x, z_{n+1}, \omega) = \sum_j \mathbf{D}_n(x_j, s_x)\mathbf{E}_n(x_j, s_x, \omega) \\ \int_{-\infty}^{\infty} \Omega_j(x' - x_j)\mathbf{v}(x', z_n+, \omega)\, e^{i\omega s_x x'} dx',\end{aligned} \tag{3-12}$$

while equation (3-10) becomes

$$\mathbf{v}(x, z_{n+1}+, \omega) = \frac{\omega}{2\pi} \sum_k \Omega_k (x - x_k) \int_{-\infty}^{\infty} \mathbf{D}_n^{-L} (x_k, s_x) \mathbf{b}(s_x, z_{n+1}, \omega) e^{-i\omega s_x x} ds_x \ . \qquad (3\text{-}13)$$

Substituting (3-12) into (3-13), and interchanging the order of integrations, gives

$$\begin{aligned} \mathbf{v}(x, z_{n+1}+, \omega) = & \frac{\omega}{2\pi} \sum_k \Omega_k (x - x_k) \\ & \sum_j \int_{-\infty}^{\infty} \mathbf{Y}_n^{(jk)}(x' - x, \omega) \Omega_j (x' - x_k) \mathbf{v}(x', z_n +, \omega) dx', \end{aligned} \qquad (3\text{-}14)$$

where

$$\mathbf{Y}_n^{(jk)}(y, \omega) = \int_{-\infty}^{\infty} \mathbf{D}_n^{-L} (x_k, s_x) \mathbf{D}_n (x_j, s_x) \mathbf{E}_n (x_j, s_x, \omega) e^{i\omega s_x y} ds_x \ . \qquad (3\text{-}15)$$

Application of equation (3-14) entails the following steps:

1. For each j, apply the windowing function to v.
2. For each j and k, apply (matrix) convolution of the windowed v by $\mathbf{Y}_n^{(jk)}$, summing over j.
3. For each k apply windowing function to the result of 2, and sum over k.

Step 2 unfortunately makes this approach inefficient, compared with the more direct approach of equations (3-5) or (3-6), as it requires computation of the matrix convolution for all input and output window combinations. So, unlike the homogeneous case (which can be thought of as one input window, one output window), the advantage of using a 3-by-3 interface-propagator matrix for extrapolation are outweighed by the additional cost of using interface-propagators for all window pairs. An implemention of equation (3-14) has not been attempted, due to this undesirable cost.

Is this a general conclusion, or an artifact of the choice of where NSPS and GPSPI integrals have been introduced?

3.2.2.2 Approximate interface-propagator

One could consider, as an alternative, direct approximation of equation (3-2) by a GPSPI operator, as follows

$$\mathbf{v}(x, z_{n+1}+, \omega) = \frac{\omega}{2\pi} \int_{-\infty}^{\infty} \mathbf{W}_{n+1}(x, s_x) \mathbf{E}_{n+1}(x, s_x, \omega) \mathbf{v}(s_x, z_n+, \omega) e^{i\omega s_x x} ds_x \,, \tag{3-16}$$

where

$$\mathbf{W}_{n+1}(x, s_x) = \mathbf{W}(x, s_x; z_{n+1}+, z_{n+1}-) = \mathbf{D}_{n+1}^{-L}(x, s_x) \mathbf{D}_n(x, s_x) \,. \tag{3-17}$$

In a windowed form this becomes:

$$\begin{aligned} \mathbf{v}_{PSPI}(x, z_{n+1}+, \omega) = \frac{\omega}{2\pi} \sum_j \Omega_j (x - x_j) \\ \int_{-\infty}^{\infty} \mathbf{W}_{n+1}(x_j, s_x) \mathbf{E}_{n+1}(x_j, s_x, \omega) \mathbf{v}(s_x, z_n+, \omega) e^{i\omega s_x x} ds_x. \end{aligned} \tag{3-18}$$

Equation (3-18) describes a relatively efficient algorithm, which consists of applying both phase shift operators and interface-propagators for each window, in the spatial slowness domain, applying inverse Fourier transforms and then summing the spatially windowed results. Because the matrices involved are 3-by-3, equation (3-18) has the same cost advantage as equation (3-2) when compared to equation (3-5). Another advantage with equation (3-18) is that the terms in **W** are can be selected to discriminate against some modes, such as P-S conversion. However, comparison of numerical results from using equation (3-18) with those using equation (3-5) suggest that it gives a worse approximation when the assumption of smooth model variation is violated. With reference to Figure 3.1, an explanation of this observation is now provided.

3.2.2.3 Accuracy of approximate interface-propagator of equation (3-18)

First of all it is important to reiterate that GPSPI and NSPS are approximations to the exact solution. The nature of the approximation can be understood by considering extrapolation as generation of Huygens wavefronts using locally constant parameters (Margrave and Ferguson, 1998): velocity for the acoustic case, anisotropic stiffnesses for the elastic case. The parameters of the wavefield extrapolator are either those of the output position (GPSPI) or of the input position (NSPS), rather than those which characterize the path between the two. The error in this approximation decreases as the depth step becomes smaller, but in the presence of discontinuous lateral changes it never disappears. In the case of acoustic extrapolation the result is a phase error, but in the elastic case a more serious error can occur if we are not careful, due to polarization. Consider the extrapolation of data from point A to point B in Figure 3.1, across the boundary between medium 1, and medium 2. Assume also that there is a change in the polarization of the shear waves associated with the boundary. If GPSPI extrapolation is performed using equation (3-5), then the decomposition and recomposition matrices used are $\mathbf{D}_n^{-L}(x_2, s_x)$ and $\mathbf{D}_n(x_2, s_x)$, corresponding to the output point B, with lateral position x_2. These are *self-consistent*, in the sense that the polarization of the P, S1 and S2 modes are taken to be the same at A and B. Similarly NSPS extrapolation using equation (3-6) uses decomposition and recomposition matrices defined at the input point with lateral position x_1. While they clearly will give results different from equation (3-5), they are once again self-consistent. Now, consider using equation (3-18). At point A, the interface propagator used is $\mathbf{W}_n(x_1, s_x)$, which implies decomposition based on medium 1 parameters. At point B, the interface propagator used is $\mathbf{W}_{n+1}(x_2, s_x)$, which implies recomposition based on medium 2 parameters. These are *self-inconsistent* operators. For example, suppose the orientation of the axis of symmetry differs between the two media by 90°. The polarization of S1 in medium 1, becomes approximately the polarization of S2 in medium 2. The result of using equation (3-18) is an unwanted flipping of modes, as energy which started at point A with one polarization is interpreted at point B to have a completely different polarization. It is in fact the need for self-consistency which gives rise to the (expensive) interaction between windows in equation (3-15).

The errors resulting from extrapolation across a discontinuity with equation (3-18) are illustrated in the following section in Figure 3.5. However, as shown in Figure 3.6, the errors are small in the presence of *continuous* changes in polarization. Hence, one could choose to use the less accurate, but more efficient equation (3-18) provided the changes in anisotropy axis are gradual.

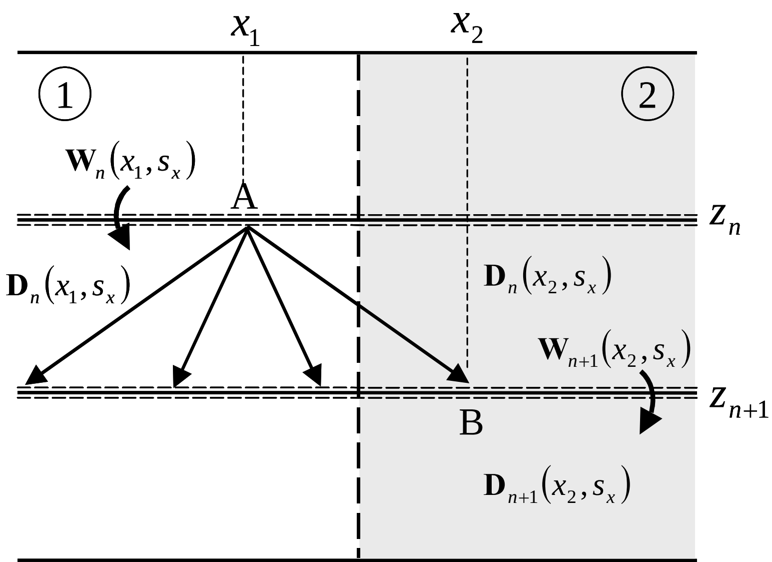

Figure 3.1. Extrapolation across a lateral discontinuity. Medium 1 (white) and medium 2 (shaded) are homogeneous with different anisotropic symmetry axes.

3.3 Results

The use of the above extrapolation operators is now illustrated with numerical results.

3.3.1 GPSPI and NSPS elastic extrapolation tests

Figure 3.2 illustrates the result of extrapolating three impulses by 400m downwards in a single step, for an HTI medium with an abrupt change in symmetry direction in the center. Two homogeneous extrapolations are shown for reference. In (a), the extrapolation is for a homogeneous medium with a symmetry axis in the *x*-direction. In (b), the extrapolation is for a homogeneous medium with symmetry axis at 45° to the *x* direction. In (c) and (d) the medium is the same as in (a) for the left half, and the same as in (b) for the right half. In (c), extrapolation has been performed using the windowed GPSPI algorithm of equation (3-5), with a fixed window size of 80m (8 times trace spacing) and using linearly tapered windows. For GPSPI the windowing is applied to the output, which is clearly visible in the abrupt onset of S1 energy in the center of the section. In (d), the NSPS algorithm of equation (3-6) has been used, with the same window parameters as in (c). Since the windowing is applied on input for NSPS, it is observed that 2 of the 3 impulses contribute to the S1 energy (the second impulse lies on the boundary, which explains the lower S1 amplitude associated with it. Figure 3.3 shows the reverse extrapolation of the GPSPI and NSPS results in Figure 3.2. The ideal result would be three bandlimited spikes only present on the vertical (Z) component. Note that, as was found to be the case for scalar extrapolation, the NSPS operator appears to invert the GPSPI result and vice versa. This suggests that for the (vector) elastic case, as has been proven in the (scalar) acoustic case by Margrave and Ferguson (1998), NSPS and GPSPI are adjoint operators when used in opposite directions. This is verified in Appendix H, where it is shown that for an appropriate definition of the inner product between two *vector* wavefields, the adjoint operator to GPSPI [equation (3-3)] is NSPS [equation (3-4)] in the opposite direction.

3.3.2 Comparison with interface-propagator method

Figure 3.4 shows two models used to test the interface-propagator approximation in equation (3-18), one with a discontinuous 90° change of symmetry axis, and the other with a linear change of symmetry axis over several windows.

For the discontinuous jump [Figure 3.4(a)] the physics of anisotropic wave-propagation dictate that *no energy should be generated on the Y component*, since the *x-z* plane is a plane of symmetry for both left and right halves of the model. In Figure 3.5, the GPSPI extrapolation of three impulses by 200m, using equation (3-5) ((a) and (b)), is compared with the result using equation (3-18) ((c) and (d)). In both cases linearly tapered windows of 40m (4 times trace interval) are used. The wave-mode amplitudes are shown in (a) and (c). The corresponding displacements are shown in (b) and (d). In (b) the Y component amplitude remains zero as it should, whereas in (d) one observes (incorrect) assignment of energy onto the Y component. In this case, it is seen that equation (3-18) gives significantly erroneous results in polarization, which are not present for equation (3-5). Of course, it is still true for equation (3-5) that there are errors of phase due to the GPSPI approximation.

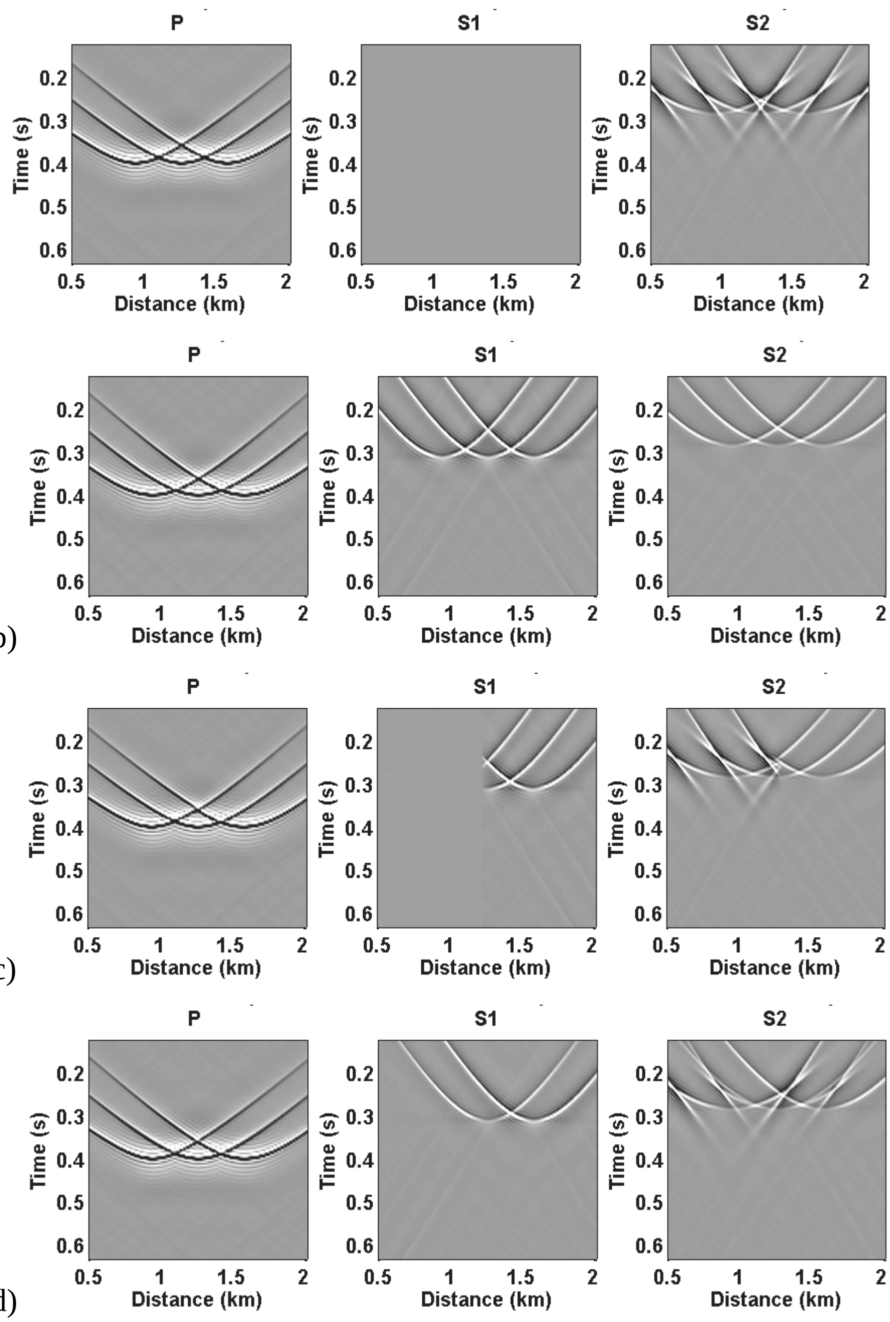

(a)

(b)

(c)

(d)

Figure 3.2. Example of elastic GPSPI and NSPS extrapolation in a single step for a medium with a discontinuous change of anisotropic symmetry direction. (a) Homogeneous model with 0° symmetry axis; (b) homogeneous model with 45° symmetry axis; (c) GPSPI using linearly tapered windows spaced at 80m; (d) NSPS using same windows for discontinuous model.

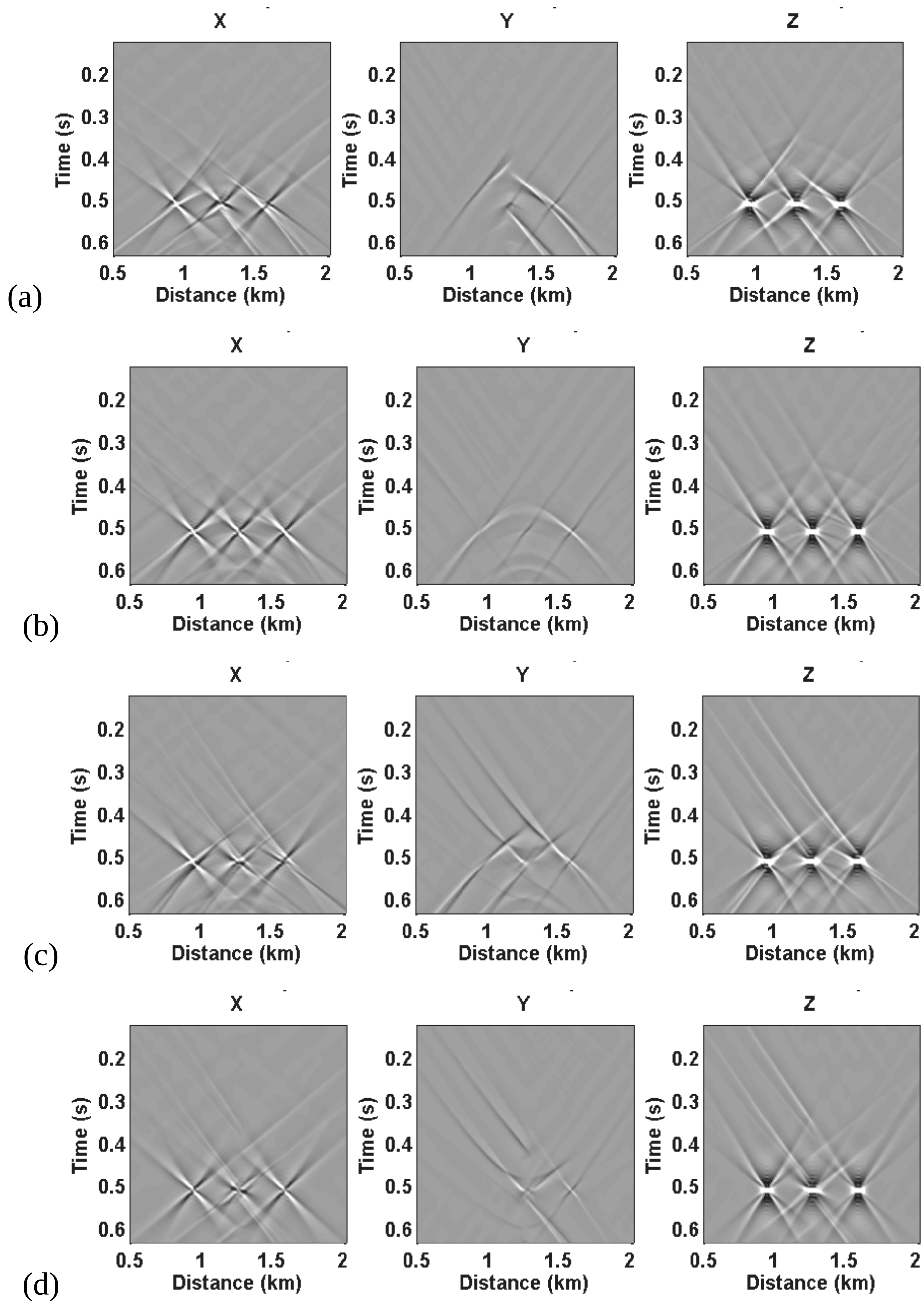

Figure 3.3. Inverse extrapolation (a) GPSPI forward and reverse; (b) GPSPI forward, NSPS reverse; (c) NSPS forward and reverse; (d) NSPS forward, GPSPI reverse.

The last example, in Figure 3.6, considers the above comparison for the continuously varying symmetry axis direction of Figure 3.4(b). In contrast to the abrupt change of symmetry direction in the previous example, it is no longer correct to expect absence of energy on the Y component, as the transition includes symmetry directions in all azimuths between 0° and 90°, which certainly generate rotated polarizations. Furthermore there is now very good agreement between the results using equation (3-5) and those using equation (3-18) (compare (b) and (d)), as anticipated. This supports the assertion that equation (3-18) may still be appropriate for cases where there are expected to be smooth changes in anisotropy.

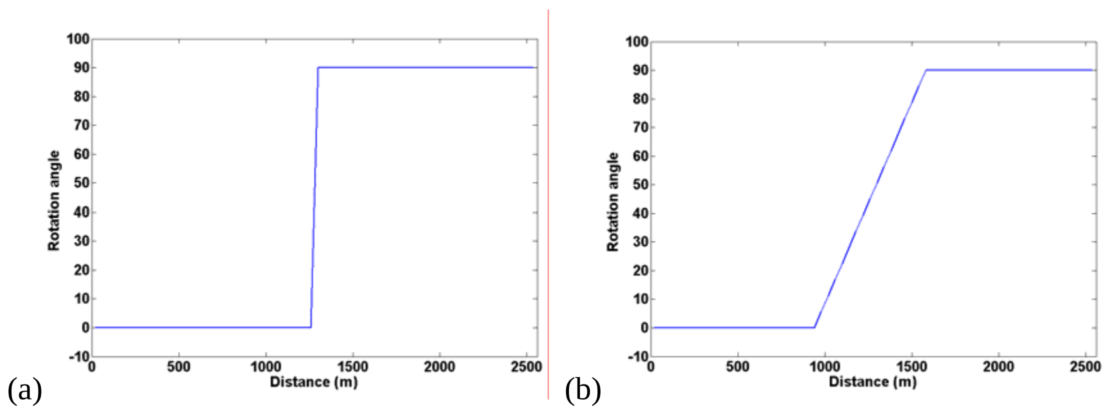

Figure 3.4. Rotation angle variation along 2-D line; (a) discontinuous jump; (b) gradient.

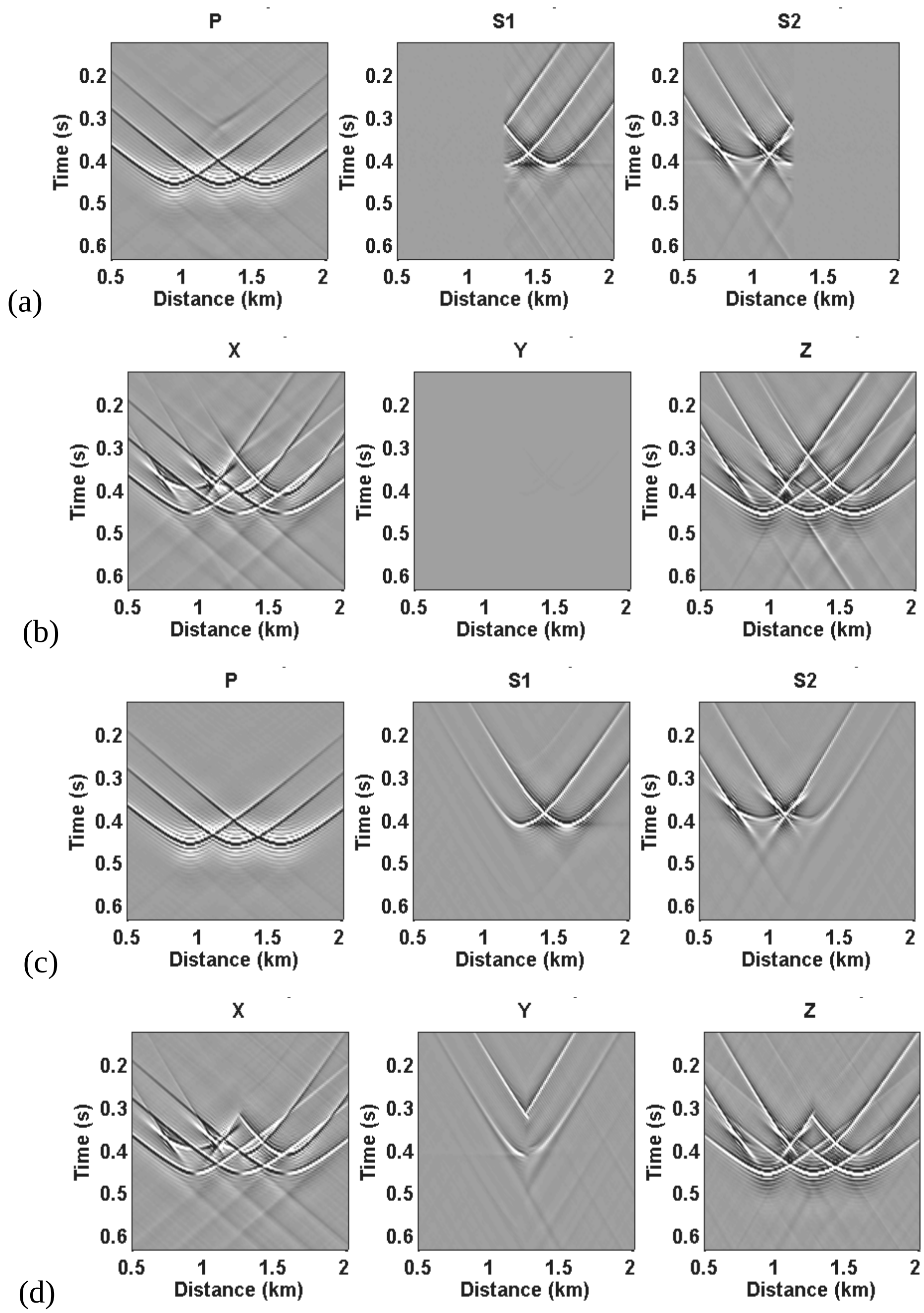

Figure 3.5. GPSPI with 40m window spacing for abrupt change of anisotropic symmetry direction. (a) Extrapolation using full displacement-stress representation at interfaces; (b) displacements corresponding to (a); (c) extrapolation using interface-propagators; (d) displacements corresponding to (c).

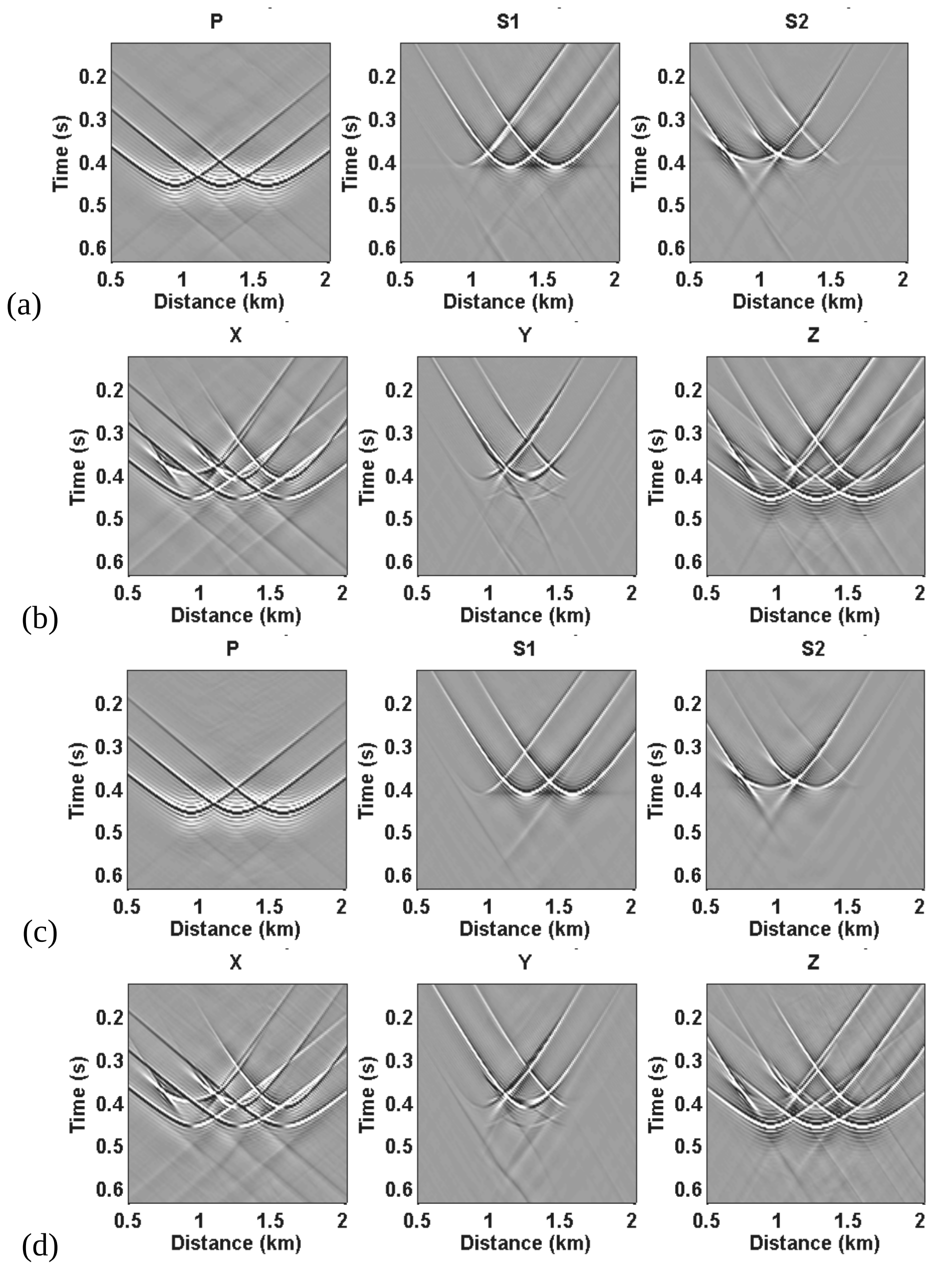

Figure 3.6. GPSPI with 40m window spacing for gradual change of anisotropic symmetry direction. (a) Extrapolation using full displacement-stress representation at interfaces; (b) displacements corresponding to (a); (c) extrapolation using interface-propagators; (d) displacements corresponding to (c).

3.4 Chapter summary

The GPSPI and NSPS methods have been used to extend the elastic wavefield extrapolation algorithm to media with lateral variations, including changes in the HTI symmetry axis. This can be done in more than one way, with a choice not only of GPSPI vs. NSPS, but whether to use full extrapolation of the displacement-stress wavefield, or the more compact extrapolation of wave-modes using interface-propagators. The interface-propagators, if posed in a form which retains the efficiency advantage, have associated errors in the presence of rapid changes of symmetry axis. Generally, one would therefore advocate the use of the full displacement-stress extrapolation. Nevertheless, if the medium can be assumed to have slowly varying changes of symmetry axis, then numerical results suggest the more efficient interface-propagator method is appropriate.

For the remainder of this thesis only the GPSPI formulation is developed further. This is done in the interests of definiteness and avoiding repetitiveness. It is not intended to imply a preference for one algorithm over the other. Moreover, the perceptive reader will understand that there are no fundamental obstacles to developing the theory which follows based upon the NSPS formulation. As illustrated above, the results obtained would be very similar, particularly for the typical depth step sizes used within a prestack migration code – the ultimate goal of this work.

CHAPTER FOUR: ISOTROPIC AND ANISOTROPIC ELASTIC PSPI METHODS

4.1 Introduction

In Chapter 2 an algorithm for extrapolation of elastic wavefields was described. In Chapter 3 this was extended to laterally variable media. The laterally variable algorithm was formulated in terms of generalized PSPI (GPSPI) and NSPS type methods. The theory was developed for extrapolation using the ideal but costly ΨDO, given in equations (3-3) and (3-4). In addition, a more practical implementation based upon spatial windowing was described (see section 3.2.1). However, these algorithms were described in general terms without reference to any particular scheme for designing the windows employed. The examples of GPSPI and NSPS were implemented using fixed spatial windows.

The purpose of this chapter is to explore two specific approaches to implementation. The starting point is the GPSPI framework described in the previous chapter. On one hand, the focus is narrower than that previously presented, since the NSPS framework is not pursued here. On the other hand, it goes deeper, in that some of the key practical issues for handling spatial variation are investigated.

The first implementation is an adaptive extrapolation algorithm appropriate for anisotropic elastic media. This will be referred to as "phase shift plus adaptive windowing" (PSPAW). The second implementation is an alternative elastic PSPI extrapolator that is more closely related to the standard PSPI algorithm of Gazdag and Sguazzero (1984). This can be applied when the medium is *elastic* and *isotropic*.

4.2 Isotropic vs. anisotropic parameterization for PSPI

Consider equation (3-3), which describes the GPSPI algorithm. As written it is expensive, since it is not an inverse Fourier transform, but rather a Fourier integral operator. Therefore, it cannot be performed using an FFT. To implement (3-3) in a code would involve performing the integral for every output point, using a matrix of operators, with a cost proportional to N_x^2, where N_x is the number of spatial points in the discretised domain. A more practical implementation of this equation involves some form of windowing or interpolation, using a smaller set of representative or reference operators. Assuming there are N_{ref} reference operators, the cost becomes proportional to

$$N_{ref} N_x \log_2 (N_x).$$

Then, provided, $N_{ref} \log_2 (N_x) << N_x$, this approach is significantly less expensive than full GPSPI.

The traditional PSPI approach (Gazdag and Sguazzero, 1984) is to compute several wavefields with reference velocities, return each to the spatial domain with inverse FFTs, and interpolate the results. However, in the case of *anisotropic* elastic wavefield extrapolation, the traditional approach has a major drawback, which is now explained.

4.2.1 Drawback to standard PSPI for anisotropic elastic media

The minimum number of parameters required to represent an HTI medium is six, which can be defined (among various equivalent ways) as: V_{P0}, V_{S0}, the P- and S-wave velocities of propagation along the symmetry axis; $\varepsilon, \delta, \gamma$, the Thomsen (1986) parameters; and ϕ, the orientation of the axis of symmetry within the horizontal plane. The generalization of Gazdag and Sguazzero's approach would be to form a set of reference operators based on sampling each of the parameter axes, and generating an operator for each combination of parameters in the sampled parameter space.

A subspace with just 3 of the 6 parameters is illustrated in Figure 4.1, where each node represents a unique reference operator. The space shown has only 125 nodes, assuming (conservatively) that only 5 reference values are required for each parameter. For 6 dimensional parameter space, the total number of reference operators required is $5^6 = 15625$. The full representation with 6 parameters is clearly intractable, unless the dependence on the parameters is somehow decoupled. In general this is not possible.

In section 4.4, the special case of an isotropic medium is examined, where the parameter dependence is approximately separable. In section 4.3, we focus on the spatial windowing approach instead.

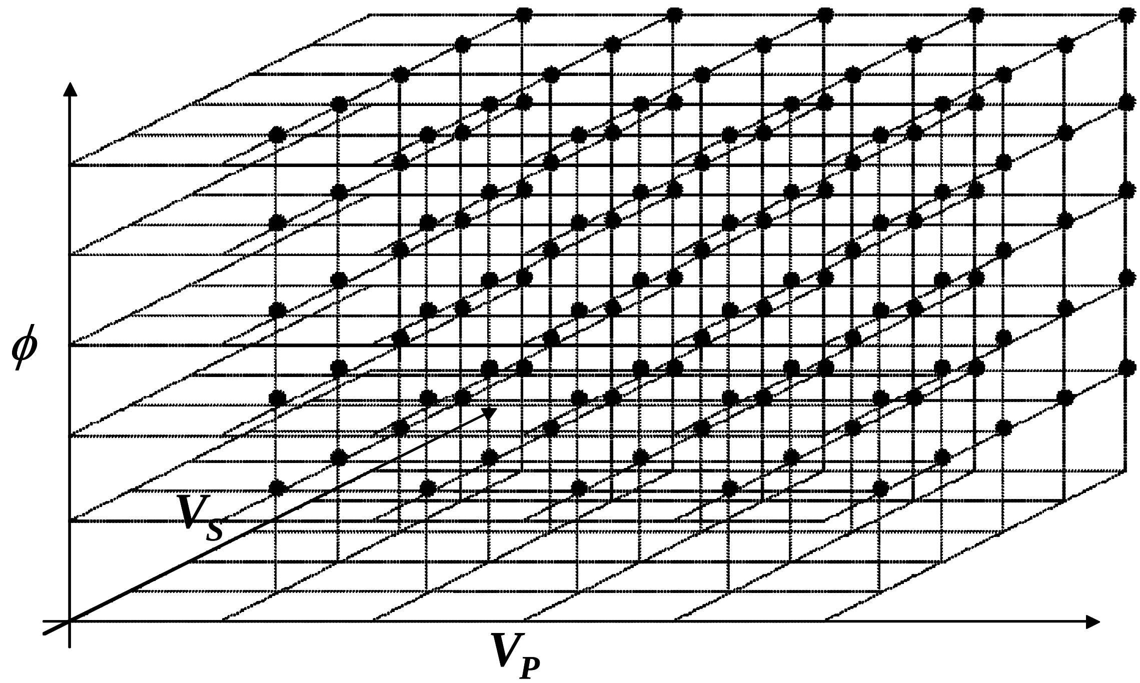

Figure 4.1. Three-dimensional subspace of the parameter space describing an HTI medium. Each node here represents one of 125 unique reference operators.

4.3 Adaptive windowing

Spatial windowing is an alternative approach to parameter interpolation. For scalar extrapolation, windowing has been applied by Margrave and Ferguson (1999), and subsequently refined by Grossman et al. (2002a). The basic idea is to apply operators which are approximately valid over some subset of the image domain, and window the results to include only that part of the domain. It is important that the sum of the windows is unity. Usually the windows are chosen to be smooth and overlapping. The overlap implies that every output point, in practice, is the interpolated result from at least two different windows. There is therefore a very close link to standard PSPI, which is based on interpolating results of extrapolation using two different reference velocities, as described by Gazdag and Sguazerro (1984). Nevertheless, the two approaches are not identical, since the interpolation weights in standard PSPI depend on the velocity of the output point only, whereas the interpolations weights in the window approach depend on the distance from the spatial reference points only.

When considering elastic migration, particularly anisotropic elastic migration, the difference between these two approaches becomes significant for efficiency. As explained in section 4.2.1, the standard approach leads to an intractable number of reference operators (and hence extrapolations) to capture possible variability in the medium. However, if instead the operators are designed for spatial windows (over regions for which an average set of anisotropic parameters is acceptable) the number of extrapolations depends only on the lateral variability of the medium.

Spatial windowing could be implemented using a uniform partition of unity, consisting of fixed size windows which are simple translations of a "mother" window. However, in order to capture the variability of the medium for each extrapolation step, the size of the window required would be constrained by the fastest varying part of the medium. This again would lead to an excessive number of windows, and hence extrapolations. Instead, the number of windows can be kept to a minimum by using an adaptive approach. This is now described.

4.3.1 The PSPAW algorithm

The algorithm will be referred to as “phase shift plus adaptive windowing” (PSPAW). The PSPAW algorithm is related to the adaptive Gabor method (Grossman et al., 2002a), although the Gabor transform is not actually used here. In PSPAW, spatial windows are constructed by combining elementary small windows, called “atoms”, into larger windows, referred to as “molecules”. The molecules are built up along the horizontal spatial direction until some acceptance criterion is violated. At this point a new molecule is started. In this way, large windows are used when the velocity variation is mild, but smaller windows are used in areas of rapid variation. For the scalar extrapolation of Grossman et al., the acceptance criterion is based purely on velocity changes. For the elastic HTI case under consideration here, this is not possible, because there are 3 modes, each with a velocity which depends upon phase angle.

For vector extrapolation, the following procedure is proposed:

1. Phase slowness is computed for P, S1 and S2 modes, for a fixed set of phase angles using the anisotropic parameters at the spatial center of each atom.
2. Within each molecule, a record is kept of the average, minimum and maximum phase slownesses, for each phase angle. The average is computed using Schoenberg and Muir’s (1989) calculus for addition of anisotropic layers. In

addition, the average, minimum and maximum symmetry-axis azimuths are recorded.

3. A new atom is accepted to the current molecule on condition that including it does not cause the range between minimum and maximum slowness to exceed some limit, for any mode. This limit is determined by requiring that the maximum phase error does not exceed one-half a cycle, at the maximum frequency.
4. A new atom is accepted only if the symmetry axis variation within the molecule will remain less than some specified limit (10° is typical).
5. If either of the criteria in 3 or 4 is violated, a new molecule is created starting with the current atom.

4.3.2 Phase velocity

Step 1, above, is illustrated in figure 4.2, except that phase velocity is displayed instead of slowness. For the isotropic part of the model, to the right, the P velocity is constant with phase angle, and both S velocities are equal and constant. For the HTI part, to the left, there are variations in all three velocities with phase angle, and the separation of S1 and S2 velocities is evident.

Step 4 is important for two reasons. First, it does not make sense to compare two S1 or two S2 phase slowness curves from nearby positions, unless the two symmetry axes are also closely aligned. Second, the decomposition and recomposition matrices $\mathbf{D}_n^{-1}$ and $\mathbf{D}_n$ in equation (3-3) are also subject to spatial variation, which depends on both the velocities and also the orientation of the symmetry axis.

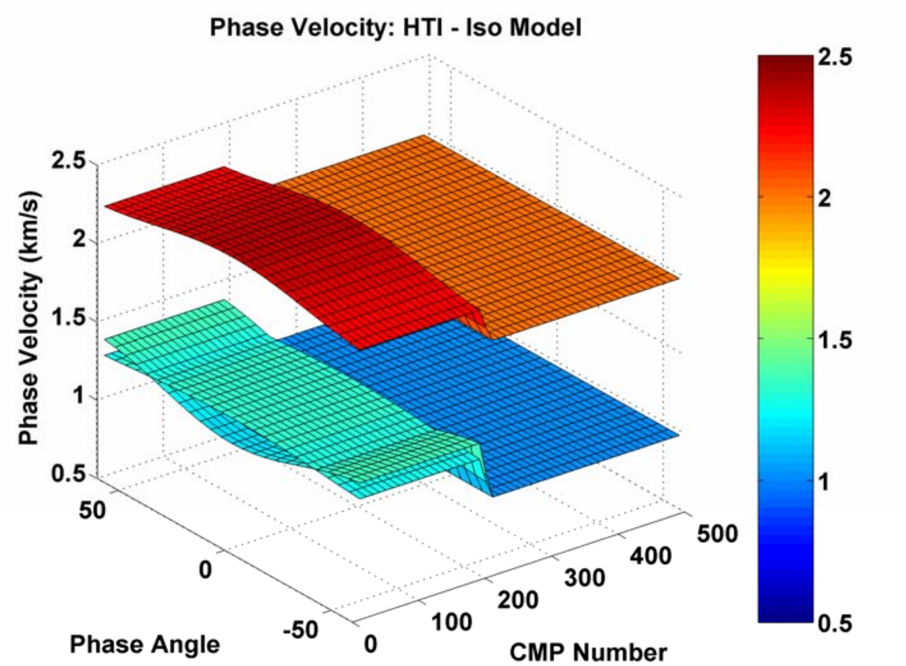

Figure 4.2. Phase velocity curves as a function of horizontal position and phase angle for a medium with a step-type transition from an HTI medium (left) to an isotropic medium (right). Upper sheet is the P-wave slowness, lower sheets are S1 and S2 slownesses.

4.3.3 Atoms and molecules: operator "chemistry"

The issue of basic atom design for scalar extrapolation has been discussed at some length in Grossman et al. (2002b), and the extension to 2-D windows for 3-D extrapolation[1] is analyzed in Bale et al. (2002). A brief overview is sufficient for our purpose here.

The fundamental concept is that a set of atoms should cover the domain of interest in such a way as to form a partition of unity (POU), as given by equation (3-8). The simplest example of a POU is a set of boxcars which cover the domain but do not overlap. However, it is well-known from signal processing that multiplication by a boxcar in the spatial domain is equivalent to convolution by a "sinc" ($\sin x/x$) function in the wavenumber domain, and that this leads to unwanted ringing, known as Gibbs' phenomenon. Another simple example of a POU is the set of triangular (linear)

[1] The two dimensions required of the windows are the two directions transverse to the direction of extrapolation, usually the x and y directions for 3-D extrapolation.

windows, which overlap by half their width [see Figure 4.6(a) in next section]. However, a triangular window can be constructed from convolving two boxcar windows, implying that in the wavenumber domain it has the shape of a squared sinc function. Hence, multiplying an operator by such a window would also cause Gibbs' phenomenon, though less extreme than the boxcar.

Mathematically, the difficulty with both of these choices is that while they have compact support[1] in the spatial domain, they do not have compact support in the wavenumber domain. Compactness in the wavenumber domain is related to differentiability, or "smoothness", in the spatial domain. Therefore a desirable quality of a windowing function is a high order of differentiability.

A related issue is that they have poor localization properties. There are absolute limits on simultaneous localization of a function in both space and wavenumber, imposed by the uncertainty principle. This is well-known from quantum mechanics as Heisenberg's uncertainty principle (e.g. Landshoff and Metherell, 1979), where it is associated with the inherent uncertainty in measuring position and momentum simultaneously. In fact, this arises due to the simple linear connection between the wavenumber and momentum vectors in quantum mechanics. The more fundamental uncertainty, that between spatial and wavenumber domains, is implicit in the properties of the Fourier transform. For example, a Dirac delta function is precisely local in space but completely non-local in wavenumber, since

$$\int_{-\infty}^{\infty} e^{ikx}\delta(x-x_0) = e^{ikx_0} .$$

Ideally, then, a window of choice for the POU would have optimum localization in both space and wavenumber; would have high order of differentiability; and would be have compact support spatially, or nearly so.

4.3.3.1 The Gaussian atom

A Gaussian function that can be used as an atom has the form,

---

[1] The term "compact support" is here used in its mathematical sense, as describing functions which are non-zero on a closed finite subset of the domain.

$$g(x) = \frac{\Delta x}{\sigma\sqrt{\pi}} e^{-x^2/\sigma^2} \quad ,$$

where σ is the "halfwidth" of the Gaussian (standard deviation) and Δx is the separation between atoms. The Gaussian function displays a host of desirable properties, making it particularly well suited for use as an "atom" in a POU:

1. The Gaussian is infinitely differentiable, as may be readily verified.
2. The Gaussian has optimal localization properties in the spatial and Fourier domains: it is the only function that exactly minimizes the uncertainty relationship, the fundamental limit on the product of resolutions in both domains. In fact, the Fourier transform of a Gaussian function is another Gaussian, given by

$$\hat{g}(k_x) = \Delta x e^{-\pi^2\sigma^2 k_x^2} \ .$$

3. The Gaussian is *not* compactly supported, since it is non-zero everywhere. However, as shown in Bale et al. (2002), it decays sufficiently rapidly to allow truncation within approximately 6σ, so that the error is within machine precision.
4. The Gaussian does not yield an exact POU. However, it is a very good approximation to one for good choices of Δx and σ (Margrave and Lamoureux, 2001). Figure 4.3 illustrates the approximate construction of a constant unity function by summation of basic Gaussian functions.

The result has a desirable "isotropic" response, in that the window function is invariant under rotation in the horizontal plane.

With respect to this last point, the 2-D Gaussian is given by the product of Gaussians along the 2 axes

$$\begin{aligned} h(x,y) &= \frac{\Delta x}{\sigma_x\sqrt{\pi}} e^{-x^2/\sigma_x^2} \ \frac{\Delta y}{\sigma_y\sqrt{\pi}} e^{-y^2/\sigma_y^2} \\ &= \frac{\Delta x \Delta y}{\sigma_x \sigma_y \pi} e^{-\left(x^2/\sigma_x^2 + y^2/\sigma_y^2\right)} \end{aligned} \ .$$

See Bale et al. (2002) for a discussion of POUs constructed in two or more dimensions, including a proof that the 2-D Gaussian is the only function which achieves the isotropic response described here.[1] Figure 4.4 illustrates the approximate construction of a 2-D unity function by summation of 2-D Gaussian functions. Alternatives to the Gaussian have been explored in Grossman et al. (2002b).[2]

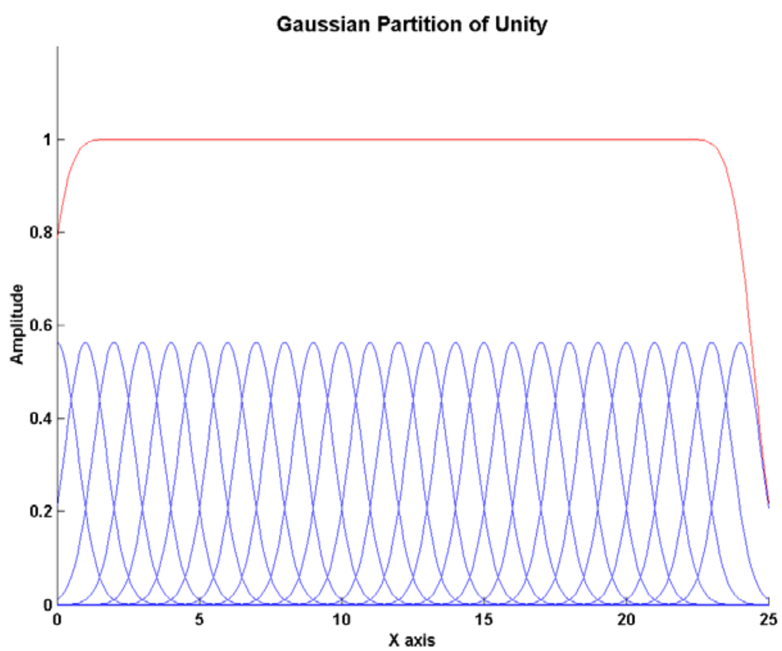

Figure 4.3. One-dimensional partition of unity using a Gaussian atom. The numbering along the *x*-axis refers to the Gaussian atom number. Roll-off effects occur because a finite number of Gaussians are used.

---

[1] Although this property is not immediately relevant to the application within this thesis, where the scope has been limited to 2-D extrapolation, it is potentially important should the methods described here be extended to 3-D extrapolation.

[2] It is possible, for example, to form a spline-based window (referred to in the above reference as a "Lamoureux window") which is compact in the strict sense. Strict compactness allows efficient implementation without truncation effects or the need to taper the window. However, in achieving compactness, other properties are sacrificed. Unlike the Gaussian, it is not infinitely differentiable, although since an arbitrary degree of differentiability can be obtained, this particular drawback is somewhat academic. Other limitations of spline-based windows are: they cannot achieve the Heisenberg limit of localization in both domains, and; they are not isotropic when extended to higher dimensions, since it can be shown that only the Gaussian satisfies this demand. The question of which type of window is "best" depends on particulars of the extrapolation problem, and is in any case an open question. In this thesis, the Gaussian window is used as the basic atom.

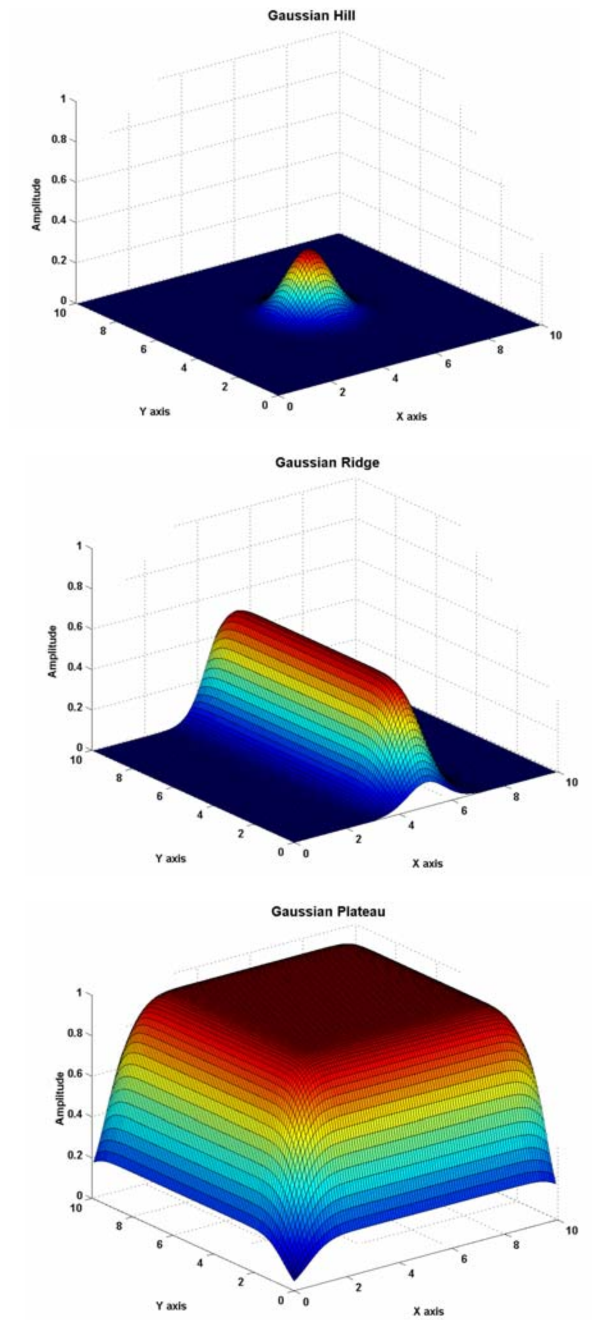

(a)

(b)

(c)

Figure 4.4. Almost exact partition of unity using 2D Gaussian ("Gaussian hill") atoms (a). Summation of 2D Gaussians along a constant *x* coordinate of grid gives the "Gaussian ridge" (b). Summing Gaussian Ridges for all *x* coordinates gives the Gaussian plateau (c). Edge effects can be removed by extending summation beyond domain of interest.

4.3.4 Examples of PSPAW

4.3.4.1 Triangular vs. Gaussian windows

A simple example is now presented to compare the extrapolation responses using two different types of fundamental atom design, a triangular window and a Gaussian window. Figure 4.5 shows the P and S-wave velocity profiles used. The constant velocity zones to the left and right of the model are extrapolated with a single molecule each. The central area, with a velocity gradient, requires several molecules to handle lateral velocity variation. In total 9 molecules are needed. The two different window designs are illustrated in Figure 4.6. In both cases the atoms are spaced 80m apart, and the width is 160m. In the linear case width means the full width, but in the Gaussian case the "width" is that part of the Gaussian lying within a single standard deviation. The Gaussian window is truncated after 4 standard deviations, without noticeable effect.

An impulse located at 1.28km and 0.511s is placed on the Z component of the input record, which is then extrapolated downwards by 200m. First, for reference, the "exact" response is determined by applying the generalized PSPI of equation (3-3). This is achieved by limiting the window size to a single CDP in the region of the velocity gradient. The result, shown Figure 4.7, is regarded as the best solution possible using PSPI type methods, and is used to compare the subsequent windowed results.

In Figure 4.8 the extrapolated shear-wave response is shown for both the linear atoms, in (a), and the Gaussian atoms, in (c). The extrapolations appear broadly comparable in the *x-t* domain, both to each other and to the "exact" result of Figure 4.7(a). However, a comparison of their frequency-wavenumber (FK) transforms, in (b) and (d), with the ideal result of Figure 4.7(b) indicates that the linear atoms introduce Gibbs phenomenon, expressed as a "ringiness" in the spectrum, as predicted from theory. On the other hand, the greater smoothing inherent in the Gaussian atoms, does result in some loss of high frequency response.

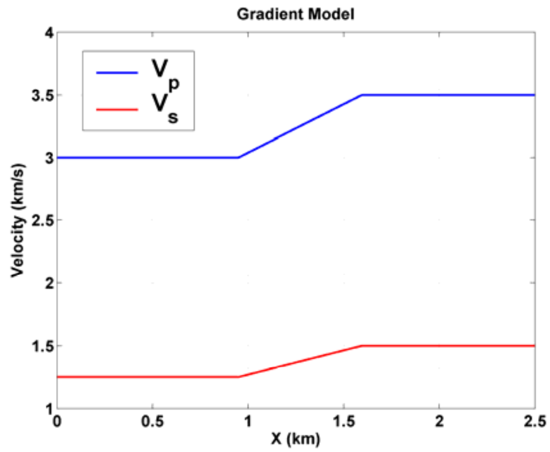

Figure 4.5. Model used to compare linear and Gaussian window extrapolator responses in Figure 4.8.

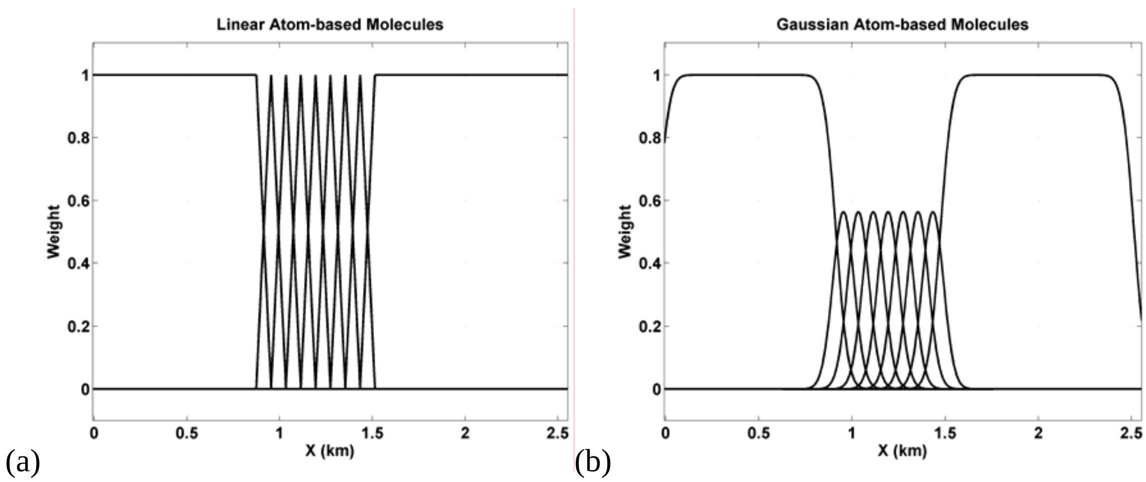

Figure 4.6. Partitions of unity for model in Figure 4.5: (a) using linear atoms to build molecules; (b) using Gaussian atoms. In both cases the fundamental atoms are separated by 80m (or 16 CDPs). The linear atom width is 160m (32 CDPs). The Gaussian atom has a standard deviation of 80m, corresponding to a "width" of 160m between -1 and +1 standard deviations.

4.3.4.2 HTI medium with variation in symmetry axis

An HTI model with the stiffness coefficients given in Table 2.1 was used to test the PSPAW algorithm, using an impulse on the vertical component as before. Though the stiffnesses were not varied spatially, the direction of the symmetry axis was varied between 0° and 90° over a central part of the model 320m in width, as shown in Figure

4.9 (a). The resulting partition of unity for this model gives 6 windows ("molecules"), as shown in Figure 4.9 (b). In addition to the variation in the partition of energy between S1 and S2 due to the rotation in the extrapolation, there is also a variation in the phase velocity surfaces as the S1 and S2 directions change relative to the inline direction. This is illustrated in Figure 4.10. Figure 4.10 also shows the subset of phase angles used for the evaluation in step 1 of the PSPAW algorithm, of section 4.3.1, indicated by the seven black curves on each of the surfaces. These angles are found to adequately capture the variability which results from the change in symmetry axis. Of course, if only the phase velocities for vertical incidence were used (as in the isotropic case), the algorithm would have not detected any change, since these velocities are spatially constant. It is both this spatial variation of the phase velocity for non-zero phase angles, and the variation in the symmetry axis direction, which trigger the generation of new molecules in the PSPAW algorithm. In this case, deviation in the symmetry axis orientation was accepted with a tolerance of 30°.

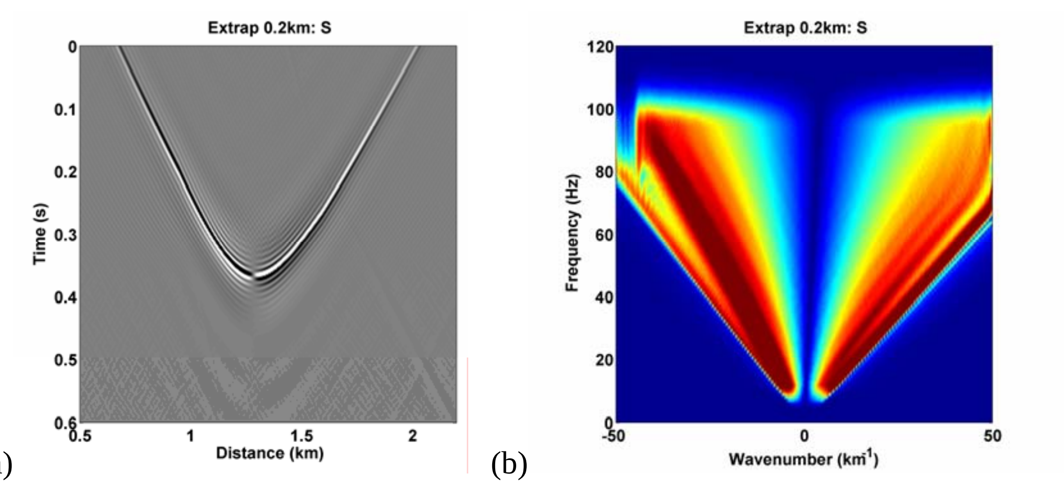

(a) (b)

Figure 4.7. Extrapolator impulse response for model shown in Figure 4.5, using "exact" operator. The exact operator is the limiting form of the PSPI operator, known as generalized PSPI, and given by equation (3-3). The impulse response is shown in the distance-time (*x*-*t*) domain in (a), and the magnitude of the frequency-wavenumber spectrum (the "FK amplitude spectrum") is shown in (b).

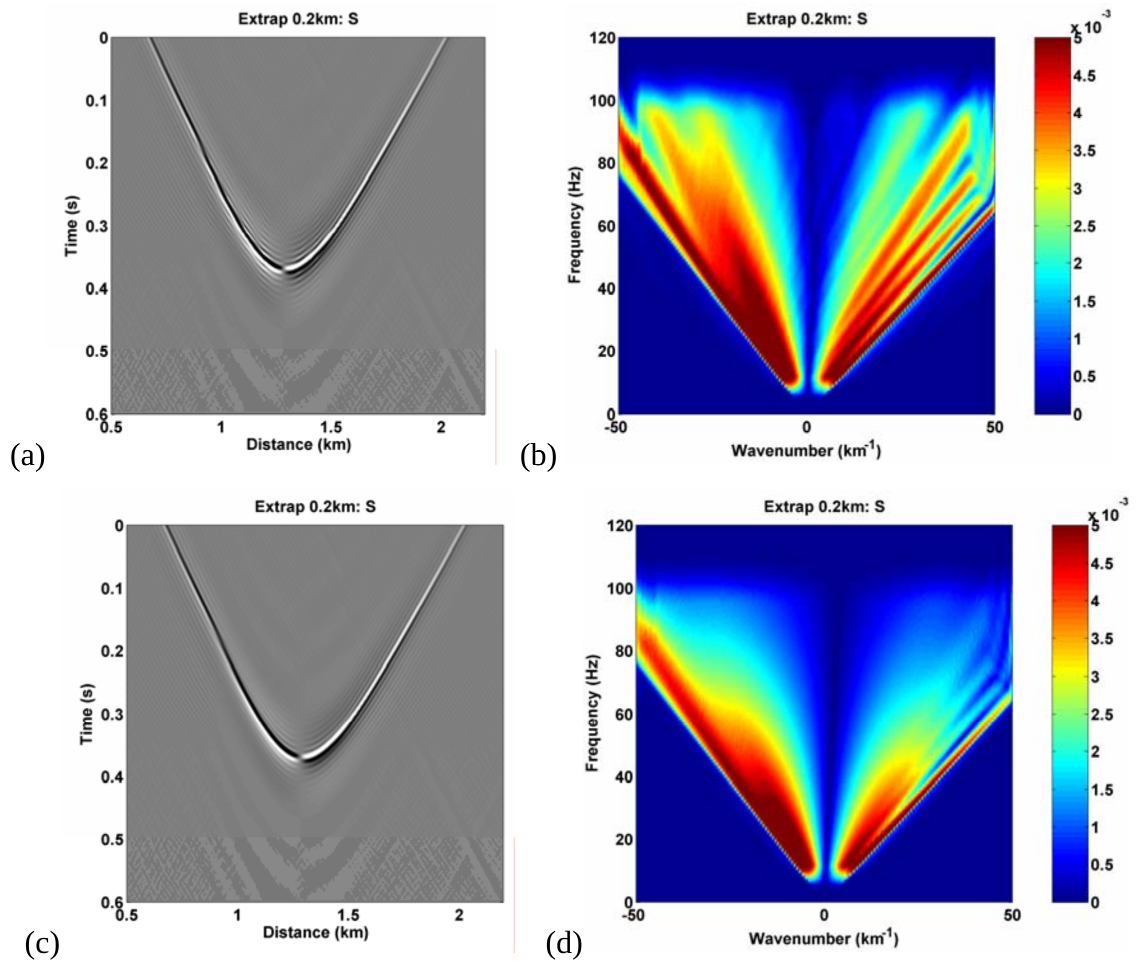

Figure 4.8. Extrapolator impulse response for model shown in Figure 4.5, using: (a) linear atoms [Figure 4.6 (a)], and; (c) Gaussian atoms [Figure 4.6 (b)]. The FK amplitude spectrum of the impulse response for the linear atoms (b) shows the characteristic Gibbs phenomenon, absent from the response using Gaussian atoms (d). Both should be compared with the exact operator of Figure 4.7.

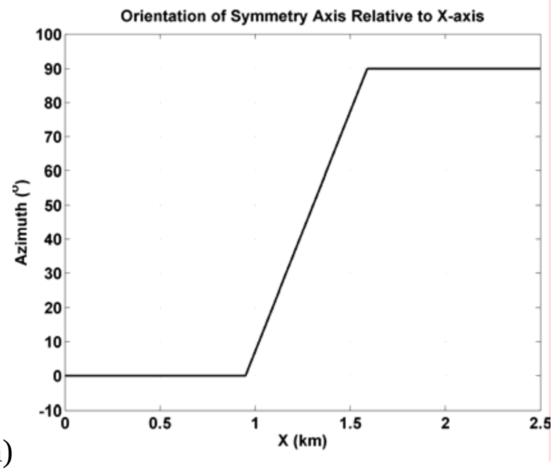

(a)

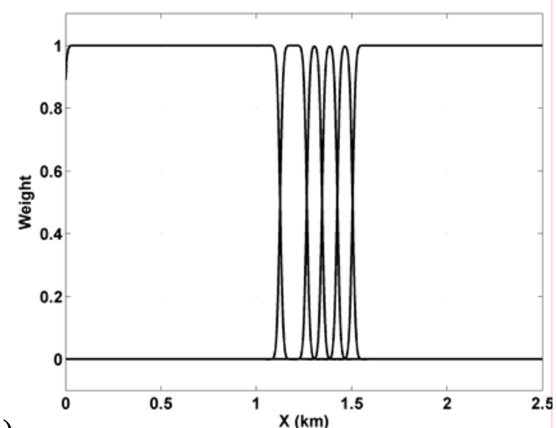

(b)

Figure 4.9. (a) Spatial variation of symmetry axis for example in Figure 4.11. (b) Resulting partition of unity using Gaussian atoms to construct molecules. Each atom is a Gaussian with standard deviation equal to 20m or 4 times the CMP interval. Based on the acceptance criteria, the molecules shown in (b) have 51 and 49 atoms for the constant regions on the left and right, respectively. For the linear ramp in the center, the molecule selection process is influenced both by the variation in phase velocity and the variation in symmetry direction, resulting in variable sizes. In this case, deviation in the symmetry axis orientation was accepted with a tolerance of 30°.

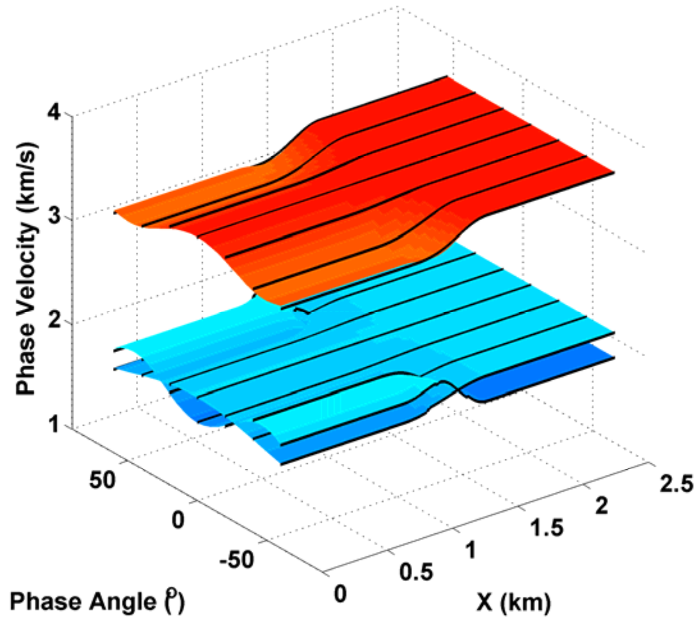

Figure 4.10 Variation of phase velocity with phase angle and spatial position. Although the elastic properties do not change, the gradual rotation of the symmetry axis through 90° [Figure 4.9(a)] causes the propagation direction to vary from the symmetry axis plane (left) to the isotropy plane (right). The black lines indicate the phase angles used to check the acceptance criteria in the PSPAW algorithm (section 4.3.1).

The results of the elastic extrapolation are shown in Figure 4.11. For reference the extrapolation is first performed using the ideal GPSPI operator defined by using equation (3-3) in its ideal form, with a basic window ("atom") size equal to the CMP interval. This is assumed to give the optimal result, since no windowing or interpolation is used, and is shown in Figure 4.11(a). Figure 4.11(b) shows the result of using PSPAW, with the 6 windows of in Figure 4.9(b), to extrapolate. Comparing the two results, it is clear that the PSPAW method gives the primary branch of the operator accurately, though it smooths some of the details associated with the edges of the gradient zone. This makes sense, since the real medium has a discontinuity in the first derivative (of the symmetry axis direction) which is smoothed by the Gaussian windows. An important advantage of PSPAW compared to full GPSPI is cost. There is approximately a factor of 10 runtime difference between Figure 4.11 (a) and (b).

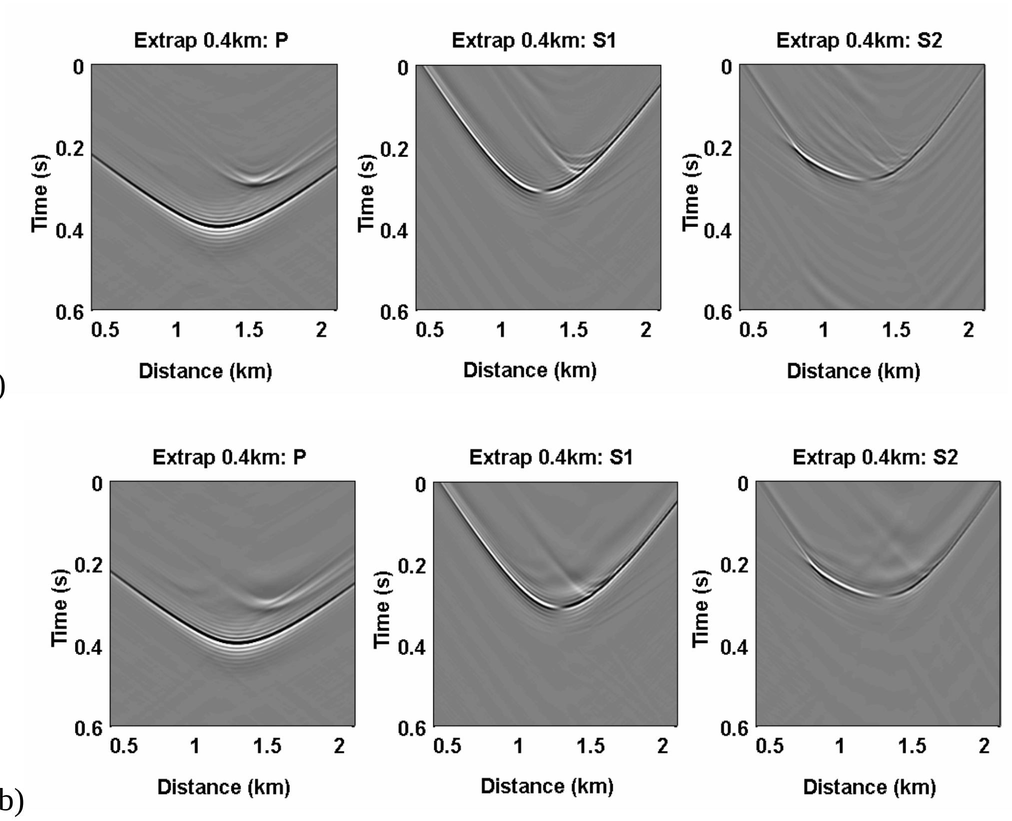

(a)

(b)

Figure 4.11. Extrapolation of impulse downwards by 400m through the HTI model with symmetry axis variation of Figure 4.9 (a). (a) using an 'exact' GPSPI algorithm by forcing window sizes to be the same as the CMP spacing, and; (b) using PSPAW algorithm with partition of unity shown in Figure 4.9 (b). The run-time to generate (a) was approximately 10 times that required for (b).

4.4 Alternative algorithm for isotropic media: PSPI

The algorithm described in section 4.3 is applicable to isotropic media as well as to HTI media. However, an alternative approach is also possible.

In the case of an isotropic medium, the number of parameters is reduced from 5 to 2; namely the P- and S-wave velocities. The phase-shift operators for each mode depend on only a single parameter, just as for the acoustic extrapolation problem. In general, the composition and decomposition operators $\mathbf{D}$ and $\mathbf{D}^{-1}$ have a coupled dependence on both velocities, but this coupling is weak, as discussed below. This observation suggests that the PSPI interpolation approach introduced by Gazdag and Sguazerro (1984) might be appropriate for isotropic extrapolation. In particular, the drawback to this method referred to in section 4.2.1 is significantly less important in the isotropic case.

In the isotropic case, the vertical slownesses (which determine the phase shifts) for P-wave and S-wave modes are

$$q_P = \sqrt{1/\alpha^2 - p_x^2} \tag{4-1}$$

and

$$q_{S1} = q_{S2} = \sqrt{1/\beta^2 - p_x^2} \,. \tag{4-2}$$

where α and β are the P-wave and S-wave velocities for the layer in question.[1]

The P-wave and S-wave eigenvectors for an isotropic composition matrix **D** are calculated in Appendix C. Equations (C-2) and (C-3) show that even though the displacement eigenvector for the P-wave is independent of the S-wave velocity, the traction vector is not. Therefore, the complete eigenvector $\hat{\mathbf{b}}_P^D$, a column vector of **D**, is dependent on the S-wave velocity. So is the corresponding row-vector $\hat{\mathbf{g}}_P^D$ in the decomposition matrix $\mathbf{D}^{-1}$. This implies that we cannot exactly decouple the handling of P- and S-waves within the decomposition and recomposition steps. However, in the case that $\alpha = \gamma_0 \beta$, with γ_0, the V_P / V_S ratio, being constant for a given layer, the dependence on β in equation (C-3) can be replaced with a further dependence on α.

Surprisingly, perhaps, the S-wave eigenvectors given in equations (C-4) and (C-5) are *not* dependent on the P-wave velocity.

4.4.1.1 Laterally invariant V_P / V_S

If it is assumed that the V_P / V_S ratio is constant within each layer, then each eigenvector is controlled by a single parameter – the velocity of the corresponding wave-mode. In this case, a "conventional" PSPI approach can be employed, as follows:

1. Choose N reference P-wave velocities $\{\alpha_1, \alpha_2, \alpha_3, \ldots, \alpha_N\}$ and define N reference S-wave velocities based on the constant V_P / V_S ratio, γ_0, by $\beta_J = \alpha_J / \gamma_0$ for $J = 1, \ldots, N$.

[1] The use of α and β instead of v_P and v_S (as used in earlier chapters) is convenient, as it makes for less cumbersome notation when indexing different reference values.

2. For each reference P-wave velocity, decompose the wavefield using the decomposition matrix designed with that velocity.
3. Extrapolate P-wave and S-wave wavefields using the appropriate vertical slowness for that mode.
4. Interpolate the results for both P and S wavefields at each output location based upon local velocity, and the two bracketing reference velocities for each mode.

4.4.1.2 Laterally variable V_P / V_S

Even if the V_P / V_S ratio varies within the layer, the above algorithm, with some modifications, will still be accurate for all steps except for computing the P-wave polarization in the composition and decomposition matrices. The modified algorithm begins by computing the V_P / V_S ratio based upon the ratio of mean P- and S-wave velocities, $\overline{\alpha}$ and $\overline{\beta}$, over the aperture required for extrapolation (in a shot migration scheme this can be restricted to the variation within the aperture for each shot). That is

$$\gamma_{ave} = \overline{\alpha} / \overline{\beta} \tag{4-3}$$

Next, the ranges of P- and S-wave velocity are adjusted, as follows:

$$\begin{aligned}
\alpha_{\min} &\leftarrow \min(\alpha_{\min}, \gamma_{ave}\beta_{\min}) \\
\beta_{\min} &\leftarrow \min(\alpha_{\min}/\gamma_{ave}, \beta_{\min}) \\
\alpha_{\max} &\leftarrow \max(\alpha_{\max}, \gamma_{ave}\beta_{\max}) \\
\beta_{\max} &\leftarrow \max(\alpha_{\max}/\gamma_{ave}, \beta_{\max}).
\end{aligned} \tag{4-4}$$

This is done to ensure that the reference velocities chosen are matched via a constant V_P / V_S ratio given by γ_{ave}.

The P- and S-wave reference velocities are then selected based upon the harmonic sampling criteria of Gazdag and Sguazzero (1984). Since the actual V_P / V_S ratio varies laterally, the interpolation of P- and S-wave wavefields does not always use the corresponding reference values. For example, the P-wave might be interpolated using reference (P-wave) velocities *J* and *J+1*, whereas the S-wave might be interpolated using reference (S-wave) velocities *K* and *K+1*. This is possible since the phase shift's dependence on velocity is decoupled.

For the modal decomposition and recomposition, with variable V_P / V_S, the situation is more complicated. The composition matrix depends on both P and S velocities. We do not want to compute N^2 versions of $\mathbf{D}_n$ and $\mathbf{D}_n^{-1}$ corresponding to every possible combination of P and S velocity. That would be prohibitively expensive. Instead, the corresponding reference velocities are used, so that the V_P / V_S ratio is always γ_{ave}. In addition, distinct displacement-traction vectors $\mathbf{b}_P$ and $\mathbf{b}_{SH}$, $\mathbf{b}_{SV}$, are maintained, instead of the total displacement-traction **b**. The composition equation (2-15) is then written

$$\begin{aligned}\mathbf{b} &= \mathbf{D}\mathbf{v} \\ &= \begin{pmatrix} \hat{\mathbf{b}}_P & \hat{\mathbf{b}}_{SH} & \hat{\mathbf{b}}_{SV} \end{pmatrix} \begin{pmatrix} v_P \\ v_{SH} \\ v_{SV} \end{pmatrix} \\ &= \begin{pmatrix} \mathbf{b}_P & \mathbf{b}_{SH} & \mathbf{b}_{SV} \end{pmatrix},\end{aligned} \tag{4-5}$$

where only the down-going (or up-going) waves are considered (omitting the U or D superscript for brevity), and where $\hat{\mathbf{b}}_M$ are the eigenvectors associated with modes M, so that $\mathbf{b}_M = v_M \hat{\mathbf{b}}_M$ for $M \in \{P, SH, SV\}$. The qualifiers SH and SV are used rather than S1 and S2, since isotropy is assumed here. This extra book-keeping enables the appropriate local velocity to be employed for each mode, as described in Appendix I.

In the case of the P-wave, this will result in a slight error, since the decomposition matrix includes a dependence on the (true) V_P / V_S ratio, which has been replaced by the average value γ_{ave}. Numerical tests in section 4.4.2 indicate that this error is relatively small for reasonable variation of V_P / V_S.

4.4.2 Examples

In this section, the PSPI algorithm described in the preceding section is applied to a Ricker wavelet impulse, located at an offset of 1.28km and two-way time 0.511s. In all of the examples in this section, the extrapolation is done in 50 steps of 4m, to match the likely use of the extrapolation within a prestack migration scheme. This is done for various types of medium, to test the validity of the approximations being employed, in particular when the V_P / V_S ratio is variable. For the sake of comparison, the limiting case of GPSPI is used as a benchmark. This is generated by using equation (3-3) in its ideal form, with a basic window ("atom") size equal to the CMP interval. This is assumed to give the optimal result possible for each model (albeit slowly), since no interpolation or windowing is employed.

4.4.2.1 Single layer, constant V_P / V_S

The first model, a single layer with piecewise constant ("blocky") velocity variation in the lateral direction, is illustrated in Figure 4.12. The layer has a constant V_P / V_S ratio equal to 2. Also shown are the values of the reference velocities, as determined by the harmonic sampling criteria of Gazdag and Sguazzero (1984), for the case of only 3 reference velocities. (Note that the highest S-wave velocity and the lowest P-wave velocity are both equal to 2km/s, and are coincident on the plot as a result).

The results of extrapolating downwards 200m through the model are shown in Figure 4.13, using different numbers of reference velocities. Comparison of the result using 3 velocities (b), with the exact result in (a), suggests more than 3 reference values are needed for this model. The result obtained with 7 velocities (c), is not noticeably inferior to that obtained with 20 velocities (d), and both compare well with the exact result.

In the example of this section, there is no vertical velocity variation in the medium, so that the PSPI algorithm in effect only operates on the phase shift, and the polarizations in the composition and decomposition matrices have no impact. Next, a model with two layers is examined to verify accuracy of the interpolation on the decomposition and recomposition steps.

4.4.2.2 Two layers, constant V_P / V_S

The second model contains two layers, the top with piecewise constant velocity variation in the lateral direction, and the second with constant velocities is illustrated in Figure 4.14. Both layers have a common constant V_P / V_S ratio equal to 2. Since this is the case, the model satisfies the assumptions of section 4.4.1.1, and it is expected that accurate results can be obtained with the PSPI algorithm described there.

The results are given in Figure 4.15, using: (a) the exact operator, and; (b) PSPI with 7 reference velocities. A careful comparison suggests only minor differences between the two algorithms.

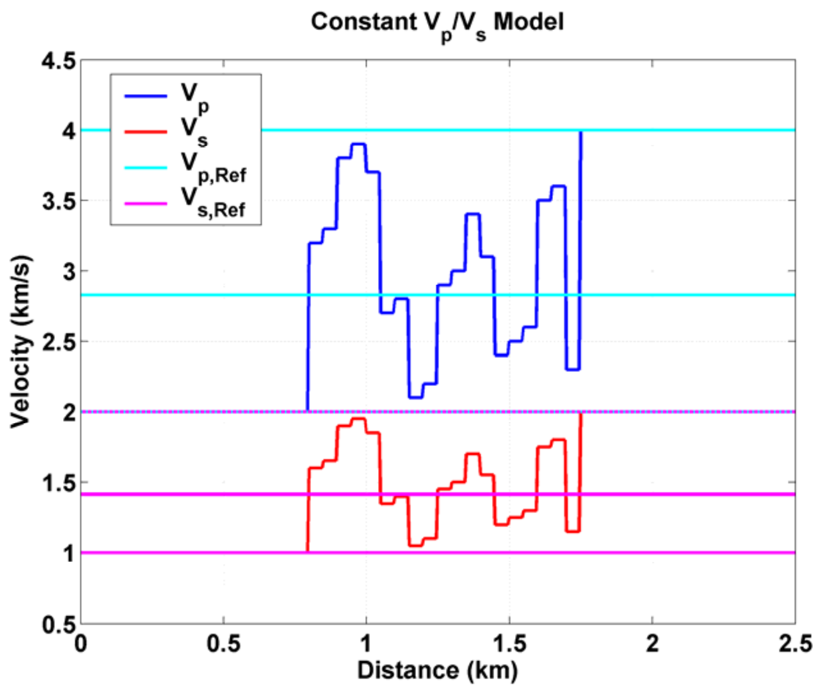

Figure 4.12. First model for evaluation of PSPI extrapolators. The V_P / V_S ratio here is constant, and equal to 2. The cyan and magenta horizontal lines show the reference velocities for P- and S-wave extrapolations respectively, in the case of 3 reference velocities.

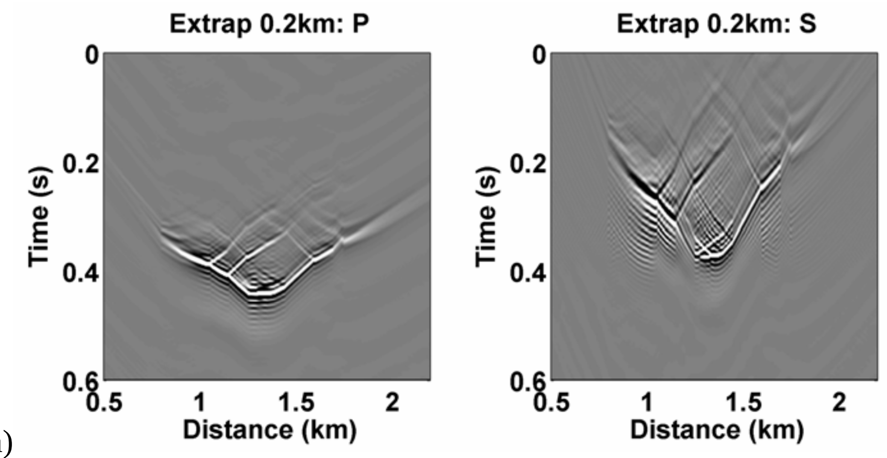

(a)

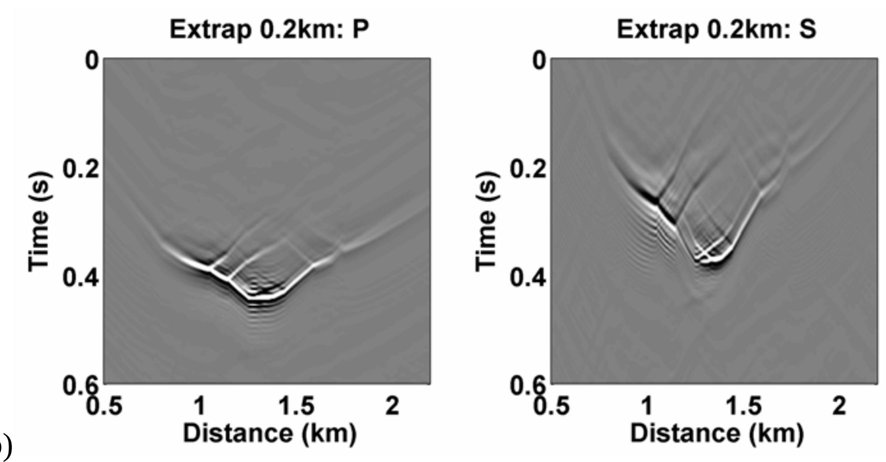

(b)

Figure 4.13. Extrapolation of impulse at 0.511s, downwards through model of Figure 4.12, using 50 steps of 4m each. The exact result is shown in (a), where "exact" means using equation (3-3) with window sizes reduced to a single CDP, so that each spatial output point uses a different set of parameters for extrapolation. Other results using PSPI algorithm of section 4.4.1.1, using: (b) 3 P-wave and 3 S-wave velocities;

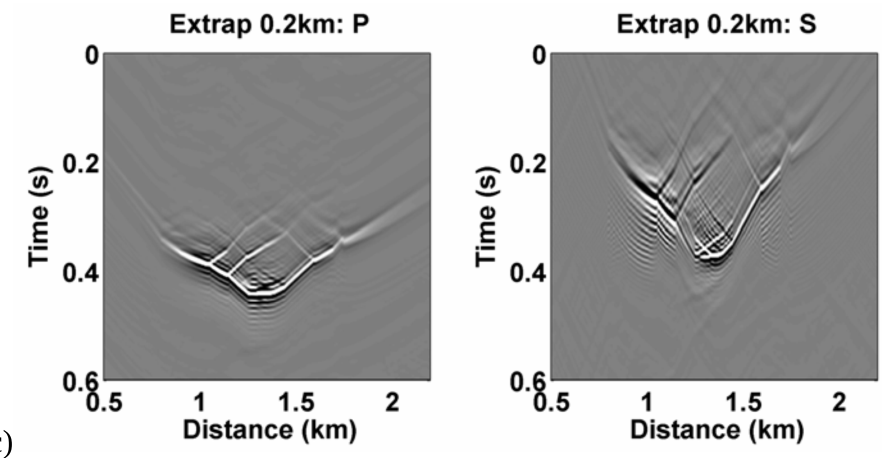

(c)

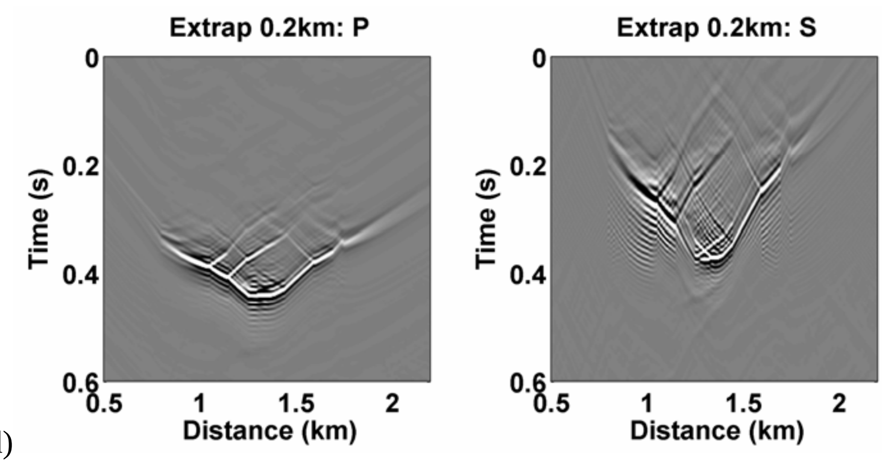

(d)

Figure 4.13 (continued) (c) 7 P-wave and 7 S-wave velocities; (d) 20 P-wave and 20 S-wave velocities. Results in (b), (c) and (d) should be compared with the exact result in (a).

This result is an important addition to the result of the previous section, since the transition across the boundary involves decomposition and recomposition based on polarizations, with interpolation of the results, as described in section 4.4.1.1. However, this test was using a model with constant V_P / V_S ratio, where no approximations are needed, so good agreement is not unexpected. Next, the approximation for variable V_P / V_S ratio is tested.

4.4.2.3 Two layers, variable (piecewise constant) V_P / V_S

Figure 4.16 shows a two layer model (a), in which the first layer has variation in the V_P / V_S ratio. As shown in (b), the V_P / V_S ratio varies between 2.0 and 3.0, and jumps discontinuously.

Figure 4.17 shows the results of extrapolation in this model using the exact approach (a), compared with using PSPI with 7 reference velocities (b), using the approximate algorithm described in section 4.4.1.2. As expected, the results are kinematically equivalent. That is, the operator shapes are the same. However, there are some visible differences in amplitudes along the impulse responses. These are evident most noticeably on the second branch of the S-wave operator, a part of the operator which corresponds to mode conversion from P to S. The error in the PSPI operator in (b) is believed to be caused by the approximation error on the P-wave decomposition as described in section 4.4.1.2, and Appendix I [see equation (I-2)].

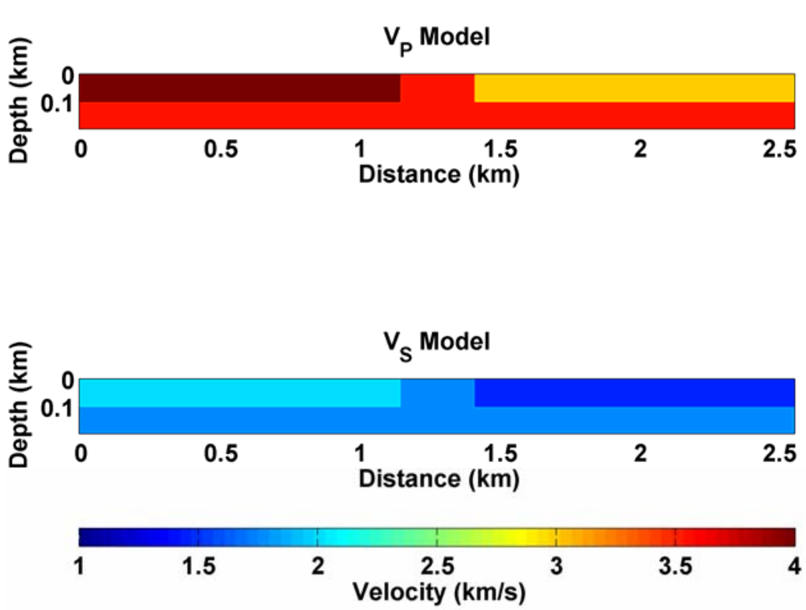

Figure 4.14. Two layer model with constant V_P / V_S ratio in both layers, used to test algorithm of section 4.4.1.1. The results of extrapolation through this model are shown in Figure 4.15.

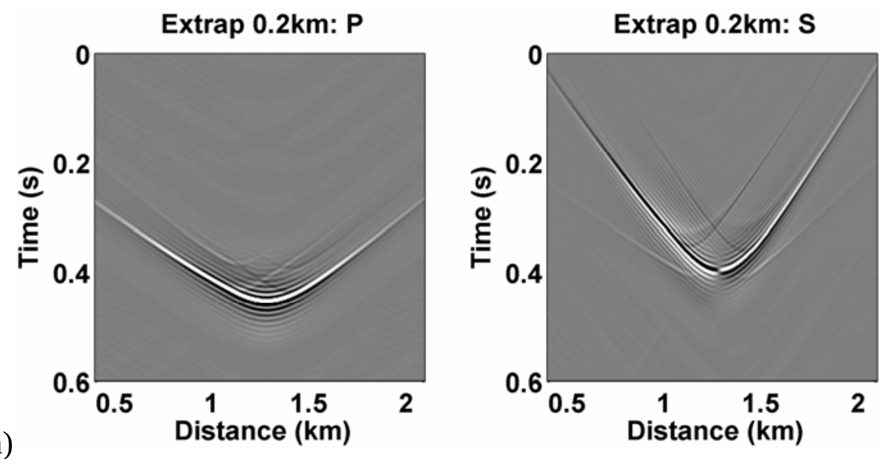

(a)

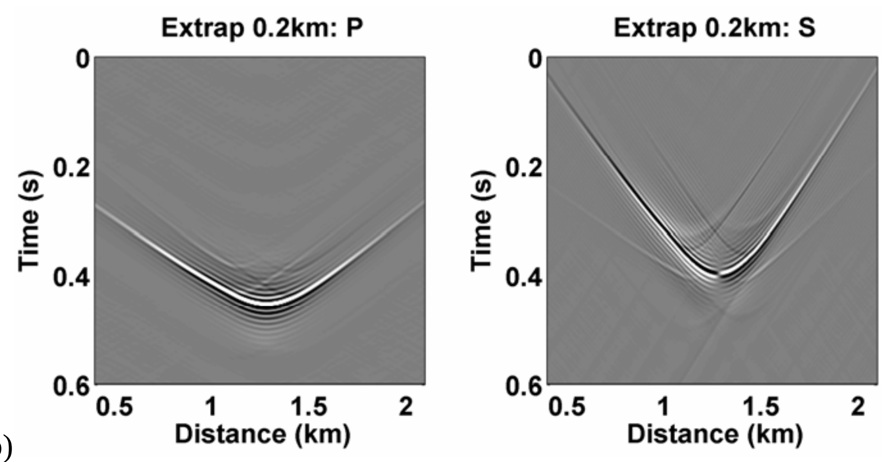

(b)

Figure 4.15. The results of extrapolation in model of Figure 4.14. The "exact" solution, using equation (3-3) with windows equal to the CDP interval, is shown in (a). The solution using the approximation of section 4.4.1.2 with 7 reference velocities is shown in (b).

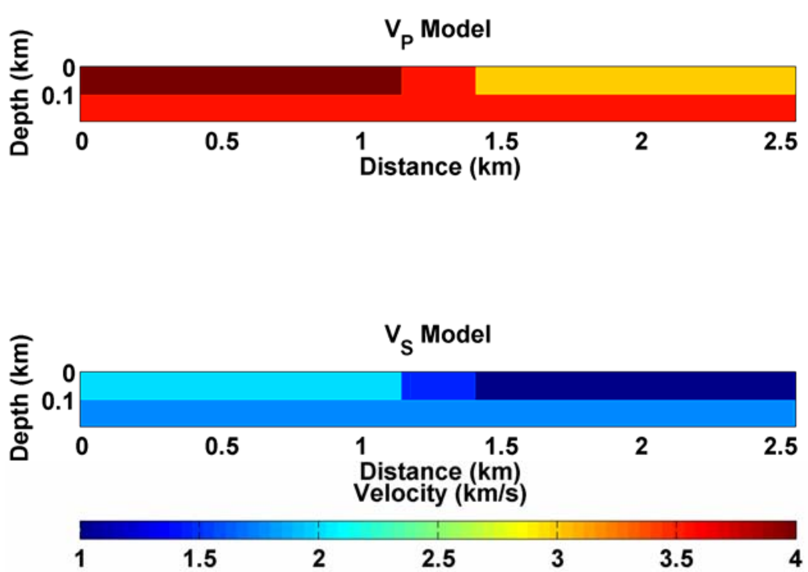

(a)

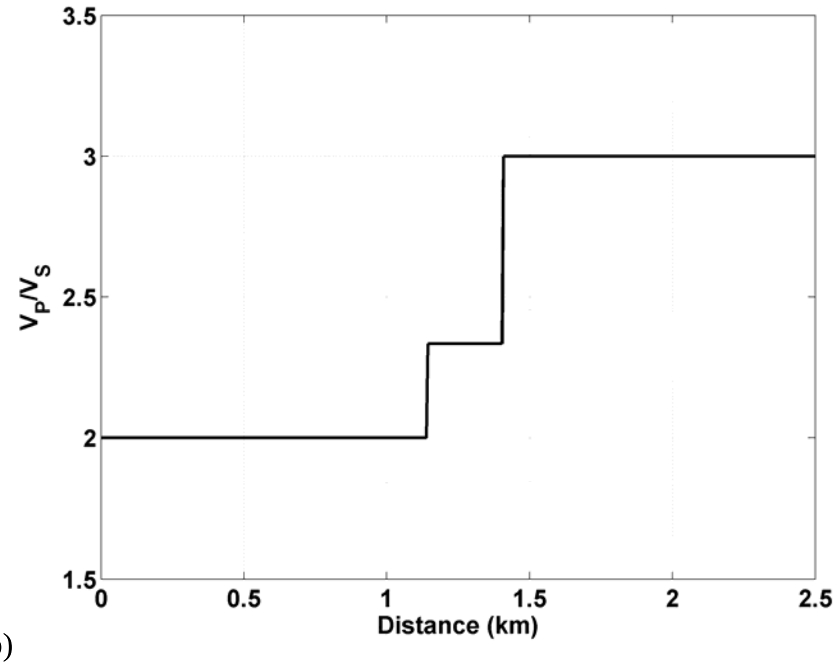

(b)

Figure 4.16. Two layer model (a) with variable V_P / V_S ratio in top layer (b), used to test effect of approximation in section 4.4.1.2. The results of extrapolation through this model are shown in Figure 4.17.

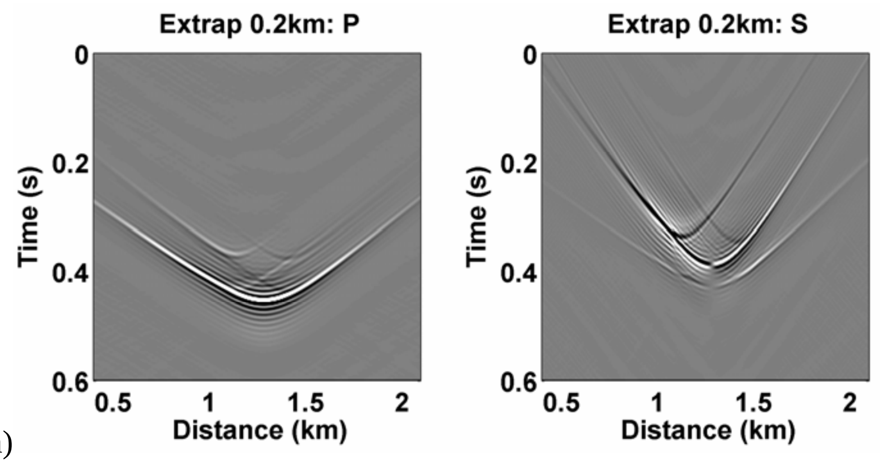

(a)

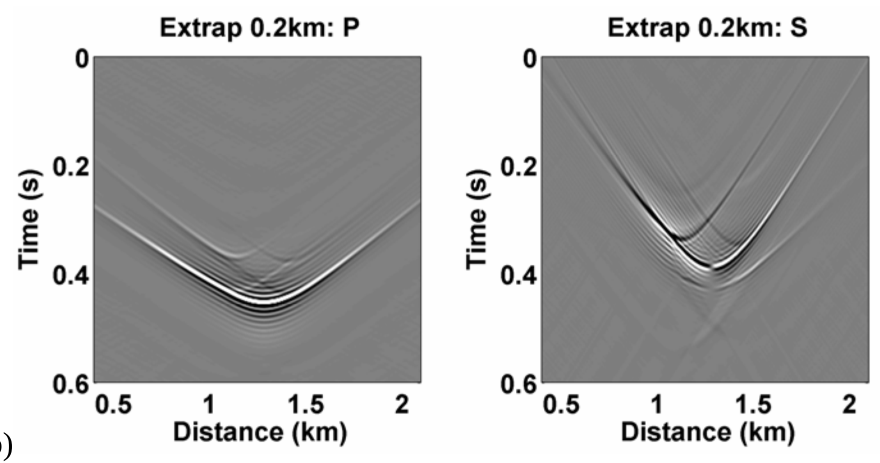

(b)

Figure 4.17. The results of extrapolation in model of Figure 4.16. The "exact" solution, using equation (3-3) with windows equal to the CDP interval, is shown in (a), the solution using the approximation of section 4.4.1.2 with 7 reference velocities is shown in (b).

4.4.2.4 Two layers, variable (continuous) V_P / V_S

The final example is also a two layer example, with variable V_P / V_S ratio in the upper layer. However, in this case the velocities vary continuously, without any jumps, and the V_P / V_S ratio varies between 2.0 and 2.5 (see Figure 4.18).

The extrapolation results are shown in Figure 4.19. As before, the comparison is between the exact result (a) and the result of PSPI with 7 reference velocities (b). In the absence of discontinuous velocity changes, the approximation of section 4.4.1.2 appears to give results which are very close to the exact operator.

4.5 Chapter summary

In this chapter the algorithmic details of isotropic and anisotropic elastic wavefield extrapolation using PSPI methods have been explored. Two alternative approaches to handling lateral heterogeneity have been presented, the first based upon spatial windowing functions, and the second more closely related to the conventional PSPI interpolation of velocities, commonly used in scalar wavefield extrapolation.

Because of the higher dimensionality of parameter space, the only viable option for anisotropic extrapolation is believed to be the use of spatial windowing functions. These are designed adaptively using Gaussian basis functions or "atoms". The choice of the Gaussian is motivated by some of its desirable mathematical properties such as optimal localization (defined as satisfying the Heisenberg uncertainty limit), smoothness and natural isotropy when extended to multiple spatial dimensions. The basic atoms are combined into "molecules", using acceptance criteria based upon restricting variation of phase velocity and of the symmetry axis within each such molecule.

For isotropic extrapolation, an alternative approach has been proposed. This approach exploits the approximate separability of the operator dependence on the P- and S-wave velocities. This allows an essentially conventional PSPI algorithm, but with implicit interpolation of the decomposition and recomposition steps. The algorithm is accurate for constant V_P / V_S ratio within each extrapolation step, and numerical examples suggest the approximation involved for a variable V_P / V_S ratio is acceptable.

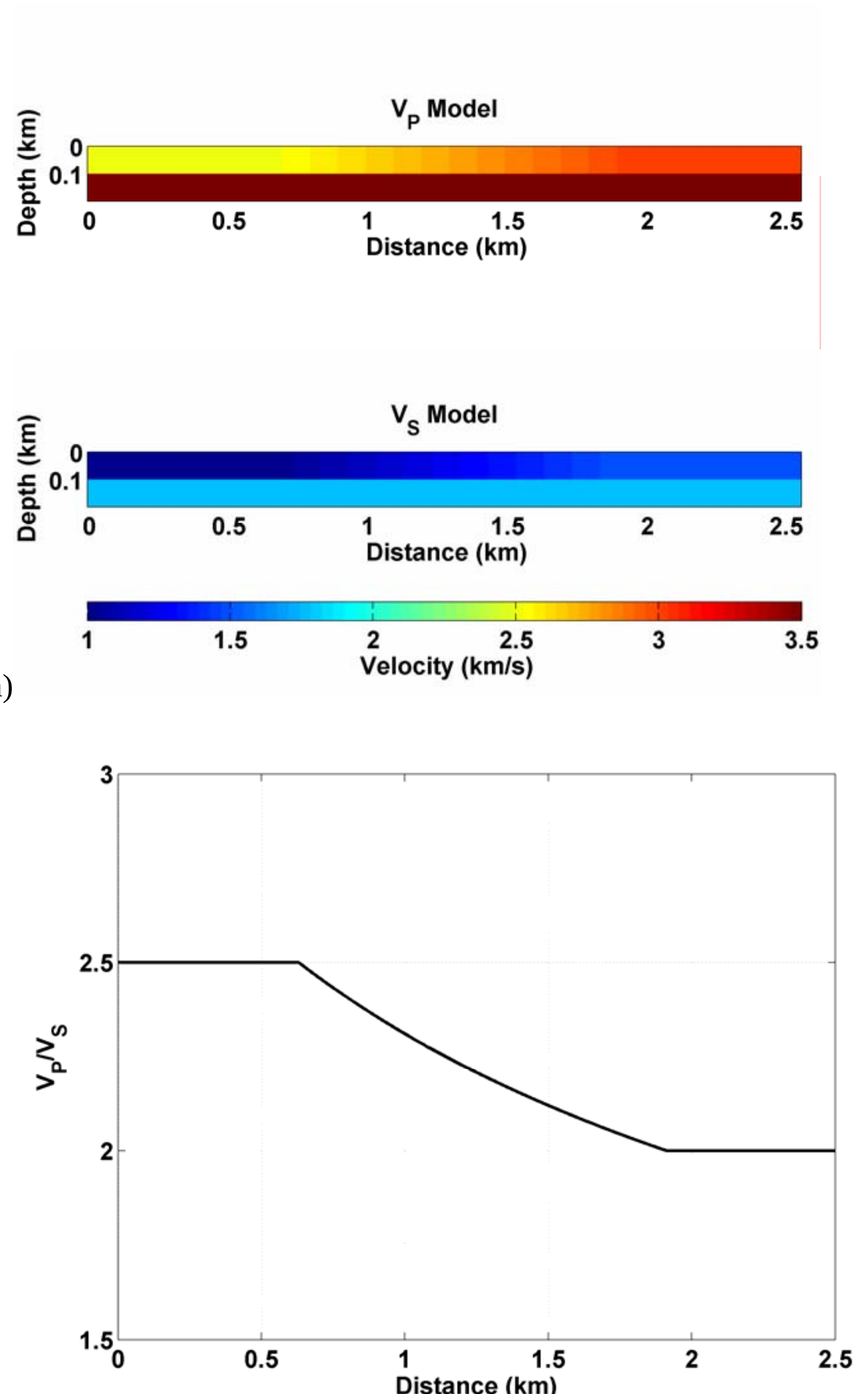

(a)

(b)

Figure 4.18. Two layer model (a) with variable V_P / V_S ratio in top layer (b), used to test effect of approximation in section 4.4.1.2. Both P-wave and S-wave velocities have linear gradients in the top layer. The results of extrapolation through this model are shown in Figure 4.19.

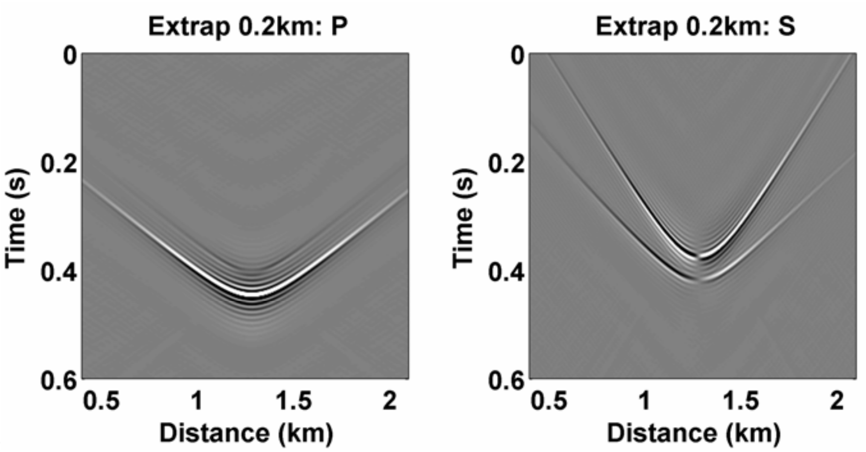

(a)

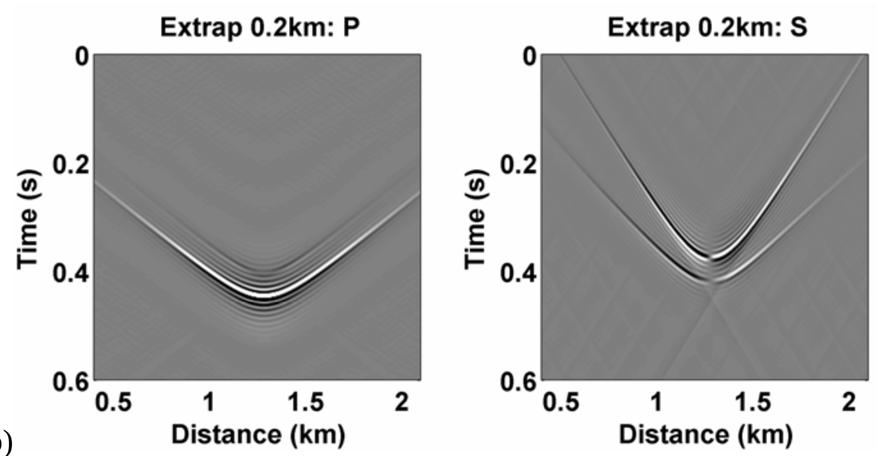

(b)

Figure 4.19. The results of extrapolation in model of Figure 4.18. The "exact" solution, using equation (3-3) with windows equal to the CDP interval, is shown in (a), the solution using the approximation of section 4.4.1.2 with 7 reference velocities is shown in (b).

CHAPTER FIVE: ELASTIC SHOT RECORD MIGRATION

5.1 Introduction

In this chapter, the extrapolation methods developed in the preceding three chapters are used to construct an elastic wave-equation shot record migration algorithm.

Wave-equation migration fundamentally consists of two steps, wavefield extrapolation and imaging. Of these, wavefield extrapolation is the most demanding, both theoretically and computationally. Elastic wavefield extrapolation has been described in chapters 2 to 4. A key additional step discussed in the present chapter is the imaging condition. This has much in common with standard scalar migration imaging conditions, but some subtleties arise due to the different propagation modes involved.

Further algorithmic aspects, which are obvious adaptations of existing methods for scalar migration, are briefly discussed here: anti-aliasing of the imaging condition; interpolation to finer output sampling in depth; and split-step (or phase-screen) corrections.

The shot-record migration is used to generate impulse responses for different configurations, and is tested on a synthetic example with an HTI layer inserted between two isotropic layers.

5.2 Migration operator design

5.2.1 Imaging condition

During elastic wavefield extrapolation the displacement wavefield is decomposed into three wave-modes P, S1 and S2, in each layer. To distinguish between the source wave-modes and the receiver wavefields, the notation of previous chapters is modified slightly. For forward extrapolation of the down-going wavefield from the source, the vector of wave-mode amplitudes is given by

$$\mathbf{w}_D = \begin{pmatrix} w_P^D & w_{S1}^D & w_{S2}^D \end{pmatrix}^T = \mathbf{D}_D^{-1}\,\mathbf{b}_{D,src}\,. \tag{5-1}$$

For backward extrapolation of the up-going wavefield from the receiver, they are given by the wave-mode vector

$$\mathbf{v}_U = \begin{pmatrix} v_P^U & v_{S1}^U & v_{S2}^U \end{pmatrix}^T = \mathbf{D}_U^{-1}\,\mathbf{b}_{U,rcv}. \tag{5-2}$$

In these and subsequent equations, the layer subscript *n* is omitted, while sub- and superscripts *U*, *D*, *src* and *rcv* are used to distinguish up-going from down-going, and shot from receiver wavefields. The wave-mode amplitude wavefields, $\mathbf{w}_D$ and $\mathbf{v}_U$ are by-products of the extrapolation of shot and receiver wavefields using equations (3-3).

The goal of elastic migration, assuming a P-wave source, is to produce images corresponding to P-P reflectivity, and P-S reflectivity for the isotropic case, or P-S1 and P-S2 reflectivity for the HTI case.[1] To obtain these images, an imaging condition must be applied. Two types of imaging condition are possible: a correlation imaging condition; and a deconvolution imaging condition.

5.2.1.1 The correlation imaging condition

A *correlation* imaging condition between the corresponding elements of equations (5-1) and (5-2) is written

$$I_{MN}^{corr.}(x,z) = \int_0^{\omega_{\max}} \overline{w}_M^D(x,z,\omega)\, v_N^U(x,z,\omega)\, d\omega, \tag{5-3}$$

where I_{MN} is the image for down-going mode *M*, and up-going mode *N*, where $M, N \in \{P, S1, S2\}$. The overscore here denotes complex conjugation.

5.2.1.2 The deconvolution imaging condition

A *deconvolution* imaging condition (Claerbout, 1971) is written

$$I_{MN}^{decon.}(x,z) = \int_0^{\omega_{\max}} \frac{\overline{w}_M^D(x,z,\omega)\, v_N^U(x,z,\omega)}{\left|w_M^D(x,z,\omega)\right|^2 + \varepsilon}\, d\omega, \tag{5-4}$$

where the division is stabilized by the addition of the small real value, ε.

In principle the deconvolution imaging condition is preferable. Claerbout defines the amplitude of a reflector as the ratio of the upgoing reflected wavefield to the downgoing incident wavefield, which leads to (5-4). The division by the source

[1] Additional images such as S1-S2 are also possible, if the source generates shear energy.

wavefield spectral density term $\left|w_M^D(x,z,\omega)\right|^2$ corresponds to correcting for the geometrical spreading of the source wavefield, which would otherwise remain present in the image. This leads to an operator which is asymmetric in amplitude, even when dealing with pure modes. Geiger (2001) placed the deconvolution imaging condition within the context of linear estimation theory, and showed that the integral in equation (5-4) corresponds to forming a least-squares estimate from measurements of frequency dependent reflectivity. The main disadvantage of the deconvolution imaging condition is the risk of small values for some frequencies in the denominator. This is addressed in equation (5-4) by the addition of the "white noise" stability term, ε.

The correlation condition, on the other hand, is less ambitious. The correlation condition relinquishes the goal of recovering the true amplitude, in favour of robust estimation of the phase response of the reflector.

5.2.2 Split-step correction

Both the PSPI and PSPAW algorithms described in chapter 4 are implemented with a split-step correction (Stoffa et al., 1990), also known as phase-screen (Fisk and McCartor, 1991; Huang et al., 1999). The split-step correction improves the accuracy of extrapolation for small angles. This is done by applying a residual phase shift in the spatial domain to correct for the difference between the reference and actual velocities. This is also referred to as the "thin lens" correction. A related wavefield interpolation (Fu, 2004) is applied, to enable image output at finer depth sampling than the extrapolation step.

For application of the split-step correction in anisotropic extrapolation, only the zero angle ($\theta = 0$) phase velocity is corrected for – since it is this velocity which is applicable to the vertical static shift applied. A consequence is that any variations in the anisotropy parameters that leave the zero angle phase velocity unaltered will have no effect on the split-step correction, and are in that sense "invisible".

5.2.3 Image condition aliasing

Zhang et al. (2003) point out that there is an often neglected operator aliasing effect in prestack wave-equation migration. This effect occurs because the source and receiver wavefield are cross-correlated (or deconvolved, if a deconvolution imaging condition is used) according to corresponding image point locations in the extrapolated wavefields. The correlation is applied in the spatial domain after applying inverse Fourier transforms. Correlation involves a series of multiplicative operations. Since multiplication in the spatial domain is equivalent to convolution in the wavenumber domain, there is an associated risk of wrap-around to wavenumbers which are twice the Nyquist wavenumber. Zhang et al. (2003) correct for this effect by generating output at half of the receiver interval, so that the spatial Nyquist wavenumber for the image is twice that of the extrapolated wavefields. This anti-aliasing procedure has been applied in the elastic migration algorithm of this chapter.

5.2.4 Source Green's function

Care is needed when generating the down-going source wavefield, according to the type of source function being modelled. As shown in Wapenaar (1990), the one-way representation for a monopole source function, such as an airgun marine source, is found by convolving the source function by an "inverse square root operator": defined by division of the source function (a bandlimited impulse) by the vertical wavenumber for each mode, $k_z^{(M)}$ on the first extrapolation step. If this step is neglected, there are angle dependent amplitude errors, and more obviously a 90° phase error.

However, if the source to be modelled is a dipole source, corresponding to a vertical force such a vibroseis, then this correction is not required (Wapenaar, 1990).

5.2.5 Repolarization steps

The term "repolarization step" is used to indicate the combination of recomposition and decomposition (to and from the displacement-stress form), across a boundary, as described by equations (2-15) and (2-16). In previous chapters, these repolarization steps have been described as being applied after every extrapolation step. However, for practical implementation within a shot migration algorithm (in which the extrapolation steps are generally small in size), repolarization steps are not carried out at every depth level, for both stability and efficiency reasons.

5.2.5.1 Stability

To understand the stability issue, recall from Chapter 2 that we can define an interface propagator $\mathbf{W}_{AB}$, for a change of medium, by a product of the composition matrix for medium A, $\mathbf{D}_A$, and the decomposition matrix for a different medium B, $\mathbf{D}_B^{-1}$, (i.e. $\mathbf{W}_{AB} = \mathbf{D}_B^{-1}\mathbf{D}_A$). The stability issue arises near the evanescent cut-off, where the product $\mathbf{W}_{AB}$, becomes ill-conditioned. Although $\mathbf{W}_{AB}$ is not singular (in fact the determinant is unity), it has a very large condition number[1] at this point. This results in numerical instability if the medium is rapidly changing. A discontinuous lateral change in the parameters of the medium is sufficient to cause this, since some amount of energy propagates across the lateral boundary on every depth step. This produces a growth in amplitude in the area between the evanescent cut-offs for media A and B. The amplitude growth appears to be polynomial, since the interface propagator is effectively multiplied by itself on every depth step. This problem is mitigated, but not solved, by the use of complex velocities as described in section 2.2.3.

A practical solution to the problem is to reduce the frequency of the repolarization steps to every few depth steps. This allows the evanescent suppression, which is exponential, to counteract the polynomial growth due to the ill-conditioning. Ten steps appear to be adequate, based on empirical tests. A model with a sharp contrast in medium parameters is tested in section 5.3.2.1, demonstrating instability using 5 depth steps.

5.2.5.2 Efficiency

A second reason for applying the repolarization step sparingly is cost. For an isotropic medium test with seven reference velocities, the cost of the repolarization step averages approximately eight times the cost of an extrapolation step alone. The details of cost depend on a number of variables, and the implementation in Matlab is not necessarily the most efficient possible. Nevertheless, it is assumed that the relative cost of a repolarization step and a pure extrapolation step are reasonably reflected by these

---

[1] The condition number of a matrix is the ratio of maximum to minimum eigenvalues Strang, G., 1988, Linear Algebra and its Applications, Harcourt Brace Jovanovich.

figures.

In the examples of this chapter, repolarization was performed at every 10th depth step, or every 100m of depth. In between these repolarization steps, the extrapolation proceeds as independent scalar extrapolations for P, S1 and S2 wavefields [see equations (2-17) and (2-18)]. For the fault planes, this has the effect of approximating the dips by a "stair-case" with each step having a 100m depth. The accuracy of this approximation, and the possibility of better approximations, have not been addressed within this thesis. They would be a fruitful avenue for further investigation.

5.3 Impulse responses

The impulse response of a linear system can be considered to provide a complete description of the system's behaviour. This is true because the response of the system to an arbitrary input is derived by a linear superposition of the impulse responses weighted by the components of the input, and can be described by (possibly multidimensional) convolution.

When generating impulse responses for conventional (scalar) migration, the impulse response depends upon the shot-receiver offset, and on the time of the impulse (as well as the model of course). When impulse responses for elastic migration are generated, there are four further variables: (1) the source component excited; (2) the receiver component to which the impulse is assigned; (3) the wave-mode on the source side, and; (4) the wave-mode on the receiver side. The first two might be considered as data space variables, and the second two as image space variables. The kinematics of the impulse response depend on the wave-modes, and *not* the components excited. However, the impulse response dynamics (amplitudes) *do* depend on the components excited. For example, an impulse on the vertical component for a vertical source excitation, gives responses on the P-wave and S-wave images which differ from those arising from an impulse on the horizontal inline component for the same source.

For this reason, observing the full characteristics of the operator would require examination of impulse responses for 3 source directions, and 3 receiver directions, and for *each* of these, potentially 9 different mode combinations involving P, S1 and S2 for source and receiver side. Such exhaustive analysis is unlikely to lead to a deeper understanding of the migration, and in any case would be unwieldy. The impulse responses shown within this section are chosen selectively instead, to illustrate certain key points.

All the impulse responses are generated using a bandlimited representation of an impulse, a Ricker wavelet with dominant frequency of 60Hz.

5.3.1 Isotropic homogeneous model

Impulse responses are generated for an offset of 512m, with an impulse at a two-way time of 510 ms. Even the simplest of models, for a medium which is homogeneous and isotropic, gives impulse responses which have some interesting, and perhaps unexpected, features. It is worth considering these before moving on to the more complex examples of HTI media. Doing so helps us to distinguish between those features which are associated with elastic migration operators in general, and those which are specifically related to anisotropy.

The impulse response can be regarded as the set of all possible reflector positions and amplitudes which cause the observed impulse to be present on the seismic trace for this particular offset and time. Consider Figure 5.1, which depicts the P-SV reflections from possible reflectors in the earth.[1] Two reflector segments, labelled A and B, are assumed to lie on the isotime surface corresponding to our impulse time.

[1] Recall that the SV mode is the shear-wave mode which is polarized in the plane of propagation, and is coupled to the P-wave mode, for isotropic media.

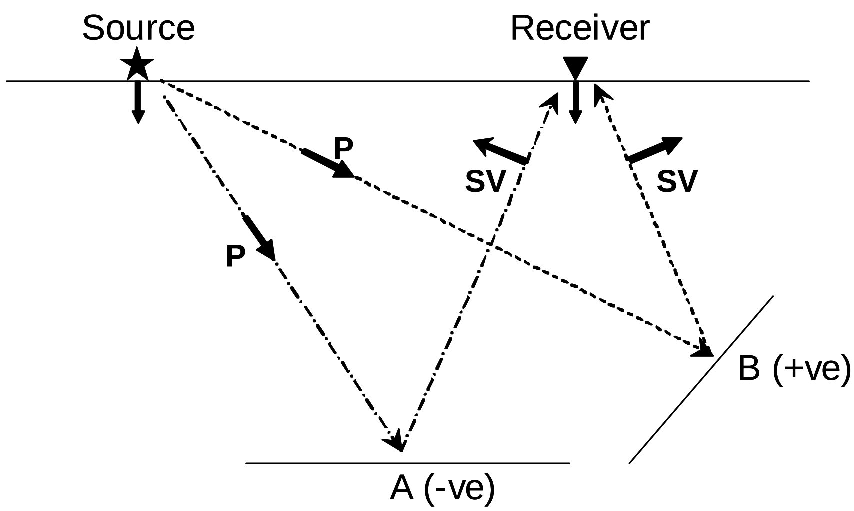

Figure 5.1. Reflection polarities associated with a positive impulse on the vertical receiver. The convention assumes that a positive P-P reflection coefficient is represented as a positive impulse (that is, as an upward motion at the receiver). Using this convention, a negative P-SV reflection coefficient at A would produce the SV particle motion shown, corresponding to a positive peak on the vertical receiver. However, at point B, a positive P-SV reflection coefficient would be required to produce upwards motion at the receiver.

In order for the amplitude of an impulse from the vertical source and vertical receiver to be positive, *and also to correspond to a P-SV reflection*, a possible reflection is one with a negative reflection coefficient on segment A. This would give rise to the SV wave polarized as shown along the dot-dash raypath. This has an upward component of vertical particle motion at the receiver. Alternatively, if the actual reflection occurs at B, then it must be positive, giving rise to the SV wave polarized as shown along the dotted raypath. This again has an upward component of vertical particle motion at the receiver, as required. From this observation, we would expect that the impulse response, which includes all possible reflection positions and their corresponding reflection coefficients, must change polarity between A and B. In fact the position of polarity change lies directly below the receiver, since it is here that the change in the sense of SV polarization is required, in order to preserve the vertical particle motion. Similar reasoning leads one to expect polarity changes associated with the source position for mode combinations which have down-going SV.

In Figure 5.2, these effects are seen on an impulse response which has been generated using the elastic shot migration, for a vertical source and *vertical* receiver. In this, and all subsequent impulse responses, the shot and receiver positions are indicated by an asterisk and a triangle, respectively. For comparison, Figure 5.3 shows the impulse response for a vertical source and *horizontal* receiver. Once again, the polarity changes of the impulse response can be understood by considering the signs of reflection coefficient required to generate positive *horizontal* particle motion at the receiver, for different reflection positions.

For vertical source and receiver polarizations, using a correlation imaging condition, the operator displays the following symmetries:

Both pure mode images (P-P and SV-SV) have impulse responses which are symmetric about the source-receiver midpoint, both kinematically and dynamically (i.e. in amplitude) [see Figure 5.2 (a) and (d)].

The P-SV and SV-P impulses responses are symmetric about the midpoint, with respect to each other. In other words, if the modes are interchanged, and the impulse response is simultaneously reflected about the midpoint, then the net result is unchanged.

For a vertical source and horizontal receiver, no such symmetries are immediately apparent. However, the vector reciprocity principle (Thomsen, 1999) implies that if this is compared with an impulse response from a *horizontal* source and *vertical* receiver, certain symmetries should be observed. The impulse response for this configuration is shown in Figure 5.4. We can observe reciprocity relationships between: P-P responses [Figure 5.3(a) vs. Figure 5.4(a)]; P-SV and SV-P responses [Figure 5.3(b) vs. Figure 5.4(c) and Figure 5.3(c) vs. Figure 5.4(b)]; and SV-SV responses [Figure 5.3(d) vs. Figure 5.4(d)].[1]

Some features are specific to the isotropic homogenous case. The pure mode responses, P-P [e.g. Figure 5.2(a)] and SV-SV [e.g. Figure 5.2(d)] are elliptical responses, with source and receiver at the foci, as is the case for a scalar migration in a homogenous

[1] In fact, there is an additional multiplication by -1 between corresponding images. This results from the fact that the act of interchanging source and receiver roles is not exactly a mirror image operation. The horizontal orientation of the source in Figure 5.4, and the receiver in Figure 5.3, both point in the same direction. A true mirror image reflection would have them pointing in opposite directions.

medium. Furthermore, in none of these impulse response examples is an SH-wave response generated by the impulse. For isotropic media (and also for VTI media) the SH-wave is not coupled to the P-wave or the SV-wave. Instead, it can only be generated by an impulse polarized in the direction orthogonal to propagation, i.e. parallel to the *y*-axis. An interesting point to note is that both *kinematic* and *dynamic* (amplitude) reciprocity hold true for the correlation imaging condition of equation (5-3). This occurs because the source and receiver wavefield are treated symmetrically in the correlation imaging condition.

5.3.1.1 Deconvolution imaging condition impulse response

Use of a deconvolution imaging condition rather than a correlation imaging condition has a similar impact as for the scalar migration case. The operator no longer displays dynamic reciprocity, since the source and receiver wavefields are not treated symmetrically in equation (5-4). Figure 5.5 shows the P-P (a) and P-SV (b) responses for a vertical source and a vertical receiver impulse, using the deconvolution imaging condition. These should be compared with Figure 5.2 (a) and (b).

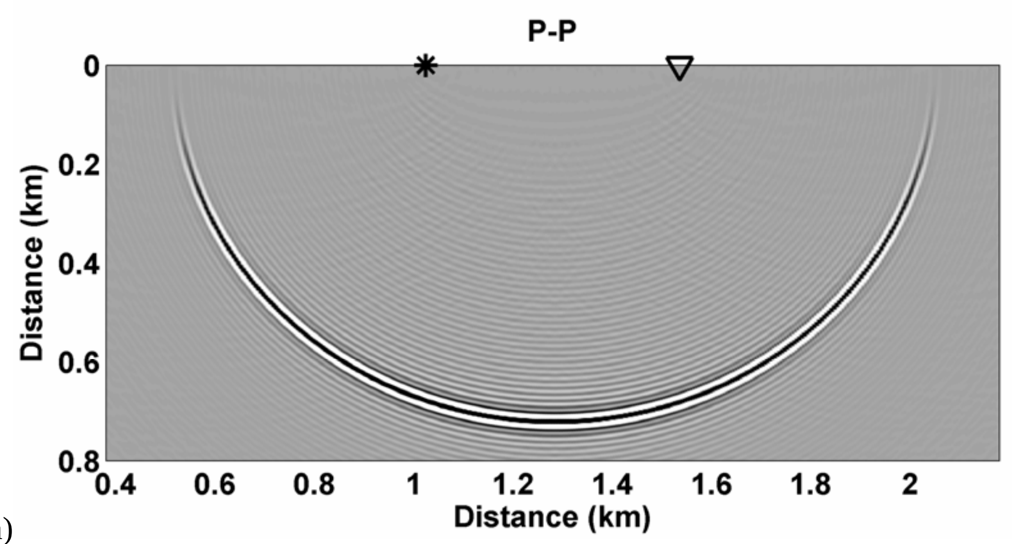

(a)

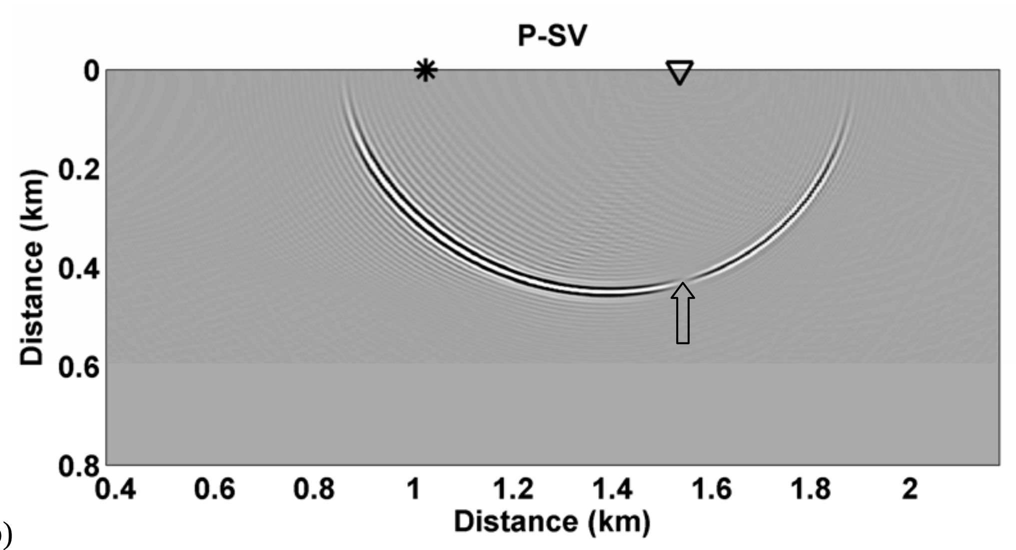

(b)

Figure 5.2. Impulse response, using correlation imaging condition, for isotropic medium with V_P=3000m/s and V_S=1500m/s. The source position is indicated by the '*', the receiver by the '∇'. The impulse is for a vertical source and vertical receiver component. Different mode combinations are (a) P-P; (b) P-SV; (c) SV-P, and; (d) SV-SV. There is no response for SH (either shot or receiver) in this case, since the impulse has no out of plane component. Polarity changes occur at locations, indicated by the arrows, where the vertical component of shear-wave particle motion changes sign. (see Figure 5.1 for an explanation of the P-SV case).

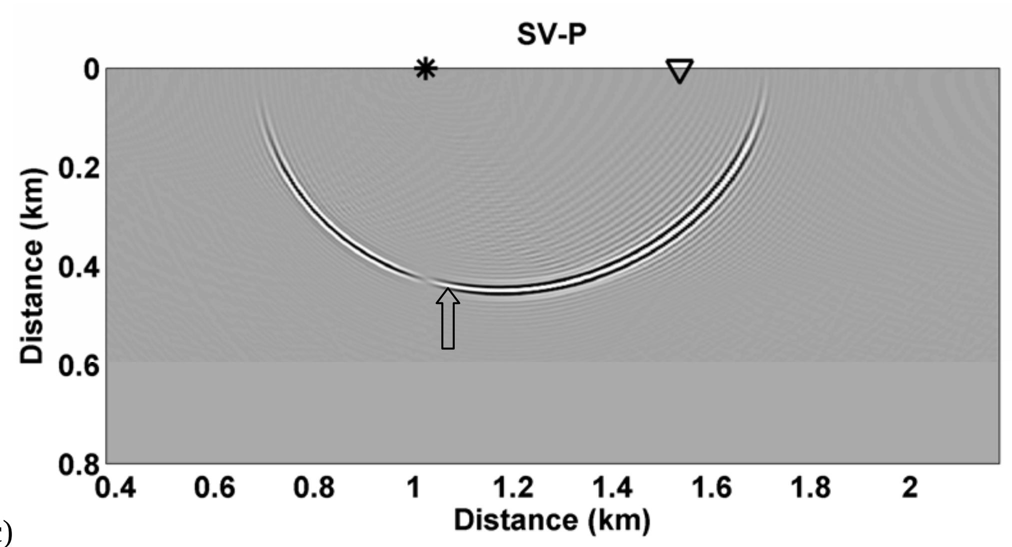

(c)

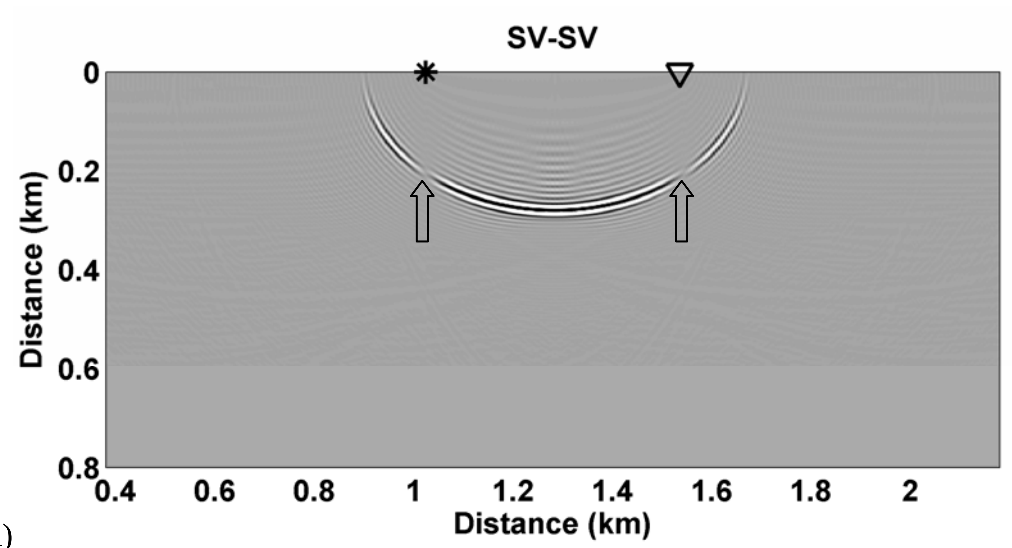

(d)

Figure 5.2 (continued)

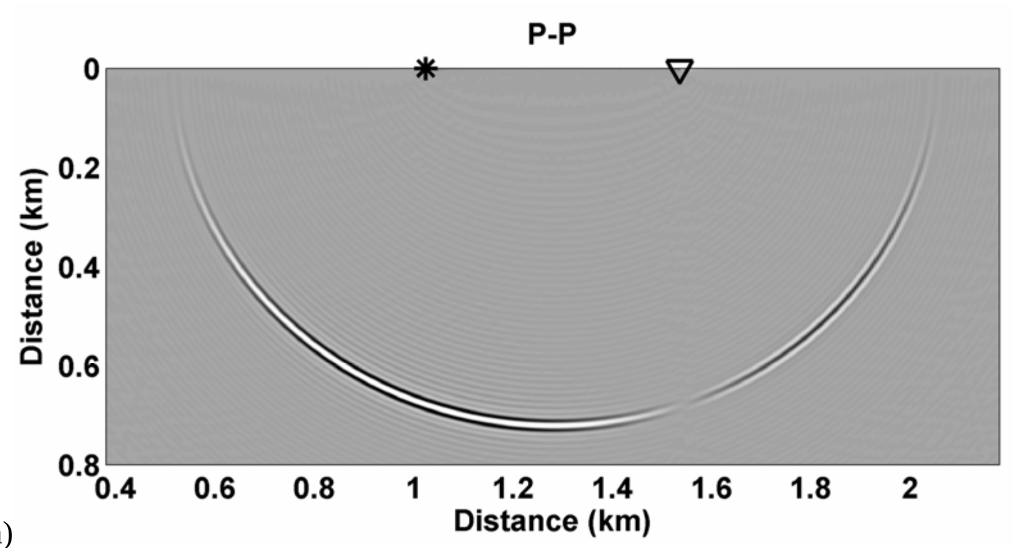

(a)

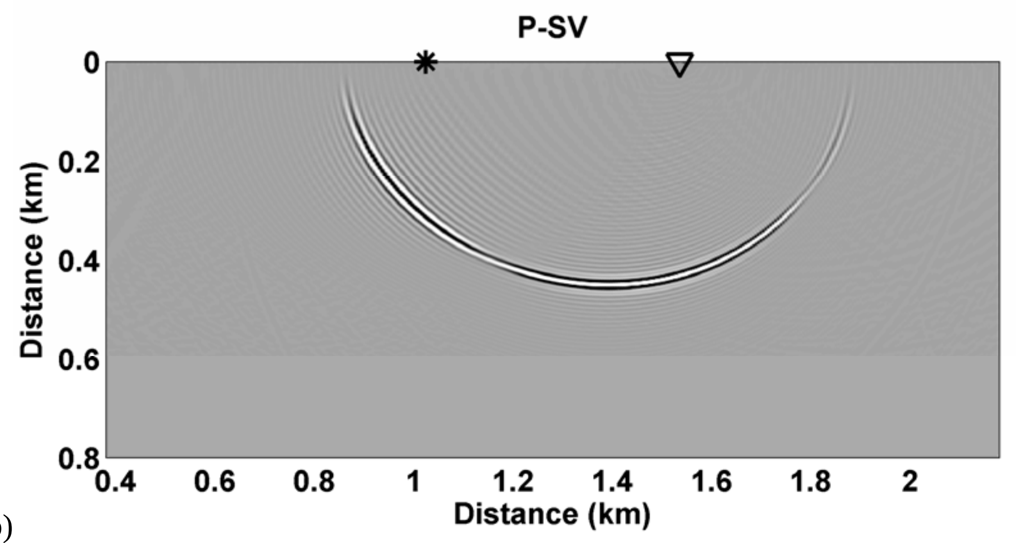

(b)

Figure 5.3. Impulse response, using correlation imaging condition, for isotropic medium with V_P=3000m/s and V_S=1500m/s. The impulse is for a vertical source and horizontal receiver component. Compare with Figure 5.2, the impulse response for a vertical receiver. In this case, polarity changes occur - at the position of the receiver - when the horizontal component of particle motion changes sign: on the P-P image (a), and SV-P image (c).

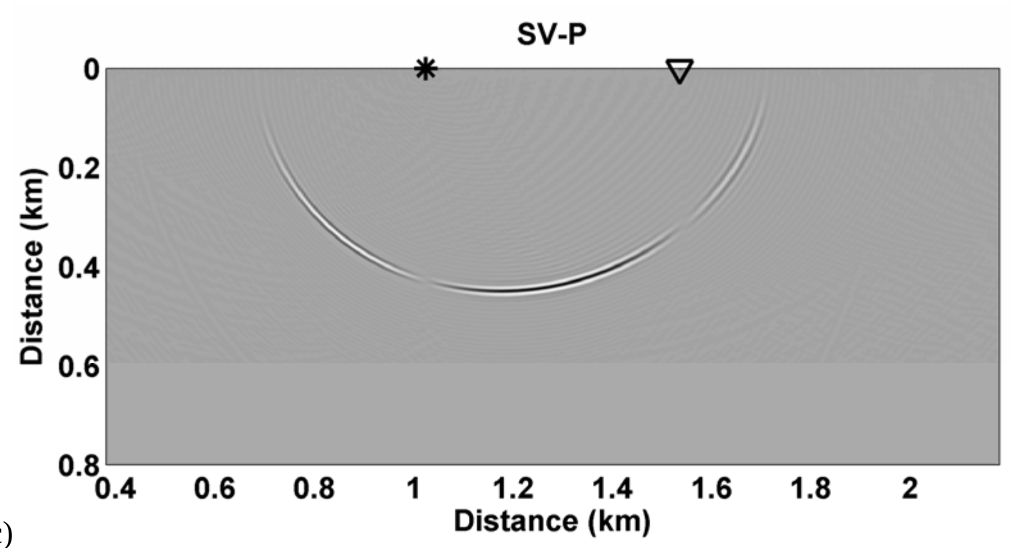

(c)

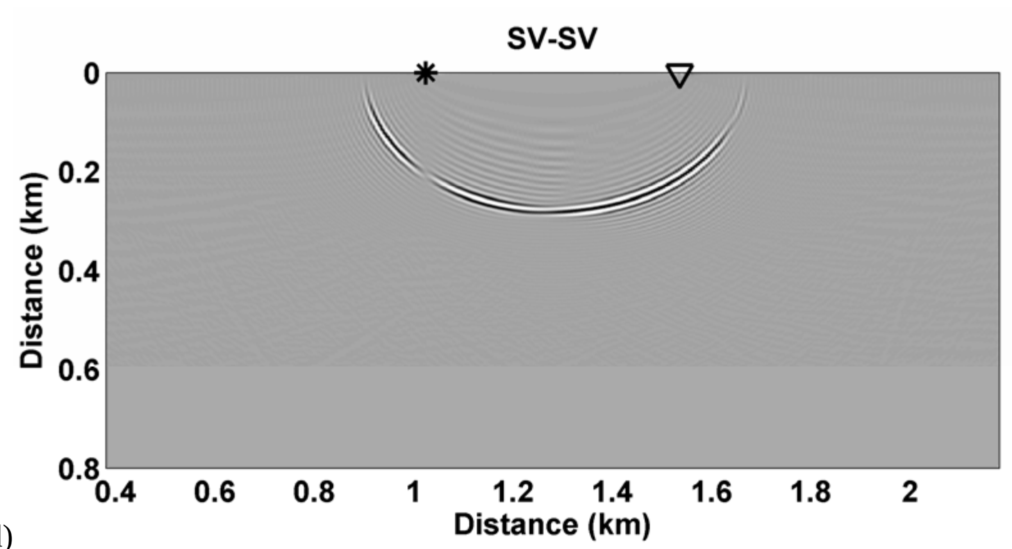

(d)

Figure 5.3 (continued)

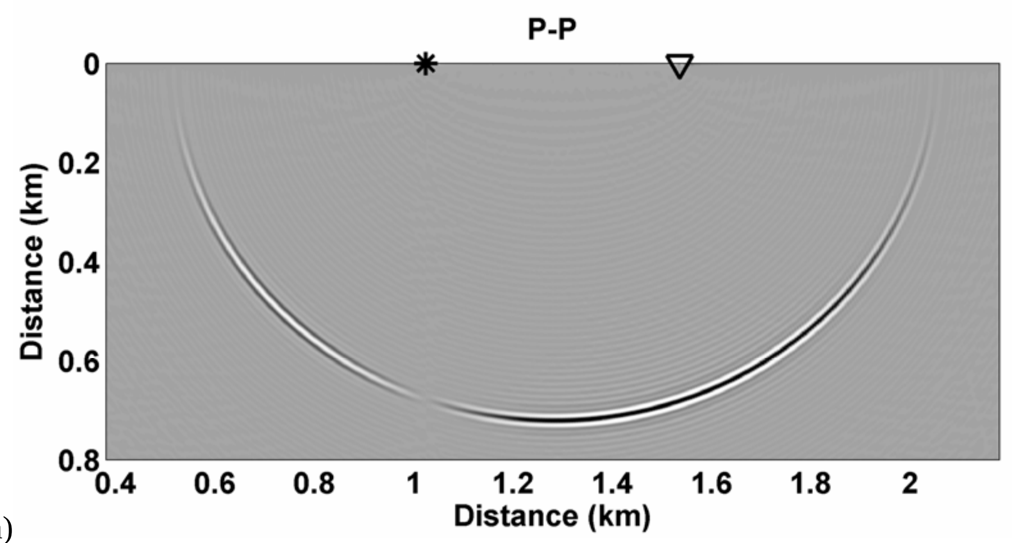

(a)

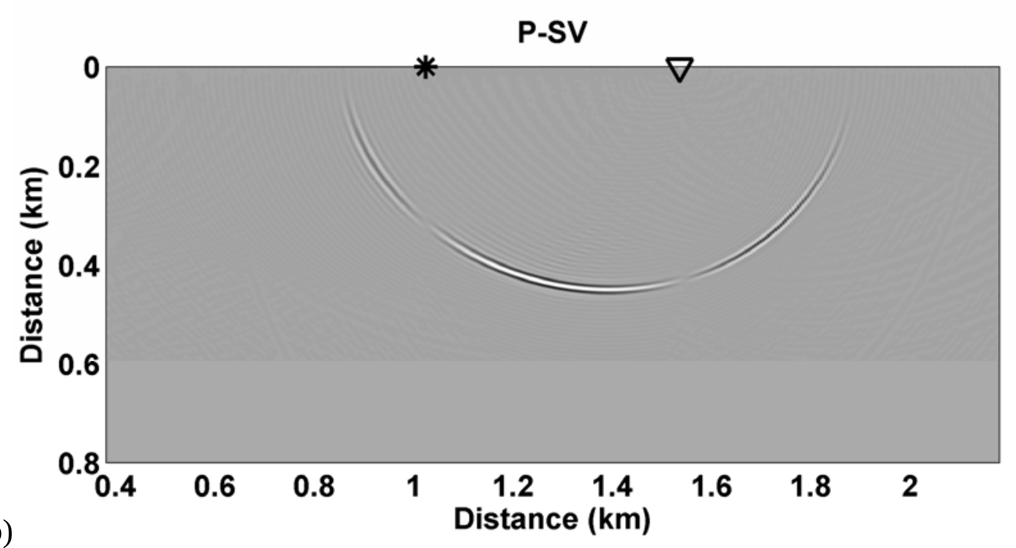

(b)

Figure 5.4. Impulse response, using correlation imaging condition, for isotropic medium with V_P=3000m/s and V_S=1500m/s. The impulse is for a *horizontal* source and *vertical* receiver component. Compare with Figure 5.3, the impulse response for a vertical source receiver and horizontal receiver. In particular observe reciprocity relations between: P-P responses [Figure 5.3(a) vs. Figure 5.4(a)]; P-SV and SV-P responses [Figure 5.3(b) vs. Figure 5.4(c) and Figure 5.3(c) vs. Figure 5.4(b)]; and SV-SV responses [Figure 5.3(d) vs. Figure 5.4(d)].

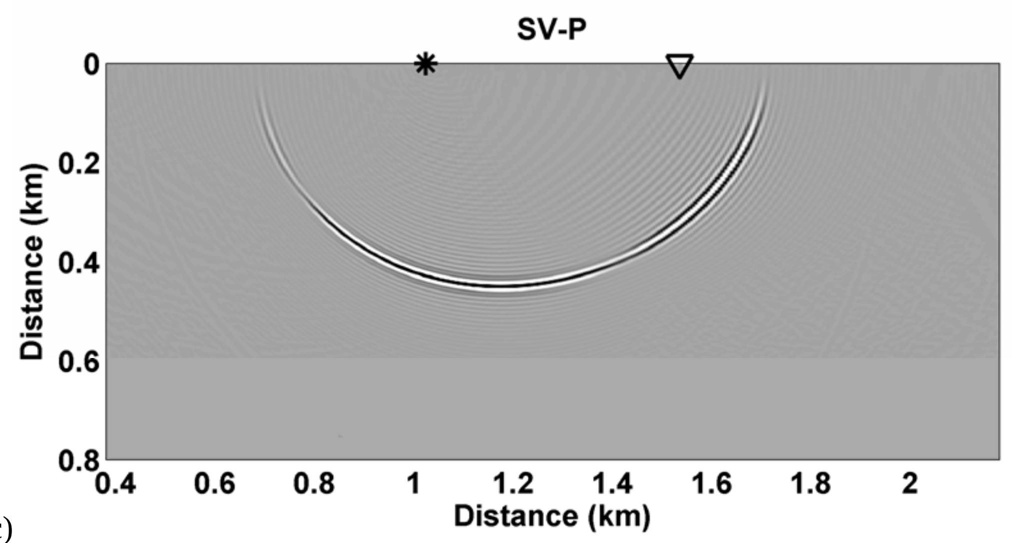

(c)

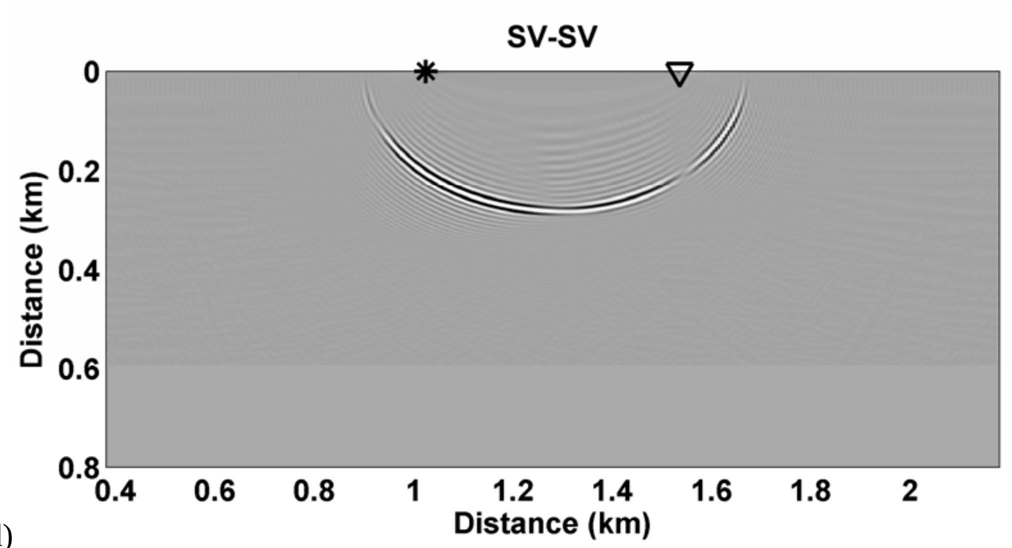

(d)

Figure 5.4 (continued)

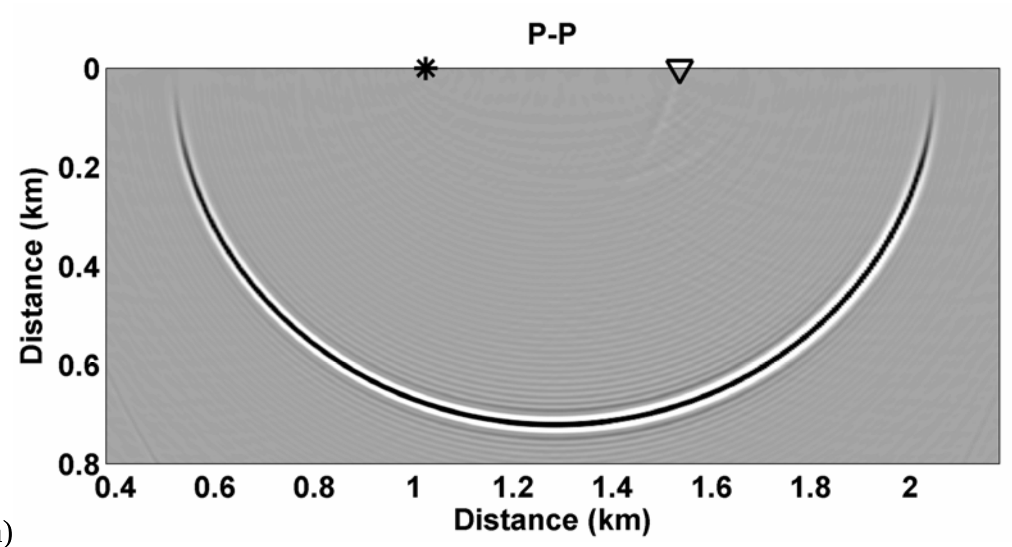

(a)

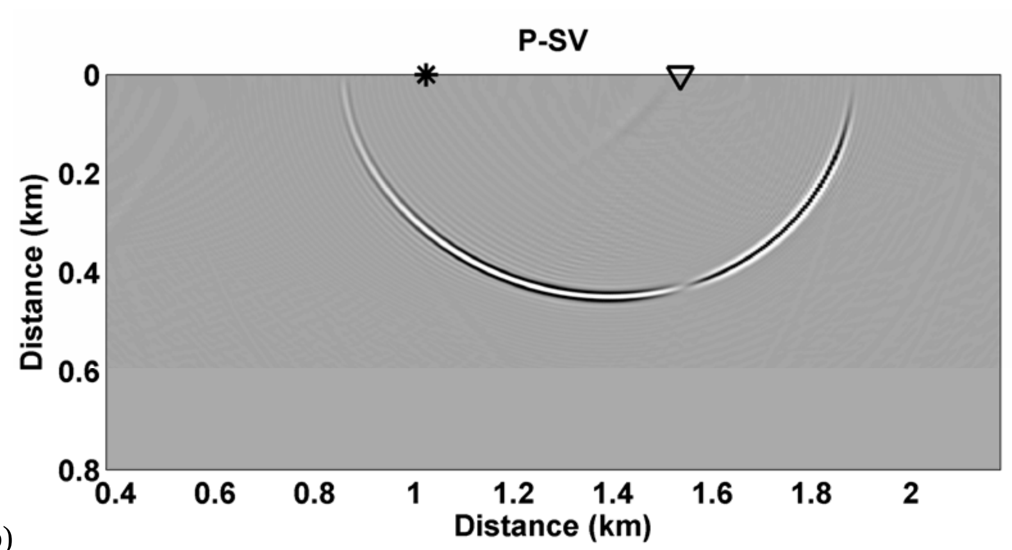

(b)

Figure 5.5. Impulse response, using deconvolution imaging condition, for isotropic medium with V_P=3000m/s and V_S=1500m/s. Only mode combinations P-P (a) and P-SV (b) are shown. Compare with Figure 5.2 (a) and (b).

5.3.2 Isotropic laterally inhomogeneous model

Consider the vertically homogeneous, isotropic medium, with lateral variations of P and S velocity as shown in Figure 5.6. This model is used to illustrate two aspects of the elastic operators: the effect of the repolarization steps and the split step correction.

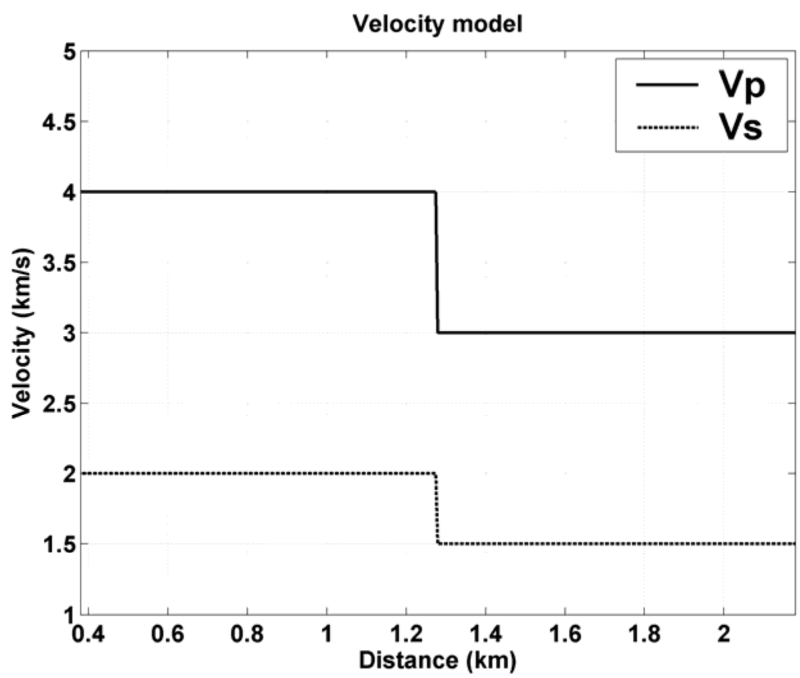

Figure 5.6. Lateral variation of P and S velocities for impulse response tests.

5.3.2.1 Repolarization

The repolarization step is used to repartition energy from P to S, and back, in the isotropic case (it has a more important role in repartitioning energy between S1 and S2 modes for the HTI case). One effect of this is that lateral changes in velocity result in some local mode conversion in propagation. Figure 5.7 illustrates the impulse response for the vertically homogeneous but laterally inhomogeneous medium of Figure 5.6, without applying any repolarization steps (except for the initial decomposition at the surface). In other words, the migration in this case uses pure scalar extrapolation, after the initial wavefield decomposition.

Compare this example with Figure 5.8. This shows the impulse response from migration with repolarization after every 10 depth steps. The repolarization steps here have the effect of including a "shadow" SV-SV response on the P-SV response. The most plausible explanation for this shadow is that SV down-going energy is being momentarily converted into P-wave energy at the velocity contrast location, before being included in the P-SV imaging condition. The net result is an event with the kinematics of the SV-SV response, but which is registered on the P-SV section. The converse can also occur. This explains the presence of a P-SV shadow on the SV-SV section.

As discussed in section 5.2.5.1, applying repolarization too frequently can lead to instability in the presence of strong medium contrasts, such as that of Figure 5.6. In Figure 5.9, the migration impulse response is generated using a repolarization step after every five depth steps. This results in an unstable extrapolation, due to the poor condition number of the interface propagator used near the evanescent boundary. Remedial steps are possible, such as smoothing the velocity field, as shown in Figure 5.10. This mitigates the problem (Figure 5.11), by effectively reducing (locally) the size of velocity contrast. However, this is at the undesirable cost of seriously limiting lateral resolution. It seems preferable to accept the limitation on the frequency with which repolarization can be applied.

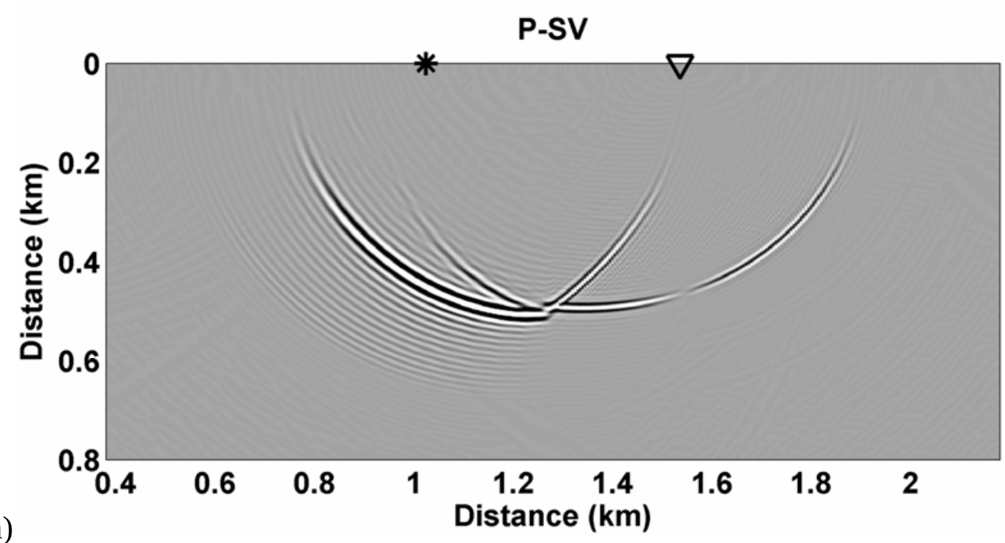

(a)

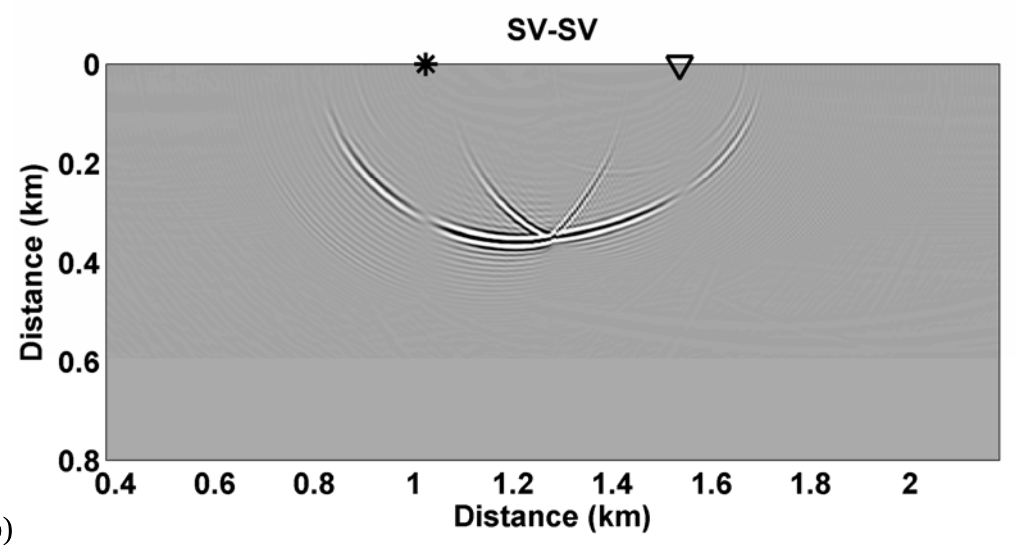

(b)

Figure 5.7. Impulse response using two reference velocities, but omitting repolarization steps. After initial wavefield decomposition at the surface, the P and S modes are extrapolated independently.

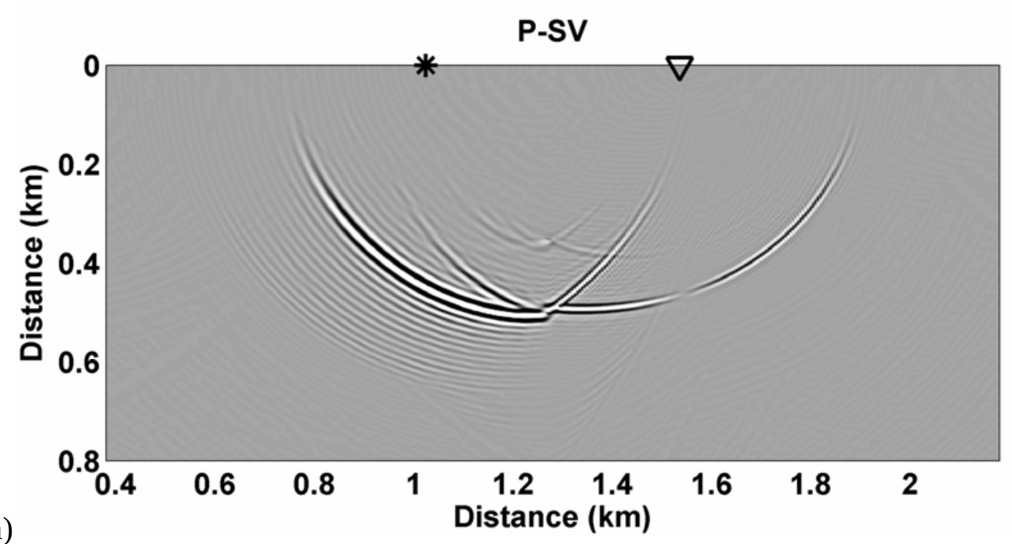

(a)

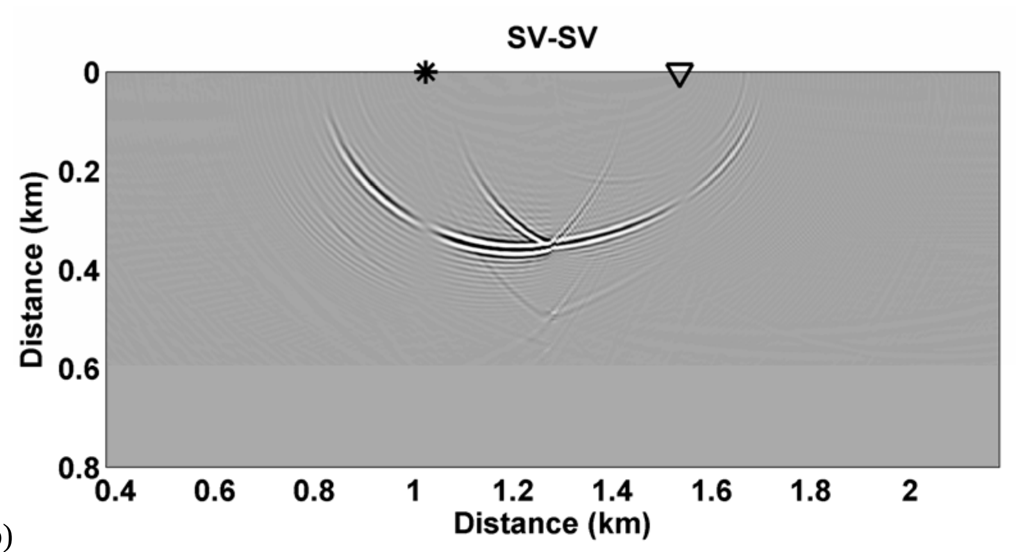

(b)

Figure 5.8. Impulse response using two reference velocities, with repolarization steps every 10 extrapolation steps. The repolarization steps permit the conversion of P to S and vice versa at the vertical boundary. This results in an "echo" of the SV-SV response present on the P-SV response (a), due to local mode conversion of S-wave energy to P-wave energy at this interface. Similarly there is an echo of the P-SV impulse response on the SV-SV response. Compare with Figure 5.7, where no echos are present.

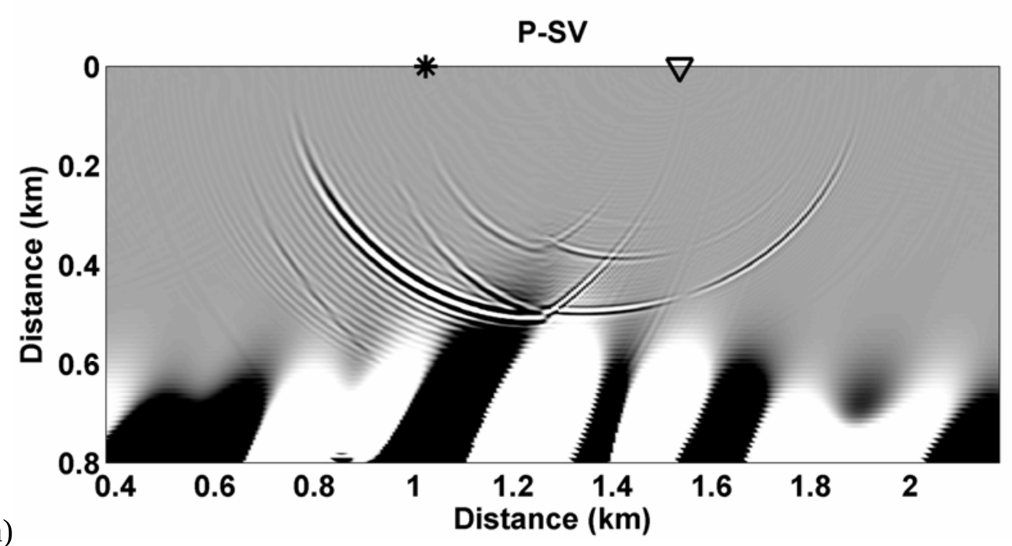

(a)

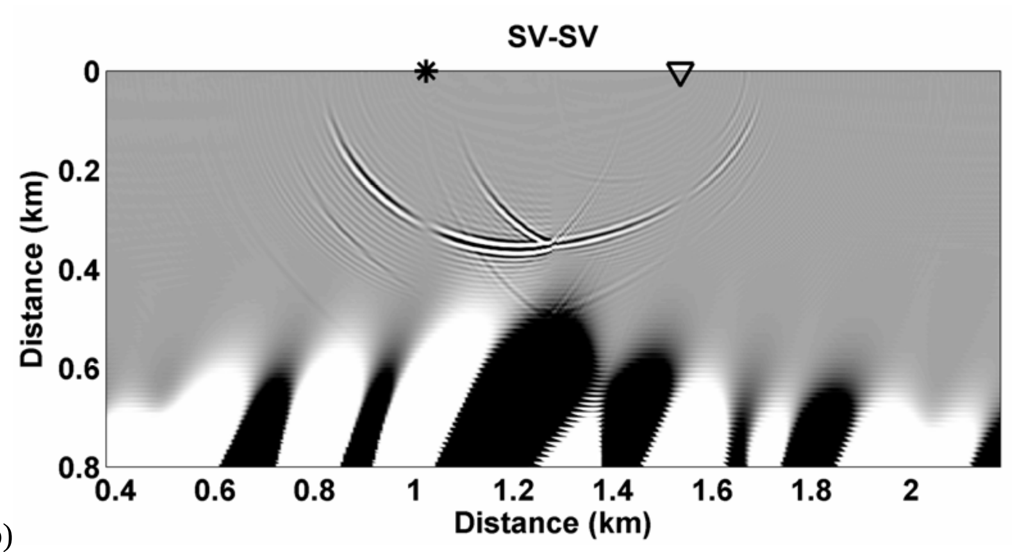

(b)

Figure 5.9. Impulse response using two reference velocities, with repolarization steps every 5 extrapolation steps. The transmission of energy across the boundary and poor condition number of the interface propagator near the evanescent boundary causes an unstable response. For less frequent repolarization steps, this is suppressed by the evanescent damping (Figure 5.8).

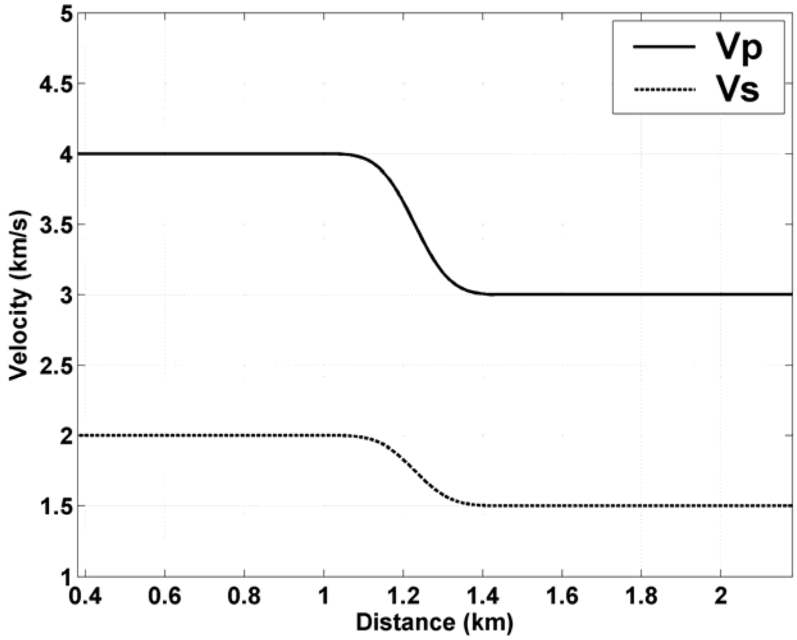

Figure 5.10. Lateral variation of P and S velocities by smoothing velocities in Figure 5.6, using a 20 point Gaussian window.

5.3.2.2 Split-step correction

Figure 5.12 compares the impulse response generated for this medium using a single reference velocity with a split-step correction (b), with the "exact" impulse response from PSPI with two reference velocities (a). The split-step correction gives accurate results for the small dips, but is inaccurate at larger dips. In practice, it is applied in conjunction with PSPI or PSPAW to improve the accuracy of the operators in the presence of rapid velocity variations.

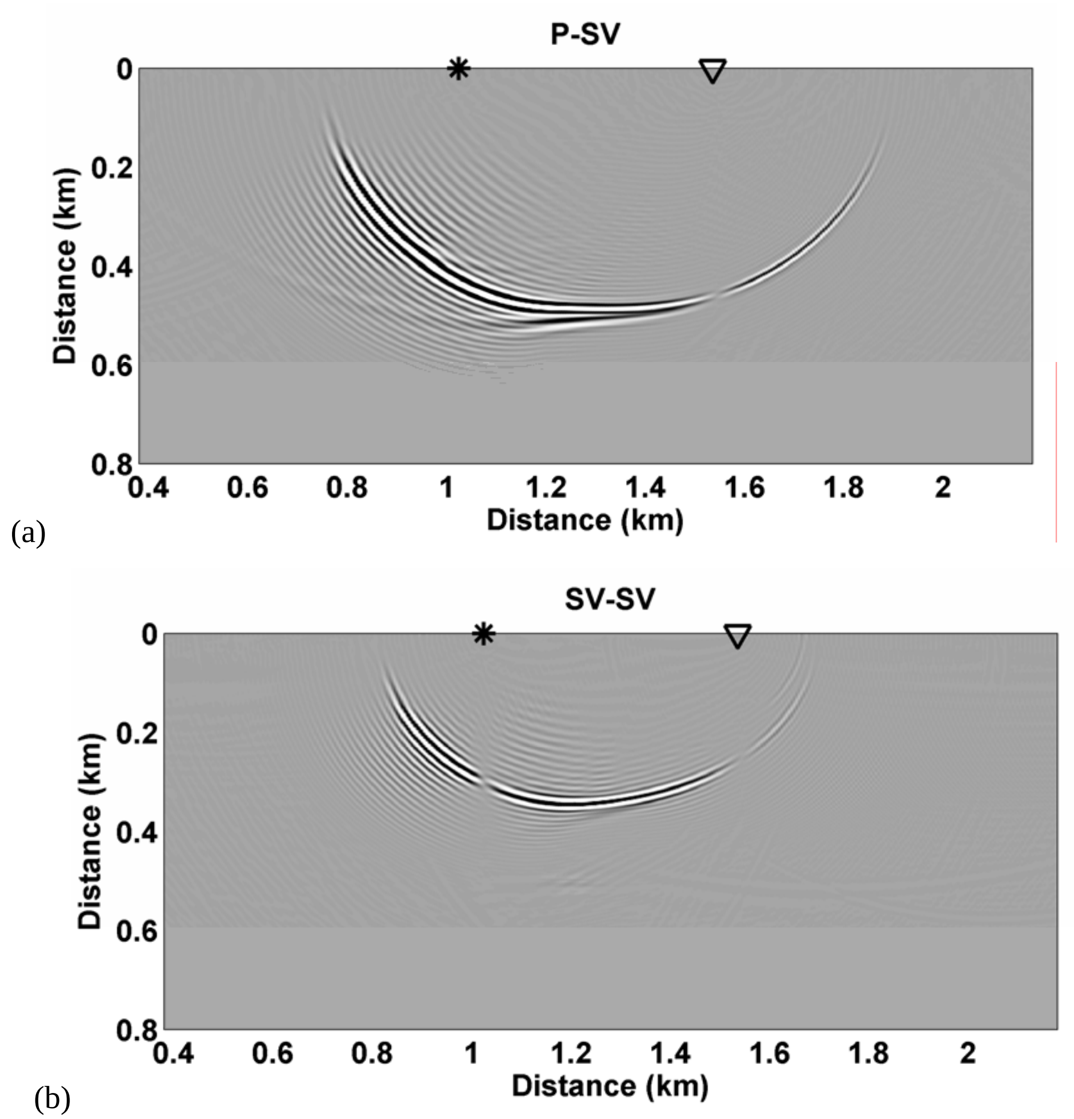

Figure 5.11. Impulse response for smoothed velocity model of Figure 5.10, with repolarization steps every 5 extrapolation steps, using seven reference velocities. The instability is suppressed, but at the expense of sacrificing lateral resolution.

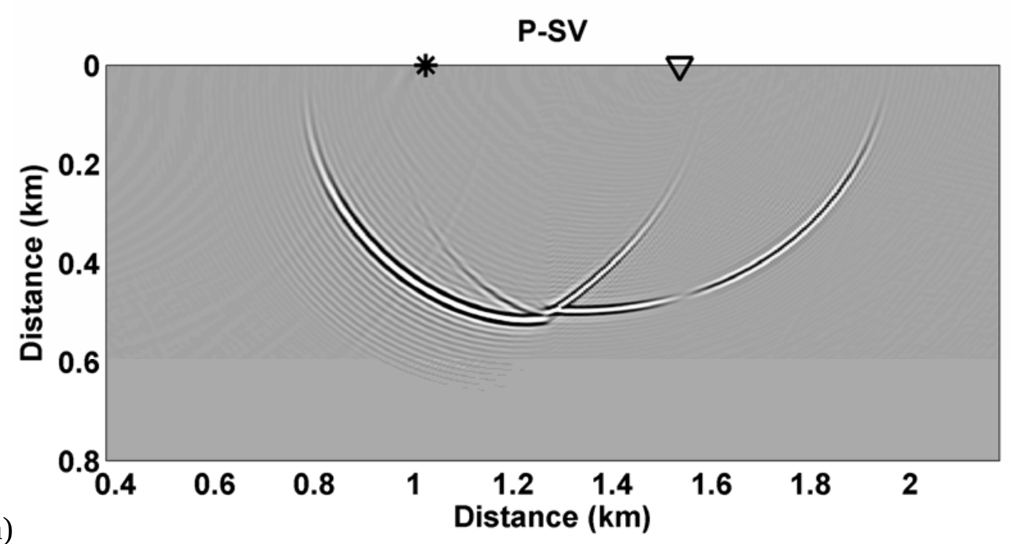

(a)

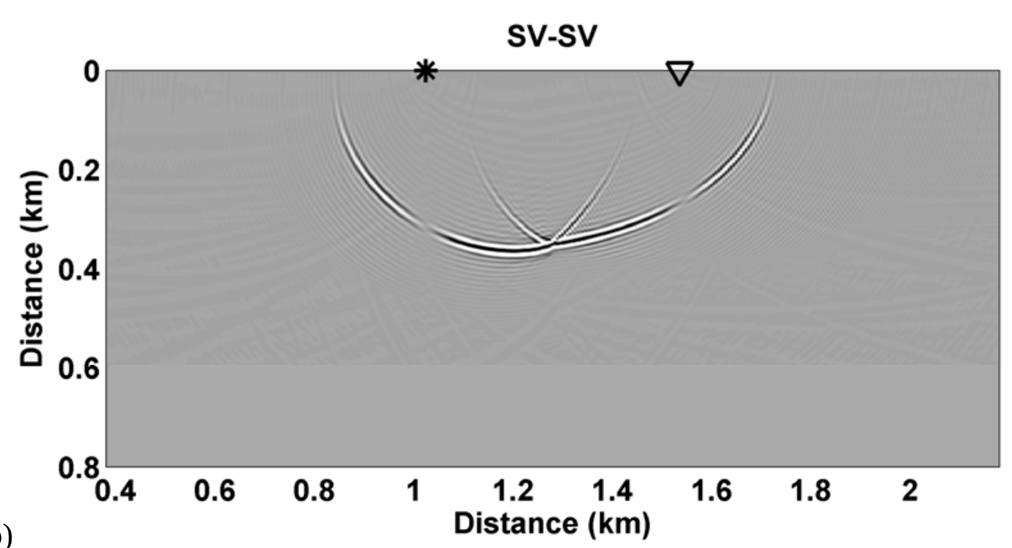

(b)

Figure 5.12. Impulse responses using only a single reference velocity with a split-step correction, for medium in Figure 5.6. Compare with PSPI using two reference velocities Figure 5.7 and Figure 5.8. The reference velocity used for the split-step correction is the harmonic mean of the two velocities. Split-step correction is accurate for small dips.

5.3.3 HTI homogeneous model, with symmetry axis parallel to line direction

The introduction of HTI anisotropy creates a number of effects. These will now be now examined.

First, the case where the axis of symmetry is aligned with the propagation plane is considered, as shown in Figure 5.13. This means that we can think in terms of an S2-mode which is equivalent to a (quasi-)[1] SV-mode, and an S1-mode which is equivalent to a SH-mode. If the axis of symmetry was orthogonal to the plane of propagation, then these identifications would be reversed.

Figure 5.14 shows the impulse response for a vertical source and vertical receiver in an HTI medium with parameters of Table 2.1. The most significant changes from the isotropic impulse response is the non-elliptical shape of the pure mode responses [(a) and (d)], and the presence of triplications in the shear-waves [(b), (c) and (d)]. Triplications arise whenever the phase-slowness surface has a concavity. This is the case for SV-mode propagation in the plane containing the symmetry axis, using the parameters of Table 2.1, as can be seen from Figure 2.3. The subject of phase-slowness concavity and corresponding triplication in the impulse response is explored in Dellinger's (1991) Ph.D. thesis, Appendix B.

For a symmetry axis parallel to propagation direction, the HTI impulse response shares many attributes with the isotropic case. For example, the reasoning illustrated in Figure 5.1 is still valid, and polarity reversals occur at the shot or receiver coordinate associated with down-going or up-going SV-wave modes respectively [Figure 5.14 (b)-(d)]. As for the isotropic and VTI cases, for this choice of HTI symmetry axis, the SH-wave mode is not coupled to P- or SV-wave modes. An impulse polarized within the propagation plane generates only P- and SV-wave modes.[2] To generate a pure SH-wave, an impulse on the Y- (crossline-) source and receiver component is needed. Figure 5.15 illustrates the resulting SH-wave impulse response, using the same parameters as for

---

[1] The term quasi- is technically necessary for anisotropic media, as discussed in section 1.2.2. However, for brevity it will be omitted in the remainder of this chapter.
[2] In section 5.3.4, it will be seen that this behaviour is not true for an arbitrarily oriented symmetry axis.

Figure 5.14. Unlike the SV-wave, there are no concavities in the SH-wave phase velocity, and there are therefore no triplications present in the impulse response.

5.3.4 HTI homogeneous model, with symmetry axis at 45° to line direction

Let us now consider the case of an HTI medium with a symmetry axis rotated in the horizontal plane by 45°, relative to the line direction, as depicted in Figure 5.16.
The resulting impulse response is shown in Figure 5.17, once again using vertical source and receiver components. Only the P-wave mode source responses are shown. In contrast to the previous example, both S1 and S2 responses are generated from the P-wave mode source, due to the coupling between all three modes. The S1-P and S2-P images (not shown) are related to the P-S1 (b) and P-S2 (c) responses respectively by symmetry about the midpoint.

Consideration of the corresponding phase velocity curves in Figure 2.4 indicates that there are no concavities in either S1 or S2 phase slowness curves. Consequently, no triplications are observed in the impulse response. See Dellinger's (1991) Ph.D. thesis for a very thorough illustrated analysis of the relationship between the 3-dimensional anisotropic phase-slowness surfaces and the 2-dimensional slices through them, which determine the presence or absence of features such as triplications.

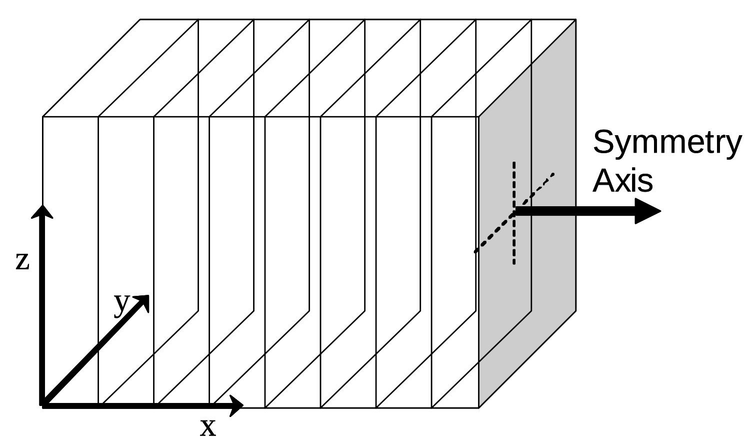

Figure 5.13. Symmetry axis oriented parallel to inline direction (plane of propagation).

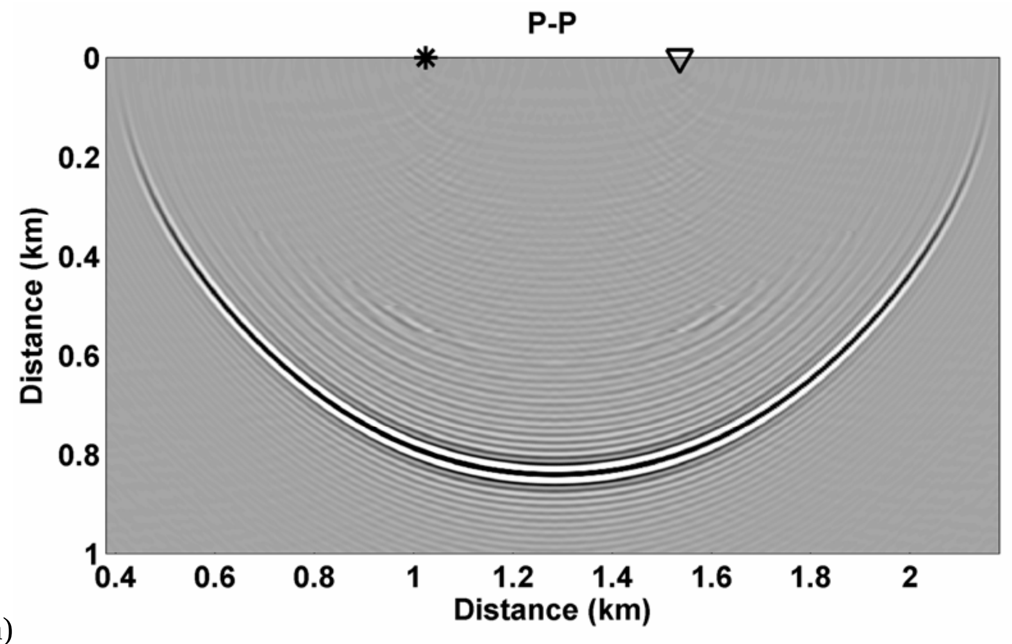

(a)

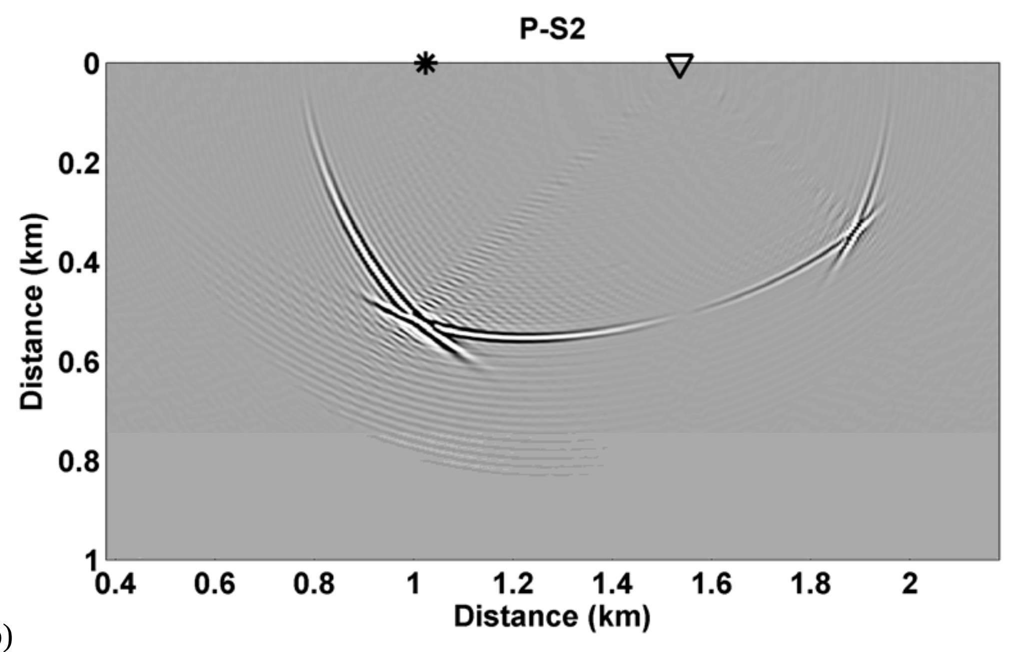

(b)

Figure 5.14. Impulse response, for HTI medium with stiffness coefficients given in Table 2.1, and symmetry axis parallel to line direction. The impulse is for a vertical source and vertical receiver component. Mode combinations P-P (a), P-S2 (b), S2-P(c) and S2-S2 (d) are shown. Since the plane of propagation contains the symmetry axis, the S2 mode could also be considered as an SV mode. Triplications occur due to VTI-type behaviour of phase velocity in symmetry axis plane.

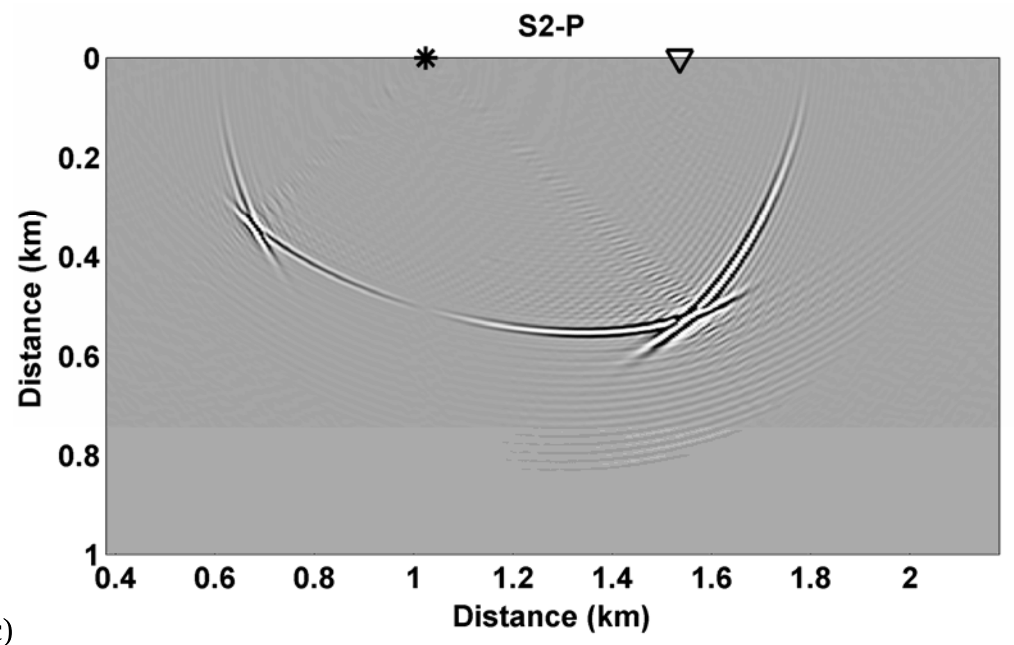

(c)

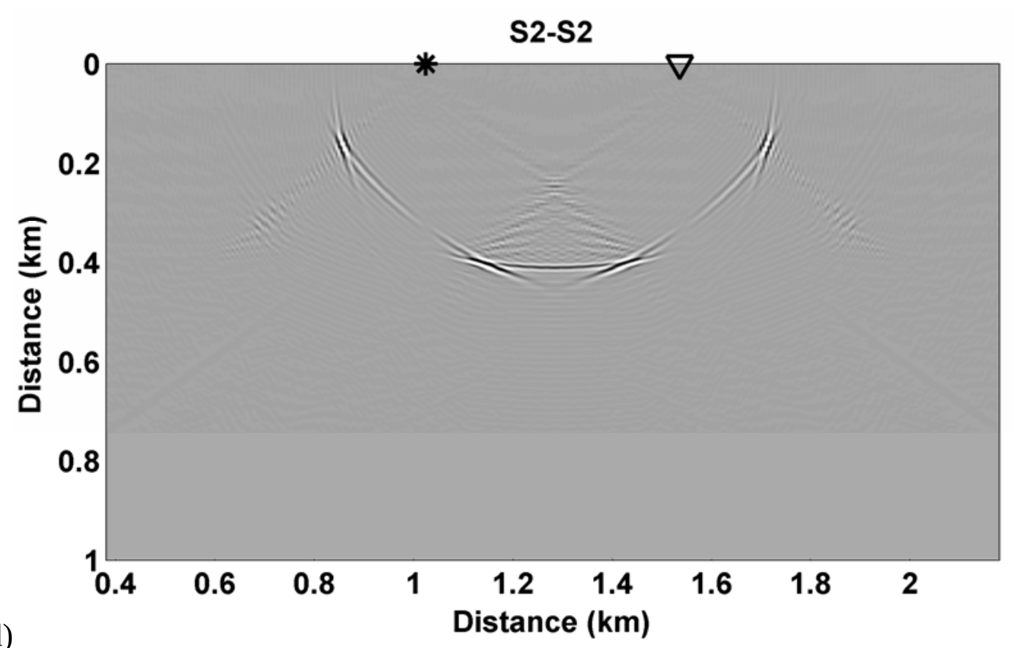

(d)

Figure 5.14 (continued)

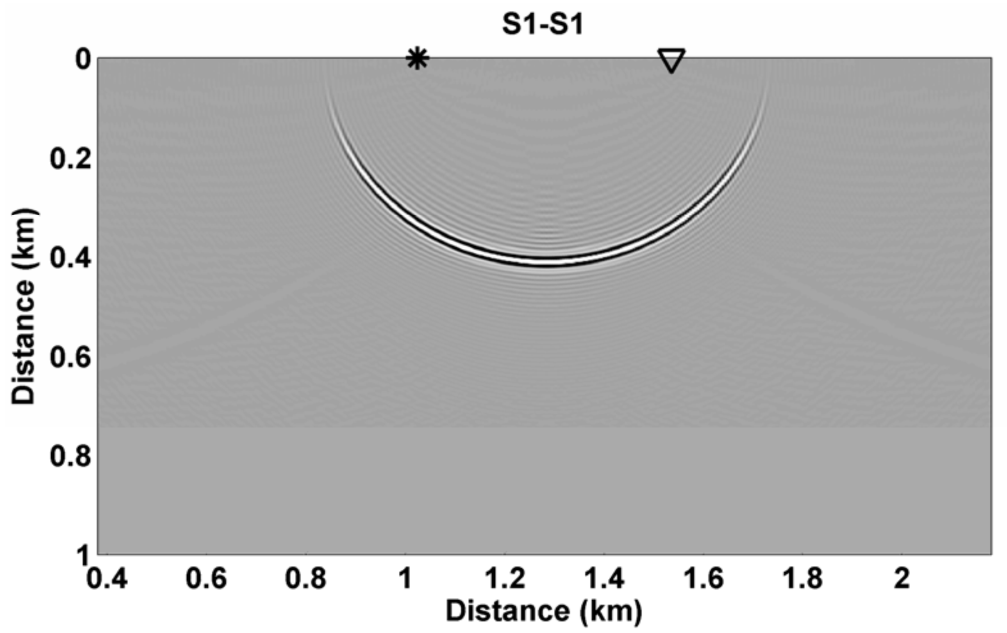

Figure 5.15. Impulse response, with parameters as in Figure 5.14 , but using crossline (Y) source and receiver components. Since the plane of propagation contains the symmetry axis, the S1 mode could also be considered as an SH mode, and is decoupled from the P and S1 modes.

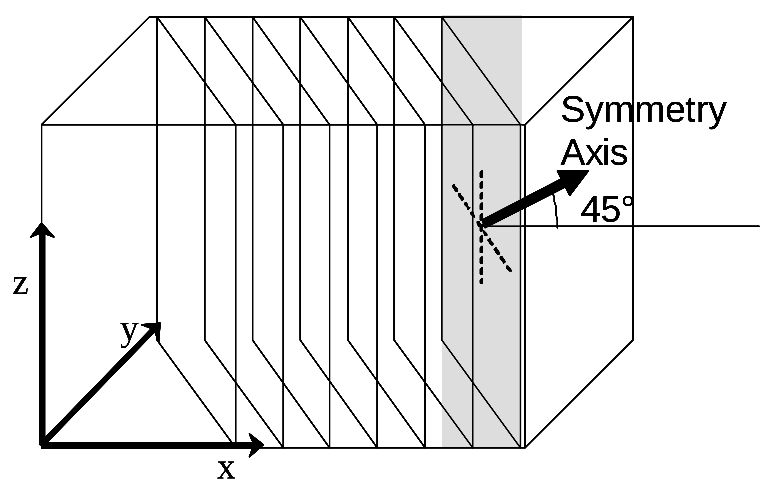

Figure 5.16. Symmetry axis oriented in the horizontal plane 45° from inline direction (propagation is parallel to the *x*-*z* plane).

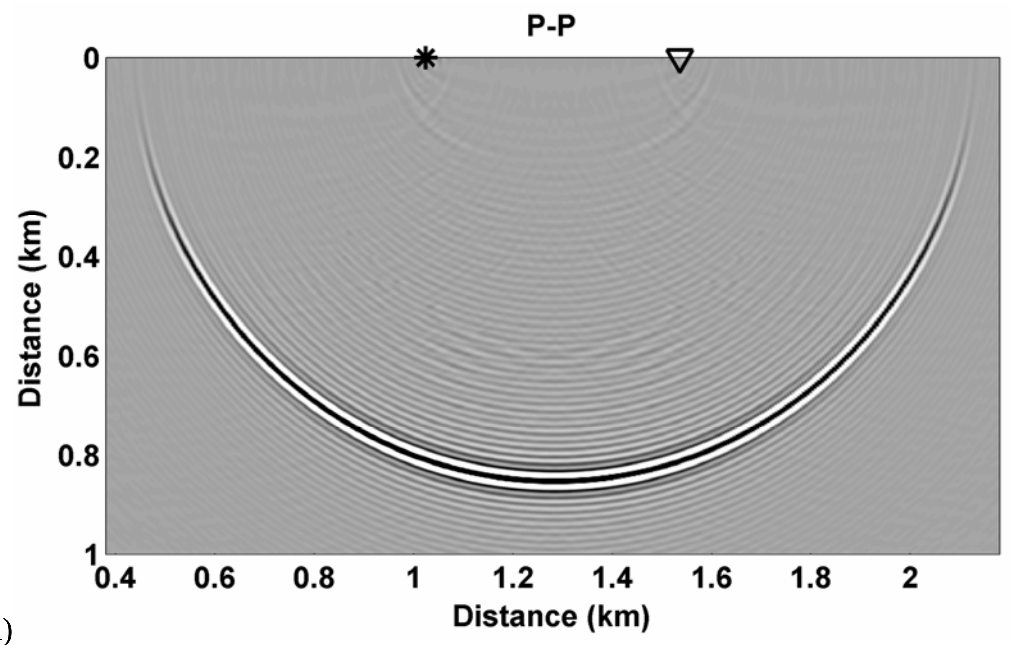

(a)

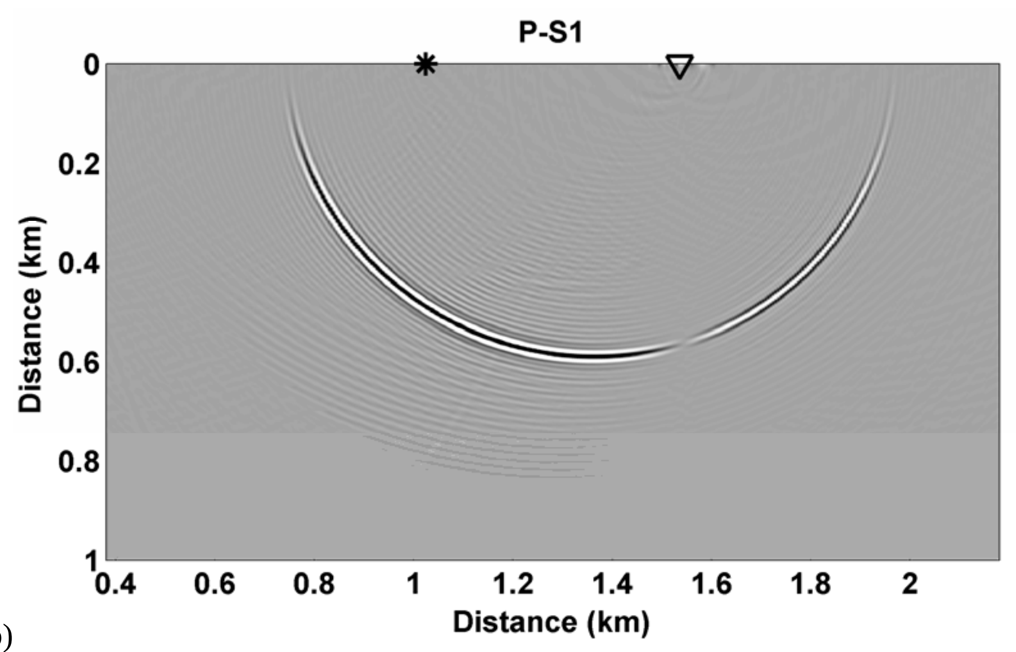

(b)

Figure 5.17. Impulse response, for HTI medium with stiffness coefficients given in Table 2.1, and symmetry axis rotated in the horizontal plane by 45° relative to line direction. The impulse is for a vertical source and vertical receiver component. Mode combinations P-P (a), P-S1 (b) and P-S2 (c) are shown.

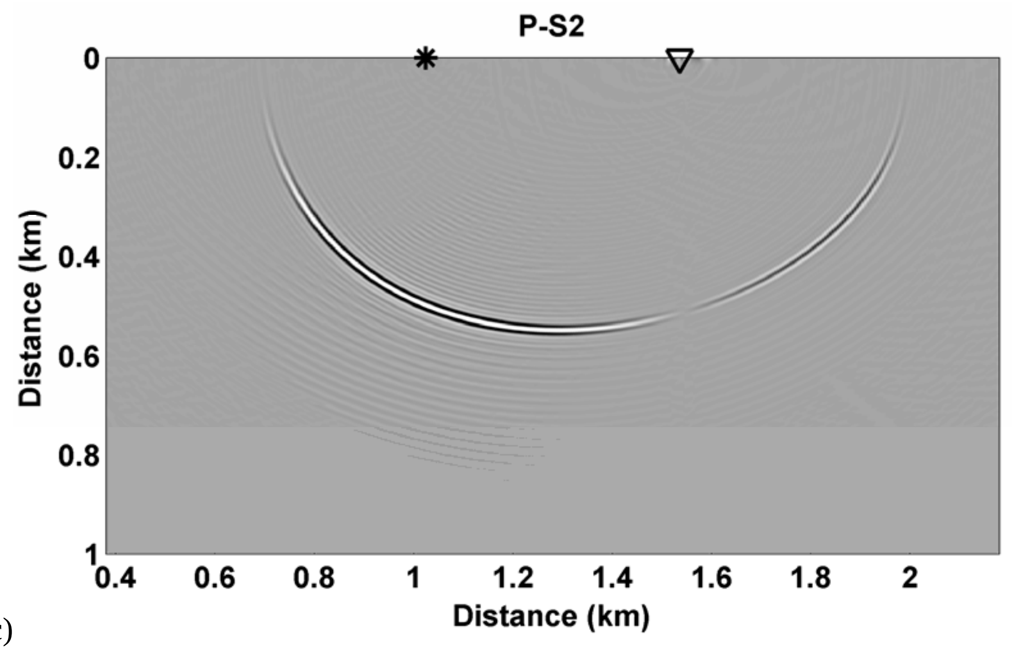

(c)

Figure 5.17 (continued)

5.4 Migration of HTI modeled data

The elastic shot-record migration developed in this chapter, based upon the PSPAW extrapolators of Chapter 4, has been tested on a synthetic HTI dataset. This was modelled using the pseudospectral technique, as used for the example in Chapter 2. A description of the 3-D pseudospectral modeling algorithm used is given in Bale (2002a; 2002b; 2003). A 2-D version of the code has been applied here.

The model and geometry for the test are shown in Figure 5.18.

5.4.1 Extrapolated wavefields

During migration, the extrapolated wavefields are extracted at several depth positions to illustrate the gradual resolution of the shear-wave splitting. The positions displayed are indicated by the dashed lines marked A, B and C, in Figure 5.18. Depth level A (500m) lies at the interface between the isotropic medium and the left side of the faulted HTI layer. Similarly depth level B lies at the upper interface for the middle portion of the HTI layer, and depth level C at the upper interface for the right side of the HTI layer.

Figure 5.19 shows the P-wave source wavefield (a), and the three modes, P, S1 and S2, of the receiver wavefield (b-d) at the depth step at A in Figure 5.18. The position of the downgoing source wavefield is indicated by the dashed line on each wavefield. Where this coincides with the downward extrapolated receiver wavefield, an image of the reflector at the left side of level A is formed. Interestingly, there is energy on both S1 and S2 wavefields corresponding to this reflection, but not on the P wavefield (b). This is a result of the relative asymmetry of the S-wave raypaths and the aperture of the receiver spread. Since the reflector is flat, the P-wave specular[1] reflection would take place at source-receiver midpoints. However none of the source-receiver midpoints for this source lie on the reflector. As pointed out by Bleistein et al., (2001, p.152), non-specular energy is generated from an interface, but is significantly lower in amplitude (in the high frequency limit) than the specular ray. On the other hand P-S wave conversions have asymmetric raypaths which permit specular reflections on this reflector for the source position and some of the left-most receivers.

To see the impact of progressing from the isotropic layer into the HTI layer, the wavefield is plotted at each horizontal boundary of this layer. This is done for two depth steps: one just on the interface, and one after transmission through it. For example, Figure 5.19 shows the entire wavefield just above level A (i.e. still in the isotropic layer), whereas Figure 5.20 shows the shear-wave parts of the wavefield just after crossing level A, such that the left-hand side of the wavefield has entered the HTI medium. Similarly Figure 5.21 and Figure 5.22 show the wavefield just above and just below level B respectively. The size of the depth step is 10m. Since the difference is only a single depth step, the kinematic effects are minor. However, careful comparison of the S1 and S2 wavefields on either side of each boundary shows the impact of the repolarization steps in the elastic extrapolators.

[1] According to Webster's online dictionary specular means "Capable of reflecting light like a mirror". It is used in geometrical optics and in seismology to specify those ray-paths which have incident and reflection angles which obey Snell's law at the reflector. For P-P reflections this implies that the angle of incidence is equal to the angle of reflection. For P-S reflections, the S-wave ray generally has an angle which is less than the P-wave angle, leading to a reflection closer to the receiver for a flat reflector.

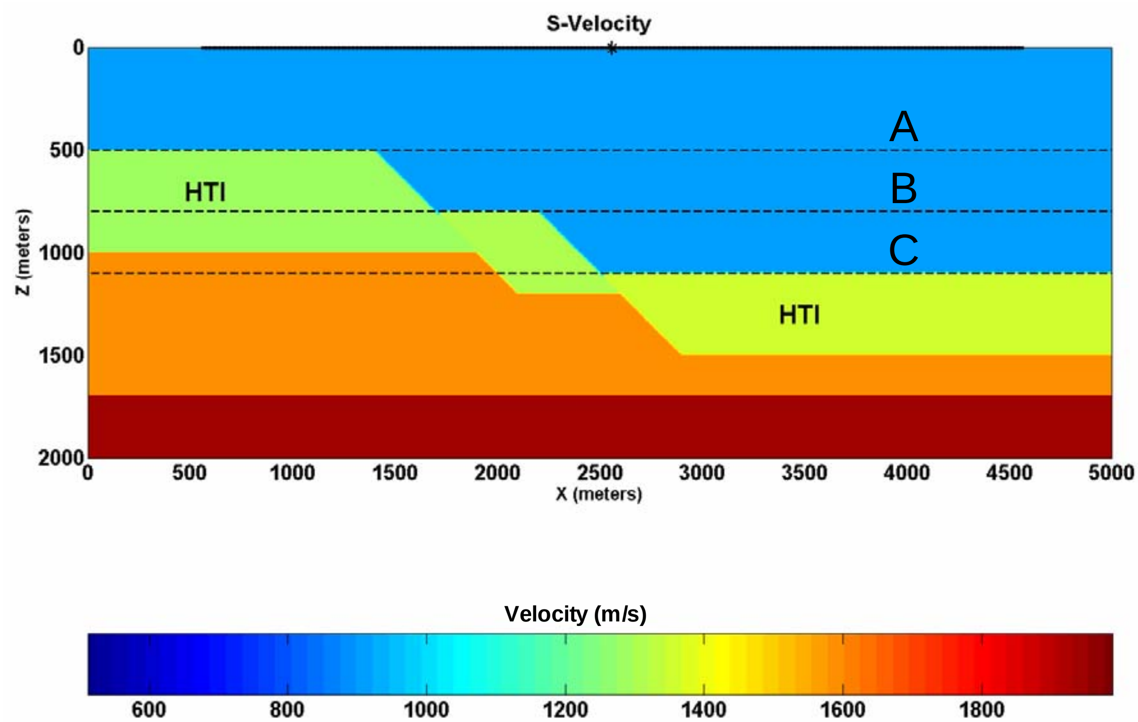

Figure 5.18. Model for synthetic tests. Top (blue) and bottom two (orange and red) layers are isotropic. Middle, faulted layer is HTI, with parameters based on those in Table 2.1, but with spatial variation of density: the left block has $\rho = 2300 kg/m^3$; the middle block has $\rho = 2200 kg/m^3$ and the right block $\rho = 2100 kg/m^3$. The receiver line, extending from 560m to 4560m with 10m receiver spacing, is indicated by black dots on the surface. Shot positions range from 160m to 4960m, and have a 10m interval. The shot at 2560m is indicated by the asterisk. The extrapolated wavefield from this shot is examined, in subsequent figures. The three dashed horizontal lines labelled A, B and C, are the depth levels referenced in later figures.

The shear-wave arrivals measured at the surface are complicated due to the shear-wave splitting in the HTI layer. As the downward extrapolation proceeds, these wavefields become gradually simplified as the rotation implicit in the operator isolates the S1 and S2 arrivals onto their respective components (Figure 5.20, Figure 5.22). The black solid arrows indicate shear-wave arrivals of interest. Compare the top arrows (at approximately 1.3 seconds) for the wavefield just *above* level A [Figure 5.19(c), (d)] with the corresponding wavefield just *below* level A [Figure 5.20(a), (b)]. These arrows indicate energy which has been converted to shear waves at the bottom of the left block in the faulted layer. Where double S-wave events are observable in both of the first two sections, these have been resolved into single events on the S1 and S2 sections, in Figure

5.20. Similarly the bottom arrows in these two figures indicate energy reflected from the reflector at 1700m depth, which has become split on passage through the left block of the faulted layer. Once again, the double events on the section just above level A are resolved into single events on the S1 and S2 section, after crossing the boundary.

Figure 5.21 and Figure 5.22 show the same effect on the split shear-wave energy for the middle block of the faulted layer, by examining the wavefield just above and just below level B.

Finally, the shear-wave sections immediately above and below level C are shown in Figure 5.23 and Figure 5.24, respectively. These show the same effect on the shear waves which have propagated through the right-hand block of the HTI faulted layer.

5.4.2 Migration images

Figure 5.25 illustrates the migrated images that result from application of the elastic shot record migration algorithm on the HTI modeled data. The correlation imaging condition has been used. Although the deconvolution condition is theoretically superior for amplitude recovery, it was found to generate unwanted artifacts in the shallow part of the section. The elastic migration used the exact model shown in Figure 5.18, with a depth step of 10m and repolarization (composition-decomposition) steps every 100m.

In addition to the P-P image in (a), two separate P-S images are generated, one for the fast (S1) mode and one for the slow (S2) mode. Since the model contains both isotropic and HTI layers, it is necessary to define a convention for assigning energy to the shear-wave images when no S1 and S2 waves are naturally defined. The convention adopted here is that for isotropic layers, the SV mode is assigned to the S2 section. This is a natural identification for cases in which the HTI symmetry axis is in the plane of propagation, but is otherwise arbitrary. Based upon this convention, the S1 mode only responds to the top and bottom of the HTI layer, and not to any other interfaces. This explains the absence of the flat basement reflector in Figure 5.25(b). Also, as observed in Figure 2.4 (which uses the same model as the HTI layer of this example), the S2 polarization rotates to gradually become orthogonal to the plane of propagation as the

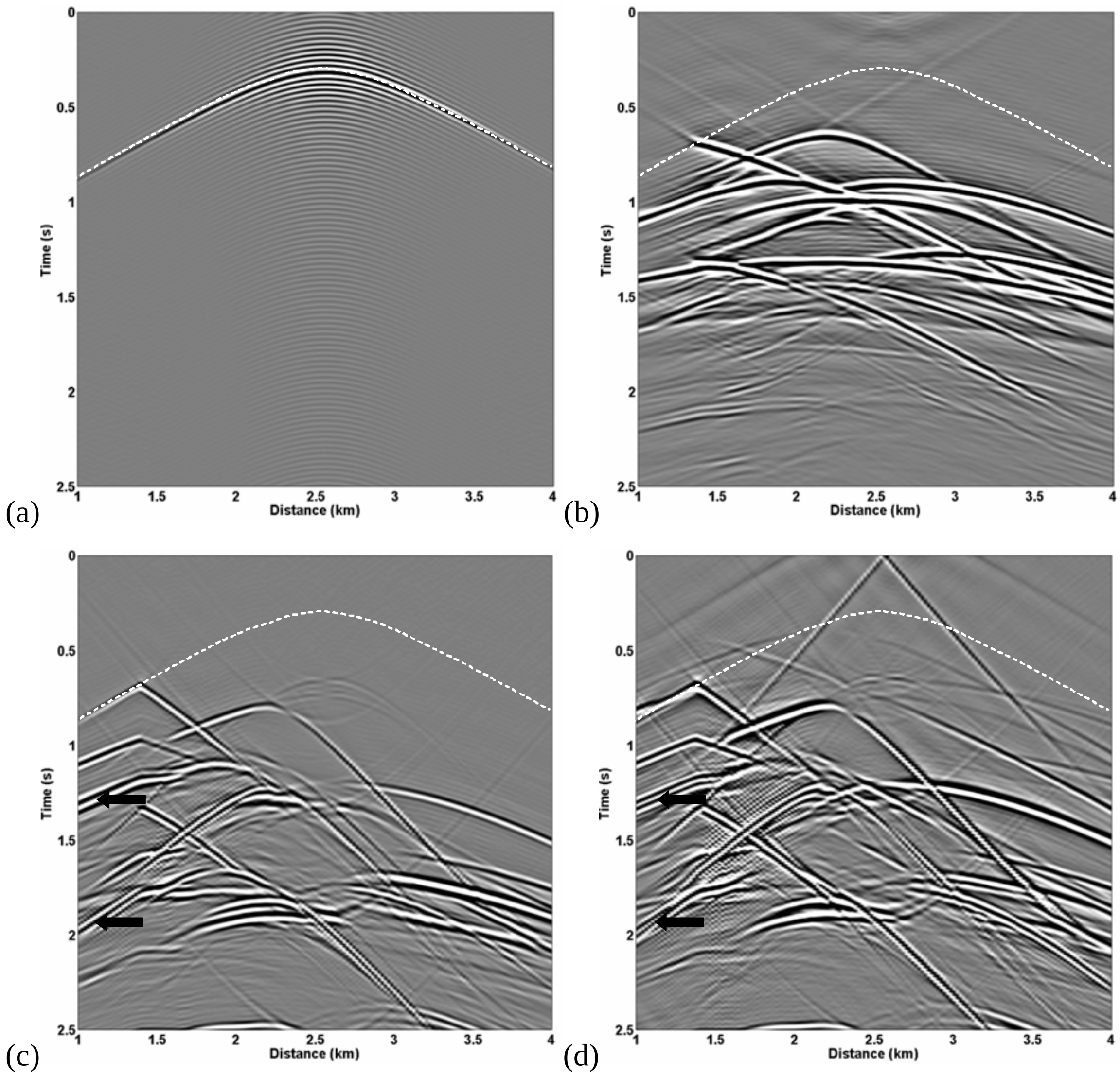

Figure 5.19. Wavefield immediately *above* level A: (a) downward extrapolated P-wave source wavefield; (b) downward extrapolated P-wave receiver wavefield; (c) downward extrapolated S1 receiver wavefield; (d) downward extrapolated S2 receiver wavefield. White dashed line shows position of source wavefield, coincident with receiver wavefield for top of HTI layer at left side. The black arrows indicate split shear-wave arrivals, arising from transmission through left-hand block of HTI layer. The S1 and S2 arrivals are represented in the isotropic coordinate frame of the first layer, and are not properly resolved.

incidence angle increases. This observation explains the relative weakness of the dipping structure on P-S2 (c) compared to P-S1 (a). Evidence of the stair-step approximation in the repolarization step can also be observed as artifacts on the shear-wave images. A satisfactory solution to this problem has not yet been discovered.

For comparison, Figure 5.26 shows the result of migrating the same anisotropic data using isotropic migration. The velocities used are the vertical P-wave velocity and the vertical fast shear wave (S1) velocity. The P-P image, in (a), shows some indication of defocusing. Overall, this image is comparable to the HTI migrated image of Figure 5.25(a). However, the P-S2 image, in (b), suffers from the presence of the split shear waves which have not been isolated, in contrast to the results in Figure 5.25(b) and Figure 5.25(c). In Figure 5.26, there is no P-S1 image, since this corresponds to the non-existent crossline (or SH) polarization with the convention used here.

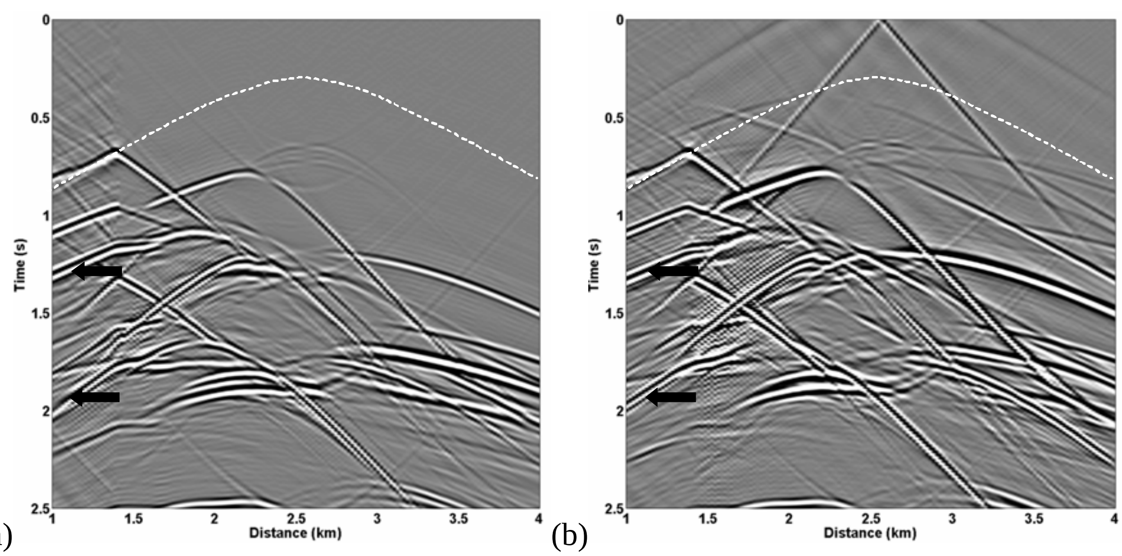

(a) (b)

Figure 5.20. Shear-wave wavefield immediately *below* level A: (a) downward extrapolated S1 receiver wavefield; (b) downward extrapolated S2 receiver wavefield. Compare with Figure 5.19 (c) and (d), respectively. The S1 and S2 arrivals are now represented in the HTI coordinate frame of the faulted layer, and are resolved. Resulting simplification of the wavefield is especially apparent on the S2 wavefield at 1.3 seconds.

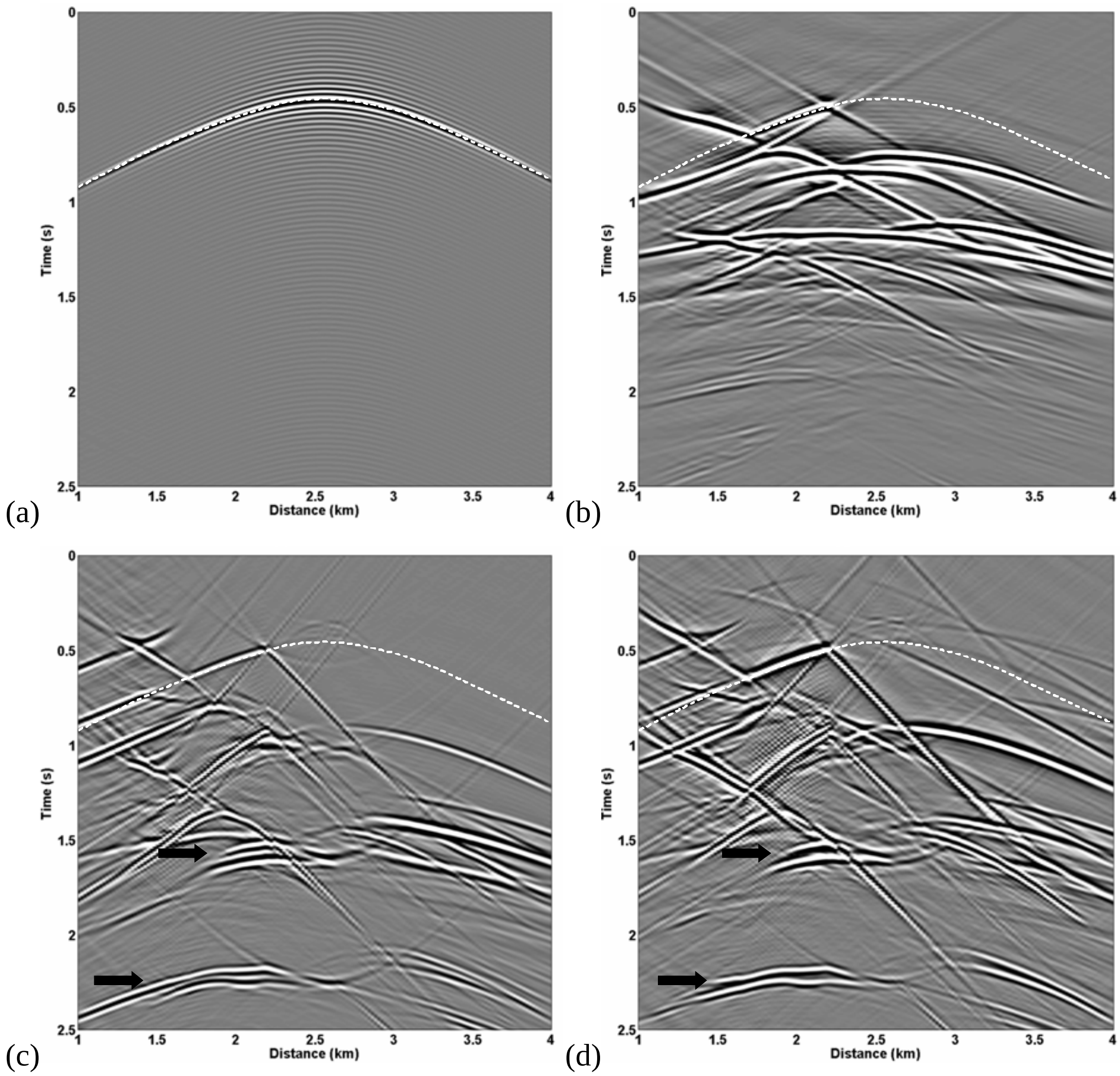

Figure 5.21. Wavefield immediately *above* level B: (a) downward extrapolated P-wave source wavefield; (b) downward extrapolated P-wave receiver wavefield; (c) downward extrapolated S1 receiver wavefield; (d) downward extrapolated S2 receiver wavefield. Position of source wavefield (white dashed line), is now coincident with receiver wavefield for top of HTI layer at middle block. Black arrows identify split shear-wave arrivals in middle block.

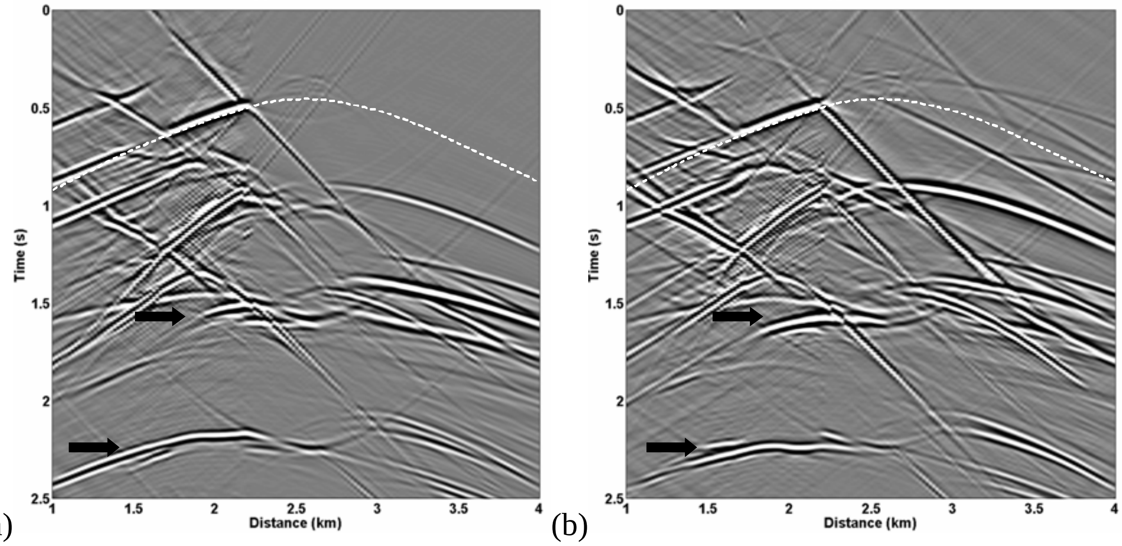

(a) (b)

Figure 5.22. Shear-wave wavefield immediately *below* level B. (a) downward extrapolated S1 receiver wavefield; (b) downward extrapolated S2 receiver wavefield. Compare with Figure 5.21 (c) and (d), respectively. The S1 and S2 arrivals in middle block are now resolved, resulting in further simplification of the wavefield.

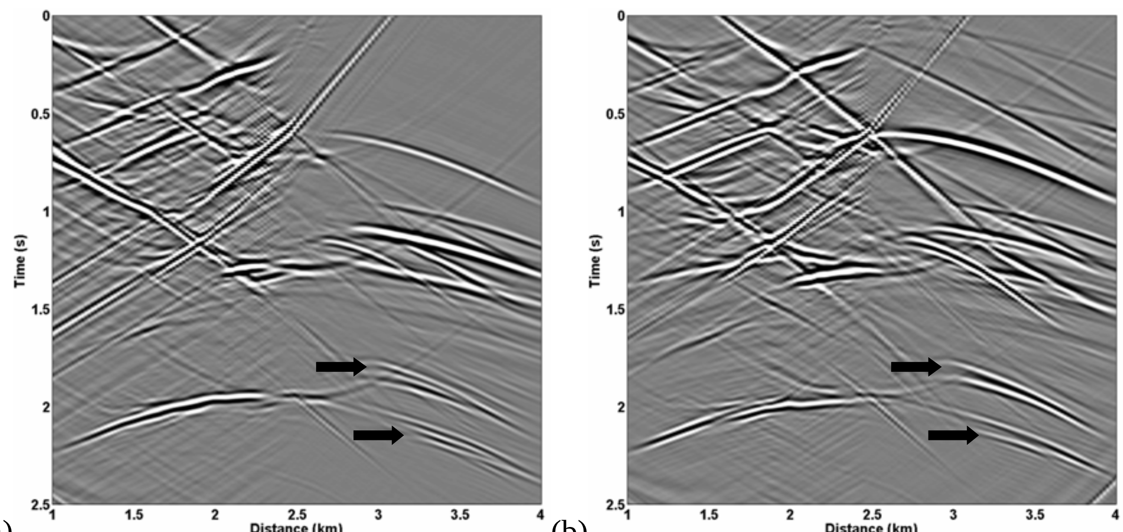

(a) (b)

Figure 5.23. Shear-wave wavefield immediately *above* level C. (a) downward extrapolated S1 receiver wavefield; (b) downward extrapolated S2 receiver wavefield. Black arrows identify shear-wave split arrivals in right-hand block.

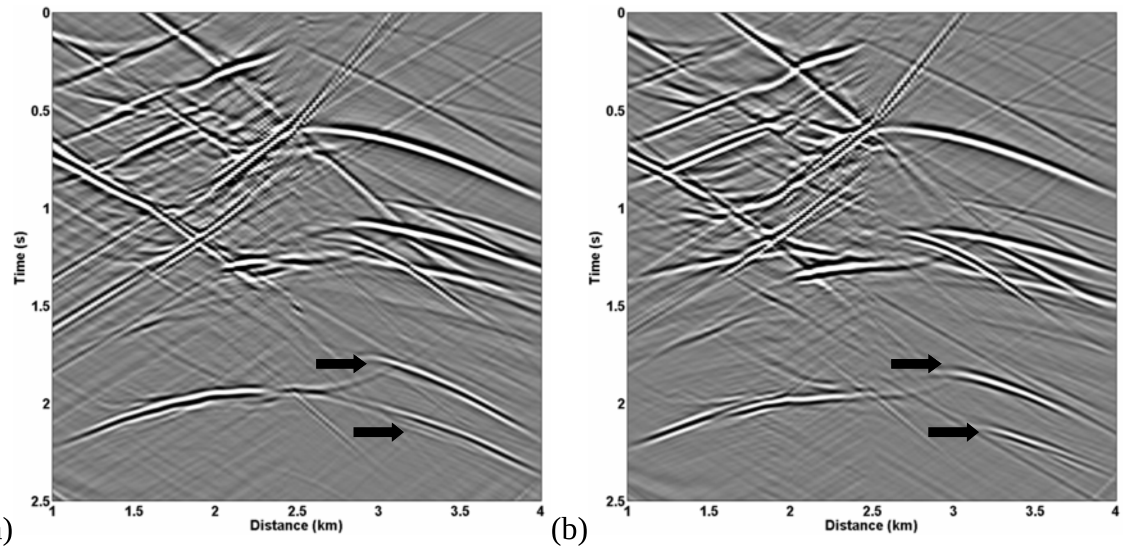

(a) (b)

Figure 5.24. Shear-wave wavefield immediately *above* level C. (a) downward extrapolated S1 receiver wavefield; (b) downward extrapolated S2 receiver wavefield. Compare with Figure 5.23.

5.5 Chapter summary

This chapter has described the construction of a shot record migration algorithm from the elastic extrapolators derived in previous chapters, utilizing either a correlation or a deconvolution imaging condition. It can be argued theoretically, and observed, that the impulse responses display certain symmetries which depend on both data space (i.e. shot component and receiver component) and image space variables (i.e. down-going and up-going wave-modes). The principle of vector reciprocity can be used as a guide for interpreting these impulse responses.

The HTI migration operators depend on the relative orientation of the shot profile and the symmetry direction. When the shot direction is parallel to the symmetry plane, the P-SV (P-S2) impulse is decoupled from SH (S2). In general, however, the HTI impulse responses contain both P-S1 and P-S2 images. Also, triplications can occur if the anisotropic phase slowness surface has concavities.

The shot-record migration was applied to modeled data, where the model included a faulted HTI layer. Snapshots at strategic depths reveal the progress of the extrapolation, and how split shear waves are resolved into their appropriate images.

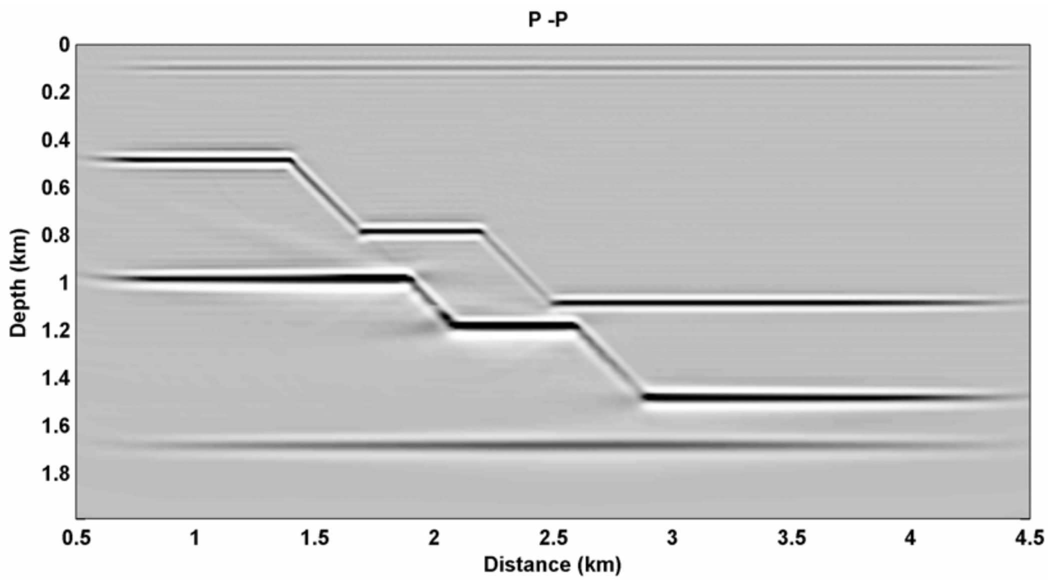

(a)

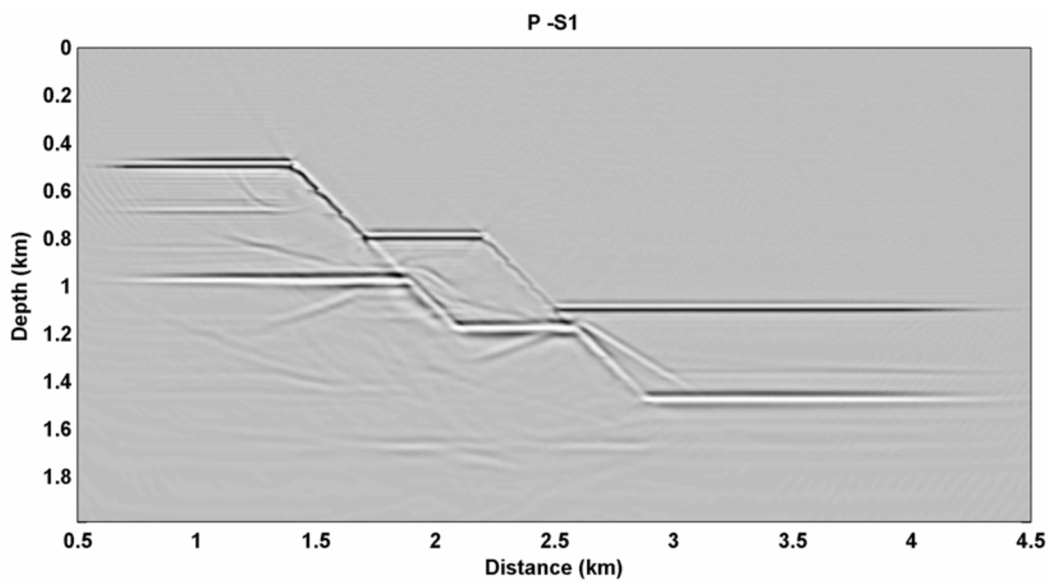

(b)

Figure 5.25. Migrated images from HTI model after HTI elastic migration, using the correlation imaging condition: (a) P-P image; (b) P-S1 image; (c) P-S2 image.

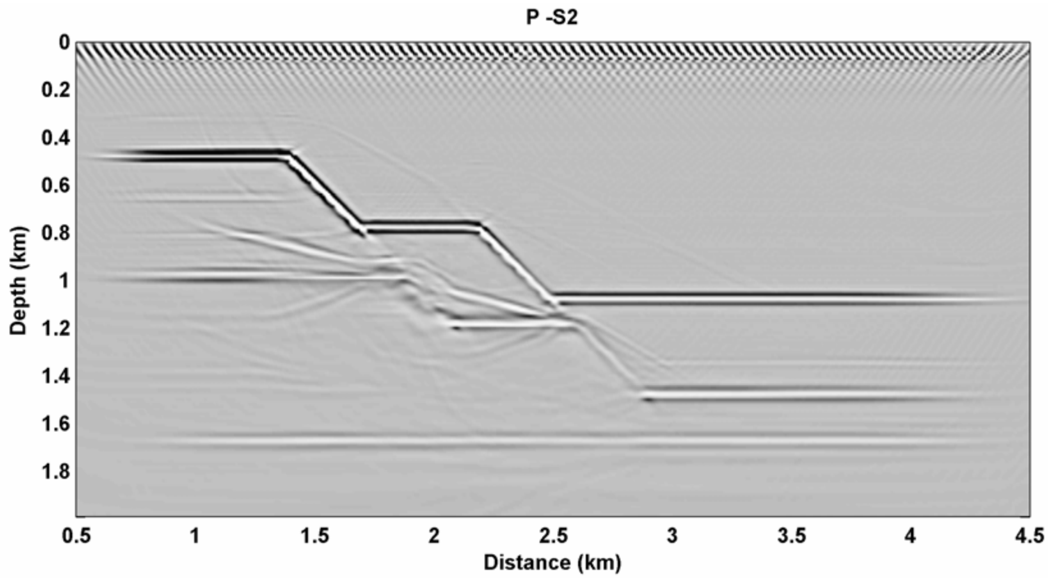

(c)

Figure 5.25 (continued)

The image obtained was acceptable, though includes some artifacts. These are believed to result from the coarse depth intervals used in the repolarization steps in the extrapolation. To overcome this problem, issues of efficiency and stability would need to be addressed. These are possible directions for future research. A comparison with isotropic migration applied on the same modeled data showed that the anisotropic migration is essential for proper resolution of the split shear-waves.

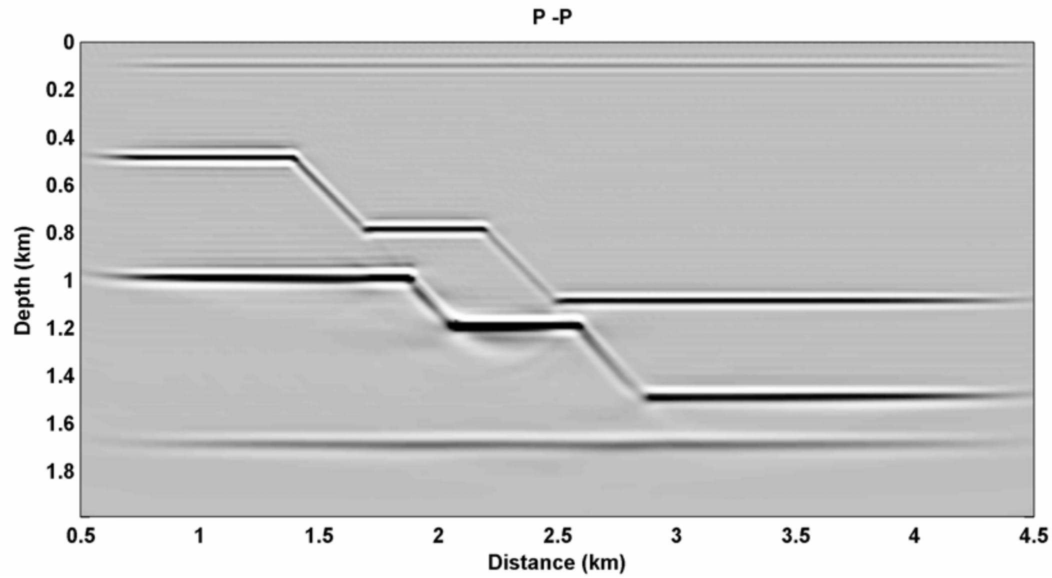

(a)

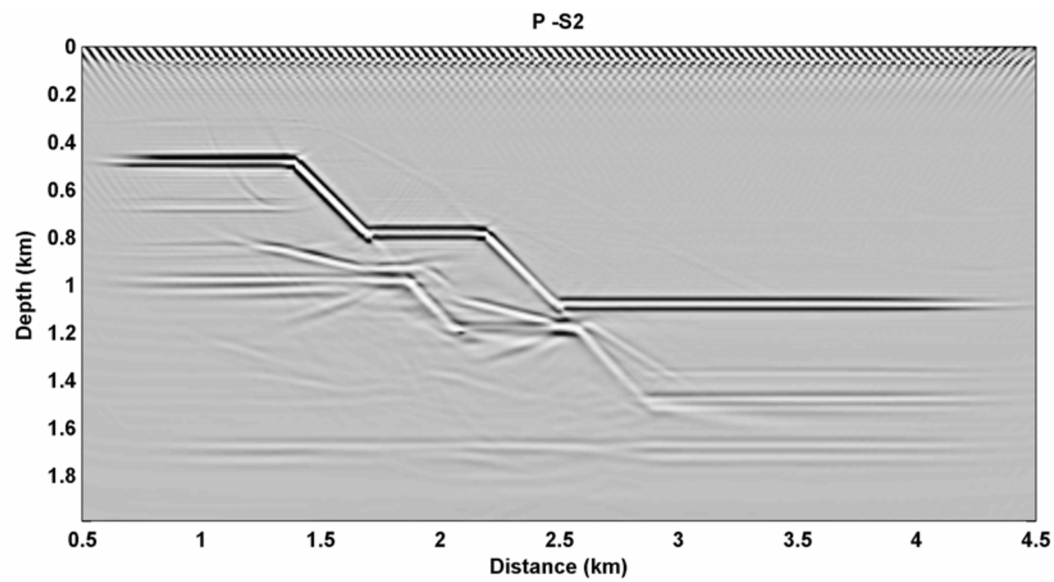

(b)

Figure 5.26. Migrated images from HTI model after isotropic elastic migration with vertical velocities, using the correlation imaging condition: (a) P-P image; (c) P-S2 image. The P-S1 image is zero, since the convention assumed here is that S1 corresponds to the crossline polarization when isotropic migration is performed. Compare with Figure 5.25(a) and (c).

CHAPTER SIX: ELASTIC SHOT-RECORD MIGRATION OF THE MARMOUSI-2 MODEL

6.1 Introduction

In this chapter the elastic shot-record migration is applied to the numerically modeled Marmousi-2 data. Unlike the model data presented in Chapter 5, these data are isotropic. On the other hand, they present a difficult imaging challenge due to the structural complexity of the model, resulting in rapid spatial variations in velocity, complex ray-paths, numerous multiples and mode conversions. Since the model is isotropic, the PSPI migration algorithm of section 4.4 may be applied.

6.1.1 Marmousi-2

The Marmousi-2 dataset was generated by the Allied Geophysical Laboratory at the University of Houston (Martin et al., 2002; Martin, 2004), using an elastic finite difference algorithm. It uses a model which is based upon the original acoustic Marmousi model (Versteeg, 1994). Like the original Marmousi model, Marmousi-2 is isotropic, yet highly heterogeneous. Unlike the original Marmousi model, it has several modifications and extensions. First, it has been extended laterally to a total line length of 17km. The extensions are less structurally complex than the central section, but include stratigraphic features and hydrocarbon accumulations. Second, it has been submerged under 450m of water and 50m of soft sediments. Finally, it is an elastic model with density and shear velocity determined from empirical rock physics equations (Greenburg and Castagna, 1992; Castagna et al., 1993).

The modelled data are very rich, including both OBC and towed streamer data.

The source signature used in the modelling was a zero-phase Ormsby (trapezoidal) wavelet 5-10Hz ramp at the low end and 60-80Hz ramp at the high end, resulting in a broader spectrum than the original Marmousi. The grid spacing used for the finite difference modelling was 1.25m, which allows adequate modelling of shear waves with velocities above 400m/s and frequencies below 65Hz without dispersion (Martin, 2004). However, the receiver spacing used for the OBC was 12.32m, which causes significant aliasing of the slower velocity arrivals.

In Martin's M.Sc. thesis (Martin, 2004) the streamer data from Marmousi-2 has been processed and imaged using different migration algorithms including a (scalar, acoustic) wave equation migration. Martin shows results both before and after application of a free surface multiple attenuation. The results after demultiple are excellent. However, no attempt to process or image the OBC data was made.

For the purposes of this dissertation, attention has been confined to the X and Z components of the OBC dataset. It is believed that this is first attempt to produce a migrated image from the OBC data.

Marmousi-2 poses contains distinctive challenges for elastic imaging. In particular, the central area, corresponding to the original model, poses considerable imaging problems. There are also very strong long period water layer multiples in the data.. These are absent from the original Marmousi data.

6.2 Migration

Before migration, the data were processed with a gapped deconvolution to partially attenuate the multiples. This gave some benefit in the stratigraphic region but not in the structural area. The direct arrival was muted.

The initial step in the migration is a single extrapolation step to redatum the shot from the sea surface to seabed, using the water velocity of 1500m/s. The shot-record elastic migration was then performed using the PSPI algorithm of section 4.4, using 9 reference operators, and including the split-step correction (Stoffa et al., 1990). The extrapolation step size used was 10m, with the PP and PS images interpolated to 2m sampling in depth, using the method of Fu (2004). The P- and S-wave velocity fields were smoothed before migration using a 100m Gaussian smoothing window in both *x* and *z* directions. The offset range included in the migration was -1000m to 1000m, and the migration aperture was extended by a further 500m on either side. The deconvolution imaging condition (section 5.2.1.2) has been used. No additional scaling has been applied.

6.2.1 Problems with boundary condition at ocean bottom

As was discussed in Chapter 2, (sections 2.3.7.1 and 2.3.7.2), there are two straightforward cases where a boundary condition is well defined. The first is where the data have been recorded on a free surface, in which case the boundary condition consists of setting the traction to zero. The second is applicable when the receivers are in an infinite half space, so that the wave propagation at the receiver level is purely up-going. In practice, this would be applicable if the data have been decomposed by a separate wavefield decomposition step, such as those proposed by Amundsen and Reitan (1995), Osen et al.(1999) and Schalkwijk et al. (2003). However, all of these methods require the presence of pressure data (i.e. hydrophones) at the seabed, which unfortunately has not been modelled in Marmousi-2. The results here were computed instead assuming a one-way wavefield, which results in an imperfect decomposition.

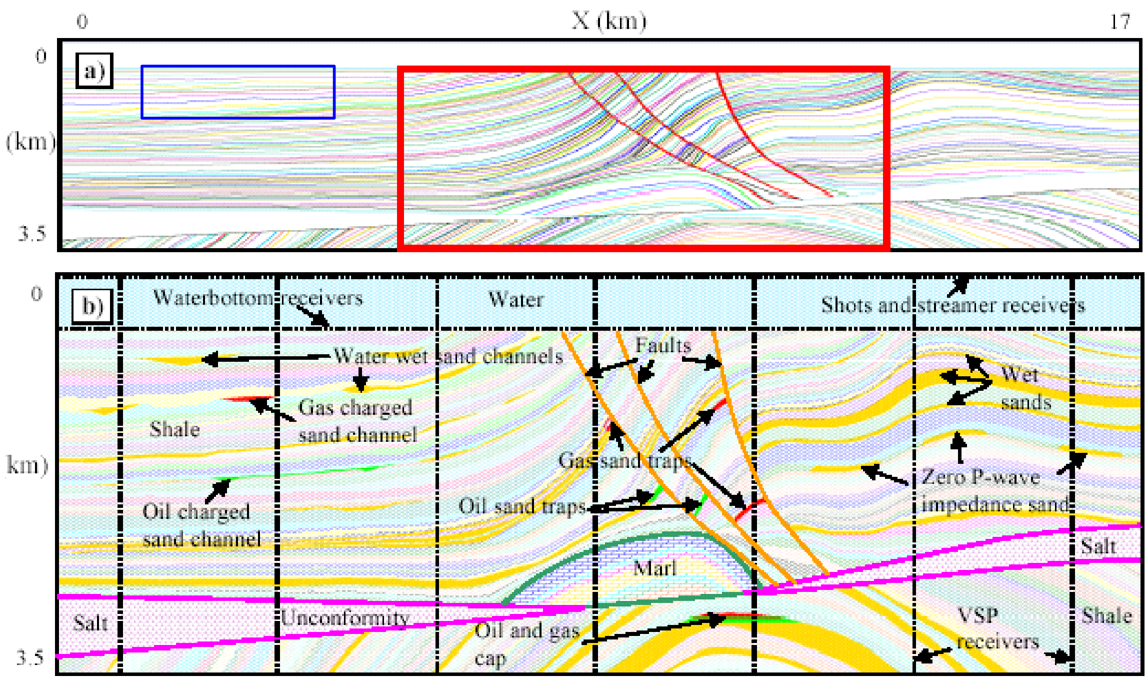

Figure 6.1. Geological model for Marmousi-2, based on the original Marmousi model with extensions. The extension of the Marmousi-2 model has been done in a manner consistent with the regional geology but with attempts to reduce the structural complexity away from the central area (a), thereby providing a dataset that possesses both simple and complex areas for AVO calibration. (used with permission).

6.2.2 Computational cost

The implementation of the elastic migration is a primarily in Matlab®, with C being used for the more compute intensive parts. The migration was run on 442 shots from Marmousi-2, with each shot having up to 164 receivers within 1km of offset. The trace length was 2500 time samples, and frequencies up to 90Hz were migrated. The extrapolation was for 300 depth steps at 10m sampling, then resampled to 2m. The migration was run on X and Z components to produce P-P and P-S images. The runtime was approximately 2 hours per shot on one node of a linux based cluster with clock speed 3GHz chip speed and 2GB RAM. Using 10 nodes, the entire dataset can be migrated in approximately 4 days.

For comparison, a scalar migration on the original Marmousi dataset with 200 depth steps, and trace length 500 samples, takes less than a minute per shot on the same architecture (Liu, 2005). The difference is explained in part by the longer trace and higher bandwidth for the elastic Marmousi, which results in about an order of magnitude higher cost. Some improvements to the cost might be achieved through tabulation of the phase shift and composition-decomposition operators. For optimal performance, complete recoding of the algorithm in C or Fortran is probably desirable.

6.3 Results

The results presented here focus on two parts of the model. First, the migration results from the structurally less complex area [indicated by the blue rectangle in Figure 5.6(a)] are considered. This is referred to as the stratigraphic area. Second, results from the central, structurally complex, area [indicated by the red rectangle in Figure 5.6(b)], which corresponds (approximately) to the original Marmousi model, are examined.

6.3.1 Stratigraphic area

Figure 6.2 shows the P- and S-wave impedance sections from a shallow, stratigraphic portion of the model, the area indicated by the blue rectangle in Figure 5.6(a). This area is considerably less structured than the central area. Note that the horizontal scale in Figure 6.2 has been compressed for display.

Figure 6.3 shows the corresponding P-P and P-S migrated images. As seen in Figure 6.3(b), the shallow P-S imaging is remarkable, displaying clear resolution advantages over the equivalent P-P section in Figure 6.3(a). This is anticipated from theory, due to the slower S-wave velocities, but is striking nonetheless.

Also of interest are the markedly different responses to the gas sand at 0.6km depth to the left of the image. Significantly, the ability of elastic wave data to provide discrimination between lithology and fluid is exhibited clearly in this example. The P waves respond to changes in both the rock matrix and the fluid fill, and are particularly responsive to gas which has a low velocity and density. In contrast, the shear waves are insensitive to the fluid fill, and so do not respond to the presence of gas.

At present, the over-migration of the P-P gas sand (evidenced by the "smile" which extends above the sand) is not understood. One possible reason would be an error in the seabed depth. The best fitting seabed depth was determined by comparing the extrapolated source wavefield at the seabed with the recorded first arrival after decomposition. Using 500m as the depth give the best matching result, shown in Figure 6.4. This differs from the stated depth of 450m. However, migration with either 450m or 500m as the seabed depth gives similar overmigration artefacts. The results here were produced using 500m.

Another possibility would be an incorrect velocity model. However, unless this was a localized effect, such errors should lead to overmigration everywhere. There does indeed appear to be other suggestions of overmigration in these sections, but not in the central complex area (section 6.3.2).

Finally, the reader should be aware that the effect is exaggerated by the very high amplitudes of the P-P response to the sand, when this is compared to the relatively low amplitude response on the P-S image. The P-P image is plotted with 1/10th of the scaling in Figure 6.5, for comparison.

6.3.2 Structural area

Figure 6.6 shows the P-wave (a) and S-wave (b) impedance sections in the central section, roughly equivalent to the original Marmousi area. The water layer is not shown.

Figure 6.7 shows the P-P and P-S migrated images for this section of the model. Both images suffer somewhat from the presence of water layer multiples, and some aliasing artifacts, as will be discussed in section 6.4.1. In this regard the P-P image is more affected by the multiples. Generally speaking, the P-P image is fairly well defined, whereas the P-S image is less clearly defined and is noisier. The reasons for this are discussed in section 6.4.

In order to assess image fidelity, parts of the PP and PS images have been redisplayed using variable area wiggle plots in Figure 6.8. The PP detailed images are superimposed on P-wave (i.e. acoustic) impedance sections, and the PS detailed images are superimposed on S-wave impedance sections. Note that the colour table is varied for the last two images [Figure 6.8 (e) and (f)], in order to clarify the structure of the model. When this is done, there is seen to be very good agreement with the image and the impedance boundaries for the PP sections, and reasonable agreement for the PS sections. However, it is noticeable that the PS fidelity deteriorates with increasing depth to a greater extent than does the PP fidelity.

Additionally, in Figure 6.8 (a) and (c), the locations of two gas-sand traps are indicated (compare with Figure 5.6). This is of interest because they give a definite response on the PP images, but are not seen on the PS images. As was mentioned previously, this is due to the fact that P-waves respond to acoustic contrasts associated with fluids, whereas S-waves only measure changes in the rock matrix.

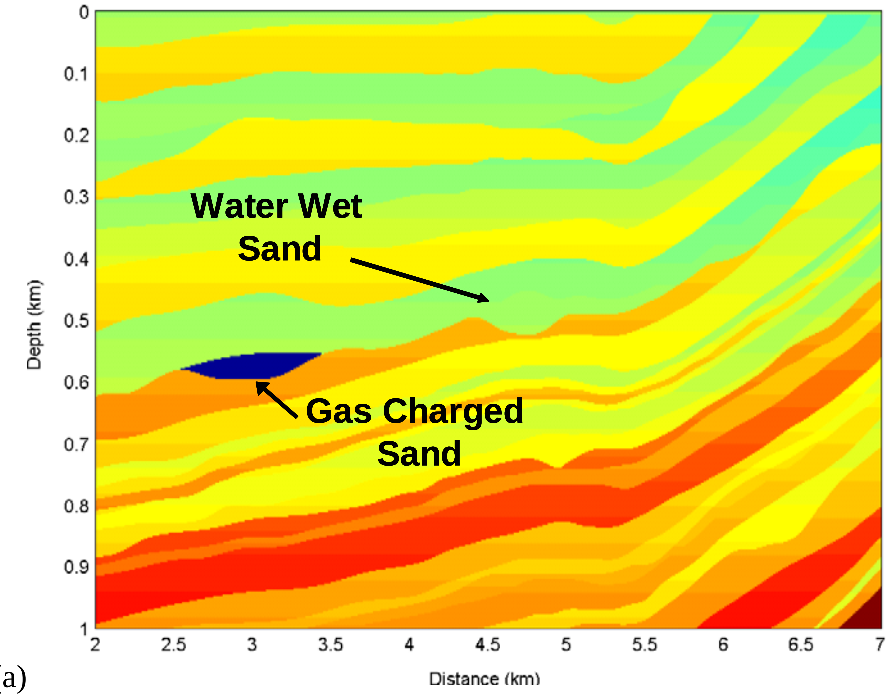

(a)

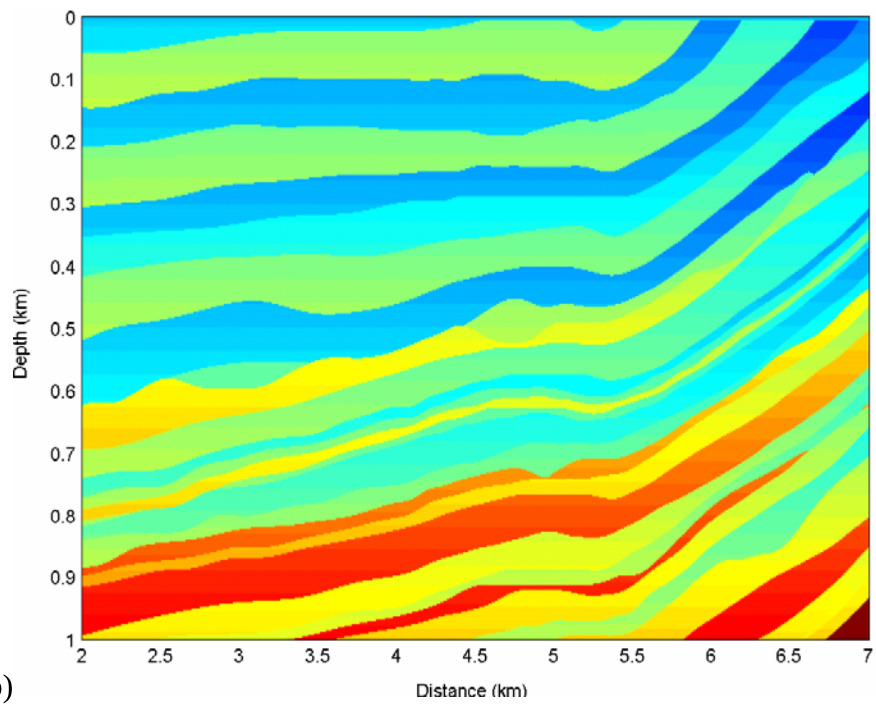

(b)

Figure 6.2. Marmousi-2 elastic model, showing (a) acoustic (i.e. P-wave) impedance and (b) S-wave impedance. This area corresponds to a shallow section on the left of the main structural area. The horizontal axis has been compressed relative to the vertical, for display purposes. The gas sand is clearly identified by its low P-wave impedance compared to local sediments.

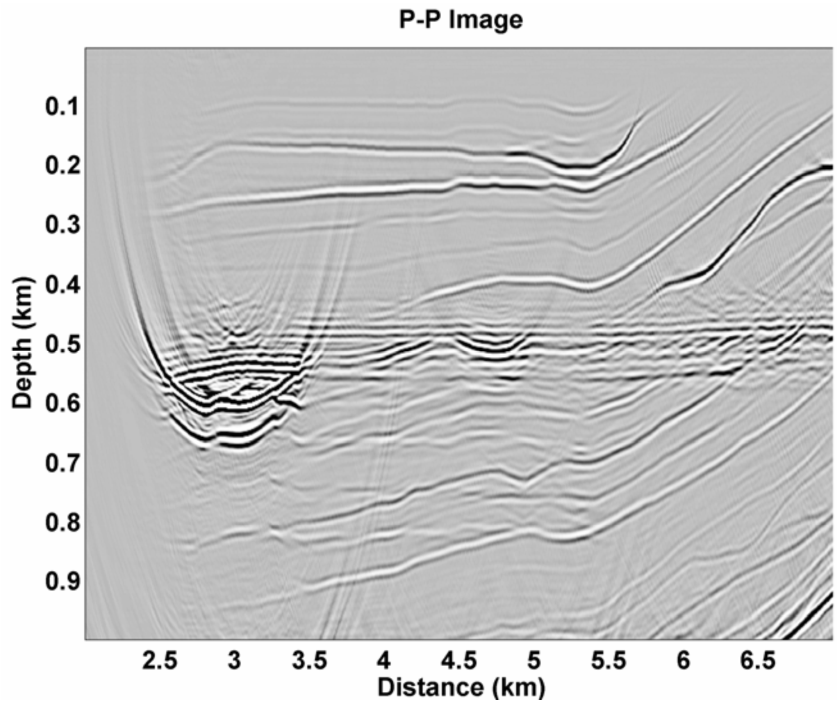

(a)

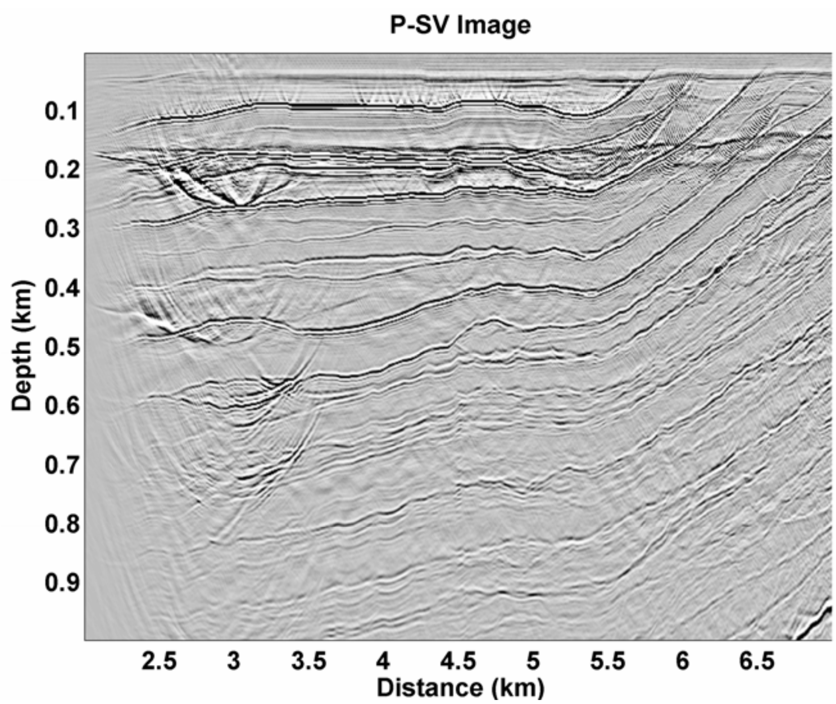

(b)

Figure 6.3. Migrated images: (a) P-P and (b) P-S of X and Z component data from elastic modeling. Area shown is that of model in Figure 6.2. Note the superior resolution of the P-S image, and the significantly weaker response to the gas sand. This is an example of fluid-lithology discrimination with elastic waves.

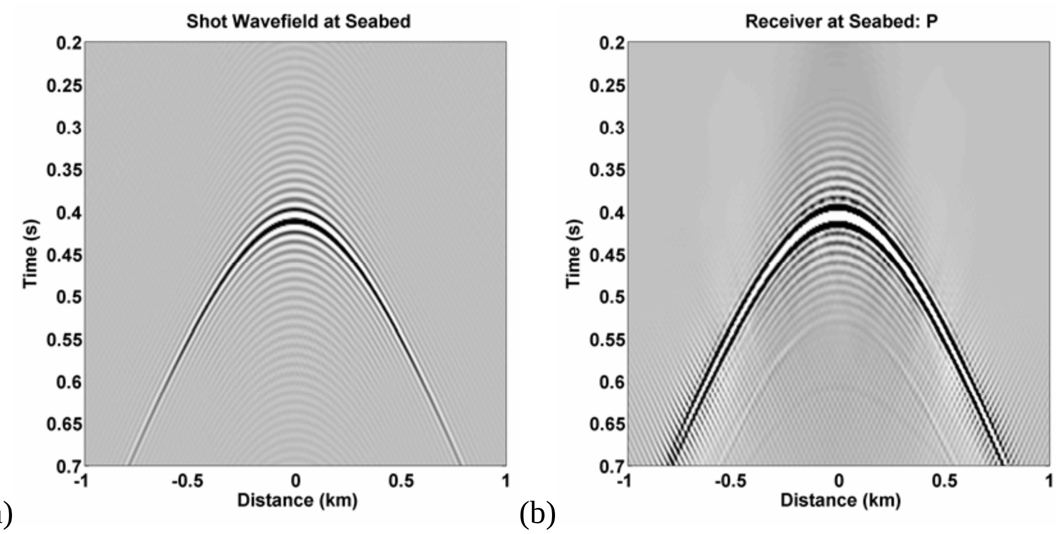

(a) (b)

Figure 6.4. Comparison of shot wavefield extrapolated to seabed with recorded P-wave wavefield at seabed, after decomposition from X and Z component data. The time of the recorded direct wave agrees well with the extrapolated shot. For actual migration this direct wave is muted.

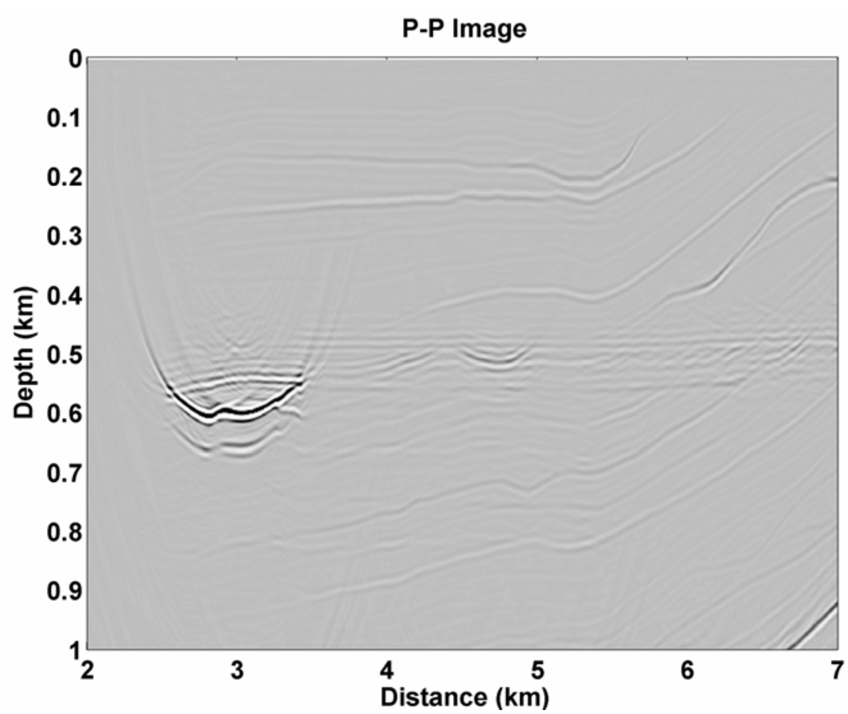

Figure 6.5. Migrated image of P-P data scaled by 0.1 compared with Figure 6.3(a).

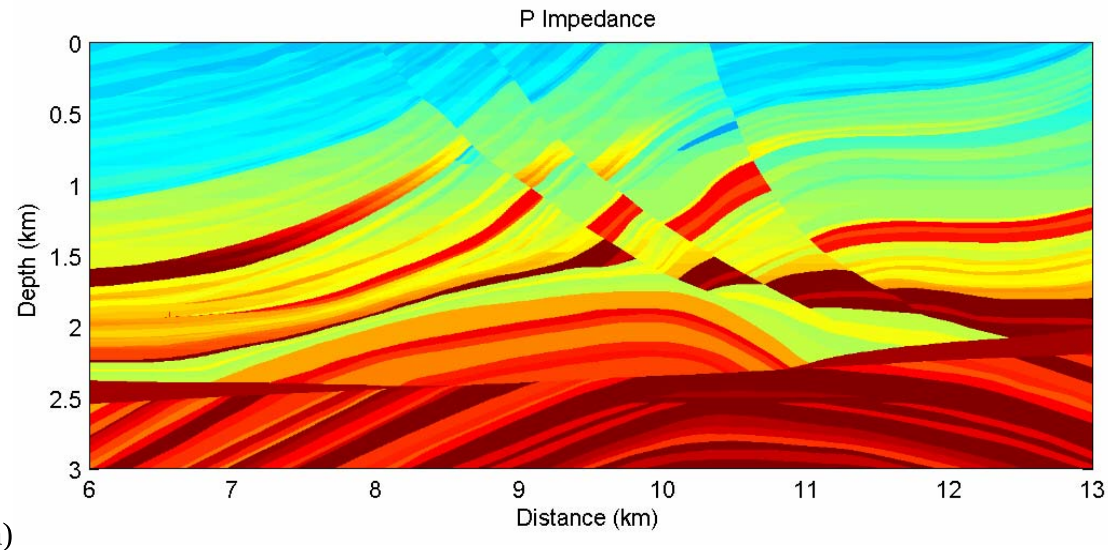

(a)

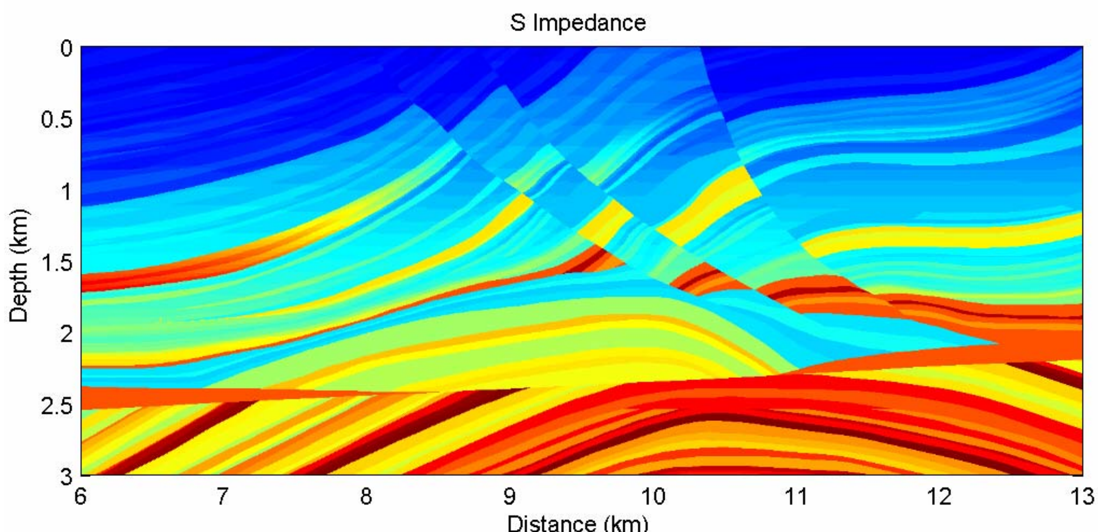

(b)

Figure 6.6. Part of Marmousi-2 elastic model, showing (a) acoustic (i.e. P-wave) impedance and (b) S-wave impedance. This area corresponds approximately to the original Marmousi acoustic model.

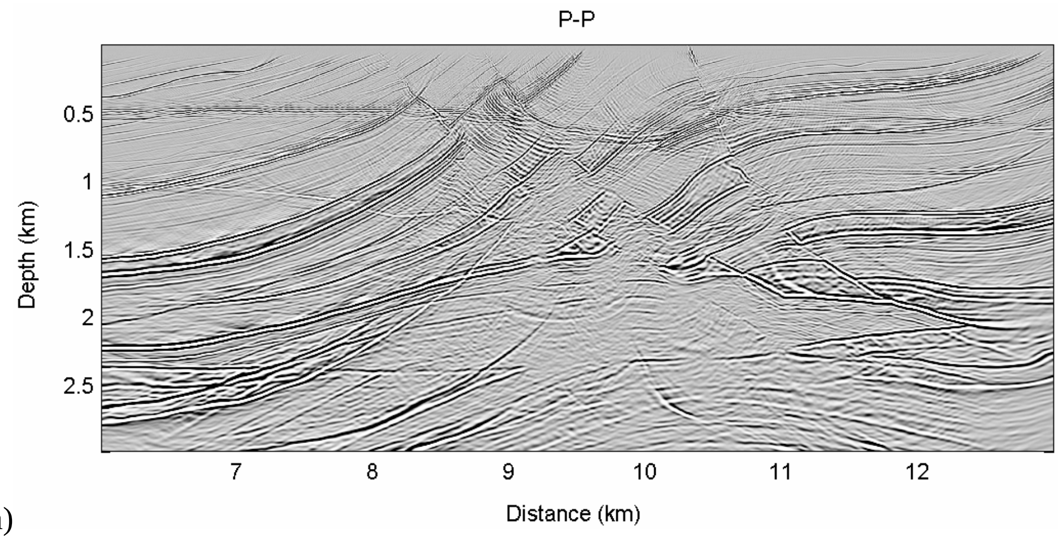

(a)

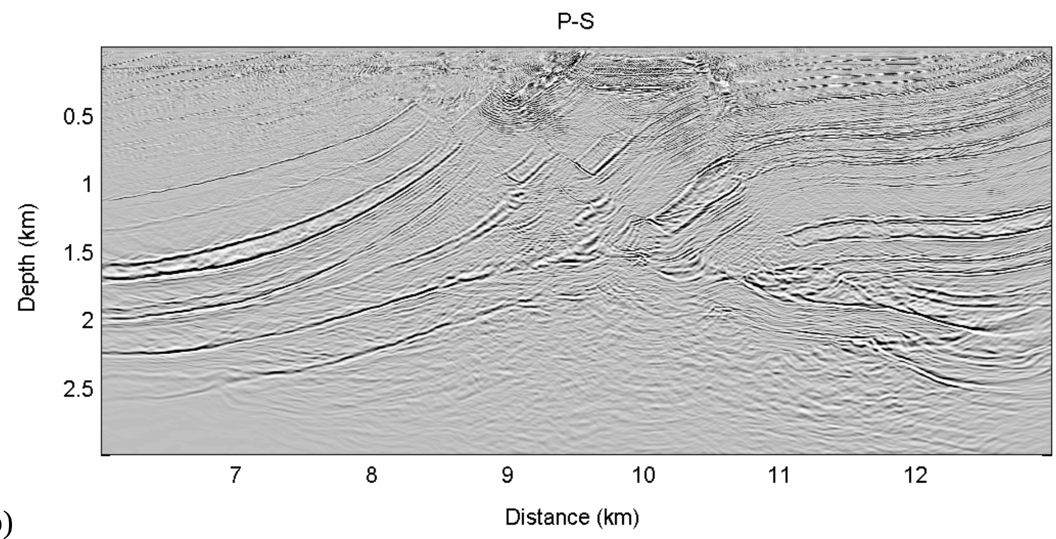

(b)

Figure 6.7. Migrated images for area shown in Figure 6.6, corresponding to original Marmousi model: (a) P-P and (b) P-S of X and Z component data from elastic modeling. Migration performed using PSPI algorithm of section 4.4, with 9 reference operators and a split-step correction. The deconvolution imaging condition has been applied.

PP PS

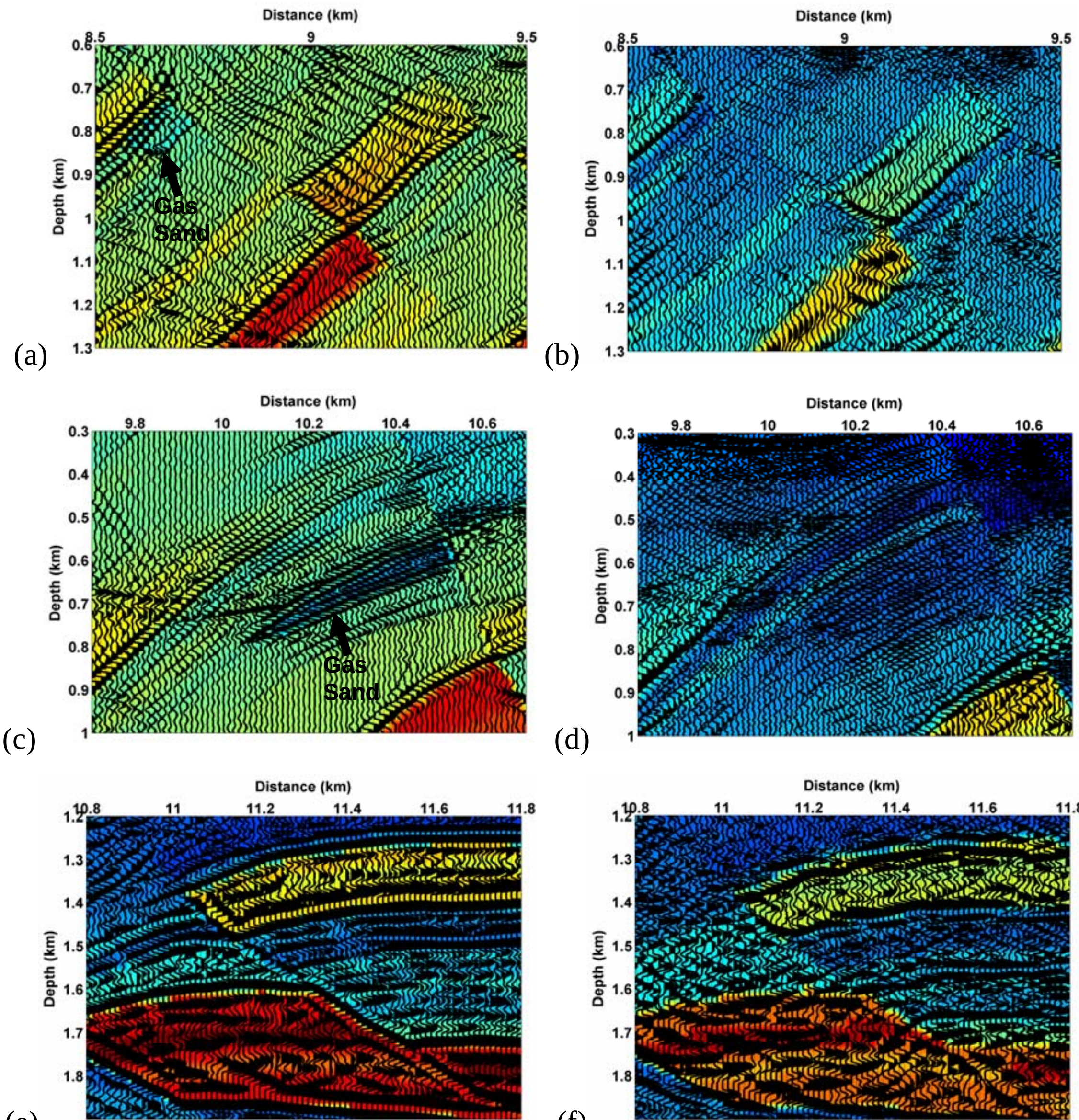

Figure 6.8. Detail of migrated images in Figure 6.7, superimposed on impedance model, for: (a) and (b) 8.5-9.5km, 0.6-1.3sec.; (c) and (d) 9.7-10.7km, 0.3-1.0sec., and; (e) and (f) 10.8-11.8km, 1.2-1.9sec. PP image on P-wave impedance is shown in (a), (c) and (e). PS image on S-wave impedance is shown in (b), (d) and (f). Also indicated in (a) and (c) are the locations of two gas-sand traps which cause strong PP response.

6.4 Discussion

There appear to be two main issues which are responsible for the relatively poorer performance of the PS imaging in the structural area, as compared with the shallow area. These are first; spatial aliasing of the converted waves in the shot record, and second; deviation of the polarity change location from zero offset.

6.4.1 Spatial aliasing of converted waves

Both the wavefield extrapolation operator and the composition/decomposition operators are designed to be correct for energy which has not been spatially aliased. However, because of the slow shear wave velocities, and the relatively coarse sampling (12.32m) of the receivers, any shear-wave energy which is propagating at large angles relative to vertical can suffer from significant spatial aliasing. This effect is important for the structural area, where the larger dips reflect much more energy at such large angles, than it is for the stratigraphic area. Figure 6.9 shows the X- and Z component data for shot 251, with lateral position 9.25km, situated near the center of the structural region (Figure 6.6). In Figure 6.10(a), the same shot is shown after wavefield decomposition at the ocean bottom.[1] Visible on both components are two sets of parallel reflections which intersect the direct arrival, as indicated. These can be identified as PP and PS reflection events arising from the steeply dipping structure which extends to the water bottom. Considering Figure 6.9, it appears on both components that the PP event is not aliased for the dominant frequencies, whereas the PS event is aliased. This observation is confirmed on the FK spectra of the decomposed data in Figure 6.10(b). The impact on the migrated image is profound. Figure 6.11 shows detailed view of the migrated images from Figure 6.7, with a horizontally compressed scale. Migration artifacts are present on both PP and PS images. Since the wavefield decomposition is incorrect for aliased energy, a substantial amount of the aliased data is present on the PP image, even though it arises from a PS reflection event.

[1] This was not fully successful. As was discussed in section 6.2.1, there is a difficulty with performing the decomposition at the water bottom in general, due to the boundary condition involved.

Compare shot record 251 (Figure 6.9 and Figure 6.10) with shot record 61 at lateral position 4.5km (Figure 6.12 and Figure 6.13, after decomposition). Observing the FK spectrum in Figure 6.13, it is clear that there is little evidence of spatial aliasing in this location. Correspondingly, there is little evidence of associated artefacts in the migrated image of Figure 6.3.

Returning to analysis of shot 251, the effect of low-pass filtering the shot record to a maximum frequency of 20Hz is shown in Figure 6.14. After this filtering, the PS reflection is no longer visibly aliased, but unfortunately the frequency content of the PP data has also been (unnecessarily) limited. In order to retain the bandwidth available for unaliased imaging of P-waves, and to reduce the effect of aliasing on PS, the following compromise is possible. The wavefield can be extrapolated with all frequencies up to 90Hz (as in Figure 6.7), but when applying the imaging condition, the frequencies used are limited to a lower number, based on the requirement that energy propagating at a given maximum angle to vertical, $\theta_{\max}$, is not aliased for the relevant mode velocity. The frequency limits for the PP and PS images are computed as

$$f_{PP,\max} = \frac{v_{P,\min}}{2\Delta x \sin\theta_{\max}},$$

$$f_{PS,\max} = \frac{v_{S,\min}}{2\Delta x \sin\theta_{\max}},$$

where Δx is the receiver sampling, and $v_{P,\min}$, $v_{S,\min}$ are the minimum P and S velocities respectively. For the area shown in Figure 6.11, this gives $f_{PP,\max} = 69.1\text{Hz}$, and $f_{PS,\max} = 18.5\text{Hz}$. The result of applying this modified imaging condition is shown in Figure 6.15. This should be compared with the results in Figure 6.11. Here, we see that most of the aliasing artefacts have been eliminated from the PS image. However, this is only a partial solution. It still leaves the effect of aliasing present on the PP image, where higher frequencies are desirable, to obtain the optimal image. Moreover, the filtering effect may be unduly harsh on less steeply dipping events which would benefit from the inclusion of higher frequencies on the PS image.

A more complete approach to addressing the aliasing problem would be to apply a prestack interpolation. Methods have been developed in the last few years which allow interpolation beyond the traditional limits imposed by aliasing (Spitz, 1991; Liu and Sacchi, 2004). Even better, would be to acquire (or in this case, numerically model) with a finer sampling of the receivers, so that much less of the useful PS reflection energy is subject to spatial aliasing!

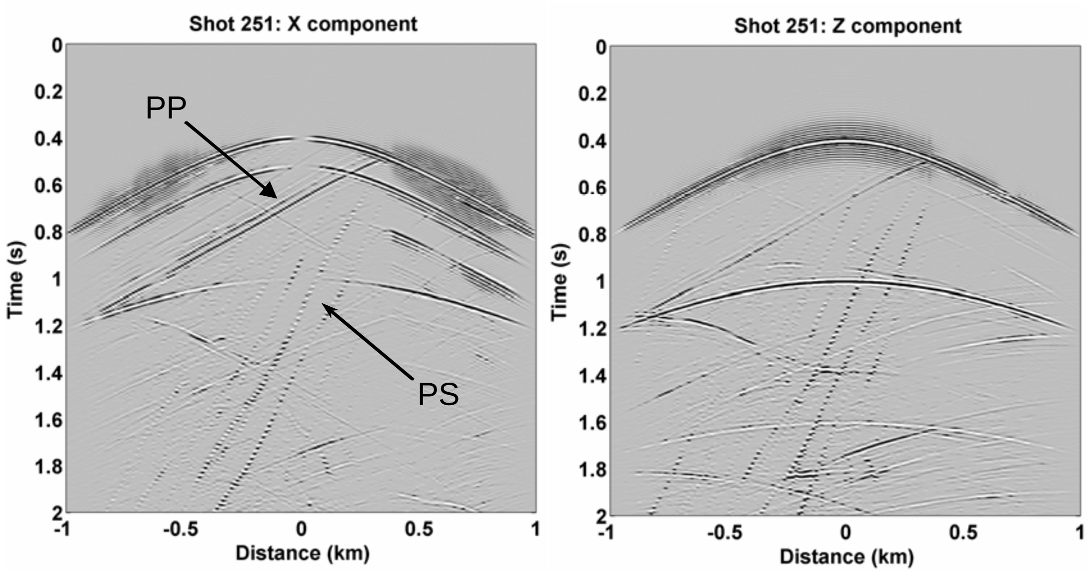

Figure 6.9. Shot 251 (9.25 km) showing reflections off of steeply dipping fault block. Note the aliasing of the PS event, further illustrated after wavefield separation in Figure 6.10. Also, observe that the polarity changes on the steeply dipping reflections occur well away from zero offset.

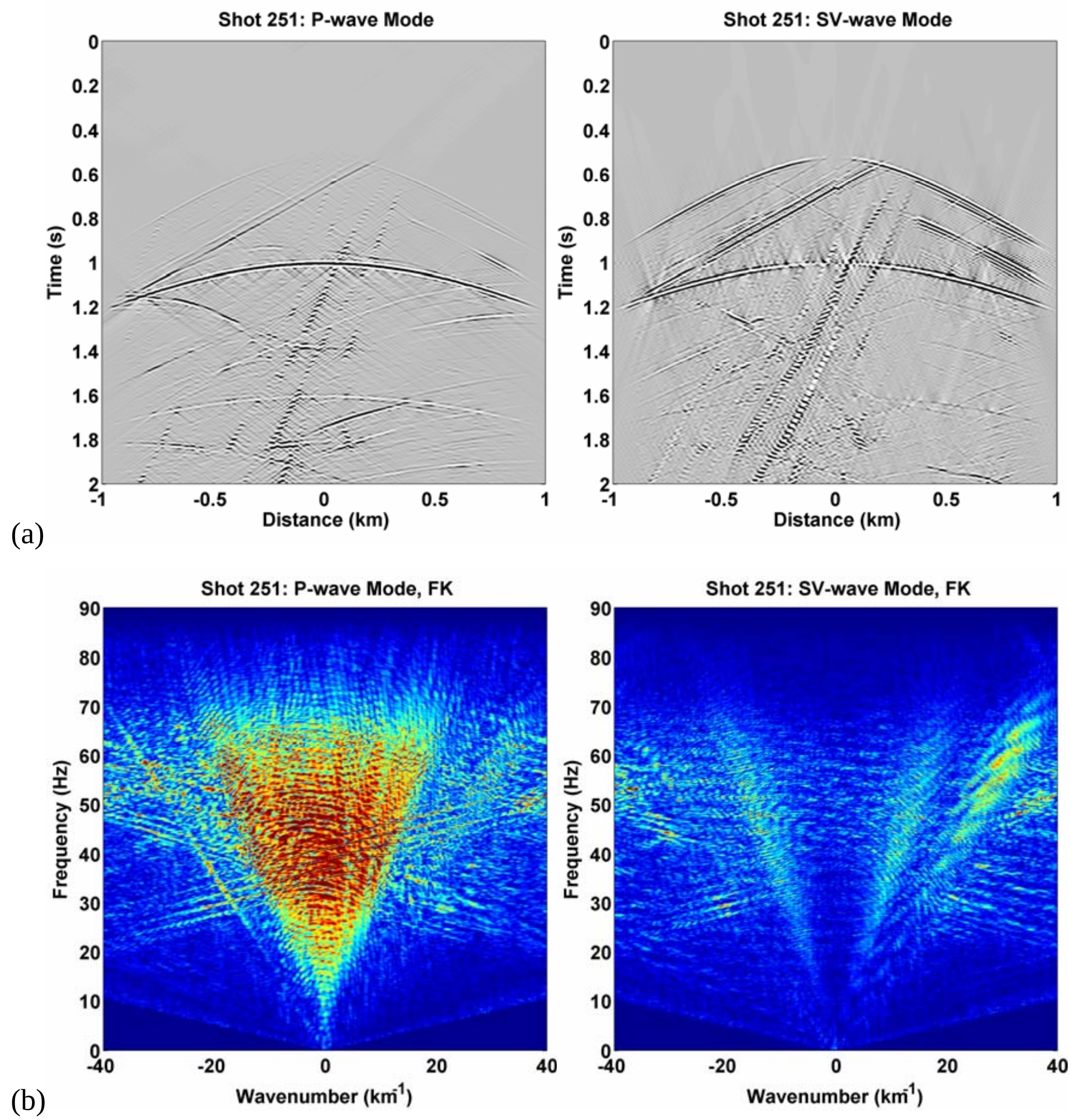

Figure 6.10. Shot 251 after wavefield separation, in (a) offset-time domain and (b) wave-number offset-frequency (FK) domain. Note the spatial aliasing (wrap-around) of the PS events.

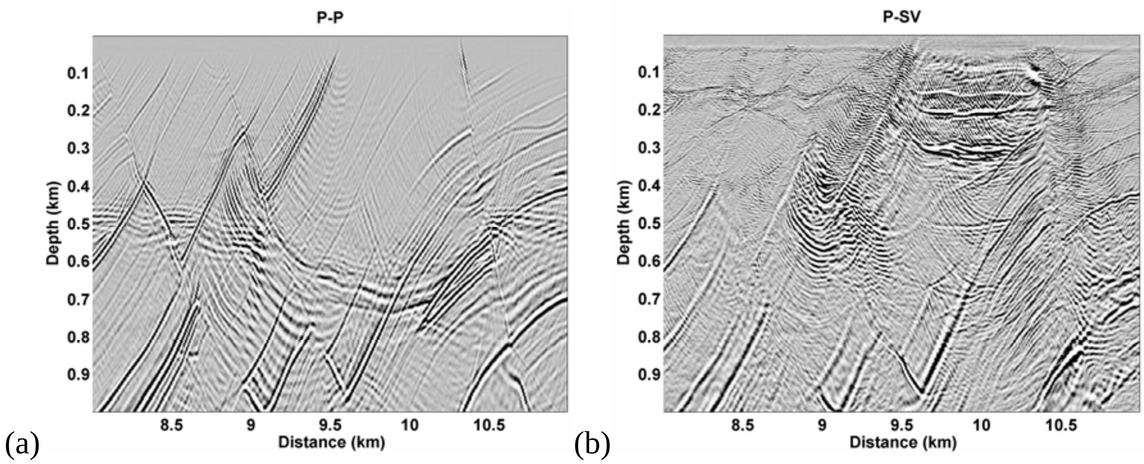

Figure 6.11. Detail of migrated images in Figure 6.7, showing effect of aliased energy on both PP and PS images.

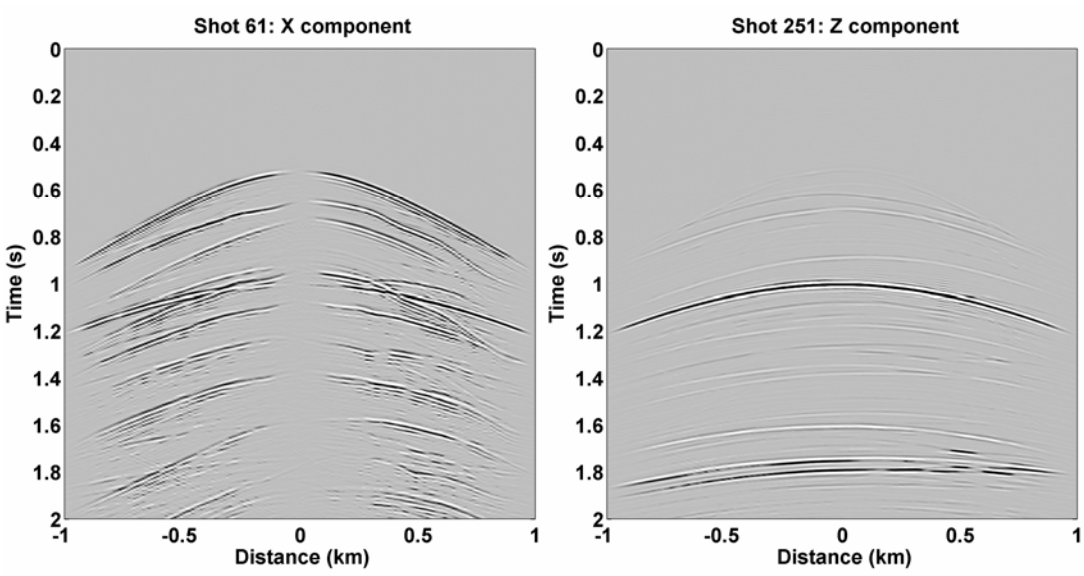

Figure 6.12. Shot 61 (4.5 km) showing reflections from more layered part of model. No aliasing is evident and the X component polarity change occurs near zero offset.

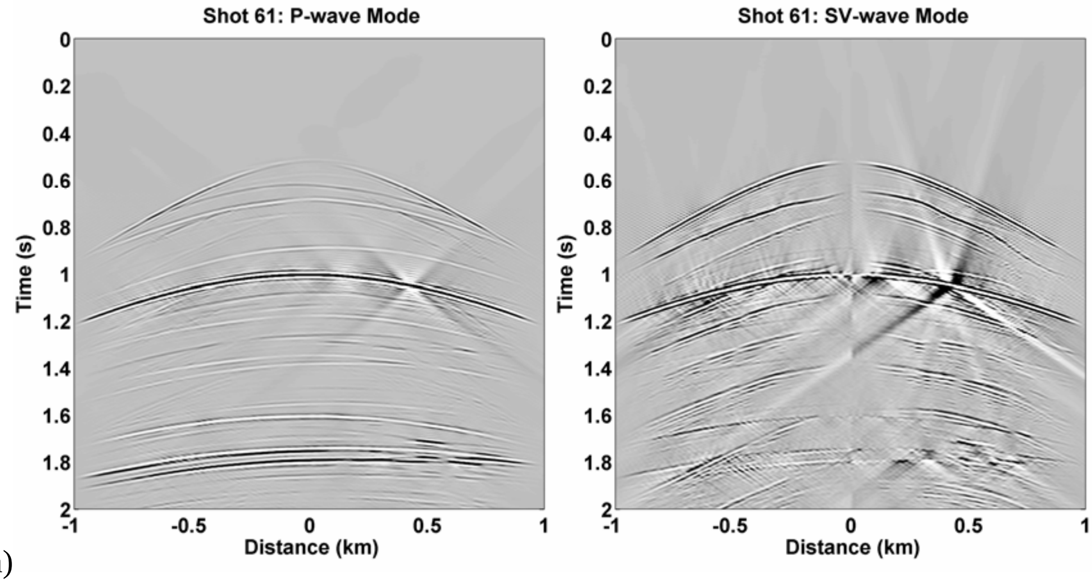

(a)

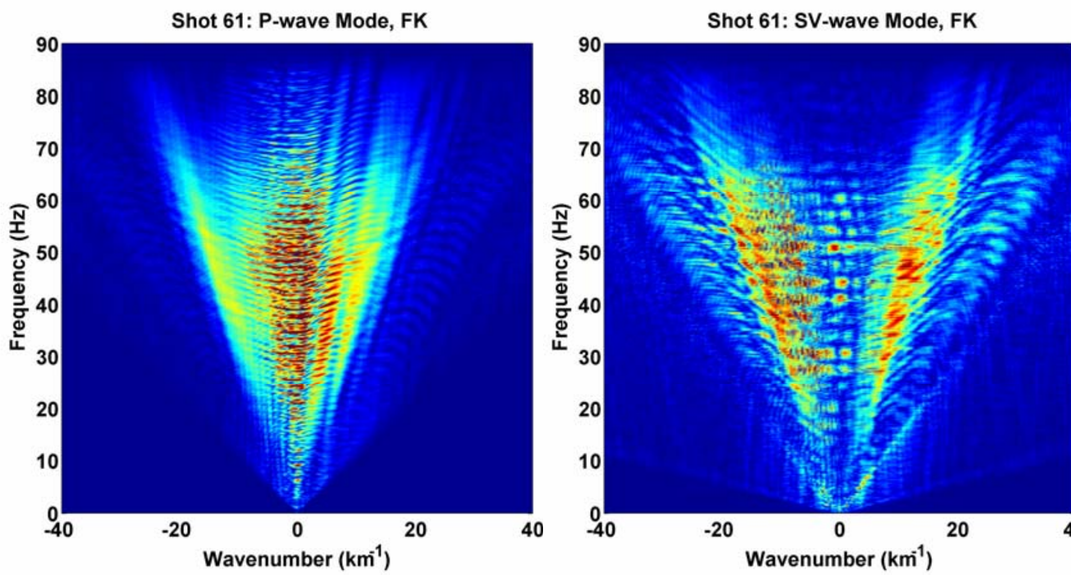

(b)

Figure 6.13. Shot 61 after wavefield separation, in (a) offset-time domain and (b) wave-number offset-frequency (FK) domain.

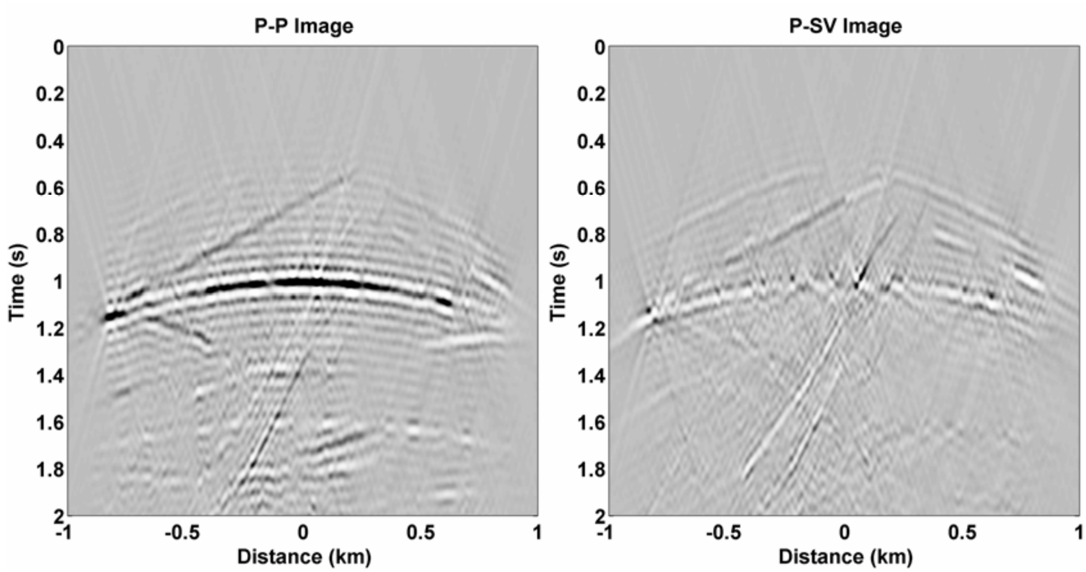

Figure 6.14. Shot 251 after wavefield separation, and application of a 20Hz high-cut filter. Note that steep dips are not aliased within this frequency range.

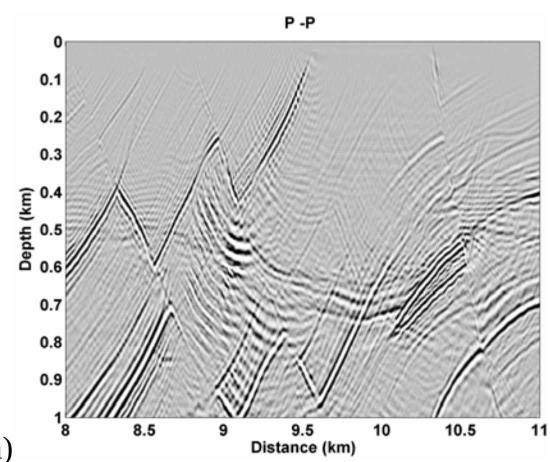

(a)

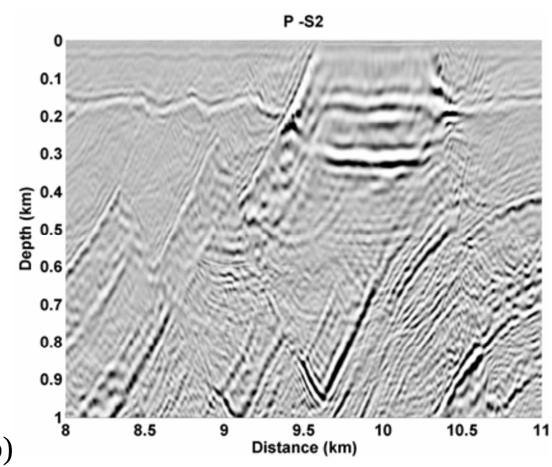

(b)

Figure 6.15. Detail of migrated images, after applying frequency limited imaging condition. Compare with Figure 5.6.

6.4.2 Deviation of polarity change from zero offset

It is a common misconception that the polarity of a converted-wave reflection changes sign at zero offset. The polarity change arises because the displacement direction of the S-wave which is generated by an incident P-wave depends on the sign of the reflection angle. The polarity change is therefore associated with the normally incident ray, which for many simple situations is synonymous with zero offset. In particular this equivalence holds if either: the V_P/V_S ratio is constant, or if the structure is horizontal (Rosales and Rickett, 2001; Sun and McMechan, 2001; Hou and Marfurt, 2002). If neither of these conditions hold, then the normal incidence ray is associated with P and S rays which have quite different paths, and generally are not coincident at the surface (therefore not zero-offset).[1] The reason for the different ray-paths is that Snell's law of refraction causes different degrees of bending for P- and S-wave rays, which are normally incident (and therefore parallel) at the image point, due to difference in the relative change in V_P and V_S along the ray-paths. This phenomenon is illustrated in Figure 6.16.

For Marmousi-2, the first of these conditions (constant V_P/V_S ratio) is not valid anywhere. This is clearly observed in Figure 6.17, which shows V_P/V_S for both the full model and a profile at the lateral position of the shot record in Figure 6.9. The variation in V_P/V_S is quite large, with values ranging from 1.58 to 5.24.

The second condition is a reasonable approximation for the stratigraphic area of the model. This is evident from analysis of the X component in Figure 6.12, where all events appear to change polarity at approximately zero-offset. By contrast for structural area the PS polarity change occurs well away from zero offset, as can be seen in Figure 6.9.

Determining the correct location of the polarity change is extremely challenging in areas of structural complexity, but can in principle be done if the model is known accurately.

---

[1] For PP events, there is also a polarity change observed on the horizontal component, which occurs (for an isotropic medium) at the location where the ray is vertical at the surface (at this location there is zero horizontal displacement for a P-wave).

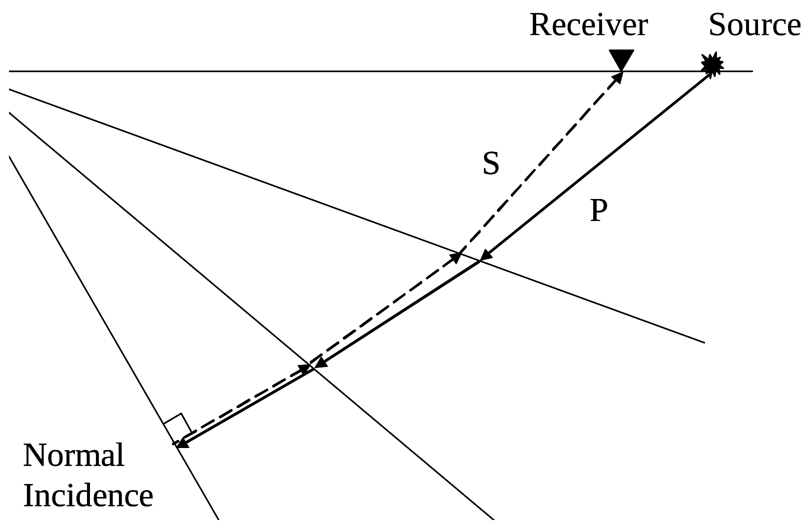

Figure 6.16. Position of polarity change for P-S conversion in a medium with variable V_P/V_S ratio, and dipping reflectors. The polarity change is associated with normal incidence at the reflector, for which the P-S reflection coefficient vanishes. Snell's law gives different amounts of ray-bending for P- and S-wave ray-paths, due to the differences in relative velocity contrast which are implied by variable V_P/V_S. Therefore the polarity change is observed at a non-zero source-receiver offset.

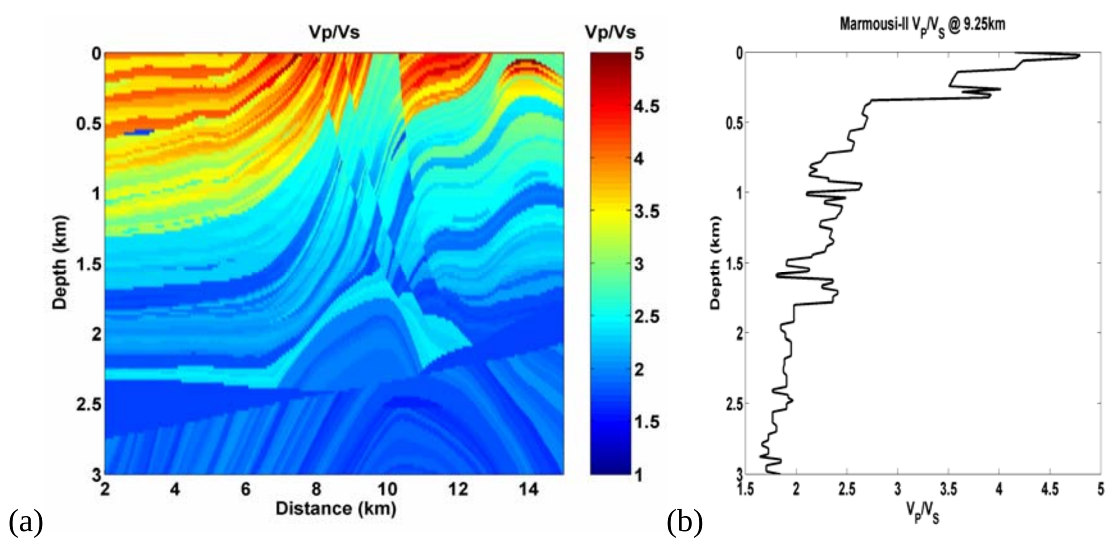

Figure 6.17. (a) Plot of V_P/V_S ratio for Marmousi-2 model. (b) Profile at lateral position 9.25km. Values range from 1.58 to 5.24.

To be applied within the context of a wave-equation migration scheme, the following steps are required:

1. Compute angle gathers for both PP (Rickett and Sava, 2002; Sava and Fomel, 2003) and PS (Rosales and Rickett, 2001; Rosales and Biondi, 2005).
2. Determine the polarity flip angle from the local structural dip in the model. Rosales and Rickett (2001) suggest using plane-wave destructors applied to the data to determine this. They go on to describe how to find the position of the polarity reversal from the structural dip. An alternative to plane-wave destructors, which might be applicable in the Marmousi-2 case, would be to measure the gradient of the velocity field to estimate local dip.

Unfortunately, the examples provided in Rosales and Rickett (2001) and Rosales and Biondi (2005) use considerably simpler synthetics than the Marmousi-2 model, with easily defined structural dip at every point. There are serious difficulties in uniquely defining a structural dip direction at every point in the Marmousi-2 model, where dipping reflectors often abut fault planes. Their method has been attempted by the present author without success on Marmousi-2. The results produced in this chapter have been corrected simply by changing the polarity of the S-wave receiver wavefield at the beginning of the first extrapolation step, as shown in Figure 6.10 and Figure 6.13. This approach has proved successful in the stratigraphic regions, but less so in the structural regions. This is as expected. Erroneous correction of the polarity is believed to be largely responsible for some of the degraded imaging of the steeper dips on the PS image in Figure 6.7(b).

6.4.3 Further comments

It is perhaps worth noting that, apart from the presence of free surface multiples, none of the deleterious effects encountered here are a problem for the surface streamer data generated for this model (Martin, 2004). Since the spatial aliasing is a low-velocity phenomenon, it is only present on OBC data which measures shear waves. It is not present on the streamer data. Additionally, ray-path related polarity changes are not present on hydrophone data.

6.5 Chapter summary

The isotropic PSPI migration algorithm of section 4.4 has been applied to a new, elastic version of the well-known Marmousi dataset. The image obtained for the stratigraphic parts of the model are excellent for both PP and PS modes, with the latter displaying the expected resolution advantages associated with shorter wavelengths. The PP image in the central structural area is also good. However, the PS image in this area suffers from effects of aliasing and from errors related to the polarity change. In both areas, the images are adversely affected by the presence of long-period free surface multiples, with these being more evident on PP than PS.

In applying the elastic migration to this dataset, several issues were encountered. These lie outside the scope of this thesis, and in some cases point to limitations in the design of the acquisition geometry used. Although these issues are not resolved here, this chapter includes some discussion of possible routes towards solution for each identified issue. It is suggested that this might provide a starting point for future work on this challenging and fruitful dataset.

CHAPTER SEVEN: SUMMARY, FUTURE DIRECTIONS AND CONCLUSIONS

7.1 Summary

As outlined in the Introduction, the development of the ideas in this thesis was initially motivated by the observation that two apparently disparate processing steps for shear waves, namely shear-wave splitting correction and wave-equation migration, were fundamentally limited when applied as separate steps to elastic data. Instead, it is more natural and theoretically accurate to combine them into an anisotropic elastic migration scheme based on *vector* wavefield extrapolation. The use of vector extrapolation distinguishes the work of this dissertation from other so-called elastic migration schemes which use scalar extrapolation of the P- and S-wavefields. This could have been done for general anisotropy, but, for practical and illustrative reasons, the scope has been limited to addressing the case of horizontal transverse isotropy (HTI). Since the extrapolation step, which includes the effect of passing from one medium to another, should ideally satisfy continuity of displacement and traction, the most natural framework for design of the wavefield extrapolators is that of anisotropic propagator matrix theory, as developed by Fryer and Frazer (1984; 1987). This existing body of theory was completely appropriate for the simplest case of extrapolation in a horizontally homogeneous medium, as described within Chapter Two. The basic steps are: (1) decomposition, in which a vector wavefield consisting of six components of displacement and vertical traction is decomposed into six eigenmodes, three upgoing and three downgoing; (2) extrapolation, in which the desired wavemodes (upgoing for receiver wavefields, downgoing for source wavefields) are propagated by one or more depth steps, and; (3) recomposition, in which the vector wavefield is reconstituted at the new depth. Careful attention must be given to the behaviour near the various critical angles, corresponding to transitions from propagating to evanescent wave behaviour. These cause polarization vectors as well as the vertical slownesses to become complex.

To be useful as an imaging tool, it is necessary to extend this theory to handle lateral velocity variations, and more generally (for anisotropic media) variations in any of the medium properties. The approach used is based upon the generalised PSPI (GPSPI) methodology, a form of ΨDO which allows the application of a spatially variable extrapolator. The existing theory of GPSPI, applicable to scalar wavefield extrapolation, was extended to vector extrapolation in Chapter Three. The adjoint form of the operator, a vector form of non-stationary phase shift (NSPS) was also discussed in that chapter, but not pursued further. The choice of GPSPI over other possible methods, such as explicit or implicit operators acting in the space-frequency domain, is not clear cut. The main advantage is one of simplicity, since both the phase shift and the decomposition-recomposition steps are applied via scalar and matrix multiplication respectively for GPSPI, whereas they would require matrix convolution for the alternatives. Furthermore, there are additional problems of stability associated with the explicit operator approach, and difficulties in design for anisotropic implicit operators. Nevertheless, it might be expected that, in the future, migration researchers might chose one of these approaches for computational efficiency reasons.

The main disadvantage with the GPSPI approach is cost – since the variation of the medium laterally requires the use of a Fourier integral operator rather than a Fourier transform. A Fourier integral operator cannot be applied directly using a fast Fourier transform (FFT).

Practical application within a migration operator therefore requires that the ideal form of GPSPI be approximated in some way. This is done either by: (1) spatial windowing, or; (2) by interpolation between parameters, leading to an algorithm akin to PSPI (Gazdag and Sguazerro, 1984). In Chapter Four it is shown that the first approach is really the only viable option for a medium with anisotropy, due to the dimensionality of the parameter space which would have to be interpolated otherwise. Therefore an appropriate adaptive windowing algorithm, PSPAW, was devised for the HTI case. This is based upon an error criterion measured over all phase angles of interest. On the other hand, it was shown that for isotropic migration, the second approach (using an approximate form of PSPI) is possible.

In Chapter Five, the wavefield extrapolators were applied within the context of a shot-record migration, using downward extrapolation of the source and receiver wavefields, together with an imaging condition, which selects the mode combinations required for output images. The migration algorithm exploits well-known additional steps such as the split-step correction, vertical interpolation of the wavefield and an anti-aliasing imaging condition. The locations of decomposition and recomposition determine where it is possible to account for phenomena such as mode conversion and shear-wave splitting. The wavefields are treated as scalar entities in between these "repolarization" depths.

This migration algorithm was demonstrated using an anisotropic elastic dataset which had been modelled using the pseudospectral technique, and compared with isotropic migration on the same dataset. The comparison shows the benefit of including the shear-wave repolarization step to handle shear-wave splitting via the anisotropic migration, a task which the isotropic migration is unable to achieve. This is most clearly and informatively seen by monitoring the downward continued receiver wavefield, as it enters and leaves the HTI layer.

The isotropic elastic migration using the PSPI approach was demonstrated on a new elastic version of the well-known Marmousi model, Marmousi-2. Various processing issues remain unsolved with this dataset, but the images are indicative of a useful algorithm. Some difficulties were encountered obtaining a satisfactory PS image from the central part of Marmousi-2. It is likely that this is due to: aliasing of the shear-wave arrivals, a consequence of the acquisition parameters chosen for modelling, and; structural effects which violate the zero-offset assumption for the location of polarity changes. In parts of Marmousi-2 where gentler dips are present, so that aliasing is not an issue and the zero-offset assumption is valid, the results obtained for the PS image are excellent.

7.2 Future directions

During the course of the work in this dissertation, a number of avenues for future work have become apparent. These basically fall into two overlapping categories: limitations in the current approach which might be overcome, and; extensions of the theory to widen the applicability of the methods. Some of these areas are now briefly discussed.

7.2.1 Stability, efficiency and the "stair-case" approximation

As mentioned in section 5.2.5, the repolarization steps are not executed on every depth step, due both to stability and efficiency considerations. A related issue is that each repolarization step is based upon the (exact) boundary conditions for a horizontal interface, whereas lateral changes are treated by the GPSPI type approximations. In particular, no account is taken explicitly of polarization changes due to medium changes across non-horizontal interfaces. The accuracy of this "stair-case" approximation is assumed to improve as the steps become smaller, but always treats the horizontal and vertical parts of a boundary condition differently. The fact that smaller steps also give rise to stability and efficiency problems, it suggests that a different approach is called for. One possibility would be to define macro-interfaces which are based on horizons where significant conversion or shear-wave splitting effects will occur, and use scalar propagators elsewhere. The extrapolation across the macro-interfaces could be applied in a rotated coordinate system with a propagation direction which is locally parallel to the normal to the interface, so that appropriate boundary conditions are applied. Extrapolation using rotated coordinate systems has been recently applied in the context of turning wave migration (Shan and Biondi, 2004). Doing this would require a more general treatment of anisotropy, since an HTI medium would be a tilted TI medium in the rotated coordinates. Since the macro-interfaces would be generally spaced at several times the depth step, this would also address efficiency and stability concerns.

7.2.2 Other anisotropic symmetry systems

The theory developed here has focused on a specific form of anisotropy, HTI. This symmetry system was selected both because it is associated with fractures, and is therefore of exploration interest, and because it illustrates the advantages of an elastic (vector) extrapolation algorithm to properly handle shear-wave splitting. However, there is no fundamental reason why the elastic extrapolation cannot be adapted for other symmetry systems. Both VTI and orthorhombic anisotropy have horizontal planes of symmetry, which make the computation of up- and down-going eigenmodes relatively straightforward, involving solution of a cubic equation (see Appendix A). Orthorhombic anisotropy may well be the system which best approximates many real world geological setting with a combination of fine layering, such as shales, and fractures, as found in carbonates. Another important system of exploration interest is tilted transverse isotropy (TTI). This would require a more significant modification to the theory in this dissertation, as it no longer has a horizontal plane of symmetry. The eigenvalues require solution of a quartic equation, and no longer appear in up- and down-going pairs. This generalization would have the additional advantage of allowing propagation in rotated coordinate systems as described in the previous section.

7.2.3 Extrapolation in 3-D

The derivation of the extrapolators has been limited to 2-D in this dissertation. However, as was discussed in section 2.3, the basic theory is applicable to 3-D. Apart from cost, the main issue which requires attention for a 3-D algorithm is the adaptation of the PSPAW algorithm to forming windows in the *x-y* plane, since each depth step requires a 2-D velocity function. As illustrated in 4.3.3, suitable windows (molecules) can be built up from Gaussian atoms, but a technique to "grow" the molecules in 2-D needs to be devised. (For 2-D extrapolation, with 1-D velocity slices, this consists of starting from one end of the model and proceeding towards the other.) Ideas from image processing or cluster analysis would likely contribute to a solution to this problem.

7.2.4 Angle gathers and polarity correction

A method for polarity correction in highly structured areas is needed if better results are to be obtained on models like Marmousi-2. The method developed by Rosales and Biondi (2005), and outlined in section 6.4.2 could be explored further. A key question is whether the best determination of polarity changes is based on the model or on the data. Except for cases of a few isolated reflections, it is likely to be difficult to asses polarity changes from the data alone. On the other hand, the model may not generally be known with sufficient confidence to predict them. Even in cases where it is known exactly (such as Marmousi-2) assigning unique dip directions at every point is problematic. Determining polarity behaviour is perhaps the *most* important issue for the use of converted waves in highly structured areas.

7.2.5 Improved factorization of the elastic Helmholtz equation

It has been pointed out (Fishman and McCoy, 1985) that the factorization of the scalar Helmholtz equation into up- and down-going square-root operators is only valid for media which are invariant in the transverse direction (i.e. horizontal for vertical extrapolation). Fishman (2002) has subsequently drawn upon developments in quantum mechanics and microlocal analysis to derive a "uniformly asymptotic" approximation to the relevant one-way operator, which factorizes the Helmholtz equation in a transversely heterogeneous medium. This has provided a sound theoretical basis for improved scalar wavefield extrapolation, and is likely to result soon in new algorithms for seismic acoustic migration. To this author's knowledge, an equivalent theory does not yet exist for the elastic wave-equation. Such a theory might well address some of the short-comings of the "stair-case" approximation described above, since the handling of lateral medium variations is done in a more correct fashion than the standard square-root operator.

7.2.6 Application to real data

The elastic migration method developed here has been applied to two synthetic datasets, one of structural simplicity but including anisotropy, and the other (Marmousi-2) much more structurally challenging. In both cases, a known model of velocity (and anisotropy in the first case) was used.

Some further issues arise if this is to be applied on real data, from a multicomponent seismic survey. The key additional complication is the fact that the earth model is a priori unknown and must be estimated from the seismic data. Depending on the structural complexity, this might be done with standard velocity analysis, or it might necessitate more advanced approaches such as tomography. [See Gray et al. (2001), for a discussion on model building for depth migration.] In addition, the azimuthal anisotropy must also be estimated. For structurally simple areas, methods such as 3-D Alford rotation (Gaiser, 2000) or transverse polarity changes (Bale et al., 2000) can be used. For structurally complex areas, this step poses challenges which require further work.

Aside from uncertainty in the earth model, the application on real data would require careful attention to issues such as: vector fidelity (required to permit vector extrapolation to be appropriate); statics for land data (with shear-wave statics typically significantly larger than P-wave statics); multiples for marine data, and; coherent noise suppression (e.g. ground roll).

An ideal initial test dataset would be either a land survey with relatively small statics or an OBC dataset with good vector fidelity and successful up-down separation using seabed hydrophones. The first would allow use of the free-surface boundary condition, and the second would permit use of the one-way condition (see section 2.2.7).

7.3 Conclusions

The extrapolation of elastic data through both isotropic, and azimuthally anisotropic, heterogeneous media has been described and demonstrated. The azimuthally anisotropic formulation achieves the natural combination of shear-wave splitting correction and migration into a single extrapolation method, enabling the simultaneous output of P-P, P-S1 and P-S2 images from a migration of multicomponent data.

An elastic version of GPSPI extrapolation has been formulated, which allows extension to laterally variable media. Additionally, two new interpolation algorithms to economically apply elastic PSPI have been described. The first, PSPAW, is applicable to arbitrary media, and the second, elastic PSPI, is appropriate for isotropic media.

The elastic extrapolation has been used in a shot-record migration to successfully image different mode combinations. This has been demonstrated using an azimuthally anisotropic synthetic, and using Marmousi-2.

REFERENCES

Aki, K., and Richards, P.G., 2002, Quantitative Seismology: Second Edition, University Science Books, Sausalito, California.

Alford, R.M., 1986, Shear data in the presence of azimuthal anisotropy: Dilley, Texas, 56th Ann. Internat. Mtg.: Soc. Expl. Geophys., Expanded Abstracts, 476-479.

Amundsen, L., and Reitan, A., 1995, Decomposition of multicomponent sea-floor data into upgoing and downgoing P- and S-waves: Geophysics, **60**, 563-572.

Auld, B.A., 1973, Acoustic fields and waves in solids, Wiley, New York.

Bale, R.A., 2002a. Modelling 3D anisotropic elastic data using the pseudospectral approach, CREWES Research Report, **14**.

____, 2002b. Staggered grids for 3D pseudospectral modelling in anisotropic elastic media, CREWES Research Report, **14**.

____, 2003, Modeling 3D anisotropic elastic data using the pseudospectral approach, 65th Mtg., Eur. Assn. Expl. Geophys., Extended Abstracts.

Bale, R.A., Dumitru, G., and Probert, T., 2000, Analysis and stacking of 3-D converted-wave data in the presence of azimuthal anisotropy, 70th Annual Internat. Mtg.: Soc. Expl. Geoph., Expanded Abstracts, 1189-1192.

Bale, R.A., Grossman, J.P., Margrave, G.F., and Lamoureux, M.P., 2002. Multidimensional partitions of unity and Gaussian terrain, CREWES Research Report, **14**.

Baysal, E., Kosloff, D.D., and Sherwood, J.W.C., 1983, Reverse time migration: Geophysics, **48**, 1514-1524.

Berkhout, A.J., 1981, Wave Field Extrapolation Techniques In Seismic Migration, A Tutorial: Geophysics, **46**, 1638-1656.

Bleistein, N., Cohen, J.K., and Stockwell, J., J.W., 2001, Mathematics of multidimensional seismic imaging, migration, and inversion, Springer, New York.

Carcione, J.M., Herman, G.C., and ten Kroode, A.P.E., 2002, Seismic modeling: Geophysics, **67**, 1304-1325.

Castagna, J.P., Batzle, M.L., and Kan, T.K., 1993. Rock Physics - The link between rock properties and AVO response. *In* Castagna, J.P., and Backus, M.M., eds., Offset dependent reflectivity -Theory and practice of AVO anomalies. pp. 135-171.

Claerbout, J.F., 1971, Toward A Unified Theory Of Reflector Mapping: Geophysics, **36**, 467-481.

Claerbout, J.F., and Doherty, S.M., 1972, Downward Continuation Of Moveout-Corrected Seismograms: Geophysics, **37**, 741-768.

Crampin, S., 1981, A review of wave motion in anisotropic and cracked elastic-media: Wave Motion, **3**, 343-391.

Crampin, S., and Chastin, S., 2003, A review of shear wave splitting in the crack-critical crust: Geophysical Journal International, **155**, 221-240.

Daley, P.-F., and Hron, F., 1977: Bulletin of the Seismological Society of America, **67**, 661-675.

Dellinger, J., 1991. Anisotropic seismic wave propagation. Ph. D., Stanford University.

Dellinger, J., and Etgen, J., 1990, Wave-field separation in two-dimensional anisotropic media: Geophysics, **55**, 914-919.

Etgen, J.T., 1988, Prestacked migration of P and Sv-waves, 58th Ann. Internat. Mtg.: Soc. of Expl. Geophys., Session: S12.4.

Ferguson, R.J., 2000. Seismic imaging in heterogeneous anisotropic media by nonstationary phase shift. Ph.D., Univ. of Calgary.

Ferguson, R.J., and Margrave, G.F., 2002, Prestack depth migration by symmetric nonstationary phase shift: Geophysics, **67**, 594-603.

Fishman, L., 2002, Applications of directional wavefield decomposition, phase space and path integral methods to seismic wave propagation and inversion: Pure Appl. Geophys., **159**, 1637-1679.

Fishman, L., and McCoy, J.J., 1985, A New Class Of Propagation Models Based On A Factorization Of The Helmholtz-Equation: Geophysical Journal Of The Royal Astronomical Society, **80**, 439-461.

Fisk, M.D., and McCartor, G.D., 1991, The Phase Screen Method For Vector Elastic-Waves: Journal Of Geophysical Research-Solid Earth And Planets, **96**, 5985-6010.

Fryer, G.J., and Frazer, L.N., 1984, Seismic waves in stratified anisotropic media: Geophys. J. Roy. Astr. Soc., **78**, 691-710.

____, 1987, Seismic waves in stratified anisotropic media-II. Elastodynamic eigensolutions for some anisotropic systems: Geophys. J. Roy. Astr. Soc., **91**, 73-101.

Fu, L.Y., 2004, Wavefield interpolation in the Fourier wavefield extrapolation: Geophysics, **69**, 257-264.

Gaiser, J., 2000, Advantages of 3-D P-S-wave data to unravel S-wave birefringence for fracture detection, 70th Ann. Internat. Mtg.: Soc. of Expl. Geophys., 1201-1204.

Gazdag, J., 1978, Wave equation migration with the phase-shift method: Geophysics, **43**, 1342-1351.

Gazdag, J., and Sguazerro, P., 1984, Migration of seismic data by phase shift plus interpolation: Geophysics, **49**, 124-131.

Geiger, H., 2001. Relative-Amplitude-Preserving Prestack Time Migration by the Equivalent Offset Method. Ph.D., Univ. of Calgary, Calgary.

Gilbert, F., and Backus, G.E., 1966, Propagator matrices in elastic wave and vibration problems: Geophysics, **31**, 326-332.

Gray, S.H., Etgen, J., Dellinger, J., and Whitmore, D., 2001, Seismic migration problems and solutions: Geophysics, **66**, 1622-1640.

Grechka, V., and Tsvankin, I., 1999, 3-D moveout velocity analysis and parameter estimation for orthorhombic media: Geophysics, **64**, 820-837.

Greenburg, M.L., and Castagna, J.P., 1992, Shear-wave velocity estimation in porous rocks: Theoretical formulation, preliminary verification and applications: Geophysical Prospecting, **40**, 195-210.

Grossman, J.P., Margrave, G.F., and Lamoureux, M.P., 2002a. Fast wavefield extrapolation by phase-shift in the nonuniform Gabor domain, CREWES Research Report, **14**.

____, 2002b. Constructing adaptive nonuniform Gabor frames from partitions of unity, CREWES Research Report, **14**.

Hale, D., 1991, Stable Explicit Depth Extrapolation Of Seismic Wave-Fields: Geophysics, **56**, 1770-1777.

Haskell, N., 1953, The dispersion of surface waves in a multilayered media: Bull. Seis. Soc. Am., **43**, 17-34.

Holberg, O., 1988, Towards Optimum One-Way Wave-Propagation: Geophysical Prospecting, **36**, 99-114.

Hou, A., and Marfurt, K.J., 2002, Multicomponent prestack depth migration by scalar wavefield extrapolation: Geophysics, **67**, 1886-1894.

Huang, L.J., Fehler, M.C., and Wu, R.S., 1999, Extended local Born Fourier migration method: Geophysics, **64**, 1524-1534.

Hudson, J.A., 1981, Wave speeds and attenuation of elastic waves in material containing cracks: Geophys. J. Roy. Astr. Soc., **64**, 133-150.

Judson, D.R., Lin, J., Schultz, P.S., and Sherwood, J.W.C., 1980, Depth migration after stack: Geophysics, **45**, 361-375.

Kennett, B.L.N., 1983, Seismic Wave Propagation in Stratified Media, Cambridge University Press, Cambridge.

Landshoff, P., and Metherell, A., 1979, Simple quantum physics, Cambridge University Press.

Le Rousseau, J.H., and de Hoop, M.V., 2001, Modeling and imaging with the scalar generalized-screen algorithms in isotropic media: Geophysics, **66**, 1551-1568.

____, 2001, Scalar generalized-screen algorithms in transversely isotropic media with a vertical symmetry axis: Geophysics, **66**, 1538-1550.

Li, X.-Y., 1997, Fractured reservoir delineation using multicomponent seismic data: Geophysical Prospecting, **45**, 39-64.

____, 1998, Fracture detection using P-P and P-S waves, 68th Annual Internat. Mtg.: Soc. Expl. Geoph., Expanded Abstracts, 2056-2059.

Liu, B., and Sacchi, M.D., 2004, Minimum weighted norm interpolation of seismic records: Geophysics, **69**, 1560-1568.

Liu, K., 2005. Stability and Accuracy Analysis of Space-frequency Wavefield Extrapolators for Depth Migration. M.Sc., University of Calgary, Calgary.

Lou, M., and Rial, J.A., 1995, Modelling elastic-wave propagation in inhomogeneous anisotropic media by the pseudo-spectral method: Geophys. J. Int., **120**, 60-72.

Lynn, H.B., 2004, The winds of change: Anisotropic rocks---their preferred direction of fluid flow and their associated seismic signatures---Part 2: The Leading Edge, **23**, 1258-1268.

____, 2004, The winds of change: The Leading Edge, **23**, 1156-1162.

Margrave, G., and Ferguson, R., 2000, Taylor series derivation of nonstationary wavefield extrapolators, 70th Ann. Internat. Mtg: Soc. of Expl. Geophys., 834-837.

Margrave, G.F., and Ferguson, R.J., 1998. Explicit Fourier wavefield extrapolators, CREWES Research Report, **10**.

____, 1999, Wavefield extrapolation by nonstationary phase shift: Geophysics, **64**, 1067-1078.

Martin, G., 2004. The Marmousi2 Model, Elastic Synthetic Data, and an Analysis of Imaging and AVO in a Structurally Complex Environment. M.Sc., University of Houston.

Martin, G., Larsen, S., and Marfurt, K., 2002, Marmousi-2: an updated model for the investigation of AVO in structurally complex areas, 72nd Ann. Internat. Mtg: Soc. of Expl. Geophys., 1979-1982.

Musgrave, M.J.P., 1970, Crystal Acoustics: Introduction to the Study of Elastic Waves and Vibrations in Crystals, Holden-Day.

Osen, A., Amundsen, L., and Reitan, A., 1999, Removal of water-layer multiples from multicomponent sea-bottom data: Geophysics, **64**, 838-851.

Rickett, J.E., and Sava, P.C., 2002, Offset and angle-domain common image-point gathers for shot-profile migration: Geophysics, **67**, 883-889.

Ristow, D., and Ruhl, T., 1994, Fourier finite-difference migration: Geophysics, **59**, 1882-1893.

Rosales, D., and Rickett, J., 2001, PS-wave polarity reversal in angle domain common-image gathers, 71st Ann. Internat. Mtg: Soc. of Expl. Geophys., 20, 1843-1846.

Rosales, D.A., and Biondi, B., 2005, Converted-waves angle-domain common-image gathers, 75th Ann. Internat. Mtg.: Soc. of Expl. Geophys., 24, 959-962.

Ruhl, T., Kopp, C., and Ristow, D., 1995, Fourier Finite-Difference Migration For Steeply Dipping Reflectors With Complex Overburden: Geophysical Prospecting, **43**, 919-938.

Saint Raymond, X., 1991, Elementary introduction to the theory of pseudodifferential operators, CRT Press.

Sava, P.C., and Fomel, S., 2003, Angle-domain common-image gathers by wavefield continuation methods: Geophysics, **68**, 1065-1074.

Schalkwijk, K.M., Wapenaar, C.P.A., and Verschuur, D.J., 2003, Adaptive decomposition of multicomponent ocean-bottom seismic data into downgoing and upgoing P- and S-waves: Geophysics, **68**, 1091-1102.

Schoenberg, M., and Muir, F., 1989, A Calculus For Finely Layered Anisotropic Media: Geophysics, **54**, 581-589.

Schultz, P.S., and Sherwood, J.W.C., 1980, Depth migration before stack: Geophysics, **45**, 376-393.

Shan, G., and Biondi, B., 2004, Imaging overturned waves by plane-wave migration in tilted coordinates, 74th Ann. Internat. Mtg.: Soc. of Expl. Geophys., 23, 969-972.

Shuvalov, A.L., 2001, On the theory of plane inhomogeneous waves in anisotropic elastic media: Wave Motion, **34**, 401-429.

Silawongsawat, C., 1998. Elastic Wavefield Modeling by Phase Shift Cascade. M.Sc., Univ. of Calgary.

Spitz, S., 1991, Seismic trace interpolation in the F-X domain: Geophysics, **56**, 785-794.

Stewart, R., Gaiser, J., Brown, R., and Lawton, D., 2002, Converted-wave seismic exploration: Methods: Geophysics, **67**, 1348-1363.

____, 2003, Converted-wave seismic exploration: Applications: Geophysics, **68**, 40-57.

Stoffa, P.L., Fokkema, J.T., Freire, R.M.D., and Kessinger, W.P., 1990, Split-Step Fourier Migration: Geophysics, **55**, 410-421.

Stolt, R.H., 1978, Migration By Fourier-Transform: Geophysics, **43**, 23-48.

Strang, G., 1988, Linear Algebra and its Applications, Harcourt Brace Jovanovich.

Sun, R., and McMechan, G.A., 2001, Scalar reverse-time depth migration of prestack elastic seismic data: Geophysics, **66**, 1519-1527.

Thomsen, L., 1986, Weak elastic anisotropy: Geophysics, **51**, 1954-1966.

____, 1988, Reflection seismology over azimuthally anisotropic media: Geophysics, **53**, 304-313.

____, 1999, Converted-wave reflection seismology over inhomogeneous, anisotropic media: Geophysics, **64**, -690.

Thomsen, L., Tsvankin, I., and Mueller, M.C., 1999, Coarse-layer stripping of vertically variable azimuthal anisotropy from shear-wave data: Geophysics, **64**, 1126-1138.

Thomson, W., 1950, Transmission of elastic waves through a stratified solid: Journal of Applied Physics, **21**, 89-93.

Ting, T.C.T., 1996, Anisotropic Elasticity: Theory and Applications, Oxford University Press., Oxford.

Tsvankin, I., 1996, P-wave signatures and notation for transversely isotropic media: An overview: Geophysics, **61**, 467-483.

____, 1997, Reflection moveout and parameter estimation for horizontal transverse isotropy: Geophysics, **62**, 614-629.

Versteeg, R., 1994, The Marmousi experience: Velocity model determination on a synthetic complex data set: The Leading Edge, **13**, 927-936.

Wapenaar, C.P.A., 1990, Representation of seismic sources in the one-way wave equations: Geophysics, **55**, 786-790.

Wapenaar, C.P.A., and Berkhout, A.J., 1989, Elastic wave field extrapolation: Redatuming of Single- and Multi-component Seismic Data, Elsevier Science Publ. Co., Inc.

Winterstein, D.F., 1990, Velocity anisotropy terminology for geophysicists: Geophysics, **55**, 1070-1088.

Winterstein, D.F., and Meadows, M.A., 1991, Shear-wave polarizations and subsurface stress directions at Lost Hills field: Geophysics, **56**, 1331-1348.

Woodhouse, J.H., 1974, Surface waves in laterally varying layered structure: Geophys. J. Roy. Astr. Soc., **37**, 461-490.

Zhang, Y., Sun, J.C., and Gray, S.H., 2003, Aliasing in wavefield extrapolation prestack migration: Geophysics, **68**, 629-633.

Zhe, J.P., and Greenhalgh, S.A., 1997, Prestack multicomponent migration: Geophysics, **62**, 598-613.

APPENDIX A: NECESSARY AND SUFFICIENT CONDITIONS FOR CUBIC SOLUTIONS TO THE KELVIN-CHRISTOFFEL EQUATION

The Kelvin-Christoffel equation has the associated characteristic equation (2-2), which is

$$\det(\mathbf{\Gamma}(\mathbf{s}) - \rho\mathbf{I}) = 0\,, \tag{A-1}$$

For a slowness vector $\mathbf{s} = (s_1 \quad s_2 \quad s_3)^T$, and 6-by-6 stiffness matrix $\mathbf{C}$, the Christoffel matrix, Γ, can be written as follows:

$$\begin{aligned}\mathbf{\Gamma} = \mathbf{G}_{11}\mathbf{s}_1^2 + (\mathbf{G}_{12} + \mathbf{G}_{21})\mathbf{s}_1\mathbf{s}_2 + (\mathbf{G}_{13} + \mathbf{G}_{31})\mathbf{s}_1\mathbf{s}_3 \\ + \mathbf{G}_{22}\mathbf{s}_2^2 + (\mathbf{G}_{23} + \mathbf{G}_{32})\mathbf{s}_2\mathbf{s}_3 + \mathbf{G}_{33}\mathbf{s}_3^2\end{aligned}\,, \tag{A-2}$$

where

$$\mathbf{G}_{11} = \begin{pmatrix} C_{11} & C_{16} & C_{15} \\ C_{16} & C_{66} & C_{56} \\ C_{15} & C_{56} & C_{55} \end{pmatrix}, \mathbf{G}_{12} = \begin{pmatrix} C_{16} & C_{12} & C_{14} \\ C_{66} & C_{26} & C_{46} \\ C_{56} & C_{25} & C_{45} \end{pmatrix}, \mathbf{G}_{13} = \begin{pmatrix} C_{15} & C_{14} & C_{13} \\ C_{56} & C_{46} & C_{36} \\ C_{55} & C_{45} & C_{35} \end{pmatrix},$$

$$\mathbf{G}_{22} = \begin{pmatrix} C_{66} & C_{26} & C_{46} \\ C_{26} & C_{22} & C_{24} \\ C_{46} & C_{24} & C_{44} \end{pmatrix}, \mathbf{G}_{23} = \begin{pmatrix} C_{56} & C_{46} & C_{36} \\ C_{25} & C_{24} & C_{23} \\ C_{45} & C_{44} & C_{34} \end{pmatrix}, \mathbf{G}_{33} = \begin{pmatrix} C_{55} & C_{45} & C_{35} \\ C_{45} & C_{44} & C_{34} \\ C_{35} & C_{34} & C_{33} \end{pmatrix},$$

and

$$\mathbf{G}_{21} = \mathbf{G}_{12}^T, \mathbf{G}_{31} = \mathbf{G}_{13}^T, \mathbf{G}_{32} = \mathbf{G}_{23}^T\,. \tag{A-3}$$

Note that these matrices can be related to the **Q**, **R** and **T** matrices used in this thesis [as defined in equation (2-7)] by

$$\begin{aligned}\mathbf{Q} &= \mathbf{G}_{11}\mathbf{s}_1^2 + (\mathbf{G}_{12} + \mathbf{G}_{21})\mathbf{s}_1\mathbf{s}_2 + \mathbf{G}_{22}\mathbf{s}_2^2 \\ \mathbf{R} &= \mathbf{G}_{13}\mathbf{s}_1 + \mathbf{G}_{23}\mathbf{s}_2 \\ \mathbf{T} &= \mathbf{G}_{33}\end{aligned}\,. \tag{A-4}$$

Irrespective of symmetry, it is assumed that the diagonal elements of $\mathbf{G}_{11}, \mathbf{G}_{22}$ and $\mathbf{G}_{33}$ are non-zero. Therefore Γ has the form:

$$\mathbf{\Gamma} = \begin{pmatrix} \hat{\Gamma}_{11}(s_1,s_2,s_3) + C_{55}s_3^2 & \hat{\Gamma}_{12}(s_1,s_2,s_3) & \hat{\Gamma}_{13}(s_1,s_2,s_3) \\ \hat{\Gamma}_{12}(s_1,s_2,s_3) & \hat{\Gamma}_{22}(s_1,s_2,s_3) + C_{44}s_3^2 & \hat{\Gamma}_{23}(s_1,s_2,s_3) \\ \hat{\Gamma}_{13}(s_1,s_2,s_3) & \hat{\Gamma}_{23}(s_1,s_2,s_3) & \hat{\Gamma}_{33}(s_1,s_2,s_3) + C_{33}s_3^2 \end{pmatrix} \qquad \text{(A-5)}$$

where the $\hat{\Gamma}_{ij}$'s are polynomials of at most degree 2 in s_1, s_2, s_3.

We now seek the most general form of $\hat{\Gamma}_{ij}$'s (and hence $\mathbf{G}_{IJ}$'s) such that the characteristic equation (2-2) is cubic (or lower degree) in s_3^2, with no odd powers of s_3, for all choices of s_1, s_2.

A.1 Lemma 1

$\hat{\Gamma}_{11}, \hat{\Gamma}_{22}$ and $\hat{\Gamma}_{33}$ must have only even powers of s_3.

Proof

Assume this is not so – i.e. assume that at least one of $\hat{\Gamma}_{11}, \hat{\Gamma}_{22}$ and $\hat{\Gamma}_{33}$ contains odd powers of s_3. Then $\det(\mathbf{\Gamma}(\mathbf{s}) - \rho\mathbf{I})$ includes the term $(\hat{\Gamma}_{11} - \rho)(\hat{\Gamma}_{22} - \rho)(\hat{\Gamma}_{33} - \rho)$, which has odd powers of s_3, violating the assumption on the characteristic equation.

A.1.1 Corollary 1

$\hat{\Gamma}_{11}, \hat{\Gamma}_{22}$ and $\hat{\Gamma}_{33}$ do not depend on s_3 at all.

This is true because, apart from the matrix $\mathbf{G}_{33}$ in equation (A-2), the other $\mathbf{G}_{IJ}$ matrices only contribute terms that are linear in s_3. Since $\mathbf{G}_{33}$ has been explicitly included along the diagonal of $\mathbf{\Gamma}$ in equation (A-5), the other terms in that matrix are at most linear in s_3. But, from A.1 Lemma 1, $\hat{\Gamma}_{11}, \hat{\Gamma}_{22}$ and $\hat{\Gamma}_{33}$ can only contain *even* powers of s_3, implying that they do not depend on s_3.

A.1.2 Corollary 2

$\mathbf{G}_{13}, \mathbf{G}_{23}$ must take the form

$$\mathbf{G}_{13} = \begin{pmatrix} 0 & C_{14} & C_{13} \\ C_{56} & 0 & C_{36} \\ C_{55} & C_{45} & 0 \end{pmatrix}, \mathbf{G}_{23} = \begin{pmatrix} 0 & C_{46} & C_{36} \\ C_{25} & 0 & C_{23} \\ C_{45} & C_{44} & 0 \end{pmatrix}. \tag{A-6}$$

This follows immediately from Corollary 1, under the condition it must hold for all s_1, s_2, which implies that both $\mathbf{G}_{13} + \mathbf{G}_{31}$ and $\mathbf{G}_{23} + \mathbf{G}_{32}$ have zero diagonals. Since $\mathbf{G}_{31} = \mathbf{G}_{13}^T$ and $\mathbf{G}_{32} = \mathbf{G}_{23}^T$, the diagonals of $\mathbf{G}_{13}$ and $\mathbf{G}_{23}$ are zero.

Hence

$$C_{15} = C_{46} = C_{35} = C_{56} = C_{24} = C_{34} = 0. \tag{A-7}$$

A.2 Lemma 2

$\hat{\Gamma}_{13}, \hat{\Gamma}_{23}$ are linear in s_3.

This is shown by direct computation. Using (A-2), (A-5), (A-6) and (A-7), we have

$$\hat{\Gamma}_{13} = C_{14} s_1 s_2 + (C_{13} + C_{55}) s_1 s_3 + (C_{45} + C_{36}) s_2 s_3. \tag{A-8}$$

and

$$\hat{\Gamma}_{23} = C_{25} s_1 s_2 + (C_{23} + C_{44}) s_2 s_3 + (C_{45} + C_{36}) s_1 s_3. \tag{A-9}$$

A.2.1 Corollary 3

$$C_{14} = C_{25} = 0. \tag{A-10}$$

This follows from equations (A-8) and (A-9). If this is not so, then $\det(\mathbf{\Gamma}(\mathbf{s}) - \rho \mathbf{I})$ would contain terms odd in s_3, resulting from the quadratic expressions $\hat{\Gamma}_{13}^2$ and $\hat{\Gamma}_{23}^2$ which arise during evaluation of the determinant.

Combining conditions given by equation (A-6) and (A-10), we have forms of the $\mathbf{G}_{IJ}$ matrices which are necessary to ensure a cubic solution

$$\mathbf{G}_{11} = \begin{pmatrix} C_{11} & C_{16} & 0 \\ C_{16} & C_{66} & 0 \\ 0 & 0 & C_{55} \end{pmatrix}, \mathbf{G}_{12} = \begin{pmatrix} C_{16} & C_{12} & 0 \\ C_{66} & C_{26} & 0 \\ 0 & 0 & C_{45} \end{pmatrix}, \mathbf{G}_{13} = \begin{pmatrix} 0 & 0 & C_{13} \\ 0 & 0 & C_{36} \\ C_{55} & C_{45} & 0 \end{pmatrix},$$
$$\mathbf{G}_{22} = \begin{pmatrix} C_{66} & C_{26} & 0 \\ C_{26} & C_{22} & 0 \\ 0 & 0 & C_{44} \end{pmatrix}, \mathbf{G}_{23} = \begin{pmatrix} 0 & 0 & C_{36} \\ 0 & 0 & C_{23} \\ C_{45} & C_{44} & 0 \end{pmatrix}, \mathbf{G}_{33} = \begin{pmatrix} C_{55} & C_{45} & 0 \\ C_{45} & C_{44} & 0 \\ 0 & 0 & C_{33} \end{pmatrix}. \quad \text{(A-11)}$$

A.2 Proposition

The forms of $\mathbf{G}_{IJ}$ in equation (A-11) are necessary and sufficient to ensure that the characteristic equation (2-2) is cubic (or lower degree) in s_3^2.

Proof

The necessary part has been proven in A.1 Lemma 1, Lemma 2 and associated corollaries. To show that it is sufficient, perform direct substitution. Using (A-11), equation (A-5) can be written as

$$\mathbf{\Gamma} = \begin{pmatrix} B_{11}(s_1, s_2) + C_{55}s_3^2 & B_{12}(s_1, s_2) + C_{45}s_3^2 & B_{13}(s_1, s_2) \\ B_{12}(s_1, s_2) + C_{45}s_3^2 & B_{22}(s_1, s_2) + C_{44}s_3^2 & B_{23}(s_1, s_2) \\ B_{13}(s_1, s_2) & B_{23}(s_1, s_2) & B_{33}(s_1, s_2) + C_{33}s_3^2 \end{pmatrix}, \quad \text{(A-12)}$$

where

$$B_{11} \equiv C_{11}s_1^2 + 2C_{16}s_1s_2 + C_{66}s_2^2$$
$$B_{12} \equiv C_{16}s_1^2 + (C_{12} + C_{66})s_1s_2 + C_{26}s_2^2$$
$$B_{22} \equiv C_{66}s_1^2 + 2C_{26}s_1s_2 + C_{22}s_2^2$$
$$B_{13} \equiv (C_{13} + C_{55})s_1 + (C_{36} + C_{45})s_2$$
$$B_{23} \equiv (C_{36} + C_{45})s_1 + (C_{23} + C_{44})s_2$$
$$B_{33} \equiv C_{55}s_1^2 + 2C_{45}s_1s_2 + C_{44}s_2^2.$$

Evaluation of $\det(\mathbf{\Gamma}(\mathbf{s}) - \rho\mathbf{I})$ using (A-12) gives a cubic in s_3^2.

Hence the most general stress-strain matrix **C**, which gives rise to a Christoffel matrix with a characteristic equation that is cubic in s_3^2 is

$$\mathbf{C} = \begin{pmatrix} C_{11} & C_{12} & C_{13} & 0 & 0 & C_{16} \\ & C_{22} & C_{23} & 0 & 0 & C_{26} \\ & & C_{33} & 0 & 0 & C_{36} \\ & & & C_{44} & C_{45} & 0 \\ & & & & C_{55} & 0 \\ & & & & & C_{66} \end{pmatrix}, \qquad \text{(A-13)}$$

with the lower half of the matrix implied by symmetry. This form corresponds to a general orthorhombic symmetry, with a horizontal symmetry plane.

APPENDIX B: SLOWNESS SOLUTIONS TO KELVIN-CHRISTOFFEL EQUATION AND ASSOCIATED BRANCH POINTS FOR HTI MEDIUM

An HTI medium has a stiffness matrix, when expressed using Voigt notation in a coordinate system such that the symmetry axis is parallel to the *x*-axis, with the form [equation (1-14)]

$$\mathbf{C} = \begin{pmatrix} C_{11} & C_{13} & C_{13} & & & \\ C_{13} & C_{33} & C_{23} & & & \\ C_{13} & C_{23} & C_{33} & & & \\ & & & C_{44} & & \\ & & & & C_{66} & \\ & & & & & C_{66} \end{pmatrix}, \tag{B-1}$$

with the constraint $C_{44} = \frac{1}{2}\left(C_{33} - C_{23}\right)$, and spaces implying zeros, as usual.

This leads to a Christoffel matrix with the form

$$\mathbf{\Gamma} = \begin{pmatrix} C_{11}s_1^2 + C_{66}s_2^2 + C_{66}s_3^2 & \left(C_{13} + C_{66}\right)s_1 s_2 & \left(C_{13} + C_{66}\right)s_1 s_3 \\ \left(C_{13} + C_{66}\right)s_1 s_2 & C_{66}s_1^2 + C_{33}s_2^2 + C_{44}s_3^2 & \left(C_{33} - C_{44}\right)s_2 s_3 \\ \left(C_{13} + C_{66}\right)s_1 s_3 & \left(C_{33} - C_{44}\right)s_2 s_3 & C_{66}s_1^2 + C_{44}s_2^2 + C_{33}s_3^2 \end{pmatrix}. \tag{B-2}$$

B.1 Slowness solutions

The required eigensolutions are found by solving the characteristic equation $\det\left(\mathbf{\Gamma}(\mathbf{s}) - \rho\mathbf{I}\right) = 0$ for the vertical slowness $q \equiv s_3$.

The velocity v is related to the slowness via

$$\frac{1}{v^2} = s_1^2 + s_2^2 + s_3^2 . \tag{B-3}$$

Following Musgrave (1970, p.95), the following quantities are defined:

$$\begin{aligned}
a &\equiv C_{33} - C_{66} \\
c &\equiv C_{33} - C_{23} - 2C_{66} = 2\left(C_{44} - C_{66}\right) \\
d &\equiv C_{13} + C_{66} \\
g &\equiv \tfrac{1}{2}\left(C_{33} + C_{23}\right) = C_{33} - C_{44} \\
h &\equiv C_{11} - C_{66} \\
H &\equiv \rho v^2 - C_{66}
\end{aligned} \tag{B-4}$$

Defining $m^2 = v^2\left(s_2^2 + s_3^2\right)$, and $n^2 = v^2 s_1^2 = 1 - m^2$, the characteristic equation leads to a cubic in *H*, which can be separated into a linear equation

$$H - \tfrac{1}{2} m^2 c = 0 \ , \tag{B-5}$$

and a quadratic equation

$$\left(H - m^2 a\right)\left(H - n^2 h\right) - m^2 n^2 d^2 = 0 \, . \tag{B-6}$$

Since the medium is transversely isotropic, it supports P-, SV- and SH-type wave-modes, with the first two having polarizations in the plane defined by the vertical and the symmetry axis, while the SH-wave is polarized in the "isotropy plane" orthogonal to the symmetry axis.

The horizontal slownesses may be expressed in terms of a radial slowness, *p*, along the propagation direction, φ (relative to the symmetry axis), by $s_1 = p\cos\varphi$ and $s_2 = p\sin\varphi$.

The first equation, (B-5), then leads to the SH-wave type solution

$$s_3^2 = q_{SH}^2 = \frac{\rho - C_{66} p^2 \cos^2\varphi - C_{44} p^2 \sin^2\varphi}{C_{44}} \, . \tag{B-7}$$

Equation (B-6) provides the P-wave and SV-wave type solutions. Rearranging into a quadratic in $q^2 = s_3^2$, we get

$$\alpha q^4 + \beta q^2 + \gamma = 0 \, , \tag{B-8}$$

where

$$\alpha = C_{66}^2 + aC_{66}$$

$$\beta = C_{66}\left[C_{66}\left(C_{66} + a\right) + \left(C_{66}\left(h - a\right) + ah - d^2\right)\cos^2\varphi\right]p^2 - (2C_{66} + a)\,\rho$$

$$\gamma = \left[C_{66}^2 + aC_{66} + \left(C_{66}\left(h - a\right) + ah - d^2\right)\cos^2\varphi - \left(ah - d^2\right)\cos^4\varphi\right]p^4$$
$$- \rho\left[\left(2C_{66} + a\right) + \left(h - a\right)\cos^2\varphi\right]p^2 + \rho^2.$$

Equation (B-8) is solved for q^2 using the standard solution for quadratics, giving a P-wave solution

$$q_P^2 = \frac{-\beta - \sqrt{\beta^2 - 4\alpha\gamma}}{2\alpha}, \qquad \text{(B-9)}$$

and an SV-wave solution

$$q_{SV}^2 = \frac{-\beta + \sqrt{\beta^2 - 4\alpha\gamma}}{2\alpha}. \qquad \text{(B-10)}$$

Equations (B-7), (B-9) and (B-10) obviously provide two solutions each for the vertical slowness, corresponding, when real, to up and down going solutions.

B.2 Branch points

Branch points occur for each mode $M \in \{P, SV, SH\}$ when q_M^2 becomes zero, corresponding to the transition between propagating energy and evanescent energy. For SH-waves this is easily seen from equation (B-7) to be at the point

$$p^2 = p_{bp(SH)}^2 = \frac{\rho}{C_{44} + \left(C_{66} - C_{44}\right)\cos^2\varphi}. \qquad \text{(B-11)}$$

For P- and SV-waves the branch points are obtained by setting $q = 0$ in equation (B-8), which then requires $\gamma = 0$. This leads to two solutions

$$p^2 = p_{bp(P,SV)}^2 = \frac{-\beta_1 \mp \sqrt{\beta_1^2 - 4\alpha_1\rho^2}}{2\alpha_1}, \qquad \text{(B-12)}$$

where

$$\alpha_1 = C_{66}^2 + aC_{66} + \left[C_{66}\left(h-a\right) + ah - d^2\right]\cos^2\varphi - \left(ah - d^2\right)\cos^4\varphi$$
.

$$\beta_1 = -\rho\left[\left(2C_{66} + a\right) + \left(h-a\right)\cos^2\varphi\right]$$

From equations (B-9) and (B-10), the P-wave branch point (with $q_P^2 = 0$), corresponds to $\beta < 0$ (recall that $\gamma = 0$ for the branch point), whereas the SV-wave branch point corresponds to a $\beta > 0$. In equation (B-12) the minus is associated with the P-wave and the plus sign with the SV-wave. This identification could be demonstrated by substitution of equation (B-12) in the formula for β in equation (B-8), to confirm that a minus sign in (B-12) leads to $\beta < 0$, while a plus sign in (B-12) leads to $\beta > 0$, though the resulting algebra is cumbersome.

An alternative argument can be made. Equations (B-9) and (B-10) imply that $q_{SV}^2 > q_P^2$ for all values of *p*. Hence q_{SV} is real when $q_P^2 = 0$, but q_P is imaginary when $q_{SV}^2 = 0$. Assuming that both slowness curves progress from real values to imaginary values as p^2 increases, it then follows that the P-wave branch points $\pm p_{bp(P)}$ are reached before the SV-wave branch points $\pm p_{bp(SV)}$. Hence $p_{bp(SV)}^2 > p_{bp(P)}^2$, which requires the plus sign to be assigned to the SV-wave in equation (B-12), as asserted.

APPENDIX C: ISOTROPIC MEDIA POLARIZATION VECTORS

Defining

$$\mathbf{A} = \boldsymbol{\Gamma}(\mathbf{s}) - \rho\,\mathbf{I}\,, \tag{C-1}$$

and assuming propagation in the *x*-*z* plane, so that $s_2 = 0$, we find for an isotropic medium, with density ρ and Lame parameters λ and μ, that

$$\mathbf{A} = \begin{pmatrix} (\lambda+2\mu)s_1^2 + \mu s_3^2 - \rho & 0 & (\lambda+\mu)s_1 s_3 \\ 0 & \mu\left(s_1^2+s_3^2\right)-\rho & 0 \\ (\lambda+\mu)s_1 s_3 & 0 & (\lambda+2\mu)s_3^2 + \mu s_1^2 - \rho \end{pmatrix}. \tag{C-2}$$

The eigenvectors are to be determined by computing the adjugate of **A**, adj(**A**), as described in (2-4), for P- and S-wave velocities, α and β, respectively, then multiplying by an arbitrary vector **w**.

C.1 P-wave solution

Choosing $\mathbf{w} = \begin{pmatrix}1 & 0 & 0\end{pmatrix}^T$, is equivalent to selecting the first column of $\mathbf{C} = \mathrm{adj}(\mathbf{A})$. The elements in the first column of **C** are given by cofactors of **A**, which are

$$\begin{aligned} C_{11} &= \left[\mu\left(s_1^2+s_3^2\right)-\rho\right]\left[(\lambda+2\mu)s_3^2+\mu s_1^2-\rho\right] \\ C_{21} &= 0 \\ C_{31} &= -(\lambda+\mu)s_1 s_3\left[\mu\left(s_1^2+s_3^2\right)-\rho\right]. \end{aligned} \tag{C-3}$$

Setting

$$\mathbf{s.s} = s_1^2 + s_3^2 = 1/\alpha^2 = \frac{\rho}{\lambda+2\mu}\,,$$

in order to obtain a P-wave solution, we get

$$\mathbf{d}^{(P)} = \frac{(\lambda+\mu)^2 \rho\, s_1}{(\lambda+2\mu)}\begin{pmatrix} s_1 \\ 0 \\ s_3 \end{pmatrix}. \tag{C-4}$$

Apart from the scaling factor, this is the solution provided in equation (2-5).

C.2 S-wave solutions

To find an S-wave solution, we must set

$$\mathbf{s.s} = s_1^2 + s_3^2 = 1/\beta^2 = \frac{\rho}{\mu}. \tag{C-5}$$

However, this has the effect of making A_{22} in equation (C-2) equal to zero. When the adjugate of **A** is calculated, **C** has only one non-zero element, C_{22}. The consequence is that, irrespective of which **w** is chosen, the resulting eigenvector $\mathbf{d} = \mathbf{Cw}$, is parallel to the *y*-axis. This corresponds to the SH-wave polarization vector in equation (2-5).

To obtain the SV-wave vector, the term $[\mu(s_1^2 + s_3^2) - \rho]$ must first be factored out of **C**. Letting

$$\mathbf{C}' = \frac{\mathbf{C}}{\mu(s_1^2 + s_3^2) - \rho}, \tag{C-6}$$

we obtain

$$\begin{aligned} C'_{11} &= (\lambda + 2\mu)s_3^2 + \mu s_1^2 - \rho \\ C'_{21} &= 0 \\ C'_{31} &= -(\lambda + \mu)s_1 s_3 . \end{aligned} \tag{C-7}$$

Then, using equation (C-5), and setting $\mathbf{w} = (1 \quad 0 \quad 0)^T$, gives the eigenvector

$$\mathbf{d}^{(SV)} = (\lambda + \mu)s_3 \begin{pmatrix} s_3 \\ 0 \\ -s_1 \end{pmatrix}. \tag{C-8}$$

This agrees with equation (2-5) aside from the arbitrary scale factor.

APPENDIX D: ISOTROPIC MEDIA DISPLACEMENT-STRESS EIGENVECTORS

In this appendix, the eigenvectors required to construct composition and decomposition matrices are evaluated for isotropic media. It is shown that the eigenvectors for each mode depend only on two parameters, one of which is the V_P / V_S ratio.

The composition matrix $\mathbf{D}$ is constructed from the eigenvectors [equation (2-21)]

$$\hat{\mathbf{b}}_i = \varepsilon_i \begin{pmatrix} \mathbf{u}_i \\ \boldsymbol{\tau}_i \end{pmatrix}, \quad i = 1, \ldots, 6. \tag{D-1}$$

where the $\mathbf{u}_i$ are found by solving the Kelvin-Christoffel equation, and the $\boldsymbol{\tau}_i$ are related to them through the stress-strain relationship. The ε_i are normalization constants, as defined by (2-28). The 6 indices correspond to three different modes with up and down-going wave directions. Once $\mathbf{D}$ is known, the decomposition matrix $\mathbf{D}^{-1}$ is given simply by equation (2-24).

Only the down-going waves are considered in the following analysis. Similar analysis applies to the up-going waves. In the isotropic case, using a coordinate frame such that SV modes are polarized in the *x*-*z* plane, the displacement eigenvector associated with the down-going P-wave is

$$\mathbf{u}_P^D = \alpha \begin{pmatrix} s_x \\ 0 \\ q_P \end{pmatrix}, \tag{D-2}$$

where α is the P-wave velocity, s_x is the horizontal slowness, and q_P is the vertical slowness for the P-wave.

Using equation (2-25) the corresponding traction eigenvector is

$$\boldsymbol{\tau}_P^D = -\alpha\rho\begin{pmatrix} 2\beta^2 s_x q_P \\ 0 \\ 1-2\beta^2 s_x^2 \end{pmatrix}, \tag{D-3}$$

where ρ is density and β is the S-wave velocity.

For the SV wave-mode the corresponding eigenvectors are:

$$\mathbf{u}_{SV}^D = \beta\begin{pmatrix} q_S \\ 0 \\ -s_x \end{pmatrix} \tag{D-4}$$

and

$$\boldsymbol{\tau}_{SV}^D = -\beta\rho\begin{pmatrix} \beta^2\left(q_s^2 - s_x^2\right) \\ 0 \\ -2\beta^2 s_x q_S \end{pmatrix}, \tag{D-5}$$

where q_S is the vertical slowness for the S-waves (SV or SH).

For isotropic propagation the SH-wave is completely decoupled from the P- and SV-waves, and can be independently extrapolated.

Because of the simple form of the decomposition matrix in equation (2-24), the above P and SV eigenvectors define fully the decomposition for the corresponding modes. Equations (D-2) and (D-3) show that even though the displacement eigenvector for the P-wave is independent of the S-wave velocity, the traction vector is not. Therefore, the complete eigenvector $\hat{\mathbf{b}}_P^D$, a column vector of $\mathbf{D}$, is dependent on the S-wave velocity. So is the corresponding row-vector $\hat{\mathbf{g}}_P^D$ in the decomposition matrix $\mathbf{D}^{-1}$. This implies that we cannot exactly decouple the handling of P- and S-waves within the decomposition and recomposition steps. However, in the case that $\alpha = \gamma_0\beta$, with γ_0, the V_P / V_S ratio, being constant for a given layer, the dependence on β in equation (D-3) can be replaced with a further dependence on α.

Surprisingly, perhaps, the S-wave eigenvectors given in equations (D-4) and (D-5) are *not* dependent on the P-wave velocity.

APPENDIX E: EIGENVECTOR NORMALIZATION AND BRANCH POINTS

In this appendix the behaviour of the normalization coefficient in equation (2-28) is examined near the evanescent cut-off points. This behaviour is important to avoid the introduction of artifacts during the composition and decomposition steps in the wavefield extrapolators of equations (2-29) and (2-30). Care about the choice of branch is required to avoid introducing discontinuous behaviour in equation (2-28), after the introduction of imaginary velocity to avoid the singularity.

Let us consider the isotropic case from an analytic point of view first. Only the P- and SV- modes are considered, as it may be readily shown that the SH-mode has the same normalization as the SV.

From equations (D-2)-(D-5), we have

$$\varepsilon_M^D = 1/\sqrt{\zeta_M} \quad \text{and} \quad \varepsilon_{SV}^D = 1/\sqrt{\zeta_{SV}}\ , \tag{E-1}$$

where

$$\begin{aligned} \zeta_P &= 2\mathbf{u}_P^D \cdot \boldsymbol{\tau}_P^D &= -2\rho\alpha^2 q_P \\ \zeta_{SV} &= 2\mathbf{u}_{SV}^D \cdot \boldsymbol{\tau}_{SV}^D &= -2\rho\beta^2 q_{SV}\,. \end{aligned}$$

If the exact (i.e. pure real) velocities, α and β, are used to calculate q_P and q_{SV}, then ζ_P ranges along the real axis between $-2\rho\alpha$ and 0, for propagating modes, and along the imaginary axis from 0 to $\pm i\infty$ for evanescent modes.

The factors ζ_P and $\sqrt{\zeta_P}$ are plotted in the complex plane for the isotropic case in Figure E.1. In this case a branch cut chosen along the positive real axis, as shown, allows evaluation of the square root without introducing a discontinuity. For the isotropic case, the square roots $\sqrt{\zeta_{SV}}$ and $\sqrt{\zeta_{SH}}$ are similarly well defined for the same branch cut.

Figure E.2, on the other hand, illustrates the situation for an HTI medium, with the parameters of Table 2.1. In this case, for both S1 and S2 modes, the function ζ_M completes a circuit around the origin. This means that the branch cut cannot be avoided when evaluating the square root. To ensure continuity, the function must be "phase unwrapped", by constraining the phase to vary smoothly as a function of slowness. Mathematically, this implies changing from one sheet of the Riemann surface to another as ζ_M completes a circuit around the origin.[1]

If the phase unwrapping is not performed, then a discontinuity in the square root arises, as illustrated in Figure E.3, which show the enlarged results, as in Figure E.2 (c) and (d), but using only the principle value of the square root. To avoid artifacts when designing the extrapolation operator, the phase unwrapped version of the normalization must be used.

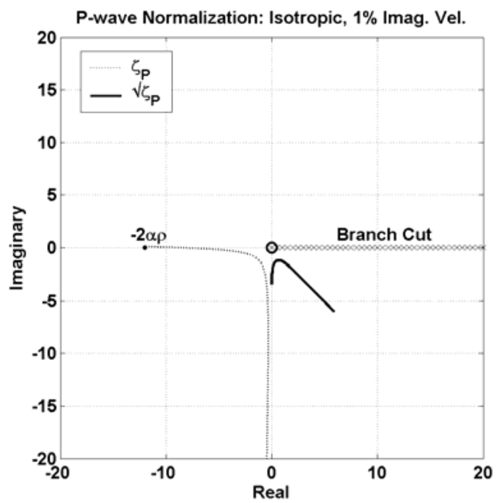

Figure E.1. P-wave normalization factors ζ_P and $\sqrt{\zeta_P}$ [see equation (E-1)], for isotropic medium with P-wave velocity 3 km/s and density 2 gm/cm^3. In calculating the normalization, the velocity has been perturbed by the addition of 1% imaginary velocity, to avoid the singular point (circle). The branch cut can be chosen to ensure a continuous evaluation of the square root. The point $-2\alpha\rho$ indicated on the ζ_P curve corresponds to vertical propagation ($s_x = 0$).

[1] For a discussion of branch cuts and Riemann surfaces, see box 6.2 on page 197 of Aki and Richards Aki, K., and Richards, P.G., 2002, Quantitative Seismology: Second Edition, University Science Books, Sausalito, California.)

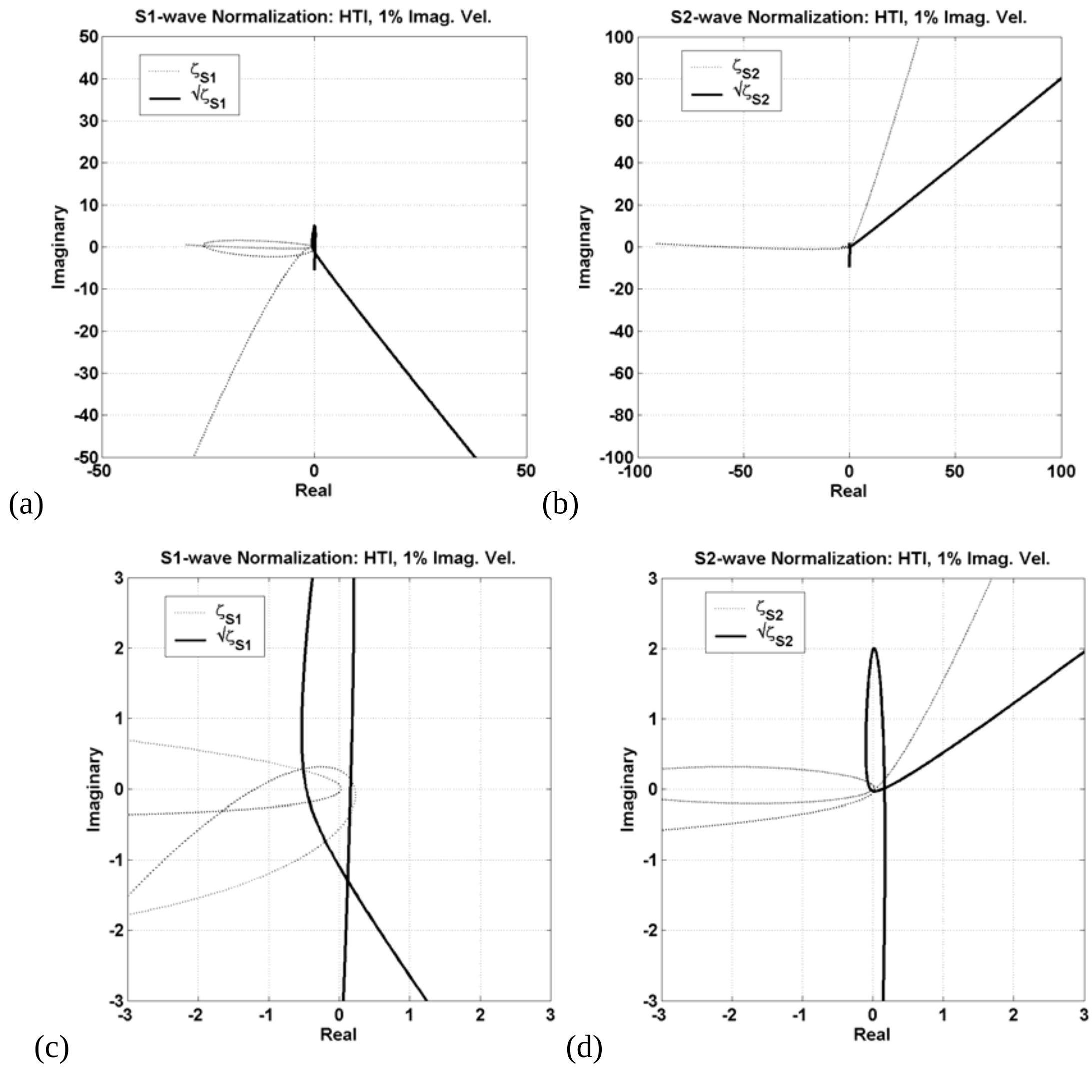

Figure E.2. Plots of: (a) S1-wave normalization factors ζ_{S1} and $\sqrt{\zeta_{S1}}$, and; (b) S2-wave normalization factors ζ_{S2} and $\sqrt{\zeta_{S2}}$, for an HTI model with anisotropy given by Table 2.1. Both factors ζ_{S1} and ζ_{S2} encircle the origin, which is a branch point, as shown in the enlarged figures (c) and (d). In order to obtain continuous values for the square root, it is necessary to move onto a different sheet of the Riemann surface.

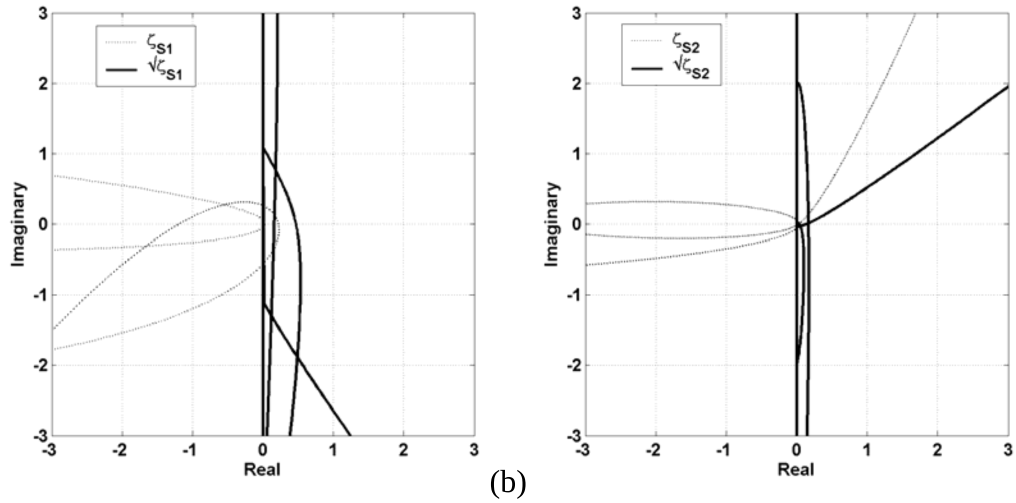

(a) (b)

Figure E.3. Plots of: (a) S1-wave normalization factors ζ_{S1} and $\sqrt{\zeta_{S1}}$, and; (b) S2-wave normalization factors ζ_{S2} and $\sqrt{\zeta_{S2}}$, using only a single sheet of the Riemann surface (i.e. without "unwinding" the phase). The result is discontinuous behaviour of $\sqrt{\zeta_{S1}}$ and $\sqrt{\zeta_{S2}}$.

APPENDIX F: RELATIONSHIP BETWEEN FORWARD DOWN-GOING AND BACKWARD UP-GOING INTERFACE PROPAGATORS

For a general medium the relationship between displacement $\mathbf{u}$ and traction τ can be written [see equations (2-7) and (2-23)]

$$\boldsymbol{\tau} = -(\mathbf{R}^T + s_3\mathbf{T})\mathbf{u}\,, \tag{F-1}$$

where

$$\begin{aligned} R_{ik} &\equiv c_{i1k3}s_1 + c_{i2k3}s_2 \\ T_{ik} &\equiv c_{i3k3} \end{aligned}.$$

There are 6 displacement eigenvectors and associated tractions, which in the case of a medium with a horizontal symmetry plane can be separated into up and down going pairs. Using the shorthand $q \equiv s_3$, and adding subscripts $M \in \{P, S1, S2\}$ to denote the wave mode, and superscripts U and D to denote up or down-going waves, equation (F-1) gives

$$\boldsymbol{\tau}_M^{U,D} = -(\mathbf{R}^T + q_M^{U,D}\mathbf{T})\mathbf{u}_M^{U,D}\,. \tag{F-2}$$

For anisotropic symmetries of orthorhombic or higher, by an appropriate choice of coordinate system such that symmetry axes are aligned along coordinates axes, we have the following form of stiffness matrix in Voigt notation:

$$\mathbf{C} = \begin{pmatrix} C_{11} & C_{12} & C_{13} & & & \\ C_{12} & C_{22} & C_{23} & & & \\ C_{13} & C_{23} & C_{33} & & & \\ & & & C_{44} & & \\ & & & & C_{55} & \\ & & & & & C_{66} \end{pmatrix}, \tag{F-3}$$

with absent entries equal to 0.

The resulting matrix forms for $\mathbf{R}$ and $\mathbf{T}$ are

$$\mathbf{R} = \begin{pmatrix} 0 & 0 & C_{13}s_1 \\ 0 & 0 & C_{23}s_2 \\ C_{55}s_1 & C_{44}s_2 & 0 \end{pmatrix} \text{ and } \mathbf{T} = \begin{pmatrix} C_{55} & 0 & 0 \\ 0 & C_{44} & 0 \\ 0 & 0 & C_{33} \end{pmatrix}. \tag{F-4}$$

Because the horizontal plane is a symmetry plane, we have the following two conditions for waves propagating upwards and downwards:

$$q_M^U = -q_M^D, \tag{F-5}$$

and

$$\mathbf{u}_M^U = \begin{pmatrix} 1 & 0 & 0 \\ 0 & 1 & 0 \\ 0 & 0 & -1 \end{pmatrix} \mathbf{u}_M^D. \tag{F-6}$$

These equations are valid for real slownesses and polarizations irrespective of the direction of extrapolation. However, for evanescent waves in which the slownesses and polarizations are complex, we have to be more careful. Equations (F-5) and (F-6) correspond to waves which decay in the direction of forward propagation. The imaginary part of slowness is positive for down-going waves and negative for up-going, leading to the correct decay. When we consider backwards propagation, on the other hand, the conjugates of the slowness and polarization must be used, to ensure correct decay. Hence the equations which are valid for *downward* extrapolation of both up and down-going waves are:

$$q_M^U = -\overline{q_M^D}, \tag{F-7}$$

and

$$\mathbf{u}_M^U = \begin{pmatrix} 1 & 0 & 0 \\ 0 & 1 & 0 \\ 0 & 0 & -1 \end{pmatrix} \overline{\mathbf{u}_M^D}. \tag{F-8}$$

Using equation (F-4), equation (F-2) gives traction for down-going waves

$$\boldsymbol{\tau}_M^D = -\begin{pmatrix} C_{55}q_M^D & 0 & C_{55}s_1 \\ 0 & C_{44}q_M^D & C_{44}s_2 \\ C_{13}s_1 & C_{23}s_2 & C_{33}q_M^D \end{pmatrix}\mathbf{u}_M^D, \tag{F-9}$$

and for up-going waves

$$\boldsymbol{\tau}_M^U = -\begin{pmatrix} C_{55}q_M^U & 0 & C_{55}s_1 \\ 0 & C_{44}q_M^U & C_{44}s_2 \\ C_{13}s_1 & C_{23}s_2 & C_{33}q_M^U \end{pmatrix}\mathbf{u}_M^U. \tag{F-10}$$

Substituting equations (F-7) and (F-8) into (F-10), recalling that the stiffness tensor **C** is real for an elastic medium, and that the horizontal slownesses s_1 and s_2 are also real, we get

$$\boldsymbol{\tau}_M^U = -\overline{\begin{pmatrix} -C_{55}q_M^D & 0 & C_{55}s_1 \\ 0 & -C_{44}q_M^D & C_{44}s_2 \\ C_{13}s_1 & C_{23}s_2 & -C_{33}q_M^D \end{pmatrix}}\begin{pmatrix} 1 & 0 & 0 \\ 0 & 1 & 0 \\ 0 & 0 & -1 \end{pmatrix}\overline{\mathbf{u}_M^D}. \tag{F-11}$$

Rearranging gives

$$\begin{aligned} \boldsymbol{\tau}_M^U &= -\begin{pmatrix} -1 & 0 & 0 \\ 0 & -1 & 0 \\ 0 & 0 & 1 \end{pmatrix}\overline{\begin{pmatrix} C_{55}q_M^D & 0 & C_{55}s_1 \\ 0 & C_{44}q_M^D & C_{44}s_2 \\ C_{13}s_1 & C_{23}s_2 & C_{33}q_M^D \end{pmatrix}}\overline{\mathbf{u}_M^D} \\ &= \begin{pmatrix} -1 & 0 & 0 \\ 0 & -1 & 0 \\ 0 & 0 & 1 \end{pmatrix}\overline{\boldsymbol{\tau}_M^D}. \end{aligned} \tag{F-12}$$

Combining (F-8) and (F-12) gives

$$\begin{pmatrix} \mathbf{u}_M^U \\ \boldsymbol{\tau}_M^U \end{pmatrix} = \begin{pmatrix} 1 & 0 & 0 & 0 & 0 & 0 \\ 0 & 1 & 0 & 0 & 0 & 0 \\ 0 & 0 & -1 & 0 & 0 & 0 \\ 0 & 0 & 0 & -1 & 0 & 0 \\ 0 & 0 & 0 & 0 & -1 & 0 \\ 0 & 0 & 0 & 0 & 0 & 1 \end{pmatrix}\begin{pmatrix} \overline{\mathbf{u}_M^D} \\ \overline{\boldsymbol{\tau}_M^D} \end{pmatrix}. \tag{F-13}$$

The eigenvector normalization scalars are related [equation (2-26)] by

$$\begin{aligned}\varepsilon_M^U &= \left(2\mathbf{u}_M^U \cdot \boldsymbol{\tau}_M^U\right)^{-1/2} \\ &= \left(\overline{-2\mathbf{u}_M^D \cdot \boldsymbol{\tau}_M^D}\right)^{-1/2} \\ &= -i\overline{\varepsilon_M^D}.\end{aligned} \tag{F-14}$$

So

$$\hat{\mathbf{b}}_M^U = \mathbf{K}\overline{\hat{\mathbf{b}}_M^D}\ , \tag{F-15}$$

where

$$\hat{\mathbf{b}}_M^{U,D} = \varepsilon_M^{U,D}\begin{pmatrix}\mathbf{u}_M^{U,D} \\ \boldsymbol{\tau}_M^{U,D}\end{pmatrix}, \tag{F-16}$$

and

$$\mathbf{K} \equiv \begin{pmatrix}-i & 0 & 0 & 0 & 0 & 0 \\ 0 & -i & 0 & 0 & 0 & 0 \\ 0 & 0 & i & 0 & 0 & 0 \\ 0 & 0 & 0 & i & 0 & 0 \\ 0 & 0 & 0 & 0 & i & 0 \\ 0 & 0 & 0 & 0 & 0 & -i\end{pmatrix}. \tag{F-17}$$

The composition matrix is $\mathbf{D} = \left(\mathbf{D}_U \quad \mathbf{D}_D\right)$, where $\mathbf{D}_{U,D} = \left(\hat{\mathbf{b}}_P^{U,D} \quad \hat{\mathbf{b}}_{S1}^{U,D} \quad \hat{\mathbf{b}}_{S2}^{U,D}\right)$, as given in equation (2-24). We therefore have

$$\mathbf{D}_U = \mathbf{K}\overline{\mathbf{D}_D}\ . \tag{F-18}$$

Now consider the relationship between up and down-going interface propagators $\mathbf{W}_{UU}$ and $\mathbf{W}_{DD}$, defined by [see equation (2-28)]

$$\begin{aligned}&\mathbf{W}_{KL}(z_n+, z_n-) = \mathbf{D}_K^{-L}\left(z_n+\right)\mathbf{D}_L\left(z_n-\right) \\ &K, L \in \{U, D\}\end{aligned}, \tag{F-19}$$

where $z_n \pm$ refer to depths infinitesimally above (-) and below(+) the depth position z_n, where a change in medium properties is assumed to take place, and $\mathbf{D}_M^{-L}$ indicates the left inverse of $\mathbf{D}_M$. In particular

$$\begin{aligned}\mathbf{W}_{UU}(z_n+,z_n-) &= \mathbf{D}_U^{-L}(z_n+)\mathbf{D}_U(z_n-) \\ &= \left[\mathbf{J}\mathbf{D}_U(z_n+)\right]^T \mathbf{D}_U(z_n-)\end{aligned}, \tag{F-20}$$

where $\mathbf{J} \equiv \begin{pmatrix} \mathbf{0}_3 & \mathbf{I}_3 \\ \mathbf{I}_3 & \mathbf{0}_3 \end{pmatrix}$.

Using equation (F-18),

$$\mathbf{W}_{UU}(z_n+,z_n-) = \left[\mathbf{J}\mathbf{K}\overline{\mathbf{D}_D}(z_n+)\right]^T \mathbf{K}\overline{\mathbf{D}_D}(z_n-). \tag{F-21}$$

To proceed further, some easily verified properties of **J** and **K** are

$$\mathbf{JK} = -\mathbf{KJ}\,,\ \mathbf{K}^T = \mathbf{K}\ \text{ and }\ \mathbf{K}^2 = -\mathbf{I}\,. \tag{F-22}$$

Using these

$$\begin{aligned}\mathbf{W}_{UU}(z_n+,z_n-) &= \left[-\mathbf{KJ}\overline{\mathbf{D}_D}(z_n+)\right]^T \mathbf{K}\overline{\mathbf{D}_D}(z_n-) \\ &= -\left[\mathbf{J}\overline{\mathbf{D}_D}(z_n+)\right]^T \mathbf{K}^2\overline{\mathbf{D}_D}(z_n-) \\ &= \left[\overline{\mathbf{D}_D}(z_n+)\right]^{-L} \overline{\mathbf{D}_D}(z_n-) \\ &= \overline{\mathbf{W}_{DD}}(z_n+,z_n-).\end{aligned} \tag{F-23}$$

So we see that once the interface propagator for down-going waves has been computed, it is trivial to obtain the corresponding propagator for up-going waves.

APPENDIX G: COMPUTATION OF THE INTERFACE PROPAGATOR FOR VERTICAL INCIDENCE

This appendix is a derivation of equations (2-35) and (2-36), which describes the interface propagator for vertical propagation across an interface between two birefringent media with identical elastic moduli, but different symmetry axes.

Consider the stiffness matrix, expressed in Voigt notation [equation (1-5)], which describes an orthorhombic medium.[1]

$$\mathbf{C} = \begin{pmatrix} C_{11} & C_{12} & C_{13} & & & \\ C_{12} & C_{22} & C_{23} & & & \\ C_{13} & C_{23} & C_{33} & & & \\ & & & C_{44} & & \\ & & & & C_{55} & \\ & & & & & C_{66} \end{pmatrix}, \qquad \text{(G-1)}$$

where, as usual, the absent entries are taken to be zero. The matrix corresponds to a coordinate frame aligned with the symmetry planes of the medium. For computation of the Christoffel matrix, it is convenient to consider the tensor form in the aligned coordinate frame, c_{ijkl}, and rotated versions of it,

$$\begin{aligned} c'_{ijkl} &= \left(\frac{\partial x'_i}{\partial x_m}\right)\left(\frac{\partial x'_j}{\partial x_n}\right)\left(\frac{\partial x'_k}{\partial x_p}\right)\left(\frac{\partial x'_l}{\partial x_q}\right) c_{mnpq} \\ &= R_{im} R_{jn} R_{kp} R_{lq} c_{mnpq} \end{aligned}. \qquad \text{(G-2)}$$

For rotation of the symmetry axis by θ about the vertical axis, the rotation matrices in equation (1-4) have the form

[1] Though orthorhombic symmetry is generally beyond the scope of this thesis, the derivation in this appendix does not require HTI assumption, and so the more general symmetry is considered.

$$\mathbf{R} = \begin{pmatrix} \cos\theta & \sin\theta & 0 \\ -\sin\theta & \cos\theta & 0 \\ 0 & 0 & 1 \end{pmatrix}. \tag{G-3}$$

The direction of propagation is assumed now to be vertical so that the slowness vector is $\mathbf{s} = \begin{pmatrix} 0 & 0 & s_3 \end{pmatrix}^T$. The Christoffel matrix in equation (1-13) then becomes [c.f. equation (2-6)]

$$\Gamma_{ik} = T_{ik} s_3^2 = c_{i3k3} s_3^2 . \tag{G-4}$$

In Voigt notation, and using the abbreviation $q \equiv s_3$, equation (G-4) reads

$$\mathbf{\Gamma} = \mathbf{T} q^2 = \begin{pmatrix} C_{55} & 0 & 0 \\ 0 & C_{44} & 0 \\ 0 & 0 & C_{33} \end{pmatrix} q^2 , \tag{G-5}$$

The plane wave solutions are then determined from substitution of (G-5) into equation (2-6). The vertical velocities are determined by the three eigenvalues, which are (assuming $C_{55} > C_{44}$)

$$q_P^2 = \frac{\rho}{C_{33}} = \frac{1}{v_P^2}, q_{S1}^2 = \frac{\rho}{C_{55}} = \frac{1}{v_{S1}^2}, q_{S2}^2 = \frac{\rho}{C_{44}} = \frac{1}{v_{S2}^2}. \tag{G-6}$$

The Christoffel matrix for a medium which has been rotated by θ relative to the coordinate axes can be computed, using equation (1-4) or the Bond transformation of equation (1-15), as

$$\mathbf{\Gamma}' = \begin{pmatrix} C_{55}\cos^2\theta + C_{44}\sin^2\theta & (C_{55} - C_{44})\cos\theta\sin\theta & 0 \\ -(C_{55} - C_{44})\cos\theta\sin\theta & C_{44}\cos^2\theta + C_{55}\sin^2\theta & 0 \\ 0 & 0 & C_{33} \end{pmatrix} q^2 . \tag{G-7}$$

Clearly the eigenvalues remain unchanged under the rotation, though the eigenvectors do change. The displacement eigenvectors are found to be

$$\mathbf{d}_P = \begin{pmatrix} 0 \\ 0 \\ 1 \end{pmatrix}, \mathbf{d}_{S1} = \begin{pmatrix} \cos\theta \\ -\sin\theta \\ 0 \end{pmatrix}, \mathbf{d}_{S1} = \begin{pmatrix} \sin\theta \\ \cos\theta \\ 0 \end{pmatrix}. \tag{G-8}$$

In order to compute the interface propagator for two such media with different symmetry axes, the first step is to obtain an expression in terms of θ for the full displacement-stress eigenvectors for the system matrix, as given in equation (2-10). Making use of equations (2-22) and (2-24), the three eigenvectors for down-going waves are found to be

$$\hat{\mathbf{b}}_P^D = (-2\rho)^{-1/2} \begin{pmatrix} 0 \\ 0 \\ 1 \\ 0 \\ 0 \\ -\rho \end{pmatrix}, \ \hat{\mathbf{b}}_{S1}^D(\theta) = (-2\rho V_{S1})^{-1/2} \begin{pmatrix} \cos\theta \\ -\sin\theta \\ 0 \\ -\rho V_{S1}\cos\theta \\ \rho V_{S1}\sin\theta \\ 0 \end{pmatrix}$$

and

$$\hat{\mathbf{b}}_{S2}^D(\theta) = (-2\rho V_{S2})^{-1/2} \begin{pmatrix} \sin\theta \\ \cos\theta \\ 0 \\ -\rho V_{S2}\sin\theta \\ -\rho V_{S2}\cos\theta \\ 0 \end{pmatrix}. \tag{G-9}$$

Similarly the three eigenvectors for up-going waves are given by

$$\hat{\mathbf{b}}_P^U = (2\rho)^{-1/2}\begin{pmatrix}0\\0\\1\\0\\0\\\rho\end{pmatrix},\ \hat{\mathbf{b}}_{S1}^U(\theta) = (2\rho V_{S1})^{-1/2}\begin{pmatrix}\cos\theta\\-\sin\theta\\0\\\rho V_{S1}\cos\theta\\-\rho V_{S1}\sin\theta\\0\end{pmatrix}$$

and

$$\hat{\mathbf{b}}_{S2}^U(\theta) = (2\rho V_{S2})^{-1/2}\begin{pmatrix}\sin\theta\\\cos\theta\\0\\\rho V_{S2}\sin\theta\\\rho V_{S2}\cos\theta\\0\end{pmatrix}. \tag{G-10}$$

Consider now two layers, separated by a horizontal interface, with the same anisotropic moduli, but with two different orientations of their symmetry planes relative to the horizontal axes, described by azimuthal angles φ for the upper layer, and θ for the lower. Using the relationship between $\mathbf{b}_i$ and $\mathbf{g}_i$ of equation (2-20), and the definition of the interface propagator in equations (2-26) and (2-27), it can be shown (after some rather tedious but straightforward algebra) that

$$\mathbf{W}_{DD}(\theta,\varphi) = \mathbf{W}_{UU}(\theta,\varphi) = \begin{pmatrix}\cos(\theta-\varphi) & -\kappa\sin(\theta-\varphi) & 0\\ \kappa\sin(\theta-\varphi) & \cos(\theta-\varphi) & 0\\ 0 & 0 & 1\end{pmatrix}, \tag{G-11}$$

and

$$\mathbf{W}_{DU}(\theta,\varphi) = \begin{pmatrix}0 & i\chi\sin(\theta-\varphi) & 0\\ i\chi\sin(\theta-\varphi) & 0 & 0\\ 0 & 0 & 0\end{pmatrix} = -\mathbf{W}_{UD}(\theta,\varphi), \tag{G-12}$$

where $\kappa = \dfrac{V_{S1}+V_{S2}}{2\sqrt{V_{S1}V_{S2}}}$ and $\chi = \dfrac{V_{S1}-V_{S2}}{2\sqrt{V_{S1}V_{S2}}}$, with the relationship

$$\kappa^2 - \chi^2 = 1. \tag{G-13}$$

As a check on the algebra, it is a requirement that the interface propagator, given by

$$\mathbf{W}(\theta,\varphi)=\begin{pmatrix}\mathbf{W}_{UU}(\theta,\varphi) & \mathbf{W}_{UD}(\theta,\varphi)\\ \mathbf{W}_{DU}(\theta,\varphi) & \mathbf{W}_{DD}(\theta,\varphi)\end{pmatrix}, \qquad \text{(G-14)}$$

has a determinant equal to unity. To check that this is the case, it is not necessary to explicitly compute the determinant, which would be somewhat arduous. Instead, it is easy to show, using equation (G-13), that

$$\mathbf{W}(\theta,\varphi)^T\mathbf{W}(\theta,\varphi)=\mathbf{I}_6, \qquad \text{(G-15)}$$

where $\mathbf{I}_6$ is the 6-by-6 identity matrix. Since $\det(\mathbf{W}^T)=\det(\mathbf{W})$, equation (G-15) can only be satisfied if $\det(\mathbf{W}(\theta,\varphi))=\pm 1$.

APPENDIX H: ADJOINT RELATIONSHIP FOR ELASTIC GPSPI AND NSPS

Margrave and Ferguson (1998) proved, for scalar extrapolation, that GPSPI in one direction is adjoint to NSPS in the opposite direction, and vice versa, under a standard inner product integral. In this appendix, a similar proof of an adjoint relationship for the elastic case is provided. The proof follows that of Margrave and Ferguson, but is made slightly more involved because it involves matrices and vectors, where commutativity cannot be assumed, and it is necessary to define a suitable inner product and adjoint.

The equations for elastic GPSPI and NSPS extrapolation, through a homogeneous medium from z_0 to z, can be written [c.f. equations (3-2) and (3-3)] as operators L_{PSPI} and L_{NSPS}, via

$$\mathbf{b}_{PSPI}(x,z,\omega) = L_{PSPI}\,\mathbf{b} = \frac{\omega}{2\pi}\int_{-\infty}^{\infty}\mathbf{P}(x,s_x,\omega)\int_{-\infty}^{\infty}\mathbf{b}(x',z_0,\omega)\exp[i\omega s_x(x'-x)]\,dx'\,ds_x\,, \qquad \text{(H-1)}$$

and

$$\mathbf{b}_{NSPS}(x,z,\omega) = L_{NSPS}\,\mathbf{b} = \frac{\omega}{2\pi}\int_{-\infty}^{\infty}\int_{-\infty}^{\infty}\mathbf{P}(x',s_x,\omega)\mathbf{b}(x',z_0,\omega)\exp[i\omega s_x(x'-x)]\,dx'ds_x\,, \qquad \text{(H-2)}$$

where

$$\mathbf{E}(x,s_x,\omega) = e^{i\omega\mathbf{\Lambda}(x,s_x)(z-z_0)}\,, \qquad \text{(H-3)}$$

$$\mathbf{\Lambda}(x,s_x) = diag\left(q^P(x,s_x) \quad q^{S1}(x,s_x) \quad q^{S2}(x,s_x)\right), \qquad \text{(H-4)}$$

and

$$\mathbf{P}(x,s_x,\omega) = \mathbf{D}(x,s_x)\mathbf{E}(x,s_x,\omega)\mathbf{D}^{-1}(x,s_x). \qquad \text{(H-5)}$$

To define an adjoint operator for either equations (3-3) or (3-4) it is first necessary to define a related inner product. Consider the following function for arbitrary displacement-stress vectors $\mathbf{b}_1$ and $\mathbf{b}_2$

$$F(\mathbf{b}_1, \mathbf{b}_2) = (\mathbf{J}\mathbf{b}_1)^H \, \mathbf{b}_2 \, . \tag{H-6}$$

where **J** is defined by equation (2-23), and $\mathbf{a}^H$ is the Hermitian transpose of a vector **a**, i.e. $\mathbf{a}^H \equiv \overline{\mathbf{a}^T}$. For real **a**, the Hermitian transpose is the same as the standard transpose. First, $F(\mathbf{b}, \mathbf{b})$ is shown to be a measure of energy, for propagating (non-evanescent) waves. Using (2-15) and (2-21), **b** is expressed in terms of the 6 eigenvectors, $\hat{\mathbf{b}}_i$, as

$$\mathbf{b} = \sum_{i=1}^{6} v_i \hat{\mathbf{b}}_i \, . \tag{H-7}$$

Now substituting (H-7) into (H-6), using (2-22) and (2-23), and recalling that all $\hat{\mathbf{b}}_i$ are real for propagating waves (though the v_i may not be)

$$\begin{aligned} F(\mathbf{b}, \mathbf{b}) &= (\mathbf{J}\mathbf{b})^H \, \mathbf{b} \\ &= \sum_{i=1}^{6} \bar{v}_i \left(\mathbf{J}\hat{\mathbf{b}}_i\right)^T \sum_{j=1}^{6} v_j \hat{\mathbf{b}}_j \\ &= \sum_{i=1}^{6} \sum_{j=1}^{6} \bar{v}_i v_j \hat{\mathbf{g}}_i^T \hat{\mathbf{b}}_j \\ &= \sum_{i=1}^{6} |v_i|^2 . \end{aligned} \tag{H-8}$$

The following inner product is now introduced

$$\begin{aligned} \langle \mathbf{b}_1, \mathbf{b}_2 \rangle &\equiv \int F(\mathbf{b}_1(x), \mathbf{b}_2(x)) \, dx \\ &= \int [\mathbf{J}\mathbf{b}_1(x)]^H \, \mathbf{b}_2(x) dx. \end{aligned} \tag{H-9}$$

To confirm that (H-9) does indeed constitute an inner product on a complex vector space, it must also be proven that

$$\langle \mathbf{a},\mathbf{b}\rangle = \overline{\langle \mathbf{b},\mathbf{a}\rangle}\ . \tag{H-10}$$

From (H-9), it is sufficient to prove that $(\mathbf{Jb}_1)^H \mathbf{b}_2 = \overline{(\mathbf{Jb}_2)^H \mathbf{b}_1}$. Making use of the definition of $\mathbf{J}$, and starting from the right hand side expression

$$\begin{aligned}(\mathbf{Jb}_1)^H \mathbf{b}_2 &= \mathbf{b}_1^H (\mathbf{Jb}_2) \\ &= \overline{(\mathbf{Jb}_2)^H \mathbf{b}_1}\end{aligned}\ .$$

Now let us define the adjoint operator $L_{PSPI}{}^{\wedge}$ for elastic GPSPI as the operator which satisfies

$$\langle L_{PSPI}\mathbf{b}_1,\mathbf{b}_2\rangle = \langle \mathbf{b}_1, L_{PSPI}{}^{\wedge}\mathbf{b}_2\rangle\ , \tag{H-11}$$

for arbitrary $\mathbf{b}_1$ and $\mathbf{b}_2$.

Evaluating the left-hand side of (H-11) gives

$$\langle L_{PSPI}\mathbf{b}_1,\mathbf{b}_2\rangle = \int_{-\infty}^{\infty}\left\{\frac{\omega}{2\pi}\int_{-\infty}^{\infty}\int_{-\infty}^{\infty}\mathbf{JP}(x,s_x,\omega)\mathbf{b}_1(x',z_0,\omega)\exp[i\omega s_x(x'-x)]dx'\,ds_x\right\}^H \mathbf{b}_2(x,z_0,\omega)dx\ . \tag{H-12}$$

Reordering the spatial integrations, and switching dummy integration variables, equation (H-12) may be written

$$\begin{aligned}\langle L_{PSPI}\mathbf{b}_1,\mathbf{b}_2\rangle &= \int_{-\infty}^{\infty}\frac{\omega}{2\pi}\int_{-\infty}^{\infty}\int_{-\infty}^{\infty}\mathbf{b}_1(x,z_0,\omega)^H\,\mathbf{P}(x',s_x,\omega)^H\,\mathbf{J}\,\mathbf{b}_2(x',z_0,\omega)\exp[i\omega s_x(x'-x)]\,dx'\,ds_x\,dx \\ &= \int_{-\infty}^{\infty}\mathbf{b}_1(x,z_0,\omega)^H\left\{\frac{\omega}{2\pi}\int_{-\infty}^{\infty}\int_{-\infty}^{\infty}[\mathbf{JP}(x',s_x,\omega)]^H\,\mathbf{b}_2(x',z_0,\omega)\exp[i\omega s_x(x'-x)]\,dx'\,ds_x\right\}dx.\end{aligned} \tag{H-13}$$

To proceed further, we need to rearrange the term $[\mathbf{JP}]^H$, using the definitions of **P**, from equation (H-5), and **J**, from equation (2-23), and using standard matrix properties

$$
\begin{aligned}
[\mathbf{JP}]^H &= \mathbf{P}^H \mathbf{J} \\
&= \left[\mathbf{D}\,\mathbf{E}(\mathbf{JD})^T\right]^H \mathbf{J} \\
&= (\mathbf{J}\overline{\mathbf{D}})\overline{\mathbf{E}}\,\overline{\mathbf{D}}^{\,T}\mathbf{J} \qquad \text{(H-14)} \\
&= \mathbf{J}\,\overline{\mathbf{D}}\,\overline{\mathbf{E}}\,\overline{\mathbf{D}}^{-1} \\
&= \mathbf{J}\,\overline{\mathbf{P}}.
\end{aligned}
$$

Substituting back into equation (H-13)

$$
\begin{aligned}
\langle L_{PSPI}\mathbf{b}_1,\mathbf{b}_2\rangle &= \int_{-\infty}^{\infty} \mathbf{b}_1(x,z_0,\omega)^H \left\{\frac{\omega}{2\pi}\int_{-\infty}^{\infty}\int_{-\infty}^{\infty} \mathbf{J}\overline{\mathbf{P}}(x',s_x,\omega)\mathbf{b}_2(x',z_0,\omega)\exp[i\omega s_x(x'-x)]\,dx'\,ds_x\right\} dx \\
&= \int_{-\infty}^{\infty} [\mathbf{J}\mathbf{b}_1(x,z_0,\omega)]^H \left\{\frac{\omega}{2\pi}\int_{-\infty}^{\infty}\int_{-\infty}^{\infty} \overline{\mathbf{P}}(x',s_x,\omega)\mathbf{b}_2(x',z_0,\omega)\exp[i\omega s_x(x'-x)]\,dx'\,ds_x\right\} dx \\
&= \langle \mathbf{b}_1, L_{NSPS}^H \mathbf{b}_2\rangle.
\end{aligned}
$$

(H-15)

By comparison with equation (3-4), when L_{PSPI} describes downward extrapolation with GPSPI, the adjoint operator L_{NSPS}^H describes upward extrapolation with NSPS.

APPENDIX I: MULTIPLE REFERENCE VELOCITY COMPOSITION-DECOMPOSITION

In this appendix, an algorithm for interpolating the isotropic composition and decomposition operators is described. The algorithm is not exact in the case of variable V_P / V_S, but is an acceptable approximation when V_P / V_S variation is moderate. To simplify notation, the layer index is dropped, to write the recomposition and decomposition matrices as $\mathbf{D}$ and $\mathbf{D}^{-1}$.

As given in equation (4-5) the displacement-stress vector $\mathbf{b}$ can be written as the sum of three displacement-stress vectors corresponding to the three modes

$$\begin{aligned}\mathbf{b} &= \mathbf{Dv} \\ &= \begin{pmatrix}\hat{\mathbf{b}}_P & \hat{\mathbf{b}}_{SH} & \hat{\mathbf{b}}_{SV}\end{pmatrix}\begin{pmatrix}v_P \\ v_{SH} \\ v_{SV}\end{pmatrix}. \\ &= \mathbf{b}_P + \mathbf{b}_{SH} + \mathbf{b}_{SV}\end{aligned} \tag{I-1}$$

The qualifiers SH and SV are used rather than S1 and S2, since isotropy is assumed here.

The wave-mode specific displacement-stress vectors $\mathbf{b}_P, \mathbf{b}_{SH}$ and $\mathbf{b}_{SV}$ may be stored separately. Since the spatial variation of P- and S-wave velocities is not necessarily according to a constant ratio, at any given output location x the total displacement-stress vector $\mathbf{b}(x, z, \omega)$, a combination of these vectors, will be obtained using different reference values.

For example, assume a set of reference media $J = 1, \ldots, N$ such that $\alpha_J = \gamma_{ave} \beta_J$. Define the reference vectors using (4-5) with each reference medium as $\mathbf{b}_{P,J}$ and $\mathbf{b}_{SV,J}$ ($\mathbf{b}_{SH}$ is independent of any parameters – and can be completely decoupled). Suppose at $x = x_0$, the local P-wave velocity α is between α_J and α_{J+1}, whereas the S-wave velocity β is between β_K and β_{K+1}, with $J \neq K$. Then we have:

$$\mathbf{b}_P(x,z,\omega)=\lambda_P\mathbf{b}_{P,J}+(1-\lambda_P)\mathbf{b}_{P,J+1}, \qquad \text{(I-2)}$$

and

$$\mathbf{b}_{SV}(x,z,\omega)=\lambda_S\mathbf{b}_{SV,K}+(1-\lambda_S)\mathbf{b}_{SV,K+1}, \qquad \text{(I-3)}$$

where

$$\lambda_P=\frac{\alpha_{J+1}-\alpha}{\alpha_{J+1}-\alpha_J} \text{ and } \lambda_S=\frac{\beta_{K+1}-\beta}{\beta_{K+1}-\beta_K}.$$

As noted in Appendix C, the vectors $\hat{\mathbf{b}}_P$ depend on both α and β, whereas the vectors $\hat{\mathbf{b}}_{SV}$ only depend upon β. So the only approximation involved in the above is using β_J rather than β_K within equation (I-2). If the variation of V_P/V_S is not large, the error involved can be expected to be small.

Similarly, for decomposition, we can write:

$$\begin{aligned}\mathbf{v}&=\mathbf{D}^{-1}\mathbf{b}\\&=\begin{pmatrix}\hat{\mathbf{g}}_P & \hat{\mathbf{g}}_{SH} & \hat{\mathbf{g}}_{SV}\end{pmatrix}^T\left(\mathbf{b}_P+\mathbf{b}_{SH}+\mathbf{b}_{SV}\right)\end{aligned}, \qquad \text{(I-4)}$$

where, from equation (2-23),

$$\hat{\mathbf{g}}_M=\mathbf{J}\hat{\mathbf{b}}_M.$$

Equation (I-4) can be evaluated directly, using appropriate reference velocities to compute $\hat{\mathbf{g}}_P$ and $\hat{\mathbf{g}}_{SV}$ - where again $\hat{\mathbf{g}}_{SH}$ is parameter-free and decouples. As for the composition equation, $\hat{\mathbf{g}}_P$ is evaluated with the correct α, but a possibly incorrect β, constrained by the average V_P/V_S ratio. In terms of reference vectors, they are written [c.f. equations (I-2) and (I-3)]

$$\hat{\mathbf{g}}_P(x,z,\omega)=\lambda_P\hat{\mathbf{g}}_{P,J}+(1-\lambda_P)\hat{\mathbf{g}}_{P,J+1}, \qquad \text{(I-5)}$$

and

$$\hat{\mathbf{g}}_{SV}(x,z,\omega)=\lambda_S\hat{\mathbf{g}}_{SV,K}+(1-\lambda_S)\hat{\mathbf{g}}_{SV,K+1}. \qquad \text{(I-6)}$$

The result, taking into account the decoupling of the SH mode, is

$$\mathbf{v} = \begin{pmatrix} \hat{\mathbf{g}}_P^T \mathbf{b}_P \\ 0 \\ \hat{\mathbf{g}}_{SV}^T \mathbf{b}_P \end{pmatrix} + \begin{pmatrix} 0 \\ \hat{\mathbf{g}}_{SH}^T \mathbf{b}_{SH} \\ 0 \end{pmatrix} + \begin{pmatrix} \hat{\mathbf{g}}_P^T \mathbf{b}_{SV} \\ 0 \\ \hat{\mathbf{g}}_{SV}^T \mathbf{b}_{SV} \end{pmatrix}. \qquad \text{(I-7)}$$

The cross-over terms $\hat{\mathbf{g}}_P^T \mathbf{b}_{SV}$ and $\hat{\mathbf{g}}_{SV}^T \mathbf{b}_P$ correspond to mode converted energy. Alternatively, the mode conversions can be neglected, to give

$$\mathbf{v}' = \begin{pmatrix} \hat{\mathbf{g}}_P^T \mathbf{b}_P \\ \hat{\mathbf{g}}_{SH}^T \mathbf{b}_{SH} \\ \hat{\mathbf{g}}_{SV}^T \mathbf{b}_{SV} \end{pmatrix}. \qquad \text{(I-8)}$$

Use of equation (I-8) rather than (I-7) essentially reduces the elastic migration to a set of scalar migrations which handle transmission effects.